ABSTRACT

Title of Document: QUANTIFYING PARTICLE PROPERTIES
FROM ION-MOBILITY MEASUREMENTS.

Mingdong Li, Doctor of Philosophy, 2012

Directed By: Michael R. Zachariah, Professor
Chemical Physics Program
Department of Mechanical Engineering and
Chemistry

Nanoparticles have received considerable interest due to the wide variety of potential applications in biomedical, optical, and electronic fields. However, our capabilities for quantitatively charactering these materials, for example in number concentration or shape are limited. The objective of this work is to develop experimentally verified theories to quantify particle properties from aerosol based ion-mobility measurement.

The use of aerosol tools is predicated on the idea that these methods offer the best chance for quantification, due to a better understanding of the physics of ion transport in the gas phase. Nevertheless this does not preclude us from using these techniques to characterize particles in liquids as will be show in the first part of this work which resolves problems associated with generating an aerosol from colloidal suspensions. In this dissertation I resolve the problem of artificial “droplet induced aggregation” during electrospray which can corrupt the eventual determination of particle size. I develop an experimentally verified statistical based model, to determine and correct this undesired artifact. Furthermore, I have found that this nominally undesired artifact can be used in a beneficial way that allows one to determine the absolute number concentration of nanoparticles in solution, without the need for calibration particles.

Mobility is one of the most important and fundamental properties of a particle. However most particle characterization approaches interpret the results of mobility measurement in the context of spherical particle transport. I have undertaken to systematically explore the mobility properties of non-spherical particles. In this dissertation I develop a theory to quantify the effect of orientation on the mobility and the dynamic shape factor of charged axially symmetric particles in an electric field. The experimental results of well-defined doublets of NIST traceable size standard 127nm, 150nm, 200nm and 240nm PSL spheres are shown to be in excellent agreement with the expected values based on my theory. More general new theories of the mobility of nonspherical particles are also proposed and compared with current theories.

I also propose a new instrument, a pulsed differential mobility analyzer (PDMA), to obtain shape information by measuring the electrical mobility under different electric fields.

QUANTIFYING PARTICLE PROPERTIES FROM ION-MOBILITY MEASUREMENTS.

By

Mingdong Li.

Dissertation submitted to the Faculty of the Graduate School of the
University of Maryland, College Park, in partial fulfillment
of the requirements for the degree of
[Doctor of Philosophy]
[2012]

Advisory Committee:
Professor [Michael R. Zachariah], Chair
[Professor George W. Mulholland]
[Professor Sheryl H. Ehrman]
[Professor Kenneth T. Kiger]
[Professor Santiago De Jesus Solares]

Dedication

To

My parents

Xiangqian Li and Renfang Guo,

My wife

Bingqing Cui

And my son

Evan Yuanhao Li.

Thank you for your unconditional love.

Acknowledgements

I owe my gratitude to all the people who have made this dissertation possible. First and foremost, I am deeply indebted to my advisor, Professor Michael R. Zachariah, for his generous support and guidance throughout the years of my graduate study. Without his invaluable suggestions and experience, this dissertation would not have been possible. I have been amazingly fortunate to have him as my advisor. His advice in my research, career and life has been one of my most valuable assets throughout my life.

I thank my co- adviser, Dr. George W. Mulholland for his consistent instructions during my graduate research. I am grateful for everything Professor Mulholland has done for me from the bottom of my heart.

I would like to thank Professor Kenneth T. Kiger, Professor Sheryl Ehrman, and Professor Santiago De Jesus Solares, for serving on my defense committeetaking time to edit my dissertation, attending my defense and giving me valuable suggestions. I also owe my sincere gratitude to the director of Chemical Physics Program, Professor Michael Coplan, who has always been there when I have troubles and need help. I would also like to give special thanks to my colleague Dr. Suvajyoti Guha, who showed me how to operate Electrospray and DMA during my first year of graduate research and collaborated with me for some experiments in this group.

Most importantly, none of this would have been possible without the unconditional love, patience and support from my family. My family, to whom this dissertation is dedicated to, has been a constant source of love and strength. I am indebted to my parents for raising me and providing me with extensive educational opportunities. I am grateful to my wife, Bingqing Cui, for continuously encouraging me and to my son, Evan Li, for being my lucky star. I would like to express my heart-felt gratitude to my family.

Table of Contents

Dedication ii

Acknowledgements iii

Table of Contents v

List of Tables ix

List of Figures xii

Chapter 1: Introduction 1

- 1.1 Aerosols 2
- 1.2. Particle Characterization and Ion-mobility Measurement 3
  - 1.2.1.Size, shape, mobility and measurement methods 4
  - 1.2.2.Instruments used for online measurement of mobility/mobility size distribution. 8
- 1.3. Scope of the Dissertation 15

Chapter 2: Quantification and Compensation of Non-specific Analyte Aggregation in Electrospray Sampling 22

- 2.1. Introduction 22
- 2.2. Theory 25
  - 2.2.1 Physical Aggregation (droplet induced aggregation) of identical particles 25
  - 2.2.2 Quantitative determination of intrinsic aggregates in solution 27
- 2.3. Materials and Methods 36
  - 2.3.1. Gold (Au) nanoparticle (NP) preparation 36
  - 2.3.2. Rmab solution preparation 37
  - 2.3.3. Particle Measurements 37
  - 2.3.4. Droplet size Measurements 38
- 2.4. Results and Discussion 39
  - 2.4.1 Evidence of droplet induced aggregation 39
  - 2.4.2 Intrinsic Dimer determination (Irreversible/Reversible, Total concentration known): Oligomerization of Rmab 45
  - 2.4.3 Intrinsic Dimer determination (Irreversible aggregation): Au-NPs 47
  - 2.4.4. Reversible oligomerization: the relationship between real equilibrium constant, K, and apparent equilibrium constant, K_{app} 50
- 2.5. Summary of Cases and Formulas 53
  - 2.5.1. Intrinsic Dimer determination (Irreversible/Reversible; Total concentration known; Monomodal and narrow droplet size distribution $f(D_d)$): 54
  - 2.5.2. Intrinsic Dimer determination (Irreversible/Reversible; Total concentration known; Bimodal droplet size distribution $f(D_d)$): 54
  - 2.5.3 Intrinsic Dimer determination (Irreversible aggregation): 55
- 2.6. Conclusions 55
- 2.7. Supplemental Information 55
  - Appendix A. 55

Appendix B. ... 59
Chapter 3: Method for Determining the Absolute Number Concentration of Nanoparticles from Electrospray Sources ... 62
3.1. Introduction ... 62
3.2. Materials and Experimental Methods ... 63
3.2.1. Gold nanoparticle preparation ... 63
3.2.2. Rmab solution preparation ... 64
3.2.3. Electrospray Particle Generation and Differential Mobility Measurements ... 65
3.2.4. Droplet Size Measurements ... 66
3.3. Theory of Determining the Absolute Number Concentration ... 67
3.3.1. Droplet induced aggregation of identical particles (monomers) from droplets of identical size generated by ES ... 69
3.3.2. Droplet induced aggregation of monomers and dimers in solution from droplets : General case ... 70
3.4. Results and Discussion ... 74
3.4.1. Determination of absolute number concentrations by serial dilution ... 74
3.4.2. Determination of absolute number concentrations by changing droplet size: Application to measurement of Rmab protein ... 80
3.5. Summary of Limiting Cases and Corresponding Formulas ... 84
3.5.1. Monomodal and narrow droplet size distribution, $f(D_d)$ ... 84
3.5.2. Bimodal droplet size distribution, $f(D_d)$ ... 85
3.6. Conclusions ... 86
3.7. Supporting Information ... 87
S1: Two approximations for quantifying droplet induced dimers under some limiting conditions ... 87
S2: Combining the approximations above with two experimental strategies, serial dilution and changing droplet size, to obtain absolute number concentration of nanoparticles and protein in solution. ... 90
S3: ... 93
Chapter 4: The Effect of Orientation on the Mobility and Dynamic Shape Factor of Charged Axially Symmetric Particles in an Electric Field ... 95
4.1. Introduction ... 95
4.2. Theory ... 97
4.2.1. Orientation-Averaged-Mobility for axially symmetric particles ... 97
4.2.2. Drag force, F_{drag} , and the expression of $K_{\parallel}$ and $K_{\perp}$ ... 100
4.2.3. Orientation distribution $f(\theta)$, and the expression of $<\cos^2\theta>$ ... 101
4.2.4. Voltage – Shape Information Relationship in a DMA Measurement (Step Mode) ... 105
4.2.5 Evaluation of Mobility for Special Cases. ... 106
4.3. Results and Discussions ... 108
4.3.1. Electrical mobility as a function of applied electric field ... 109
4.3.2 Experimental Validation ... 110
4.3.3. Defining the Dynamic Shape Factor ... 114
4.4. Conclusions ... 118
4.5. Appendix. ... 118

A1. Expressions for $K_{\parallel}$ and $K_{\perp}$. ... 118
A2. The expression of two principal components of polarizability, $\alpha_{\parallel}$ and $\alpha_{\perp}$ of prolate spherical particles. ... 121
A3. Voltage – Shape Information Relationship for axisymmetric particles in a DMA Measurement ... 122
4.6. Supporting Information ... 124
Chapter 5: Mobility and Dynamic Shape Factor of Particle Doublets in Electric Fields ... 134
5.1. Introduction ... 134
5.2. Materials and Experimental Methods ... 136
5.3. Results and Discussions ... 137
5.3.1. Measurement of dynamic shape factor. ... 137
5.3.2. Theoretical Development of the Dynamic Shape Factor of an Axisymmetric Particle in an Electric Field ... 143
5.4. Conclusions ... 147
Chapter 6: Understanding the Mobility of a Non-spherical Particle ... 148
6.1. Introduction ... 148
6.2. Theory ... 152
6.2.1. Mobility of a nonspherical particle from the Averaged-Cross-Section .. 152
6.2.2. Mobility of a non-spherical particle from Averaged-Drif-Velocity ... 157
6.2.3. Mobility of a nonspherical particle from Averaged-Drag-Force Approach ... 160
6.3. Materials and Experimental Methods ... 163
6.4. Results and Discussions ... 164
6.4.1. The prerequisite of three approaches ... 164
6.4.2. Comparing three approaches by applying to a rod in fully random orientation. ... 171
6.4.3. Comparing three approaches with the experimental result for TMV ... 173
6.4.4. Comparing three approaches with the calculation results for GroEL in literature ... 175
6.5. Conclusion ... 176
6.6. Appendix. ... 177
A.1. Particle body fixed coordinate, space fixed coordinate and Euler angles φ, ψ, θ ... 177
A.2. Simplifying the averaged cross-section integral in Eqn.(6-5) for a convex particle with hard collisions ... 182
A.3. Orientation distribution due to Brownian rotation ... 185
Chapter 7: Development of a Pulsed-Voltage Differential Mobility Analyzer: A Method for Measuring Shape Parameters for Non-Spherical Particles. ... 187
7.1. Introduction ... 187
7.2. Theoretical models for shape measurement ... 190
7.2.1 Orientation-Averaged-Mobility for Axisymmetric Particles ... 191
7.2.2 Orientation-Averaged-Mobility for Prolate Ellipsoid: Applied to General Agglomerate Structure ... 193

    7.2.3 Voltage – Shape Information Relationship in a DMA Measurement (Step Mode) 195
  7.3. Pulsed Differential Mobility Analyzer (PDMA) 196
  7.4. Experimental 200
    7.4.1. Alignment effects of non-spherical particles in an electric field. 200
    7.4.2. Pulser system and PDMA Evaluation 203
  7.5. Results and Discussion 205
    7.5.1. Evidence for the alignment effect of non-spherical particles in a constant electric field 205
    7.5.2. The alignment effect of non-spherical particles in a pulsed electric field 208
  7.6. Conclusion 213
Chapter 8: Conclusion and Future Work 215
  8.1. Conclusion 215
  8.2. Future Work 218
    8.2.1. On the Potential of using Bio-Nanoparticles as Standard Reference Materials for Mobility Calibration 218
    8.2.2. Droplet Size Measurements 222
    8.2.3. Pursuing a general theory to quantify the mobility of non-spherical particles 223
Bibliography 224

List of Tables

Chapter 2

Table 2-1. Ratios of observed dimers to monomers from DMA measurement by varying the ES droplet volumes, and the ratios of dimers to monomers after correction for drop induced dimers based on our model (the strategy in Section 2.4.2) for Rituxan at concentration of 100 μg/mL at pH 7 in 20 mmol/L ammonium acetate buffer. ……………………………………………………………………………..44

Table 2-2. The ratios of observed dimers to monomers at pH 7 from DMA measurement, the ratios of intrinsic dimers to monomers calculated based on Eqn. (2-22, 2-30) and the ratio of dimers to monomers measured by Analytical Ultracentrifuge for Rmab……………………………………………………………46

Table 2-3. Ratios of observed dimers to monomers from DMA measurement, and the ratios of intrinsic dimers to monomers calculated based on Eqn. (2-32) for 10nm Au-NPs. ………………………………………………………………………………49

Chapter 3

Table 3-1. Comparison of ES-DMA measured concentrations for the 1× Au-NPs samples and that of UV/VIS of Au-NPs (sample #1 to sample #4). For each sample, the total number concentration of monomer whether free or aggregated, Cp1+ 2Cp2, is calculated and compared with the total number concentration obtained from UV/VIS and supplier specification…………………………………………………...…76

Table 3-2. The total number concentrations of monomer whether free or aggregated of 1× Rituxan sample, C_{p1}+ $2C_{p2}$, are calculated based on the observed numbers of monomer and dimer measured with ES-DMA-CPC at various dilutions at pH7 in 20 mmol/L ammonium acetate buffer and the dilution-method, Eqn.(3-13,3-14). The values then are compared with the known total number concentration, 100 μg/mL...79

Table 3-3. The ratios of observed dimers to monomers for Rmab measured in ES-DMA experiments at pH 7 and at a concentration 100 μg/mL with the chamber pressures in ES at 3.0 psi (2.07*10^4 Pa) and 3.7 psi (2.55*10^4 Pa). For each experiment, the total number concentration of monomer whether free or aggregated, C_{p1}+ $2C_{p2}$, is calculated based on Eqns. (3-7) (3-12) and compared with the known total concentration, 100 μg/mL……………………………………………………83

Chapter 6

Table 6-1. Summarizing three approaches in Section 6-2 for the expressions of drag force and electric mobility of non-spherical particles……………………….……...162

Table 6-2. The criterion values of τ_0 / τ_t are calculated for various diameters and aspect ratios of rods. For each rod with random orientation, the corresponding averaged projected diameter and the mobility diameters from Averaged-Drift-Velocity and Averaged-Drag-Force approaches, respectively, are also shown. …...169

Table 6-3. The experimental mobility diameter from DMA is compared with the three diameters calculated from three approaches. The diameter from averaged-drift-velocity approaches shows the closed value to experimental value as expected.…………………………………………….....…………………..174

Table 6-4. Using the three approaches in this work and approximating GroEL as a rod with length =14.3nm and diameter =13.3nm accounting for the finite diameter of air 0.3nm, we calculated the results of GroEL in the table, and compared to the values from software program using the crystal structure of GroEL, and also compared with the value calculated from Hogan’s model…………………….………………175

Chapter 7

Table 7-1. The experimental conditions on which the system yields data for low electric field and high electric field..…………………………...……….…….204

Chapter 8

Table 8-1. Full Width at Half Maximum normalized by Mean of the size distributions of Au, PSL and Bio colloidal nano-particles in Fig. 8-1 and 8-2…………….….221

List of Figures

Chapter 1

Figure 1-1. The instruments used for mobility/mobility size distribution online measurement……………………………………………………………………….….……8

Figure 1-2. An example of a size distribution result of an aggregate using ES-DMA-CPC technique………………………………………………………………..….9

Figure 1-3. A schematic diagram of a constant output atomizer……………………10

Figure 1-4. Schematic of an electrospray (ES)…………………..………………12

Figure 1-5. Schematic diagram of a cylindrical DMA……….…………………..13

Figure 1.6. A schematic of an ultrafine CPC. …………………………..………15

Chapter 2

Figure 2-1. Physical representation of the probability distribution of induced and intrinsic aggregate distributions from electrospray. ………….………………….…..28

Figure 2-2. (a). ES monomodal and narrow droplet size distribution (20 mmol Ammonium Acetate with the chamber pressure in ES at PSI 3.7(2.55*10^4 Pa) and a carrier gas in ES of 1 L/min purified air and 0.2 L/min carbon dioxide) for Rituxan samples in section 2.4.1.1 and 2.4.2. **(b).** ES droplet with a bimodal size distribution (2 mmol Ammonium Acetate with the chamber pressure in ES at PSI 3.7(2.55*10^4 Pa) and a carrier gas in ES of 1 L/min purified air and 0.2 L/min carbon dioxide) for Au-NPs sample #1 and sample #2 in section 2.4.3…………………………….…32

Figure 2-3. ES monomodal and narrow droplet size distribution (20 mmol Ammonium Acetate with the chamber pressure in ES at PSI 3.7(2.55*10^4 Pa) and a carrier gas in ES of 1 L/min purified air and 0.2 L/min carbon dioxide). The monomodal approximation can be improved by using three average droplet volumes in three regions and solving Eqn.(2-20) and (2-21)……………………………….……34

Figure 2-4. The observed ES-DMA size distributions of Rituxan concentration at 5 µg/mL (star), 10 µg/mL (circle), 25 µg/mL (triangle), 50 µg/mL (square), and 100 µg/mL (rhombus) at pH7 in 20 mmol/L ammonium acetate buffer with the chamber pressure in ES at PSI 3.7(2.55*10^4 Pa)……………………………………………40

Figure 2-5. The ratios of dimer to the total number of dimer and monomers at pH 7 observed by ES-DMA as a function of Rituxan concentration at 5 µg/mL, 10 µg/mL, 25 µg/mL, 50 µg/mL, and 100 µg/mL (rhombus). Ratios from droplet induced dimers (line with filled square) at the same concentrations calculated based on Eqn. (2-6)...42

Figure 2-6. ES droplet size distributions at pH 7 in 20 mmol/L ammonium acetate buffer. The triangle, rhombus and circle distributions are those of the same sample with the chamber pressure in ES at 2.3 PSI (1.59*10^4 Pa), 3.0 PSI (2.07*10^4 Pa) and 3.7 PSI (2.55*10^4 Pa) respectively…………………………..…………………..…44

Figure 2-7. ES-DMA size distributions of 10 nm Au-NPs, sample #1. The rhombus, square and triangle data markers are those of 2-times, 4-times and 8-times dilutions of the original sample, respectively. Each of the discernable oligomer peaks are labeled. respectively. ………………………………………………………………………49

Figure 2-8. The fraction of insulin dimer vs. insulin total in the concentration range of 2mol/L to 200mol/L at pH 3.3 and 22°C (rhombus) as measured by Nettleton et al.[1] using Nano-ES/MS (line with open diamonds). The ratio of dimer / (monomer +

dimer) calculated by Eqn. (2-37) using the droplet induced dimer for the concentration range of 2mol/L to 200mol/L (line with filled squares). ……………..…52

Figure 2-S.1. *b* particles randomly distributed in *a* droplets………………………..56

Figure 2-S.2. No dimers. ……………………………………………………………..57

Figure 2-S.3. One dimer and remainder are monomers……………………………..57

Chapter 3

Figure 3-1. Schematic of electrospray process showing the resulting measured particle size distribution observed due to droplet induced aggregation. There are no intrinsic dimers in the original solution. However, after the ES, induced dimers are observed in the analytical spectrum and statistical analysis can be used to deduce the original monomer concentration in solution . The y-axis label "dN/dD_p" is defined by the total number of particles in the range [D_p, D_p+ dD_p] divided by the size interval, $dD_{p.}$ …………………………………………………………………………….…68

Figure 3-2. (a). ES monomodal and narrow droplet size distribution measured from sucrose at 20 mmol Ammonium Acetate buffer (section3.2.4), and used for Rmab samples at the same buffer condition in section 3.4.1.ii. **(b).** ES droplet with a bimodal size distribution measured from sucrose at 2 mmol Ammonium Acetate buffer (section3.2.4), and used for Au-NPs sample #3 and sample #4 in section 3.4.1.i. The y-axis label "dN/dD_p" is defined by the total number of particles in the range [D_p, D_p+ dD_p] divided by the size interval, dD_p……………………………….……...72

Figure 3-3. ES-DMA size distributions of 10 nm Au-NPs, sample #4. The rhombus, square and triangle data markers are those of 2-times, 4-times and 8-times dilutions of the original sample, respectively. Each of the discernable oligomer peaks are labeled.

The y-axis label "dN/dD_p" is defined by the total number of particles in the range [D_p, D_p+ dD_p] divided by the size interval, dD_p……………………………………………76

Figure 3-4. The total number concentration of monomer whether free or aggregated, C_{p1}+ $2C_{p2}$, calculated based on Eqn.(3-10) and (3-11) is divided by the total number concentration $C_{uv\text{-}vis}$ obtained from UV/VIS and vendor specification. The x-axis is the experiment index number. The circle and rhombus symbols are those for 2x and 4x dilution pairs and for 4x and 8x dilution pairs, respectively. Lower dilution pairs (solid circles) provide more accurate results…………………………………….……..78

Figure 3-5. (a). ES droplet size distributions measured from sucrose at pH 7 in 20 mmol/L ammonium acetate buffer(section3.2.4) at pressures of 3.0 psi ($2.07*10^4$ Pa) (open symbols) and 3.7 psi ($2.55*10^4$ Pa)(closed symbols). **(b)**. Observed ES-DMA size distributions of Rmab at pH7 in 20 mmol/L ammonium acetate buffer at chamber pressures of 3.0 psi ($2.07*10^4$ Pa) (open symbols) and 3.7 psi ($2.55*10^4$ Pa) (closed symbols). Each of the discernable oligomer peaks are labeled. The y-axis label "dN/dD_p" is defined by the total number of particles in the range [D_p, D_p+ dD_p] divided by the size interval, d$D_{p…}$……………………………..…………………81

Figure 3-S1. Equivalent final droplet size measurement using sucrose solution in section 3.2.4, where C_s is the sucrose concentration (volume to volume) and D_s is the dried sucrose diameter…………………………………………...………………..94

Chapter 4

Figure 4-1. Theoretical calculations of our theory and Kim's theory on the effect of the electric field on the scaled mobility, $(Z_p\text{-}Z_{p,random})/\ Z_{p,random}$, for nanowires with diameter d_f=15nm and various aspect ratios in free molecular regime. (30,000 v/cm is the air breakdown limit.)……………………………………………………………110

Figure 4-2. Comparison of theoretically predicted nanowire length: curves are for nanowires random rotating, fully aligned and aligned by combined energy (i.e. free charge+polarization), respectively, with the lengths measured by TEM analysis in Kim et. al. (2007), as a function of electrical mobility diameter measured with DMA. The drag force expressions of rod in both free molecular and transition regimes are used……………………………………………………………………………………112

Figure 4-3. The relative combined electrical energy (i.e. free charge+polarization) in Eqn. (4-20) at $\theta=0$ to thermal energy is shown as a function of experimentally measured electrical mobility diameter (D_m). At each points, the dipole polarization energy (U_p) normalized by the energy from free charge (U_e) at $\theta=0$ is plotted. The drag force expressions of rod in both free molecular and transition regimes are used in computing the aspect ratios……………………………………………………………113

Figure 4-4. Direction of drag force and velocity for a nonspherical particle and reference sphere used in the definition of dynamic shape factor are shown. The drift velocity of the nonspherical particle has components other than just the direction of the external force. The left side of this figure shows the basis of the widely-used shape factor , while the right side shows the basis of our proposed definition of dynamic shape factor………………..……………………………………………..114

Chapter 5

Figure.5-1. Three mobility size distributions of PSL particles with 149.4nm primary particle diameter measured at 2 l/min, 8 l/min and 15 l/min sheath flow rates in a step mode DMA. The mobility diameter of doublets decreases with increasing sheath flow rate, which corresponds to increase the magnitude of electric field, while the mobility diameter of singlets does not change. This figure shows clearly the alignment effect of the electric field for doublets of PSL particles……………………………….……139

Figure 5-2. The opened symbols are measured dynamic shape factors (DSF) of the doublets of 127.1nm, 149.4nm, 202.4nm, and 239.9nm primary PSL spheres based on Eqn.(5-3) for various magnitudes of electric field, which are corresponding to various sheath flow rates (Q_{sh} from 1.5 l/min to 20 l/min) in a step mode DMA. The dashed curves are theoretical DSF values from our model calculated based on Eqn. (5-4) with the permittivity of particles chosen as infinity. The filled symbols are theoretical DSF values at two limits, fully random (low electric field) and fully aligned (high electric field), based on Dahneke (1982)[2] and Cheng et al. (1988)[3]....140

Figure 5-3. **(a)** The orientation probability density sin(θ)f(θ) versus θ (where $\int_0^{\pi} f(\theta)\sin\theta d\theta=1$) for the doublet of 149.4nm primary spheres at various electric fields. **(b)** The orientation probability density sin(θ)f(θ) versus θ at a fixed electric field (5k volts/cm) for doublets of various size primary spheres…………………..….142

Figure 5-4. The square symbols and triangle symbols are measured dynamic shape factors (DSF) of the doublets of 103.6nm and of 100.7nm primary PSL spheres based on Eqn.(5-1,5-2) for various magnitudes of electric field, which are corresponding to various sheath flow rates (Q_{sh} from 1.5 l/min to 30 l/min) in a step mode DMA. The curves are theoretical DSF values from our model calculated based on Eqn. (5-4) with $\chi_{\parallel}$ = 1.003 from Figure 52 and with the relative permittivity of particles equal to infinity. Our theoretical curves with the relative permittivity of particles equal to infinity are off the experimental results with unknown reason……….……………145

Chapter 6

Figure 6-A.1. Three Euler angles φ, ψ, θ, relate the particle body fixed coordinate system (x', y', z') to the space fixed coordinate system (x, y, z)………….……….178

Figure 6-A.2. Demonstrating an incident molecule hitting small area dS on a convex particle and showing the relationship between the angle χ and angle ζ. ………….…..183

Chapter 7

Figure 7-1. Axisymmetric particles, for example a nanowire, alignment in a uniform electric field with charge at the end of the wire. …………………….…………....192

Figure 7-2. Theoretical calculation of the effect of t electric field on the scaled mobility for various aspect ratios for a prolate ellipsoid with minor axis 2b =15nm . 30,000 v/cm is the air breakdown limit……………………………………………194

Figure. 7-3 Oscillating electric field to align particles (wires or aggregates). In this example, the pulse frequency is 100Hz, the duty cycle is 50%, with a 2000 volts pulse on …………………………………………………………………...…..197

Figure. 7-4. Illustration of the relationship between the electric field and the pulse width to maintain a constant average field. Duty cycles vary from 100% , 50% to 25% with pulse frequency 100Hz, and the corresponding fields are 1000, 2000 and 4000 kV/m respectively. ………………………………………………….….…198

Figure 7-5 Measurement system with the first DMA used to separate mono-mobility particles and the pulsed DMA to both separate spheres from nanowires and to measure the aspect ratio of the nanowires……………………………………..…199

Figure 7-6. Schematic illustration of the mobility distribution of particles exiting the DMA-PDMA system. …………………………………….…………………..…199

Figure 7-7. Schematic of pulser system for generating square wave high voltage pulses. ……………………………………….…………………………..…203

Figure 7-8. Three mobility size distributions of PSL particles with 149.4 primary particle diameter measured at 4 lpm, 8 lpm and 18 lpm sheath flow rates in a step mode DMA. The mobility diameter of doublets decreases with increasing sheath flow rate, which corresponds to increase the magnitude of electric field, while the diameter of singlets does not change. This figure demonstrates clearly the alignment effect of the electric field for doubles of PSL particles. ……………………………….…206

Figure 7-9. The mobility size of TMV nanorod (a straight rigid rod which has a length $L_r \approx$ 300nm and diameter $d_r \approx$ 16-18nm) [4]. measured at 2 lpm, 3 lpm and 20 lpm sheath flow rates in a step mode long-DMA, and at 3lpm, 10lpm and 20 lpm sheath flow rates in a homemade high electric field DMA. The mobility diameter of TMV decreases with increasing the magnitude of electric field. This figure shows clearly the alignment effect of the electric field for TMV nanorod. ……………..…..207

Figure 7-10. The PSL 127.1nm and 200nm spheres were mixed in one sample, and then measured at DC voltages using a traditional long-DMA at sheath flow rates Q_{sh} =3 lpm and Q_{sh} =12 lpm. The same sample was also measured in a PDMA with flow rates Q_{sh} =3 lpm and duty-cycle=1/4 at 1Hz, 2Hz, 5Hz, 10Hz, 50Hz, 200Hz and 500Hz. The sheath flow rates and duty cycles were calibrated by making the first singlet peaks showing exactly as 127.1nm. The mobility sizes of the second singlet peaks (200nm PSL) are presented after calibrations……………………………..…209

Figure 7-11. Doublet mobility size shift of 149.4nm PSL particles with respect to the low DC voltage 3 lpm case as a function of pulse frequency, The zero frequency condition is the high DC voltage 12 lpm case. ……………………..……………..210

Chapter 8

Figure 8-1. The Size distributions of commonly used reference materials, Au10nm, Au 20nm, Au 30nm, Au 60, PSL 20nm, PSL 30nm,PSL 60nm, and PSL 100nm, which are non-bio particles……………………………….………………….………..219

Figure 8-2. The Size distributions of examples of bio particles which have potential as reference materials…………………………………………………………….220

.

Chapter 1: Introduction

Aerosol systems cover particles of a wide range of sizes, varying from millimeters to nanometers. In particular, aerosols sized between 1 and 100 nanometers, commonly referred to as nanoparticles, have received considerable interest for a wide variety of potential applications in biomedical, optical, and electronic fields. Critical for those applications are the physical understanding and experimental measurements of the properties of aerosols. Mobility is one of the most important and fundamental properties. Furthermore, with vapor-phase dispersion methods, colloidal particles in solution can now be converted to aerosol particles, and therefore can be examined using aerosol techniques by avoiding the complicated effects in a liquid environment, for instance, the online measurement of mass distribution of colloidal particles using Electro-Mass spectrometry. However, the conversion process itself may also cause problems. For example, one concern is that two or more analyte molecules or particles can potentially occupy a volume encompassing what becomes a final electrosprayed droplet. Upon evaporation of the final droplet, artificial aggregation is induced.

The findings in this dissertation fall into two main areas. The first is to study the ion mobility measurement of colloidal nanoparticles using electrospray technique. I developed a statistical model, called 'droplet-induced-aggregation' model to determine the extent to which the electrospray process induces the formation of nonspecific dimers and higher order aggregates, and to correct this undesired artifact. This model has been experimentally verified using monodispersed Au nanoparticles and protein colloidal nanoparticles such as Rmab. Furthermore, I use this model to develop a simple, fast, and accurate method to measure the absolute number concentration of nanoparticles in solution. Second, I systematically studied the mobility property of non-spherical particles. A theory is developed to quantify the effect of orientation on the mobility and dynamic shape factor of charged axially symmetric particles in an electric field. The experimental results of well-defined doublets of NIST traceable size standard 127nm, 150nm, 200nm and 240nm PSL spheres demonstrated excellent agreement with the expected values based on my theory. More general new theories on the mobility of nonspherical particles are developed and compared with current theories.

1.1 Aerosols

Defined as two-phase systems, aerosols consist of liquid and solid particles suspended in a gaseous medium[5]. Dust, cloud, fume, fog, smoke and spray are all examples of aerosols. Aerosols can form by routes of chemical reactions of gaseous components (gas-to-particle conversion) or the disintegration of liquids or solids into finer constituents such as processes of atomization or electrospray. The size of aerosol particles varies from a few nanometers to more than 100 micrometers. Studies of aerosols have been interdisciplinary, involving physics, chemistry, biology, materials science, and some other disciplines. Aerosol technology covers studies of properties, behaviors and physical principles of aerosols and the application of this knowledge to their measurement, control and manufacture. At the beginning of the 20th century, aerosol science stood at the forefront of physical science and contributed to scientists' understanding of Brownian motion and diffusion, as well as the elemental charge (the charge of one electron)[6]. In recent decades, the study of aerosols has expanded rapidly to include the application of aerosols in catalysis, aerosols as building blocks of new materials, use of aerosols in contamination control in the semiconductor industry, influence of aerosols on environmental pollution and human health, the study of the properties of nanoparticles and the effect of aerosols on global warming. Furthermore, with vapor-phase dispersion methods, such as electrospray or pressure atomization, colloidal particles in solution can now be converted to aerosol particles, and therefore can be examined using aerosol techniques. Thus properties of colloidal particles can be studied in a simpler way by avoiding the complicated effects in a liquid environment. Examples of application of this technique include the online measurement of particle size distribution uing ES-DMA, online measurement of mass distribution using ES-MS, and researches on the aggregation mechanism of colloidal bio-nanoparticles.

1.2. Particle Characterization and Ion-mobility Measurement

Despite the diversity of disciplines from which aerosols are studied, the fundamental physical principles governing aerosols remain the same and aerosol technology in different fields of study shares similar theoretical concepts and experimental techniques. Particle characterization and measurement of characteristic values are the first, and a very important, step for describing and understanding those physical principles. The concepts and theoretical models in this dissertation are discussed in a more general scenario, applicable to particles in fluid and for small ions in the air, but the experimental techniques are focused on aerosol measurements.

1.2.1.Size, shape, mobility and measurement methods

The characteristic values of a particle include size, mass, surface area, shape, density, chemical compositions, crystal structure and so on. Size is probably the most fundamental parameter of a particle. The physical and chemical properties of a bulk material usually have little to do with their size. However, as the dimension approaches to nano-scale, the properties of materials often display a strong dependency on size due to the high surface-to-volume ratio, and huge diffusivity. For instance, particles of diameters smaller than 100nm, which are usually referred to as nanoparticles, have drawn considerable attention among researchers because of their unique properties and potential applications in catalysis and energy research. The size of aerosol particles ranges widely from 0.001 to 100 micrometers. A spherical particle can be simply characterized by its geometric diameter. However, for a non-spherical particle, more shape parameters are needed. Shape information is essential for non-spherical structures such as nanorods and filaments. Gold nanorods are used in the formation of many functional composite materials thanks to their special properties of light scattering and absorption. Nanoparticles shaped like filaments can circulate in the blood much longer than their spherical counterparts and could be applied as better drug-delivery systems for treatment of diseases. Nano-building blocks with novel shapes other than sphere exhibit unique physical and chemical properties and have the potential to be used in biological labels, biological sensors, diagnosis and monitoring of diseases, and even medical clinical diagnosis. The potential usage of other particles shaped differently was also reported in catalysis.

A variety of techniques are available for obtaining the size or shape information of particles. They can be generally divided into two categories, in-situ techniques and ex-situ techniques. Ex-situ characterization methods include various electron microscopy techniques, which can provide a straightforward visual observation of the particle size and shape. However, the physical and chemical characteristics of nanoparticles may change over a brief time interval, and the sample preparation process may alter properties of nanoparticles,.For instance, evaporation of a volatile species can change properties of collected particles before analysis. Moreover, for a huge population of particles with a broad size distribution, it is inconvenient, if not impossible, to use the microscopy technique to obtain fast and accurate results of size distribution. Those significant drawbacks of ex-situ methods lead to the pursuit of alternative real-time or in-situ techniques. In-situ characterization methods and tools include various ion-mobility methods, size-exclusion chromatography (SEC), analytical ultracentrifuge (AUC) and lighter scattering. Among all in-situ techniques above, ion-mobility methods, which take advantage of the motion of charged particles in an electric field, provide the best resolution for measuring particle size distribution. This dissertation focuses on one ion-mobility technique for size measurement called Differential Mobility Analysis (DMA).

When a charged particle is placed in an electric field, it will migrate with a velocity that is related to the charge on the particle, the particle size, shape and orientation. The electrical mobility Z_p is defined as

$$Z_p = V_d/E, \qquad (1\text{-}1)$$

where V_d is the drift velocity and E is the magnitude of the electric field. DMA is a technique to measure an averaged mobility of an aerosol particle, which will be discussed in details in section 1.2.2. Since the electrostatic force is balanced by Stokes drag force, the relationship between the averaged mobility and its mobility diameter, d_m , is expressed by

$$\overline{Z_p} = q\frac{C_c(d_m)}{3\pi\eta d_m} \tag{1-2}$$

where C_c is the slip correction factor, q is the free charge on the particle, and η is the gas viscosity. For a sphere, the mobility diameter, d_m, is equivalent to its geometric diameter, but for a non-sphere, d_m is the equivalent spherical diameter, i.e., the diameter of a sphere of equivalent mobility, which contains the shape information of non-spherical particle[78]. With Eqn. (1-2), the mobility size of a particle can be readily determined with a DMA instrument.

To use Eqn. (1-2), one needs to understand the slip correction factor C_c. Aerosols are two-phase systems: a gas medium, and the particles suspended in it. Thus, the behavior of particles within the system largely depends on the interaction between the gas medium and the particles, which is affected by whether the gas can be treated as a continuous fluid similar to a liquid, or discontinuous fluid where rapidly moving molecules collide randomly with particles. The determination of that is based on the particle size relative to the spacing between the gas molecules, which is characterized by the mean free path, λ, defined as the average distance traveled by a molecule between successive collisions. At room temperature and 1 atm, the mean free path is about 67nm. Particles much larger than 2λ in size can be treated as surrounded by a continuous media, similar to particles in liquid, due to lots of gas molecules colliding with each other near the particles' surface. In such continuum regime, the relative velocity of the gas molecules right at the surface of the particle is zero and the slip correction factor C_c is one. On the contrary, particles much smaller than 2λ in size are considered as only affected by the motion of independent individual gas molecules, and the behavior of particles is governed by the molecular collision theory. In this free molecular regime, the slip correction factor is inversely proportional to d_p^2, where d_p is the particle diameter. Intermediate-sized particles in between may slip by the obstacles. Equations governing the particle motion in the transition regime are basically interpolated by the two limits. The slip correction factor C_c in all three regimes is expressed as

$$\mathrm{C}_c(d_p) = 1 + \frac{2\lambda}{d_p}[A_1 + A_2 \exp(-\frac{A_3}{2\lambda / d_p})] \tag{1-3}$$

where A_1=1.142, A_2=0.558, and A_3=0.999 given by Allen and Raabe[9] at room temperature and atmosphere pressure.

Also, in order to use the ion mobility method, one must know the distribution of charges on particles, i.e., q in Eqn.(1-2). Most ion-mobility instruments employ a bipolar diffusion charging process for particle charging, in which electrically neutral cloud of positive and negative ions migrate to the particles by Brownian diffusion and undergo charge transfer reactions with aerosol particles. Aerosol particles initially charged will lose their extra charge and particles initially neutral will acquire charges and finally lead to an equilibrium charge distribution after long exposure to bipolar ion mixtures [10]. When the bipolar charge distribution is known, raw data from the DMA can be converted into a size distribution.

In summary, a mobility measurement is a fundamental measurement. Once mobility is measured, it can be converted to mobility diameter, which is the diameter of a sphere with equivalent mobility. For a sphere, mobility diameter is the geometric diameter, but for non-spherical particles, the mobility or mobility diameter contains information about particle shape. The objective of this dissertation is to quantify particle properties using ion-mobility measurement and, furthermore, to develop new theories and extend current theories to examine the relationship between the mobility and the shape of a non-spherical particle.

1.2.2.Instruments used for online measurement of mobility/mobility size distribution.

There are three components in a complete measurement setup for mobility/mobility size distribution (Figure 1-1). The first part is an aerosol particle generator. The generator may produce aerosols in air directly by the method of synthesis, aerosolize salt solutions to solid particles or convert colloidal particles to aerosols. Examples of a generator include a pressure atomizer or an electrospray aerosol generator (ES). Then the produced aerosol particles need to pass through a selector which selects particles usually based on their mobility or mobility diameter. Differential mobility analyzer (DMA) is one of the selectors described above. Finally, the concentration of the selected particles will be measured by a particle counter, such as ultrafine Condensation Particle Counter (CPC). Figure 1-2 is an example of the size distribution result of an aggregate using ES-DMA-CPC technique.

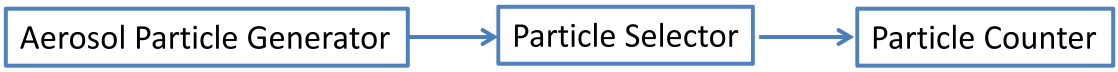

Figure 1-1. *The instruments used for mobility/mobility size distribution online measurement*

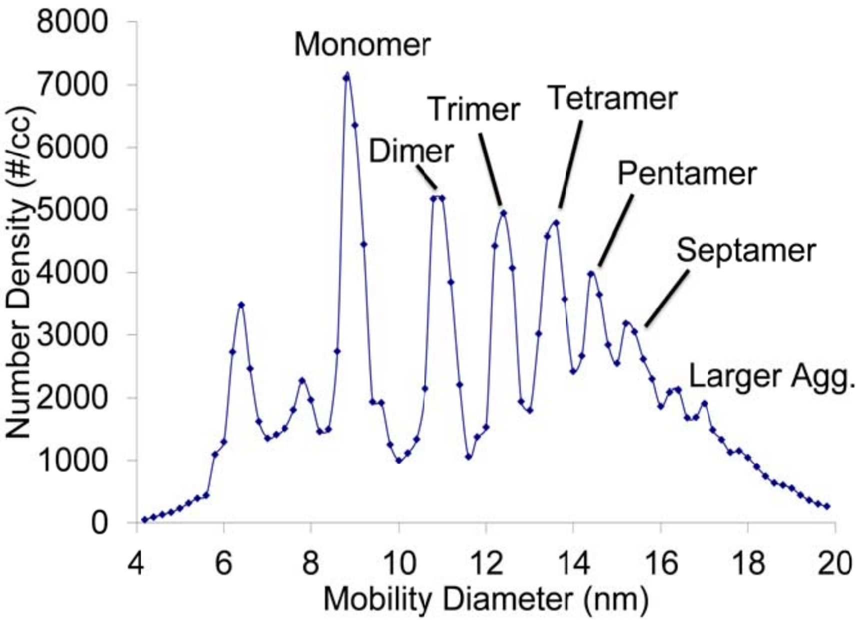

Figure 1-2. *An example of the size distribution result of an aggregate using ES-DMA-CPC technique*

- Pressure Atomizer

The pressure atomizer is a tool to generate aerosol particles from solutions. It can generate solid particles from salt solution after droplets are dried. Commonly used materials include sodium chloride, sugar, uranine, and methylene sucrose. The particle size of the aerosol is determined by the concentration of solution. Another wide-spread usage for pressure atomizer is to disperse colloidal particles to aerosol particles. For instance, a common method of generating monodisperse polystyrene latex (PSL) aerosol is to atomize monodisperse polystyrene latex (PSL) colloids. A schematic diagram of a constant output atomizer is presented in Figure 1-3.

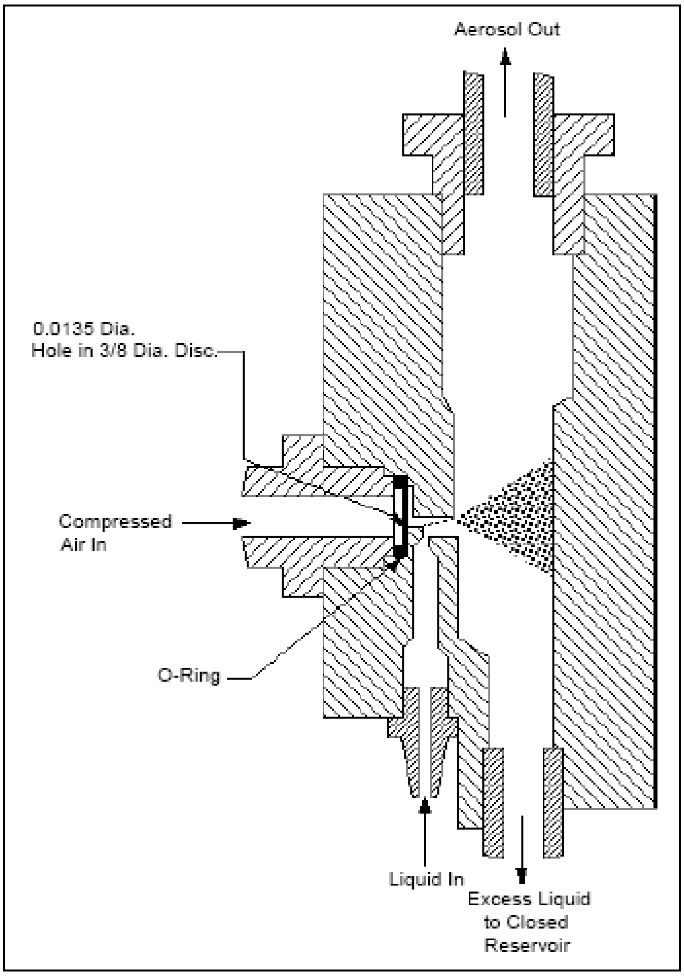

Figure 1-3. *A schematic diagram of a constant output atomizer* [8]

Compressed air expands through the orifice to form a high-speed jet. The solution is aspirated through a 1⁄16-inch-diameter tube from a closed reservoir to the atomizing section and is then atomized by the jet. Large droplets are removed by hitting on the wall opposite to the jet and excess liquid is returned to the same reservoir. Fine spray leaves the atomizer through a fitting at the top.

- Electrospray

Electrospray (ES) is a well-used tool to generate vapor-phase dispersed material. The droplet formed in ES is much more mono-dispersed and smaller in size than in a pressure atomizer. Instead of a large amount of solution needed in a pressure atomizer for one measurement, only a small amount of sample solution is sufficient for ES, which is usually stored in a 1.5 ml cone-shaped vial. ES was used initially in applications involving surface coatings, emulsions and as colloidal micro-thrusters. In the 1980s, it was discovered that ES could be used for aerosolizing bio-macromolecules, allowing their analysis by mass spectrometry (MS). Although exploratory experiments were underway as far back as 1994, the first integration of ES with DMA to analyze biomolecules can be traced back to 1996, when this technique was used to determine the size of globular proteins. Subsequently, researchers have used ES–DMA to characterize other bionanoparticles including polymers, viruses, bacteriophages, nanoparticle–bionanoparticle conjugates, and bionanoparticle–bionanoparticle conjugates, leading to a rapid increase in the number of publications reporting its use [11-13].

Schematic of an ES is shown in Figure 1-4. The analyte, typically dissolved in a volatile buffer solution, is passed through a fused silica capillary under pressure and then electrosprayed to produce and multiply charged droplets containing the analyte. The ES in this figure as shown is operating in the positive ion mode. The analyte containing droplets are then mixed with air (sometimes also supplemented with CO2) and passed through the neutralizer where the solvent from droplets continues to evaporate, and a residual charge on the particles results from diffusion charging from positively and negatively charged ions. The charged particles then enter a DMA for mobility size measurement or a MS for mass measurement. [11].

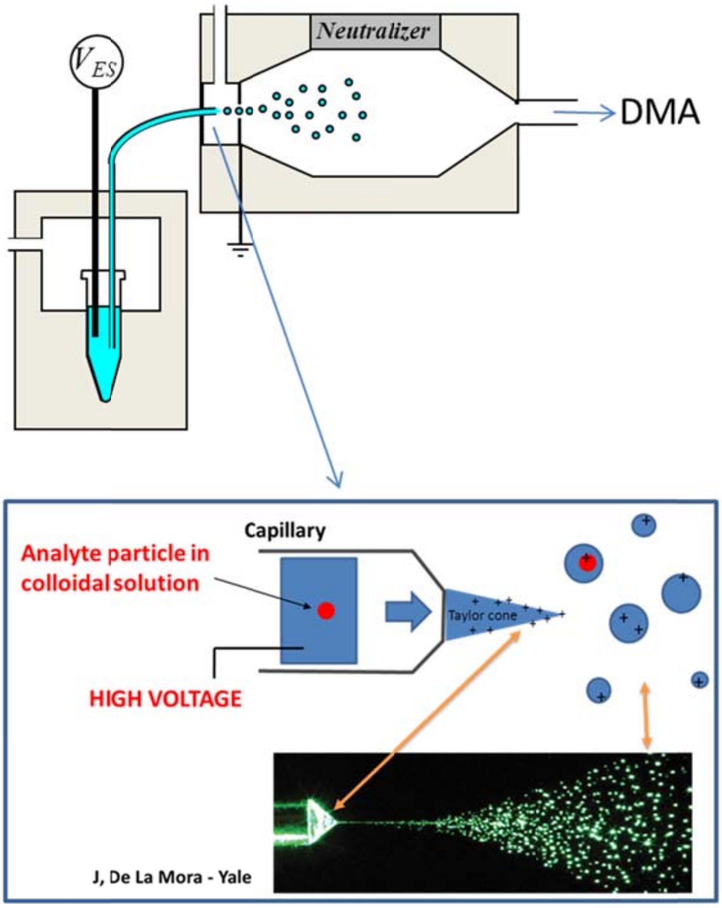

Figure 1-4. *Schematic of an electrospray (ES)*

- Differential Mobility Analyzer (DMA)

The differential mobility analyzer is an important tool for on-line particle mobility selection and mobility distribution measurement. The predecessor of the present day DMA was developed in 1957 to investigate the charging of small particles, and further modified as a source for monodisperse particles in 1970s [14]. A schematic diagram of a cylindrical DMA is presented in Figure 1-5.

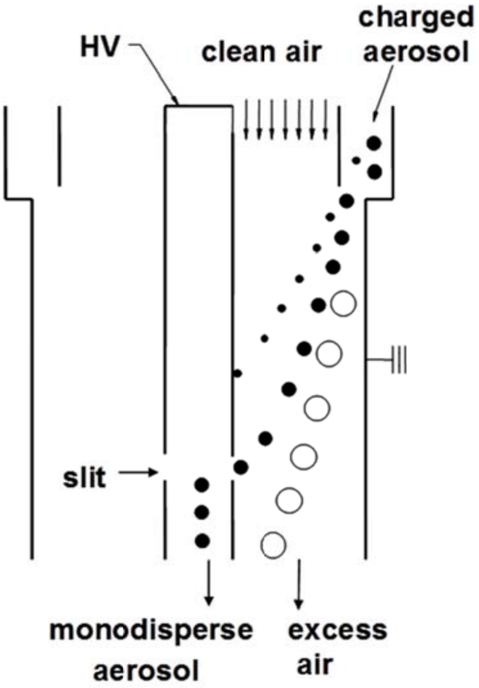

Figure 1-5. *Schematic diagram of a cylindrical DMA.*

DMA has a geometric structure with two coaxial columns. The outer column is grounded and the inner column is applied to a negative voltage, V_e. The charged aerosol particles enter the DMA through an inlet close to the outer column. The carrier clean laminar sheath flow enters from the top. Due to the electric force, the aerosol particles migrate across the gap between the outer column and the inner rod. Only mono-dispersed aerosols within a narrow mobility range which corresponds to the voltage V_e are extracted from the port located downstream in the inner rod. In brief, a DMA is a particle selecting tool based on levels of mobility. By scanning the voltage of the inner rod, particles with a serial of motilities are collected successively and present a mobility distribution. The characteristic mobility of the particles at given DMA sheath flow rate, Q_{sh} ,and applied voltage, V_e, is given by:

$$\overline{Z}_p = \frac{Q_{sh}\ln(r_{out}/r_{in})}{2\pi V_e L_d} \tag{1-4}$$

where r_{in} and r_{out} are the radii of the inner and outer electrodes, respectively, and L_d is the length of the classifier. The resolution of a DMA is defined as the ratio of Z_p to the observed range of mobilities of the transmitted particles, ΔZ_p. If the particles are large enough, diffusion is unimportant. The DMA resolution is determined by the ratio of flow rates, Q_{sh} / Q_a, where Q_a is the aerosol flow. Once mobility is measured using Eqn.(1-4), the mobility diameter is determined by Eqn. (1-2).

- Ultrafine Condensation Particle Counter (CPC)

In order to measure the particle size distribution using a DMA, an ultrafine particle counter is required. The condensation particle counter (CPC) is the most sensitive detector available, and is about a thousand times more sensitive than commercially available electrometers. Since particles smaller than 0.2 micrometer in diameter cannot be detected directly by optical techniques, the high counting sensitivity of a CPC is based on a pre-growth of ultrafine particles by condensing a working fluid on the particle. Three processes are involved in detecting[11], supersaturation of a working fluid, growth of particles by condensation of vapors, and detection of aerosol particles. A schematic diagram of an ultrafine CPC is presented in Figure 1-6. Particles pass through a heated working fluid reservoir and get saturated with the working fluid vapor. Then the aerosols and vapor enter a condenser tube at a lower temperature. The vapor cools, becomes supersaturated, and begins to condense on the particles to form larger droplets. Droplets grow by condensation to a near uniform of about 10 micrometers. A photodetector is placed downstream the flow to measure the intensity of the scattered light by the droplets. The intensity of light indicates the concentration of droplets or particles. Although extremely sensitive, the CPC suffers from a lower size limit of detection of ~2.5nm because the droplet activation efficiency is size dependent, i.e. smaller analytes are more difficult to activate at a given supersaturation of the working fluid. Modifications including employment of different working fluids and operating temperatures can lower the size limit to ~1nm.

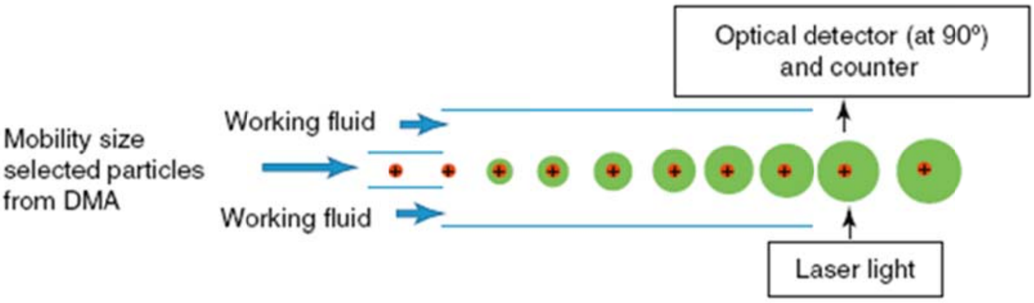

Figure 1.6. *A schematic diagram of an ultrafine CPC* [11]

1.3. Scope of the Dissertation

The dissertation focuses on quantifying particle properties from its ion mobility measurement using well-known theories and our newly developed theories or new developed instrument. The findings in this dissertation fall into two main areas. The first is to study the ion mobility measurement of colloidal nanoparticles using electrospray technique, which includes chapter 2, chapter 3 and chapter 8. The "droplet-induced-aggregation" theory for electrospray process is established and proved experimentally. The theory can be applied both to obtain the true aggregation distribution by correcting the non-specific aggregation during the process, and to determine the absolute number concentration of colloidal nanoparticles in solution. It is also proposed that certain stable bio-nanoparticles, such as some viruses which are more monodisperse and highly concentrated than current standard reference particles, have the potential to be used as standard reference materials due to their high precision in replication. The second part, which includes chapter 4 to chapter 7, is concentrated on expanding current theories for the mobility of nonspherical particles into more general theories and supporting the new theories with experiments.

Chapter 2 proposes a statistical model, called 'droplet-induced-aggregation' model[7], to determine the extent to which the ES process induces the formation of nonspecific dimers and higher order aggregates. Electrospray (ES) sources are commonly used to introduce non-volatile materials (e.g. nanoparticles, proteins, etc.) to the gas phase for characterization by mass spectrometry or ion mobility. Recent studies in our group using electrospray ion mobility to characterize protein aggregation in solution have raised the question as to whether the electrospray procedure itself induces aggregation and thus corrupts the results. In this chapter, I will establish a statistical approach to determine and correct this undesired artifact. The model is validated through ES-differential mobility experiments using gold nanoparticles and protein particles. The results show that the extent of droplet induced aggregation is quite severe, and that previously reported cut-off criterion is inadequate. The model is used in conjunction with experiments to show the true dimer concentration in a protein solution as a function of concentration and droplet size. The model is applicable to other ES source-analytical system and to higher aggregation states. [7]

In chapter 3, a simple, fast, and accurate method[15] is presented to measure the absolute number concentration of nanoparticles in solution using the 'droplet-induced-aggregation' model described in chapter 2. The method combines electrospray-differential mobility analysis (ES-DMA) with a statistical analysis of droplet induced oligomer formation described in chapter 2. A key feature of the method is that it allows determination of the absolute number concentration of particles by knowing only the droplet size generated from a particular ES-source, thereby eliminating the need for sample specific calibration standards or detailed analysis of transport losses. The approach is validated by comparing the total number concentration of monodispersed Au nanoparticles determined by ES-DMA with UV-Vis measurements. It is also discussed that this approach is valid for protein molecules by quantifying the absolute number concentration of Rituxan monoclonal antibody (Rmab) in solution. The methodology is applicable for quantification of any electrospray process coupled to an analytical tool that can distinguish monomers from higher order oligomers. The only requirement is that the droplet size distribution be evaluated. This method eliminates the need for sample specific calibration standards or detailed analysis of transport losses.[15]

Chapter 4 presents a general theory to quantify the effect of orientation on the mobility and dynamic shape of charged axially symmetric particles in an electric field[16]. The mobility of a nonspherical particle is a function of both particle shape and orientation. Thus, unlike spherical particles, the mobility, through its orientation, depends on the magnitude of the electric field. This chapter witnesses the development of a general theory for the orientation-averaged mobility applicable to any axially symmetric particle whose friction tensor and polarization energy are known, as an extension of the work of Happel and Brenner[17],. By using a Boltzmann probability distribution for the orientation, I employ a tensor formulation for computing the orientation average mobility rather than a scalar analysis previously employed by Kim et al[18] for nanowires. The resulting equation for the average electrical mobility is much simpler than the expression based on the scalar approach, and can be applied to any axially symmetric structures such as rods, ellipsoids and touching spheres. The theory is applied to the specific case of nanowires and comparied with the experimental results on the mobility of carbon nanotubes (CNT). Also presented is a set of working formulas of additional mobility expressions for nanorods and prolate spheroids in free molecular, continuum and transition regimes. The chapter is summarized in a review and examination of expressions of dynamic shape factor commonly used in the literature, followed by the proposition of a clearer definition based on the tensor approach.[16]

In chapter 5, my theory for the mobility of axisymmetric particles in an electric field as explained in the previous chapter is applied to study spherical doublets and results from experiments of the doublets of spheres larger than 125nm in size provided excellent support for the theory[8]. As described previously, the mobility of a nonspherical particle is a function of both its shape and its orientation. As a result, the stronger the magnitude of an electric field which causes nonspherical particles to align along the field direction, the larger the particles' mobility and the smaller their dynamic shape factor. As a follow-up of chapter 4, where the theory is applied to the specific case of nanowires, this chapter applies the theory to doublets of spheres and compares the theory with experimental results of doublets of NIST traceable size standard PSL particles. The results of the doublets of spheres larger than 125nm in size are shown to be in good agreement with the expected values based on our theory.

Chapter 6 provides a systematic study of the mobility of a non-spherical particle[19]. A new approach to obtain the mobility of non-spherical particles is proposed by averaging the drag force orientationally, and two other approaches in literature, averaged-cross-section and averaged-drift-velocity, are summarized and extended. The concept of orientationally averaged cross-sections (EHSS and PA) based on Chapman-Enskog theory for small gas-phase ions is re-examined when it comes to studying macromolecular ions whose surface cannot be treated as a simple specular surface, but a surface with inelastic interaction where interconversion of energy takes place. A well-accepted collision model considering inelastic collision is Epstein theory, which has been extended to include long-range potential forces by Li and Wang [20] for spherical particles. This dissertation extends the cross-section integral theory for a spherical particle in Li and Wang [20] to a convex non-spherical particle and derives this cross-section integral by simplifying to an averaged projection area multiplied by an enhancement factor for hard collisions. It is also demonstrated that the averaged projection area of a convex particle in free molecular regime is equal to its mobility diameter based on Stokes-Cunningham formula. The second approach is the averaged-drift-velocity approach which has been well used in aerosol science. Li et al.[16] extended this approach for axisymmetric particles following a Boltzmann orientation distribution due to Brownian motion. This dissertation extends this approach to a deeper level, demonstrates the expression of the mobility of non-spherical particles in a general form and discusses more symmetric cases. Furthermore, it is pointed out that this approach is only valid when the particle Brownian rotation is slow compared with the particle translational relaxation time, which usually applies to particles in transition and continuum regimes. If the particle Brownian rotation is fast, usually so in the case of small ions and particles in free molecular regime, we propose a new approach using the friction coefficient in a tensor form, called averaged-drag-force, which shares certain common assumptions with averaged-cross-section approach. A criterion is developed to facilitate justification of all approaches dsicussed above. The three approaches are then compared with one aother by being applied to study a serial randomly oriented rod. Finally, a comparison is provided between the calculation results of the three approaches with the experimental value of a rigid rod, Tabaco mosaic virus (TMV), and with the calculation results for GroEL from software program in literature.

In chapter 7, I use the theory in chapter 4 for a prolate ellipsoid, which has the possibility to be a model system for any arbitrary shaped particle or aggregate that might be described with a major and minor axis. To obtain the shape information by measuring the electrical mobility under different electric fields, we also propose a new instrument, a pulsed differential mobility analyzer (PDMA)[21]. This new instrument enables one to change the peak E-field experienced by the particle, while still maintaining the same time averaged field. In so doing method enables one to which method systematically change the average orientation of a non-spherical particle and thus its mobility. The instrument is tested on PSL singlets and doublets with precisely known size and shape, and the result shows that the PDMA would be a potential method for particle sizing and particle shape information measurements. I also report an unexplained phenomenon, which is an unknown relaxation process for non-spherical particles in PDMA measurements.

Finally, in Chapter 8, I conclude this dissertation and provide a detailed discussion of future improvements for each part of this work.

Chapter 2: Quantification and Compensation of Non-specific Analyte Aggregation in Electrospray Sampling

2.1. Introduction

Protein aggregation is a major concern with nearly all protein therapeutics because of their potential for immunogenicity in patients. One of the tools we are investigating to measure protein aggregation involves using electrospray to generate vapor phase dispersed material. These vapor phase dispersed materials can then be analyzed by ion mobility methods named differential mobility analyzer (DMA) also known as gas-phase electrophoretic molecular analysis (GEMMA) [18, 22-26] or mass spectrometry (MS)[1, 27-30] methods. These techniques have the potential to characterize the distribution of oligomeric protein species in solution.

To accurately characterize protein oligomers in solution, the electrospray process should be thoroughly understood in order to correct for any potential bias originating from droplet formation. The mechanism of ES has been treated in great detail by Kebarle and Tang[31] and Gaskell[32]. In ES, the application of a high voltage to a capillary will induce, due to columbic repulsion, small droplet formation. Those droplets undergo evaporation coupled with collisions, as well as fissions when reaching their Rayleigh limits. There are two major theories employed to explain the ES process to eventually produce gas phase analyte ions: charge residue model (CRM)[33] and ion evaporation model(IEM)[34, 35]. In the IEM it is thought that the strong E-field at the drop surface results in ion-emission at a critical drop radius. CRM suggests that droplets undergo a series of fissions to a final drop size where subsequent solvent evaporation leaves behind the residue analyte (e.g. protein, particle, virus, etc). It is well accepted that large and compact multiply charged ions, such as globular proteins, which are the analytes of interest in this work, are produced as charged residues after complete drop evaporation by CRM [36-40]. In this study we will not concern ourselves as to the detail fission process of CRM, as we will by-pass the nature of the ES-process by directly measuring the final droplet size distribution.

As mentioned, one of the potential uses of ES-DMA or ES-MS is to study oligomerization in solution. For this application one must consider whether the measured oligomer distribution reflects the actual distribution in the sample, or if the observed oligomers are an artifact of the ES process. For example, one potential concern is where two or more analyte molecules or particles occupy a volume encompassing what becomes a final electrosprayed droplet. This scenario would result in the observation of oligomers that originated from the droplet formation process.

The usual procedure in the use of a DMA is to charge neutralize the droplets with a bi-polar ion source (e.g Po-210), to yield a bipolar equilibrium charge distribution[10, 41]. The neutralizer stops the fission process at an early stage leading to larger final droplet sizes. In such a situation, the charge residue model (CRM) is expected to hold and solvent evaporation could lead to unintentional analyte oligomers. Lenggoro *et al.* [42]and Pease *et al.*[43] have presented a method to provide an upper workable concentration to mitigate this problem. Kaufman *et al.*[22] have also described a simple criterion to determine whether there are intrinsic dimers in solution based on DMA size distributions by assuming that all droplets were of the same size. However, that criterion cannot quantify the intrinsic aggregates in solution. The unintentional (non-specific) analyte aggregation may also be a problem in ES without a neutralizer. While the final droplet size is much smaller because of a series of fissions, the net effect is the same. Lane et al. [30] addressed the same non-specific analyte aggregation problem as in our work, in an ES-MS without a neutralizer and developed a Monte Carlo approach for assessing the specificity of protein oligomers observed in electrospray mass spectra. However, because they did not have a direct measure of the drop size, they assumed that all droplets were of the same size and the droplet size was selected to fit the experimental data best. They basically simulated a Poisson distribution unconsciously, which was also employed by Lewis et al. [44] and Kaufman et al. [22]. Hogan and Biswas developed two Monte Carlo based models to predict the efficiency of electrospray ionization for macromolecules [45] and to study the porous film deposition by electrohydrodynamic atomization of nanoparticle sols [46]. In their Monte Carlo based models, the size distributions of spayed particles are determined by the convolution of a Poisson distribution within the initial droplet size distribution and the initial ES droplet size distribution is represented by a lognormal distribution function. Although a lognormal distribution may be a good representation for the initial droplet size distribution of electrospray in theoretical calculation and simulation, the final droplet size distribution of electrospray can be obtained directly from experiments (Section 2.2.3.4) and is not necessarily an exact lognormal distribution (Figure 2-2a, Figure 2-2b and Figure 2-6). All the studies above did not consider a joint Poisson distribution, and so cannot quantify the intrinsic aggregates in solution correctly. Monte Carlo approaches cannot provide an explicit analytical expression to calculate the non-specific aggregation and characterize the true oligomerization in solution.

This work is focused on developing an experimentally verified theory that will enable one to distinguish ES induced aggregates from intrinsic aggregates, and without the need to model the details of the ES-Fission process, through a direct measure of the final droplet size distribution. I demonstrate my theory on our own ES-DMA work. The approach is generic to any ES process and thus can be applied equally to either ion-mobility or mass spectrometry analysis. For users only interested in implementation of the theory I provide a section that summarizes the relevant formulas in section 2.2.5.

2.2. Theory

2.2.1 Physical Aggregation (droplet induced aggregation) of identical particles

Because the spatial distribution of analytes in solution is statistical, our theoretical treatment was developed by probabilistic analysis. If a final droplet generated in ES is a random sample of the solution, and the particles in the solution are identical and independent, the probability of ***k*** particles in a given droplet obeys a Poisson distribution [22, 44, 47, 48] and is given by

$$Q(k,\lambda) = \frac{e^{-\lambda}\lambda^{k}}{k!} \tag{2-1}$$

where λ is the mean number of particles per droplet and is given by

$$\lambda = V_{d}C_{p} = \frac{1}{6}\pi D_{d}^{3}C_{p} \tag{2-2}$$

where V_d is the droplet volume, D_d is the droplet diameter and C_p is the number concentration of the particles in solution (the number of particles per volume).

Lewis *et al.* [44] and Kaufman *et al.* [22] asserted that the probability to find a certain number of particles in a single droplet follows a Poisson distribution, but did not provide a justification. I use a statistical model to justify mathematically that particles indeed follow a Poisson distribution in solution. This model is discussed in greater detail in the supplementary section.

Consider a solution containing an analyte (particles). In the period of time that one unit volume of solution is sprayed, $1/V_d$ droplets are generated, and the total number of particles passing through the capillary and thus incorporated within the droplets is C_p. If we define one event as one particle being encapsulated in a droplet, and assign Δt as the average time to generate one droplet, then the rate of this event occurring is $R=C_p/(\Delta t*1/V_d) = V_dC_p/\Delta t$. The expected number of occurrences in this interval Δt is $\lambda = R\Delta t = V_dC_p$. The probability that there are exactly *k* occurrences in this interval is given by a Poisson distribution, Q(*k*, λ), with parameter λ, Further justification on the use of a Poisson distribution is provided in Supplemental Information A.

Assuming a monomodal droplet size distribution $f(D_d)$, the average value of the Poisson distribution parameter λ, is given by

$$\overline{\lambda} = \sum_i f(D_{d,i})\lambda = C_p \sum_i \frac{1}{6}\pi D_{d,i}{}^3 f(D_{d,i}) = C_p \overline{V_d} \tag{2-3}$$

where $\overline{V_d} = \sum_i \frac{1}{6}\pi D_{d,i}{}^3 f(D_{d,i})$ is the average droplet volume. (2-4)

$$\sum_i f(D_{d,i}) = 1$$

The discussion about droplet size measurement is addressed in section 2.3.4.

Then the probability of droplet induced aggregation follows,

$$Q(k,\bar{\lambda}) = \frac{e^{-\bar{\lambda}}\bar{\lambda}^{k}}{k!} \tag{2-5}$$

where k is the order of aggregation.

If the solution contains only monomers, then based on Eqn. (2-5), the droplet induced dimer to monomer ratio is

$$\frac{Q(2,\bar{\lambda})}{Q(1,\bar{\lambda})} = \frac{\bar{\lambda}}{2} \tag{2-6}$$

In this scenario, there are no intrinsic dimers in solution. Therefore, the observed dimer to monomer ratio is the same as the induced ratio.

Equation 2-6 is useful because it provides a convenient criterion to determine if there are any intrinsic dimers in solution. Simply, if the observed dimers are higher than that computed by Eqn (2-6), we can ascribe the difference to intrinsic dimers in solution. This point has also been partially addressed by Kaufman *et al.* [22], but he assumed that all droplets were of the same size.

2.2.2 Quantitative determination of intrinsic aggregates in solution

The “dimer-to-monomer ratio” criterion, as demonstrated above, is valid if there are few to no dimers existing in the solution, but it fails where the intrinsic oligomers such as dimers, trimers etc. have a substantial contribution to the total particle concentration, as is common for solutions containing protein oligomers. In this section I present a strategy to quantify the aggregate ratio of intrinsic dimers to intrinsic monomers in solution for an arbitrary condition. This same strategy can also be expanded to quantify any higher-order aggregates. Before addressing the mathematics of the process, I consider the physical constructs of the problem.

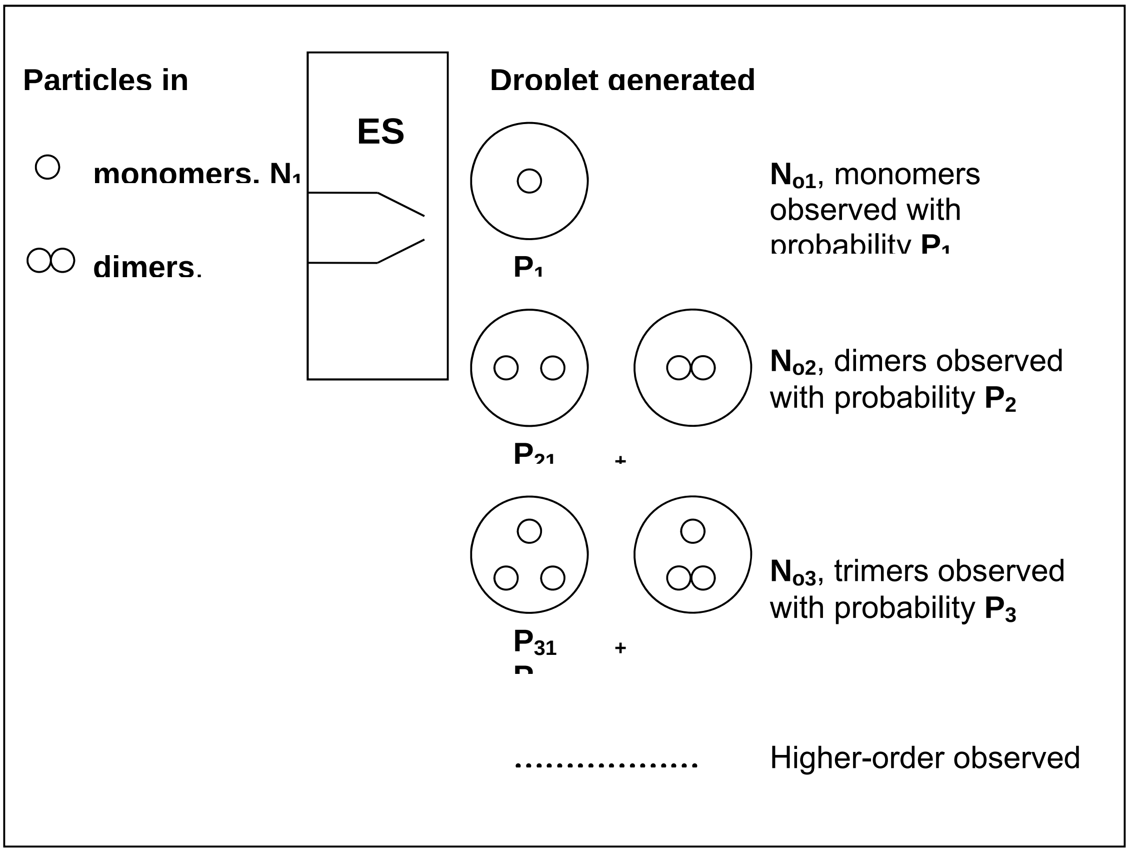

Figure 2-1. *Physical representation of the probability distribution of induced and intrinsic aggregate distributions from electrospray.*

A schematic description of how intrinsic and induced oligomers may be distributed within ES droplets is shown in Figure 2-1. Consider there are N_l monomers and N_2 dimers in solution. Following ES, N_{o1} monomers, N_{o2} dimers, and N_{o3} trimers are observed with probabilities P_1, P_2 and P_3. There is only one possible condition for observation of monomers; that is, only one monomer in a single droplet generated by ES has a probability of P_1. For observed dimers, there are two possibilities. One is that two monomers are captured within a single droplet with probability P_{21}, creating an induced dimer, and the other possibility is that there is one intrinsic dimer in a single droplet with probability P_{22}. Similarly for trimers, there are two situations, three monomers captured into a droplet with probability P_{31} or one monomer and one dimer captured within the same droplet with probability P_{32}. With this construct we can obtain the following two relationships:

$$\frac{N_{o2}}{N_{o1}} = \frac{P_2}{P_1} = \frac{P_{21} + P_{22}}{P_1} \tag{2-7}$$

$$\frac{N_{o3}}{N_{o1}} = \frac{P_3}{P_1} = \frac{P_{31} + P_{32}}{P_1} \tag{2-8}$$

Assuming the spatial distribution of monomers is random, the number of monomers in a droplet should follow a Poisson distribution with parameter λ_1,

$$Q(k,\lambda_1) = \frac{e^{-\lambda_1}\lambda_1^{\,k}}{k!} \tag{2-9}$$

$$\lambda_1 = V_d C_{p1} = \frac{1}{6}\pi D_d^{\,3} C_{p1} \tag{2-10}$$

where

C_{p1} the number concentration of monomers in solution

V_d the droplet volume

D_d the droplet diameter

The number of dimers in a droplet follows a Poisson distribution with parameter λ_2,

$$Q(k,\lambda_2) = \frac{e^{-\lambda_2}\lambda_2^{\,k}}{k!} \tag{2-11}$$

$$\lambda_2 = V_d C_{p2} = \frac{1}{6}\pi D_d{}^3 C_{p2} \tag{2-12}$$

where C_{p2} the number concentration of dimers in solution

Assuming the two Poisson distributions are independent, so

$$P_1 = Q(1,\lambda_1)Q(0,\lambda_2) = e^{-(\lambda_1+\lambda_2)}\lambda_1 \tag{2-13}$$

$$P_{21} = Q(2,\lambda_1)Q(0,\lambda_2) = e^{-(\lambda_1+\lambda_2)}\frac{\lambda_1^{\,2}}{2} \tag{2-14}$$

$$P_{22} = Q(0,\lambda_1)Q(1,\lambda_2) = e^{-(\lambda_1+\lambda_2)}\lambda_2 \tag{2-15}$$

$$P_{31} = Q(3,\lambda_1)Q(0,\lambda_2) = e^{-(\lambda_1+\lambda_2)}\frac{\lambda_1^{\,3}}{6} \tag{2-16}$$

$$P_{32} = Q(1,\lambda_1)Q(1,\lambda_2) = e^{-(\lambda_1+\lambda_2)}\lambda_1\lambda_2 \tag{2-17}$$

Eqns.(2-13) to (2-17) were obtained assuming that oligomers in ES process follow an independent joint Poisson distribution. An accurate form of (P1, P2) can be obtained using the methodology described in the statistic supplementary information S.1. I use Eqns.(2-13) to (2-17) here for the calculations in this work.

Using relations (2-13) - (2-17), (2-7) and (2-8) I get the following equation set for a single droplet size

$$\frac{N_{o2}}{N_{o1}} = \frac{P_2}{P_1} \tag{2-7}$$

$$\frac{N_{o2}}{N_{o1}} = \frac{P_3}{P_1} \tag{2-8}$$

$$P_1 = e^{-(\lambda_1+\lambda_2)}\lambda_1 \tag{2-13}$$

$$P_2 = e^{-(\lambda_1+\lambda_2)}(\frac{\lambda_1^2}{2} + \lambda_2) \tag{2-18}$$

$$P_3 = e^{-(\lambda_1+\lambda_2)}(\frac{\lambda_1^3}{6} + \lambda_1\lambda_2) \tag{2-19}$$

where

$$\lambda_1 = V_d C_{p1} \tag{2-10}$$

$$\lambda_2 = V_d C_{p2} \tag{2-12}$$

If we consider the droplet size distribution from an ES-source, f(D$_d$), a general relationship for the dimer to monomer ratio and the trimer to monomer ratio are (proof is provided in the online Supplemental Information B),

$$\frac{N_{o2}}{N_{o1}} = \frac{\int f(D_d)P_2 dD_d}{\int f(D_d)P_1 dD_d} \tag{2-20}$$

$$\frac{N_{o3}}{N_{o1}} = \frac{\int f(D_d)P_3 dD_d}{\int f(D_d)P_1 dD_d} \tag{2-21}$$

where $\int f(D_d) dD_d = 1$.

An inversion procedure could be developed for intrinsic concentrations, C_{p1} and C_{p2}, based on Eqn.(2-20) and Eqn. (2-21). Although it is difficult to solve Eqn.(2-20) and (2-21) for analytical expressions of C_{p1} and C_{p2} directly, accurate approximations can be obtained under some limiting conditions .

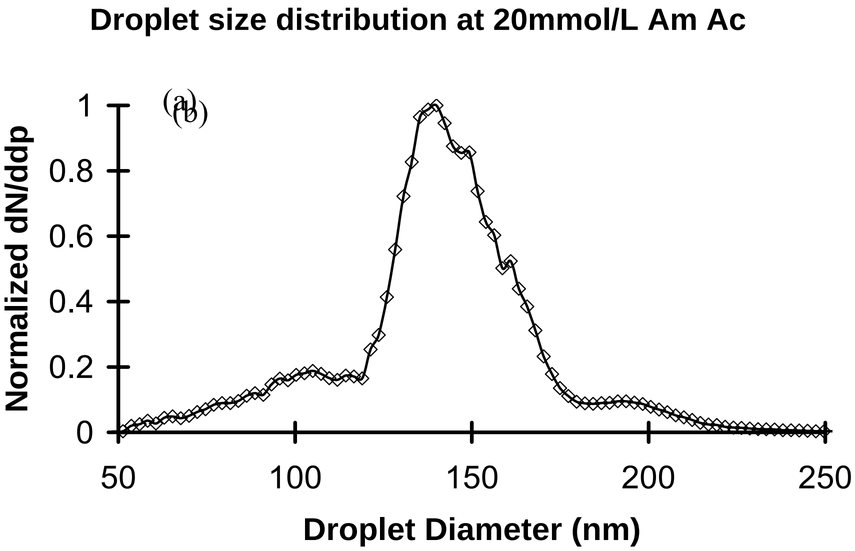

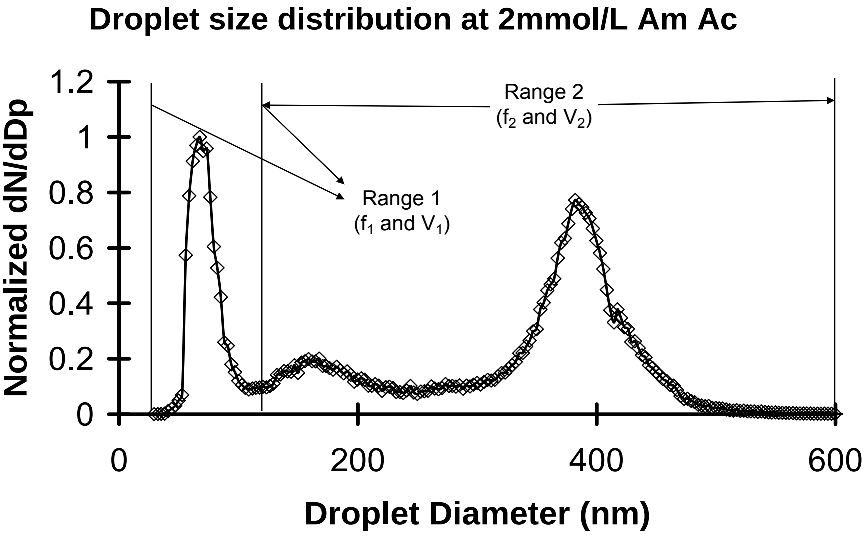

Figure 2-2. (a). *ES monomodal and narrow droplet size distribution (20 mmol Ammonium Acetate with the chamber pressure in ES at PSI 3.7(2.55*10^4 Pa) and a carrier gas in ES of 1 L/min purified air and 0.2 L/min carbon dioxide) for Rituxan samples in section 2.4.1.1 and 2.4.2.* **(b).** *ES droplet with a bimodal size distribution (2 mmol Ammonium Acetate with the chamber pressure in ES at PSI 3.7(2.55*10^4 Pa) and a carrier gas in ES of 1 L/min purified air and 0.2 L/min carbon dioxide) for Au-NPs sample #1 and sample #2 in section 2.4.3.*

Simple Cases

In this work, I consider two simple cases: Monomodal and Bimodal droplet size distributions.

(i) Monomodal and narrow droplet size distribution f(D_d)

If the droplet size distribution f(D_d) can be considered to be monomodal and relatively narrow, as example I show in Figure 2-2a, a droplet size distribution from ES measured at 20 mmol/L Ammonium acetate in sucrose based on Section 2.3.4. Eqn. (2-20) and (2-21) can be evaluated with one average droplet volume,

$$\boxed{\begin{array}{l} \dfrac{N_{o2}}{N_{o1}} \approx \dfrac{P_2|_{V_d=\overline{V_d}}}{P_1|_{V_d=\overline{V_d}}} = \dfrac{\overline{V_d}C_{p1}}{2} + \dfrac{C_{p2}}{C_{p1}} \\[3em] \dfrac{N_{o3}}{N_{o1}} \approx \dfrac{P_3|_{V_d=\overline{V_d}}}{P_1|_{V_d=\overline{V_d}}} = \dfrac{\overline{V_d}^2 C_{p1}^{\ 2}}{6} + \overline{V_d}C_{p2} \end{array}} \qquad \begin{array}{r} (2\text{-}22) \\[3em] (2\text{-}23) \end{array}$$

where

$$\overline{V_d} = \sum_i f(D_{d,i})V_{d,i} = \sum_i f(D_{d,i})\frac{1}{6}\pi D_{d,i}^{\ 3} \text{ : the average droplet volume} \qquad (2\text{-}4)$$

$$\sum_i f(D_{d,i}) = 1$$

V_d the droplet volume

D_d the droplet diameter

f(D_d) the droplet size distribution

N_{o1} the observed number of monomers after Electrospray

N_{o2} the observed number of dimers after Electrospray

C_{p1} the number concentration of monomers in solution

C_{p2} the number concentration of dimers in solution

The monomodal approximation above can be improved by using three average droplet volumes in three regions (peak-left, main peak and peak-right) in Figure 2-3 and solving Eqn.(2-20) and (2-21).

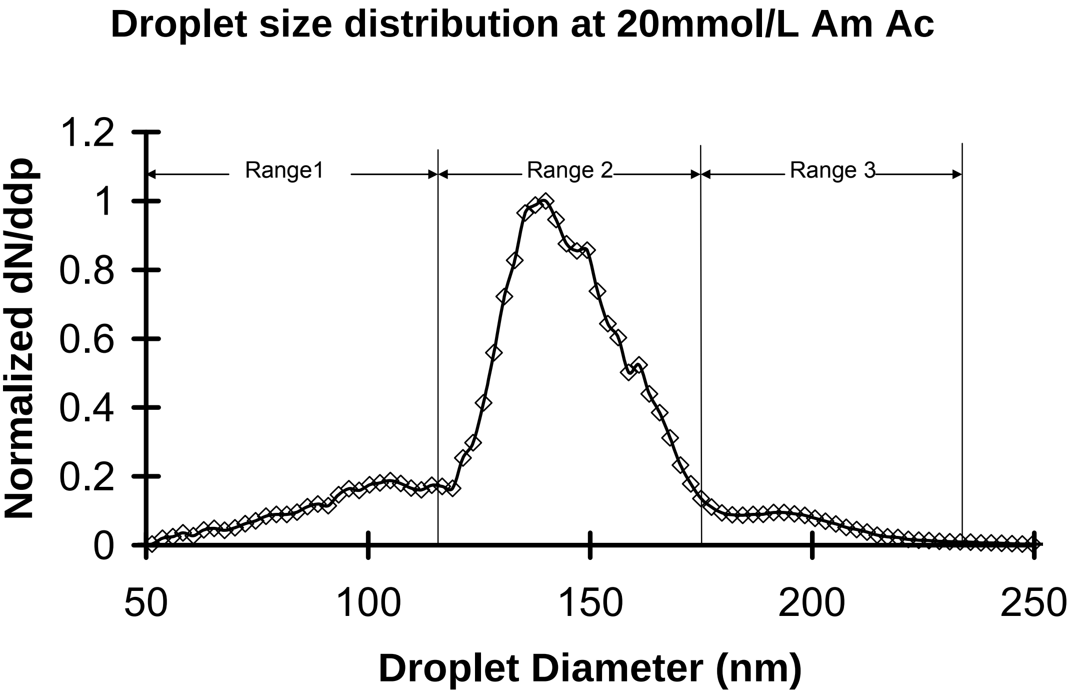

Figure 2-3. *ES monomodal and narrow droplet size distribution (20 mmol Ammonium Acetate with the chamber pressure in ES at PSI 3.7(2.55*10^4 Pa) and a carrier gas in ES of 1 L/min purified air and 0.2 L/min carbon dioxide). The monomodal approximation can be improved by using three average droplet volumes in three regions and solving Eqn.(2-20) and (2-21).*

(ii) Bimodal droplet size distribution f(D_d)

If the size distribution f(D_d) is bimodal as for example shown in Figure 2-2b, and $\overline{V_{d2}}(C_{p1}+C_{p2})$ is not much greater than unity, then Eqn. (2-20) can be approximated by using two average droplet volumes (The detail derivations and discussions are shown in Li et al [15]),

$$\frac{N_{o2}}{N_{o1}} \approx \frac{f_1 P_2\big|_{V_d=\overline{V_{d1}}} + f_2 P_2\big|_{V_d=\overline{V_{d2}}}}{f_1 P_1\big|_{V_d=\overline{V_{d1}}} + f_2 P_1\big|_{V_d=\overline{V_{d2}}}} \approx \frac{\overline{V_{d2}}C_{p1}}{2} + \frac{C_{p2}}{C_{p1}} \tag{2-24}$$

where

$$\sum_i f(D_{d,i}) = 1$$

$f_1 = \sum_i^{range1} f(D_{d,i})$:the fraction of the droplets with the sizes within range 1 including the first size mode. (2-25)

$f_2 = \sum_i^{range2} f(D_{d,i})$:the fraction of the droplets with the sizes within range 2 including the second mode (2-26)

$\overline{V_{d1}} = \frac{1}{f_1}\sum_i^{range1} f(D_{d,i})V_{d,i} = \frac{1}{f_1}\sum_i^{range1} f(D_{d,i})\frac{1}{6}\pi D_{d,i}^{\ 3}$:the average droplet volume within range 1 (2-27)

$\overline{V_{d2}} = \frac{1}{f_2}\sum_i^{range2} f(D_{d,i})V_{d,i} = \frac{1}{f_2}\sum_i^{range2} f(D_{d,i})\frac{1}{6}\pi D_{d,i}^{\ 3}$:the average droplet volume within range 2 (2-28)

The end result of this analysis shows that using experimental observation of the observed monomers, dimers and trimers (N_{o1}, N_{o2}, N_{o3}) one can use relations (2-22) *and (2-23) to obtain the concentration of intrinsic monomers and dimers* (C_{p1}, C_{p2}) *for a monodispersed droplet size distribution and under the appropriate conditions described above, use relation (2-24) for a bimodal droplet size distribution. For a general droplet size distribution, Eqn. (2-20) and (2-21) should be used.*

2.3. Materials and Methods

I demonstrate my model by examining gold nanoparticles (Au-NPs) with an ES-Neutralizer-DMA-CPC system described previously (Tsai et al. 2008). In order to show the efficacy of this technique, highly concentrated Au-NPs and large volume droplets in ES are needed. ES of highly concentrated Au-NPs is challenging because of the instability of the capillary that arises from the highly concentrated Au-NPs under low ionic strength and the presence of solution stabilizing citrate salts which can result in the formation of non-volatile particles that interfere with the DMA measurement[49]. The protocol for obtaining high concentrations of Au-NP is given below and large droplet sizes can be obtained by using low conductivity solutions along with large capillary diameters for the electrospray.

Finally I use Rituxan monoclonal antibody (Rmab) to show application of our approach to quantify protein aggregate distributions in solution.

2.3.1. Gold (Au) nanoparticle (NP) preparation

Commercially available citrate-stablized monodisperse Au colloids (10 nm, 5.7×10^{12} particles/mL, Ted Pella Inc.) were used. A 1.5 mL solution of the as-received Au colloids was centrifuged at 13,200 rpm for 45 minutes, and 1.46 mL - 1.47 mL of the supernatant was removed and replaced with an equivalent volume of aqueous 2 mmol/L ammonium acetate solution (volatile) at pH 10. This step was performed to remove most of the citrate stabilizer which would otherwise coat the Au-NPs upon ES. The pH of the ammonium acetate solution was adjusted by addition of ammonium hydroxide. The solution then was centrifuged at 13,200 rpm again for 15 minutes and 1.4 mL of supernatant was removed to obtain a highly concentrated Au-NP sample that was then electrosprayed into the DMA-CPC system. At these high concentrations, the oligomer peaks were not resolved (data not shown), and hence these samples were diluted 2×, 4×, and 8×, for the ES studies.

2.3.2. Rmab solution preparation

Formulated Rmab was purified using a Protein A affinity column. Purified Rmab was stored at -18 ºC in 25 mmol/L Tris buffer, pH 7.4, with 0.01% NaN_3 added as a preservative. Immediately prior to use in ES studies, the storage buffer was exchanged for 20 mmol/L ammonium acetate, pH 7 by washing all salts from Rmab using a centrifugal filter device with a weight cutoff of 30 kDa. The concentration of Rmab in 20 mmol/L ammonium acetate was adjusted to 1 mg/mL as verified by measuring the maximum absorbance at 280 nm and using a molar absorptivity of 236,020 $(mol/L)^{-1}cm^{-1}$. Working solutions of concentrations 100 µg/mL, 50 µg/mL, 25 µg/mL, 10 µg/mL, and 5 µg/mL were made by dilution and used for ES studies.

2.3.3. Particle Measurements

Aerosolized droplets were generated using a 40 µm inner diameter capillary for Au-NP samples and a 25 µm inner diameter capillary for Rmab mounted in an Electrospray Aerosol Generator (Model 3480, TSI Inc.) and the liquid flow rates through the capillaries were 433 nL/min and 66 nL/min respectively [50]. The ES was operated with a carrier gas of 1 L/min purified air and 0.2 L/min carbon dioxide. The aerosolized droplets were passed through a neutralizer and entered a Differential Mobility Analyzer (Model 3485 Nano DMA column, TSI Inc.) for particle size measurement, and counted with an Ultrafine Condensation Particle Counter (Model 3025A TSI Inc.) More details on the measurement method can be found in Tsai *et al.*[49].

2.3.4. Droplet size Measurements

Use of relations (2-3) or (2-4), (2-25, 26, 27, 28) requires knowledge of the droplet size. Droplet size was determined by electrospraying a known concentration of sucrose solution and measuring the resultant dry particle size. The sucrose solution (1.26 % v/v) was prepared and diluted into 20 mmol/L ammonium acetate buffer, pH 7, giving a final concentration of 0.063% v/v. The ES droplet size of this solution was evaluated by [41, 50]

$$D_d = \frac{1}{C_s^{1/3}} D_s \tag{2-29}$$

where D_d is the droplet diameter, D_s is the sucrose particle diameter after drying, and C_s is the sucrose volume/volume concentration.

Note, an alternative approach discussed in the next section that involves measurement of a series dilutions of the original analyte mitigates the need to know the drop size distribution

2.4. Results and Discussion

2.4.1 Evidence of droplet induced aggregation

To illustrate the magnitude of the problem and the errors that can occur if the droplet induced effects are not accounted for, I consider three examples. The first is a study to characterize the oligomers of Rmab at different concentrations (section 2.4.1.1) and the second where an Rmab sample at the concentration of 100 μg/mL was measured under different ES droplet volumes by varying the ES chamber pressure (section 2.4.1.2). Both experiments were operated by our ES-Neutralizer-DMA-CPC. The third is shown in the section 2.4.2 by comparing our ES-Neutralizer-DMA-CPC results with Analytical Ultracentrifuge [51, 52] measurements directly on the solution, under the same conditions.

2.4.1.1.

Firstly, the sucrose size distributions in the 20 mmol/L ammonium acetate buffer at pH 7 were obtained that provide us with the droplet size distributions for Rituxan using Eqn. (2-29). Figure 2-2 shows the droplet size distributions at pH 7 in 20 mmol/L ammonium acetate buffer of Rituxan at concentrations of 5 μg/mL, 10 μg/mL, 25 μg/mL, 50 μg/mL, and 100 μg/mL. Based on the distribution in Figure 2a and Eqn.(2-4), the average droplet volume was calculated to be $1.64*10^{-21}m^3$. The average droplet size is 141 nm which is in reasonable agreement with previous results[42, 43, 53]. According to Lenggoro *et al.*[42] and Pease *et al.* [43] the corresponding "cut-off" concentration at which observed aggregates are intrinsic to the sample is 169 μg/mL.

Figure 2-4 shows observed ES-DMA size distributions of Rituxan concentration at 5 μg/mL, 10 μg/mL, 25 μg/mL, 50 μg/mL, and 100 μg/mL with the chamber pressure in ES at PSI3.7 ($2.55*10^4$ Pa). A large proportion of oligomers are observed in these measurements.

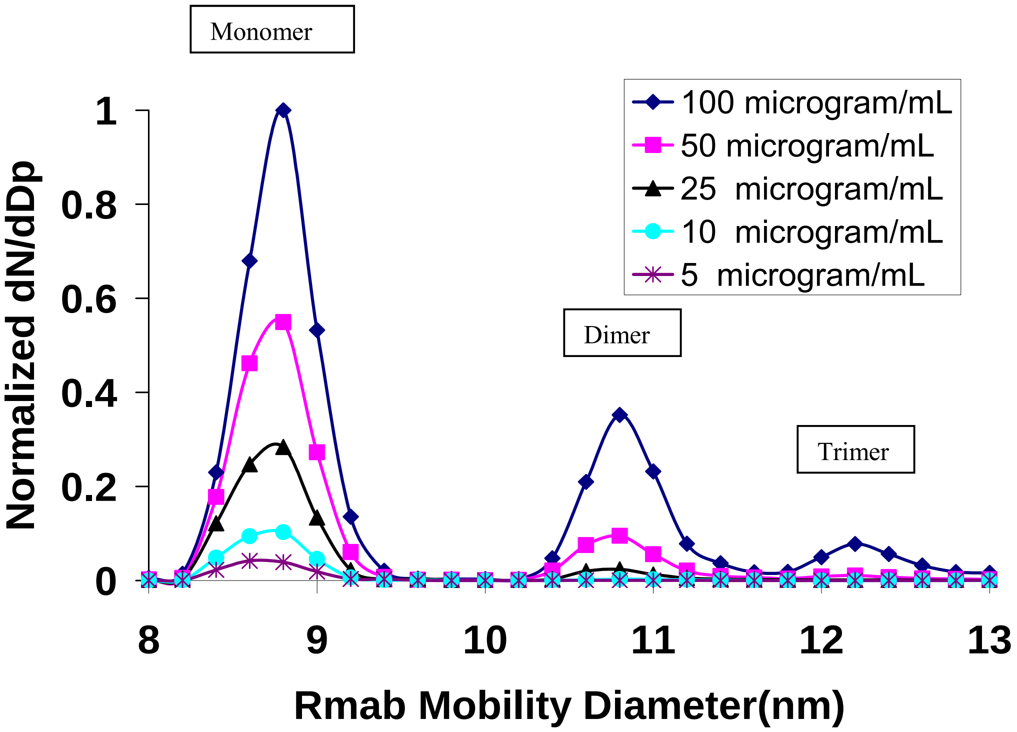

Figure 2-4. *The observed ES-DMA size distributions of Rituxan concentration at 5 μg/mL (star), 10 μg/mL (circle), 25 μg/mL (triangle), 50 μg/mL (square), and 100 μg/mL (rhombus) at pH7 in 20 mmol/L ammonium acetate buffer with the chamber pressure in ES at PSI 3.7($2.55*10^4$ Pa)*

The ratios of the number of observed dimer to the monomer against the Rituxan concentration at 5 μg/mL, 10 μg/mL, 25 μg/mL, 50 μg/mL, and 100 μg/mL are plotted in Figure 2-5 (rhombus). Based on droplet induced dimer to monomer ratio of identical particles following Eqn. (2-6), I obtain a second curve at the same concentrations in Figure 2-5 (line with filled square). The curve deduced from the droplet induced model lies slightly below the data points indicating that most dimers observed in Figure2-4 and Figure2-5 by ES-DMA are droplet induced and that the "cut-off" (169 µg/mL) criterion as used by Lenggoro *et al.* [42] and Pease *et al.*[43] significantly underpredicts the extent of the problem and is insufficient in eliminating droplet induced aggregation effects. Hence I conclude that induced aggregation is a problem at all concentrations, and that the approach described above should be used to determine the extent of physical aggregation.

To a first approximation, the difference between the experimental data and the induced dimer curve can provide the true dimer concentration. A more rigorous approach is to include the effect of intrinsic dimer present in the sample. When intrinsic dimer is present, the concentration of monomer is lower, and thus, the induced dimer fraction will also be lower. This issue could be solved using an iterative procedure; however, I described a simpler approach below.

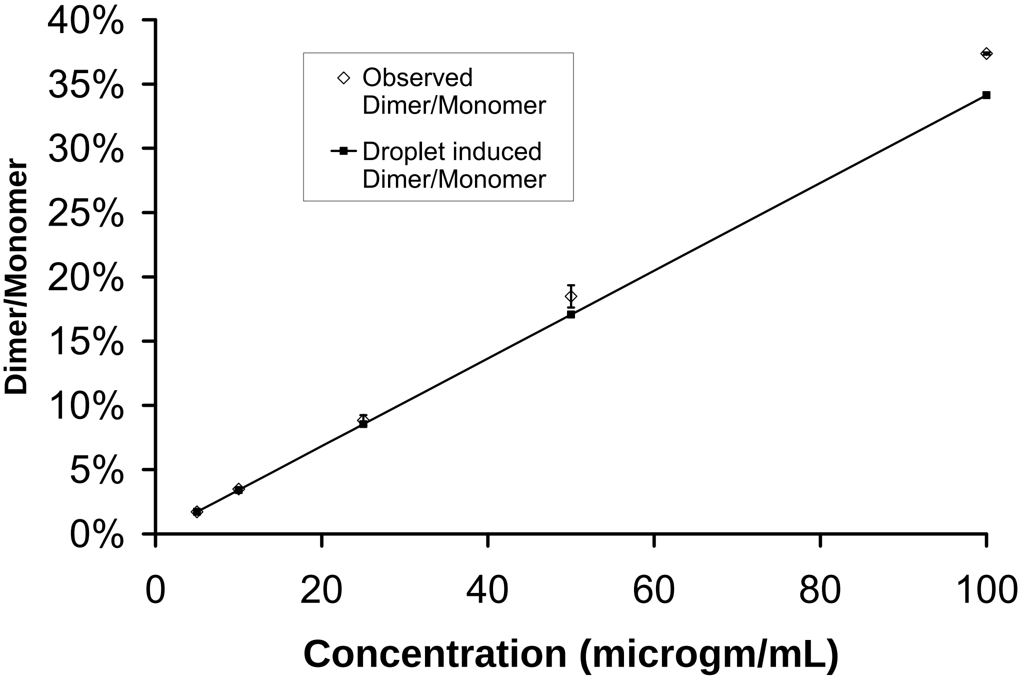

Figure 2-5. *The ratios of dimer to the total number of dimer and monomers at pH 7 observed by ES-DMA as a function of Rituxan concentration at 5 µg/mL, 10 µg/mL, 25 µg/mL, 50 µg/mL, and 100 µg/mL (rhombus). Ratios from droplet induced dimers (line with filled square) at the same concentrations calculated based on Eqn. (2-6).*

2.4.1.2.

In order to make it clearer that the observed dimers in our ES-DMA measurements of Rituxan at concentration of 100 µg/mL are not fully intrinsic in solution but mostly droplet induced, I changed the ES droplet volumes by varying the ES chamber pressure (Figure 2-6). If the observed dimers are intrinsic, the ratio of observed dimer to monomer should not change when varying the droplet size, but if a substantial part of observed dimers is droplet induced, varying the droplet size would change the ratio based on Eqn. (2-22). In Table 1, the results show that the observed dimer to monomer ratio changes from 20.6% to 29.5%, then to 37.4% for one capillary, and from 23% to 31% , then to 41% for another capillary when varying the ES chamber pressure from PSI2.3 ($1.59*10^4$ Pa) to PSI3.0 ($2.07*10^4$ Pa), then to PSI3.7 ($2.55*10^4$ Pa). This shows clearly that the observed dimers cannot be fully intrinsic. Also, after correction for drop induced dimers based on our model (the strategy in Section 2.4.2), the intrinsic dimer to monomer ratios go to 5.4%, 7.5% and 7.8% for the first capillary , and to 4%, 4.7% and 7.3% for the second capillary. The average values for the two experiments are 4.7%, 6.1% and 7.6% with the chamber pressure in ES at 2.3 PSI ($1.59*10^4$ Pa), 3.0 PSI ($2.07*10^4$ Pa) and 3.7 PSI ($2.55*10^4$ Pa) respectively, which are reasonably consistent with the Analytical Ultracentrifuge measurement directly on the solution under the same buffer condition, 4.7% . I note that our model for the calculation here is a monomodal approximation and the accuracy of this approximation is improved by the distribution of smaller droplet size since it is closer to be a monomodal distribution. I believe this is a very definitive experiment to show the droplet induced effect.

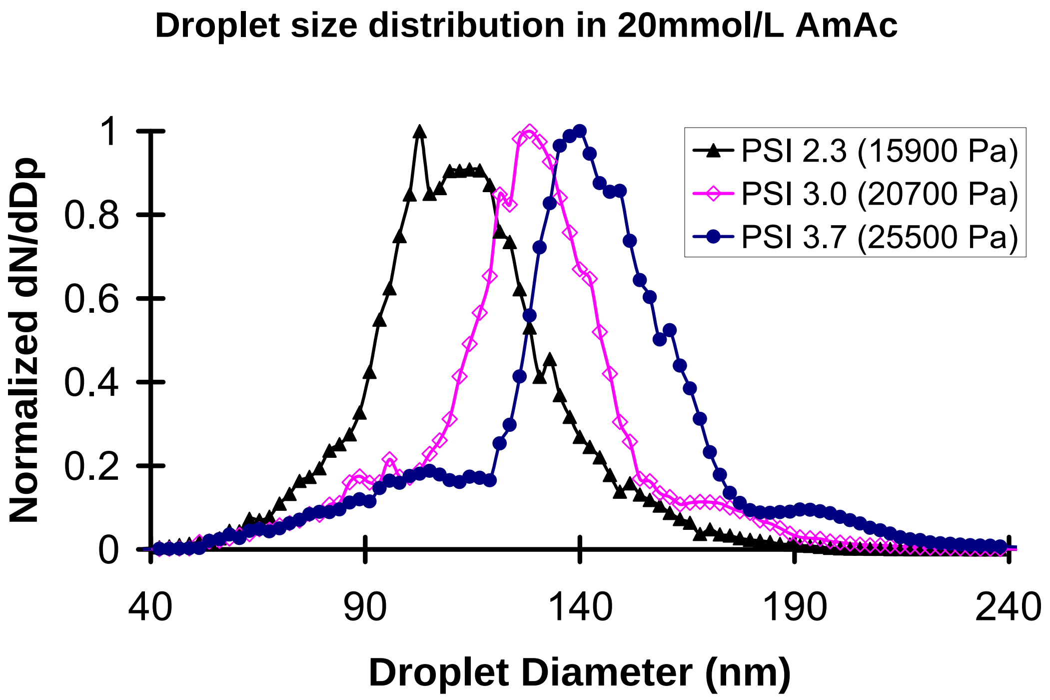

Figure 2-6. *ES droplet size distributions at pH 7 in 20 mmol/L ammonium acetate buffer. The triangle, rhombus and circle distributions are those of the same sample with the chamber pressure in ES at 2.3 PSI (1.59*10^4 Pa), 3.0 PSI (2.07*10^4 Pa) and 3.7 PSI (2.55*10^4 Pa) respectively.*

Table 2-1. *Ratios of observed dimers to monomers from DMA measurement by varying the ES droplet volumes, and the ratios of dimers to monomers after correction for drop induced dimers based on our model (the strategy in Section 4.2) for Rituxan at concentration of 100 µg/mL at pH 7 in 20 mmol/L ammonium acetate buffer.*

Capillary1	ES chamber pressure	Average final	Observed dimer	Dimer to monomer

		droplet volume (m^3)	to monomer ratio	ratio after correction for drop induced dimers.
	PSI2.3 (1.59*10^4 Pa)	8.15E-22	20.6%	5.4%
	PSI3.0 (2.07*10^4 Pa)	1.22E-21	29.5%	7.5%
	PSI3.7 (2.55*10^4 Pa)	1.64E-21	37.4%	7.8%

Capillary2	ES chamber pressure	Average final droplet volume (m^3)	Observed dimer to monomer ratio	Dimer to monomer ratio after correction for drop induced dimers.
	PSI2.3 (1.59*10^4 Pa)	9.91E-22	23.1%	4.0%
	PSI3.0 (2.07*10^4 Pa)	1.38E-21	31.0%	4.7%
	PSI3.7 (2.55*10^4 Pa)	1.84E-21	40.6%	7.3%

These two examples clearly illustrate that care should be taken in interpreting results of oligomer distributions measured from an ES source regardless of the analytical tool used.(E.G. DMA or MS).

2.4.2 Intrinsic Dimer determination (Irreversible/Reversible, Total concentration known): Oligomerization of Rmab

In this section I show a strategy to determine the concentration of intrinsic aggregates with total concentration known. I also compare my results with Analytical Ultracentrifuge [51, 52] measurements.

If we assume that only monomers and dimers are in solution and no higher aggregates, and that the total concentration C_p is known, an additional relationship can be obtained,

$$C_p = C_{p1} + 2C_{p2} \tag{2-30}$$

The ratio of intrinsic dimer to monomer of Rmab, C_{p2}/C_{p1}, can be obtained from Eqn. (2-22) and (2-30).

Using the data in Section 2.4.1.1, Table 2-2 shows the ratios of observed dimers to monomers for Rituxan at pH 7 measured in ES-DMA experiments at concentrations of 5 µg/mL, 10 µg/mL, 25 µg/mL, 50 µg/mL, and 100 µg/mL, the intrinsic ratios at the same concentrations calculated based on Eqns. (2-22) and (2-30).

Table 2-2. *The ratios of observed dimers to monomers at pH 7 from DMA measurement, the ratios of intrinsic dimers to monomers calculated based on Eqn. (2-22,2-30) and the ratio of dimers to monomers measured by Analytical Ultracentrifuge for Rmab*

	ES-DMA observed dimer to monomer ratio	Intrinsic dimer to monomer ratio after correction for drop induced dimers.	Analytical Ultracentrifuge measured dimer to momomer ratio
5 µg/mL	1.7%	0%	NA *
10 µg/mL	3.5%	0.1%	NA *
25 µg/mL	8.8%	0.4%	NA *
50 µg/mL	18.5%	2.1%	NA *
100 µg/mL	37.4%	7.8%	4.7%

* NA: not available; the sensitivity is below the detection limit.

The results in Table 2-2 demonstrate that the actual dimer concentration in solution can be considerably smaller than that measured using an ES source, particularly at high concentration. For example at 100 μg/mL the observed dimer-to-monomer was ~ 37%, while after correction, the intrinsic ratio is 7.8%. At this high concentration we were also able to compare with Analytical Ultracentrifuge measurements directly on the solution, under the same conditions, which showed good agreement with our corrected value. I think the corrected value is even lower than 7.8% if we use the general relationship, Eqn.(2-20), instead of the monomodal approximation relationship, Eqn. (2-22). The accuracy of monomodal approximation can be improved by using smaller droplet size from ES since the distribution of smaller droplet sizes is closer to monodispersed distribution.

2.4.3 Intrinsic Dimer determination (Irreversible aggregation): Au-NPs

In this section, I discuss the implementation of an experimental strategy for irreversible aggregation, based on Eqn. (2-22) or Eqn. (2-24), in which I determine intrinsic aggregate concentration, without *a priori* knowledge of the drop size distribution. This basic strategy is to obtain the ratio of intrinsic dimer to monomer by a series of measurements at various dilutions.

For the electrospraying of Au-NPs in 2mmol/L Am Ac buffer, the ES droplet follows a bimodal size distribution (Figure 2-2b). Eqn. (2-24) is used here for the calculation. Based on Eqn. (2-24), assuming the intrinsic dimers of Au-NPs in solution are nonreversible, after a 2× dilution, an additional relationship can be obtained,

$$\frac{N_{o2,2x}}{N_{o1,2x}} = \frac{\overline{V_{d2}}C_{p1}/2}{2} + \frac{C_{p2}/2}{C_{p1}/2} = \frac{\overline{V_{d2}}C_{p1}}{4} + \frac{C_{p2}}{C_{p1}} \tag{2-31}$$

where $N_{o1,2x}$ is the observed number of monomers after 2× dilution and $N_{o2,2x}$ is the observed number of dimers after 2× dilution.

Combining (2-24) and (2-31), the ratio of intrinsic dimer to monomer of Au-NPs is

$$\frac{C_{p2}}{C_{p1}} = 2\frac{N_{o2,2x}}{N_{o1,2x}} - \frac{N_{o2}}{N_{o1}} \tag{2-32}$$

Figure 2-7 shows the observed size distribution at 2×, 4× and 8× dilutions for 10 nm Au-NPs (sample #1). The DMA voltage was scanned to detect particles up to 20 nm to enable measurement of trimers that could be observed for the 2× dilution, but not for more dilute samples.

Table 2-3 shows the ratios of dimer to monomer measured with ES-DMA at 2×, 4× and 8× dilutions of Au-NPs (sample #1 to sample #4). A large proportion of oligomers are observed in these measurements. Using the theory described above we now determine the true oligomer concentration.

For each sample, the ratio of intrinsic dimer to monomer is calculated based on Eqn. (2-32), using the ratio of 2× and 4× dilution and 4× and 8× dilution. Given the instability of the ES cone-jet at low ionic strength and the propensity of the highly concentrated Au-NPs to aggregate, the intrinsic ratios calculated using 2× and 4× dilution and using 4× and 8× dilution are mostly consistent. I note that with the dilution approach, it is not necessary to know the droplet size.

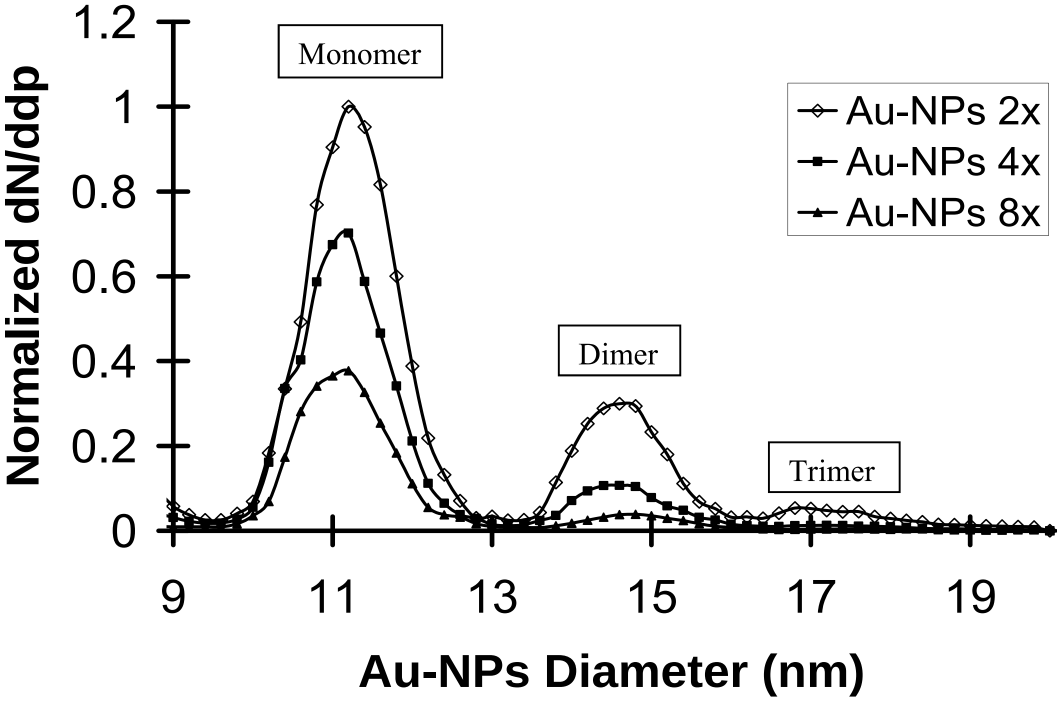

Figure 2-7. *ES-DMA size distributions of 10 nm Au-NPs, sample #1. The rhombus, square and triangle data markers are those of 2-times, 4-times and 8-times dilutions of the original sample, respectively. Each of the discernable oligomer peaks are labeled. respectively.*

Table 2-3. *Ratios of observed dimers to monomers from DMA measurement, and the ratios of intrinsic dimers to monomers calculated based on Eqn. (2-32) for 10nm Au-NPs.*

	ES-DMA observed dimer to monomer ratio			True dimer to monomer ratio (i.e. after droplet induced effects removed)	
	2x	4x	8x	based on 2x and 4x	Based on 4x and 8x
Sample #1	31.3%	17.3%	11.5%	3.3%	5.7%
Sample #2	33.2%	18.1%	12.3%	3.0%	6.5%
Sample #3	36.3%	19.5%	11.1%	2.7%	2.7%
Sample #4	35.7%	19.4%	12.1%	3.1%	4.8%

2.4.4. Reversible oligomerization: the relationship between real equilibrium constant, K, and apparent equilibrium constant, K_{app}

If the intrinsic dimers in solution are fully reversible, the number concentrations of the intrinsic monomers and dimers are connected by an equilibrium constant, K.

$$\frac{C_{p2}}{(C_{p1})^2} = K \qquad (2\text{-}33)$$

C_{p1} the number concentration of monomers in solution (particle number per unit volume)

C_{p2} the number concentration of dimers in solution (particle number per unit volume)

From Eqn. (22) and Eqn. (2-33), we get,

$$\frac{N_{o2}}{N_{o1}} = \left(\frac{\overline{V_d}}{2} + K\right)C_{p1} \qquad (2\text{-}34)$$

If not considering droplet induced aggregation, the apparent equilibrium constant, K_{app}, , is defined by the observed monomer concentration, C_{o1},and observed dimer concentration, C_{o2},by $K_{app} = \frac{C_{o2}}{(C_{o1})^2}$. We can obtain,

$$\frac{N_{o2}}{N_{o1}} = \frac{C_{o2}}{C_{o1}} = K_{app}C_{o1} \qquad (2\text{-}35)$$

By comparing Eqn. (2-34) with (2-35), the real equilibrium constant, K, can be obtained

$$K = \frac{C_{o1}}{C_{p1}}K_{app} - \frac{\overline{V_d}}{2} \qquad (2\text{-}36)$$

where C_{p1} is the number concentration of monomers in solution and C_{o1} is the observed number concentration of monomers after ES.

Since C_{o1}. is less than C_{p1} because of the induced dimer formation, we can see that the apparent equilibrium constant, Kapp, when the induced aggregation is not considered, is higher than the true value, and the difference is more than half of the droplet volume $\bar{V}_d/2$.

Using the relationships above, I discuss the results from an ES-MS (without a neutralizer) study by Nettleton *et al.* [1] to characterize the oligomers of insulin. Nettleton *et al.* plotted the fraction of dimer observed by MS against the insulin concentration from 2mol/L to 200mol/L at pH 3.3 and 22°C (Figure 2-7, rhombus). The fraction of dimer was defined as the ratio of summation of the peaks assigned to the dimer to the total signal intensity. In this insulin concentration range only monomer and dimer peaks were observed by MS, so the fraction of dimer is equal to the number of observed dimers divided by the total number of observed dimers and monomers. Nettleton *et al.* used the plot to obtain the apparent equilibrium constant, K_{app}.

Based on droplet induced aggregation of identical particles following Eqn. (2-5), the fraction of induced dimer is

$$\frac{N_{o2}}{N_{o1}+N_{o2}}=\frac{P(2,\bar{\lambda})}{P(1,\bar{\lambda})+P(2,\bar{\lambda})}=\frac{\bar{\lambda}}{2+\bar{\lambda}}=\frac{C_{p1}\bar{V}_d^*}{2+C_{p1}\bar{V}_d^*} \qquad (2\text{-}37)$$

where $\bar{V}_d^*$ is the average droplet volume, if the observed dimers are all droplet induced, and C_{p1} is the insulin number concentration under this situation.

We can estimate the average droplet volume, $\bar{V}_d^*$, by using the protein concentration and the ratio of dimer to total oligomer (Eqn. 2-37). The fourth point in Nettleton's plot is then given by $\log_{10}$[Cp]= -4.3 and the fraction of dimer = 0.6. This value is used to estimate the average droplet volume as ca. $\bar{V}_d^*=9.94\times10^{-23}\text{m}^3$. We then use this average droplet volume to calculate the fraction of dimer at other concentrations in Nettleton's plot based on Eqn. (2-37) and obtain the second curve in Figure 2-8 (line with filled squares). The curve deduced from the droplet induced model essentially superimposes on Nettleton's data and is highly suggestive that an alternative explanation to Nettleton's plot is that droplet induced aggregation is responsible for most of the dimers seen.

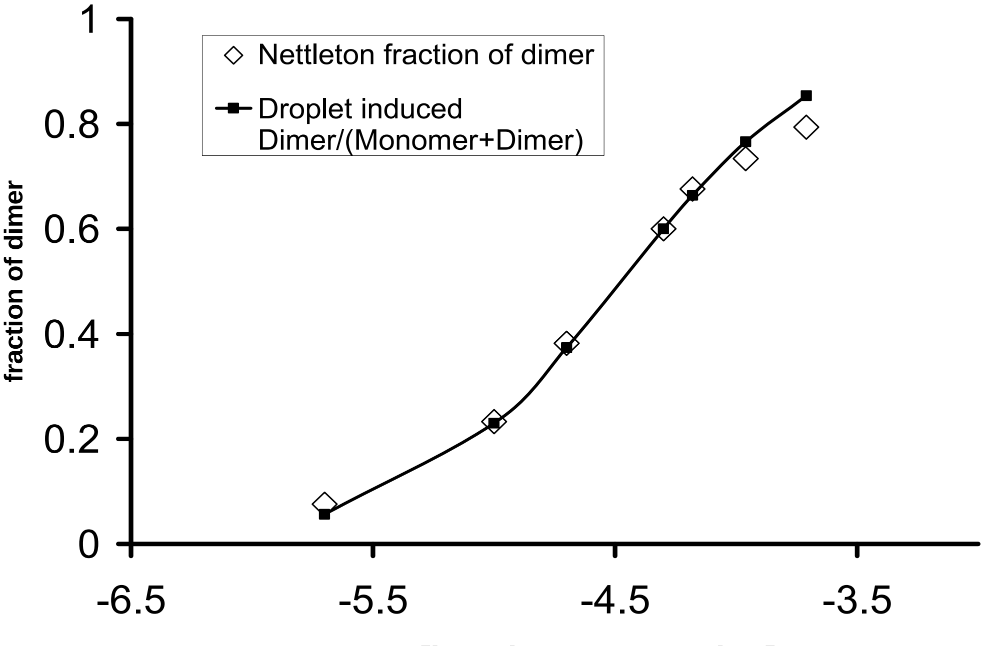

Figure 2-8. *The fraction of insulin dimer vs. insulin total in the concentration range of 2mol/L to 200mol/L at pH 3.3 and 22°C (rhombus) as measured by Nettleton et al.*[1] *using*

Nano-ES/MS (line with open diamonds). The ratio of dimer / (monomer + dimer) calculated by Eqn. (2-37) using the droplet induced dimer for the concentration range of 2mol/L to 200mol/L (line with filled squares).

Given that for the Nettleton's data I do not measure the droplet volume, my discussion necessarily assumes that the ES process of insulin is governed by the droplet induced aggregation mechanism resulting from the charge residue model, rather than any ion-emission mechanism. However, as long as the fraction of insulin particles generated by the droplet induced aggregation mechanism is a fixed value in the insulin concentration range from 2mol/L to 200mol/L, the discussion above is still valid. This is then an alternative explanation of Nettleton's plot [1].

2.5. Summary of Cases and Formulas

In this section, each limiting case and the relevant formula is listed.

Definitions:

$f(D_d)$ = the droplet size distribution, which can be measured experimentally from sucrose solution under the same buffer condition (section 2.3.4)

D_d = the droplet diameter

$\overline{V_d}$ = the average droplet volume as determined from $f(D_d)$

N_{o2} = the observed number of monomers after Electrospray

N_{o2} = the observed number of dimers after Electrospray

C_{p1} = the number concentration of monomers in original solution

C_{p2} = the number concentration of dimers in original solution

2.5.1. Intrinsic Dimer determination (Irreversible/Reversible; Total concentration known; Monomodal and narrow droplet size distribution f(D_d)):

- Only monomers and dimers are in solution; i.e. no higher aggregates.
- Total concentration of the analyte in solution, C_p, is known.

Ratio of intrinsic (in solution) dimer to monomer concentration, C_{p2}/C_{p1}, can be obtained from Eqn. (2-22) and (2-30).,

$$C_p = C_{p1} + 2C_{p2} \tag{2-30}$$

$$\frac{N_{o2}}{N_{o1}} \approx \frac{P_2\big|_{V_d=\overline{V_d}}}{P_1\big|_{V_d=\overline{V_d}}} = \frac{\overline{V_d}C_{p1}}{2} + \frac{C_{p2}}{C_{p1}} \tag{2-22}$$

2.5.2. Intrinsic Dimer determination (Irreversible/Reversible; Total concentration known; Bimodal droplet size distribution f(D_d)):

- Size distribution f(D_d) is bimodal.
- $\overline{V_{d2}}(C_{p1} + C_{p2}) \le 1$

Ratio of intrinsic dimer to monomer, C_{p2}/C_{p1}, can be obtained from Eqn. (2-24) and (2-30).

$$C_p = C_{p1} + 2C_{p2} \tag{2-30}$$

$$\frac{N_{o2}}{N_{o1}} \approx \frac{\overline{V_{d2}}C_{p1}}{2} + \frac{C_{p2}}{C_{p1}} \tag{2-24}$$

where $\overline{V_{d2}}$ the average droplet volume within range 2 (see Figure 2-2b)

2.5.3 Intrinsic Dimer determination (Irreversible aggregation):

The ratio of intrinsic dimer to monomer for irreversible aggregation, C_{p2}/C_{p1}, is

$$\frac{C_{p2}}{C_{p1}} = 2\frac{N_{o2,2x}}{N_{o1,2x}} - \frac{N_{o2}}{N_{o1}} \tag{2-32}$$

where $N_{o1,2x}$ is the observed number of monomers after 2× dilution and $N_{o2,2x}$ is the observed number of dimers after 2× dilution.

2.6. Conclusions

ES sampling is widely used to introduce non-volatile material into the gas phase for characterization by MS or ion-mobility. In using an ES sampling process for characterizing protein or nanoparticle aggregation, one must carefully evaluate if aggregates observed are intrinsic to the solution or induced by the ES process. I have developed a statistical model to calculate the intrinsic oligomer ratios in solution from the experimentally determined distributions by considering the droplet size distribution and physical induced aggregation in electrosprays. Using this approach, I show that that the extent of droplet induced aggregation can be severe. I demonstrate that droplet induced aggregation can bias data obtained by ES-MS and that data obtained by ES-MS or ES-DMA need to be carefully scrutinized to avoid erroneous interpretation. Based on our experimentally validated model, a quantitative distribution of intrinsic particle aggregation in electrospray can be obtained.

2.7. Supplemental Information

Appendix A.

This Appendix provides a justification for the use of a Poisson distribution.

A statistic model is developed to calculate the induced aggregates formed in the electrospray droplets as they dry.

In this appendix, I have only developed a Monomer-Dimer model,however more complicated models can be developed using the same strategy

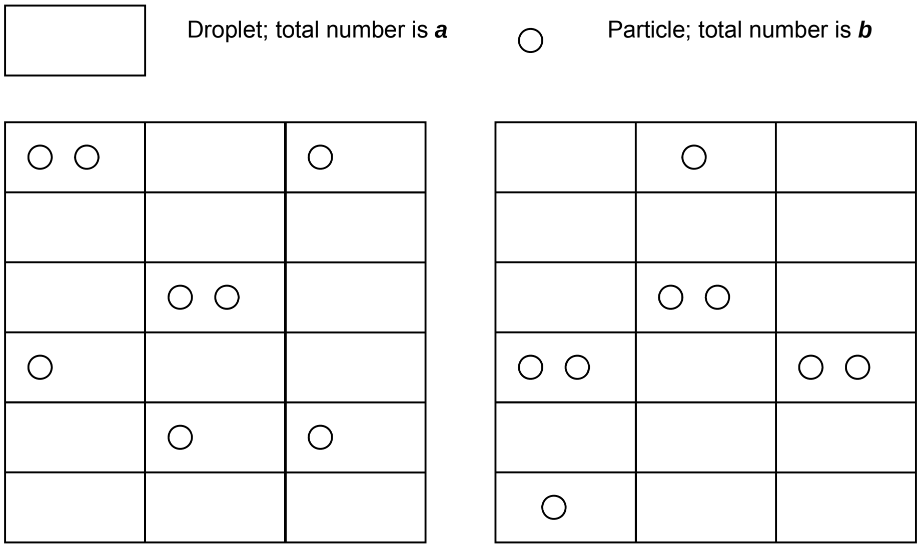

Configuration 1

Configuration 2

Figure 2-S.1. ***b*** *particles randomly distributed in* ***a*** *droplets*

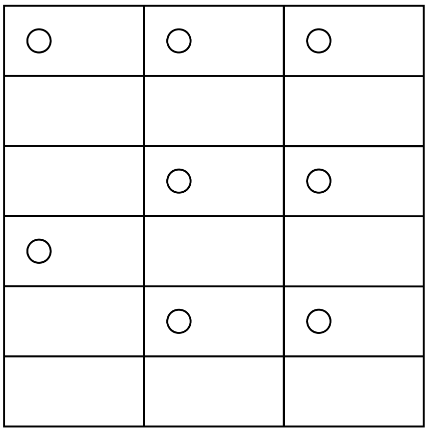

Figure 2-S.2. *No dimers.*

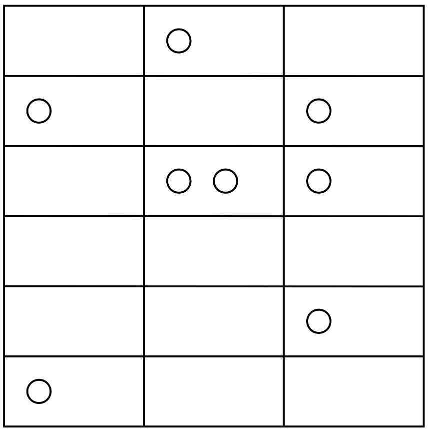

Figure 2-S.3. *One dimer and remainder are monomers*

Monomer-Dimer model.

In Figure 2-S.1 I show that assuming only monomer in solution and there are ***b*** particles randomly distributed in ***a*** droplets, that there are many possible configurations. There are 3 assumptions for this model:

1. The maximum number of particles in one droplet is 2.
2. The probability of each configuration is equal.
3. Droplets are distinguishable; particles are distinguishable.

Assuming ***b*** is an even number, there are 1+***b***/2 cases for this model.

Case 0. No dimers, (**Figure 2-S.2)**. The number of configurations in this case is,

(2-S.1)

Where C(***a***,***b***) is the binomial coefficient, number of ***b***-combinations (each of size ***b***) from a set with ***a*** elements (size ***a***).

Case 1. One dimer and ***b-2*** are monomers, showed in **Figure 2-S.3**. The number of configurations in this case is,

$$P_{2,1}(a,b) = C(a,1)C(b,2)P_1(a-1,b-2) \tag{2-S.2}$$

……

Case ***i***. There are ***i*** dimers and ***b-2i*** monomers. The number of configurations in this case is,

$$P_{2,i}(a,b) = C(a,i)C(b,2i)\frac{(2i)!}{(2!)^i}P_1(a-i,b-2i) \tag{2-S.3}$$

……

Case ***b***/2. All are dimers. The number of configurations in this case is,

$$P_{2,b/2}(a,b) = C(a,b/2)\frac{(b)!}{(2!)^{b/2}}P_1(a-b/2,0) \tag{2-S.4}$$

In Case ***i***, the number of monomers is (***b-2i***)$P_{2,i}$(***a***,***b***), and the number of dimers is ***i***$P_{2,i}$(***a***,***b***). So the total number of monomers in all cases is,

$$N_{2,m}(a,b) = \sum_{i=0}^{b/2}(b-2i)P_{2,i}(a,b) \tag{2-S.5}$$

and the total number of dimers in all cases is,

$$N_{2,d}(a,b) = \sum_{i=0}^{b/2} iP_{2,i}(a,b) \tag{2-S.6}$$

Substituting Eqs.(2-S.3) for $P_{2,i}$(***a***,***b***) in Eqs.(2-S.5), the following result is obtained:

$$N_{2,m}(a,b) = \sum_{i=0}^{b/2} C(a,i)C(b,2i)\frac{(2i)!}{(2!)^i}(b-2i)P_1(a-i,b-2i) \tag{2-S.7}$$

Similarly, substituting Eqs.(2-S.3) for $P_{2,i}$(***a***,***b***) in Eqs.(2-S.6), the total number of dimers can be expressed as,

$$N_{2,d}(a,b) = \sum_{i=0}^{b/2} C(a,i)C(b,2i)\frac{(2i)!}{(2!)^i} iP_1(a-i,b-2i) \tag{2-S.8}$$

The ratio of the number of dimers to the number of monomers based on this model is,

$$R_{2,d}(a,b) = N_{2,d}(a,b)/N_{2,m}(a,b) \tag{2-S.9}$$

Because in a specific experiment, ***a*** and ***b*** can be chosen arbitrarily, but the mean number of particles per droplet, λ = ***b*/*a*** = V_dC_p is a characteristic value for that experiment, where V_d is the droplet volume and C_p is the number concentration of the monomer particles in solution. An asymptotic relationship between $R_{2,d}$ and λ when ***a*** is large; ***a=15000*** (λ =***b/a*** =0.05, 0.1, 0.15, 0.2, 0.25, 0.3) is

$$R_{2,d}(a,b) = N_{2,d}(a,b)/N_{2,m}(a,b) = 0.5215\lambda - 0.0018 \tag{2-S.10}$$

The relationship derived in Equation 2-S.10 gives an accurate relationship for the ratio of dimers to monomers (for no higher oligomers), and is very close to what a Poisson distribution gives i.e.

$$R_{2,d} = 0.5\lambda \tag{2-S.11}$$

I therefore employ a Poisson distribution approximation for the derivation of the relationships derived in the body of the manuscript.

Appendix B.

This Appendix provides a prove for the general relationship for the dimer to monomer ratio by considering a droplet size distribution of ES, $f(D_d)$.

1. Droplets of an identical size

Assuming that following ES, N_{o1} monomers and N_{o2} dimers are observed with probabilities P_1 and P_2, the ratio of observed dimers to observed monomers for ES droplets of an identical size is given by

$$\frac{N_{o2}}{N_{o1}} = \frac{P_2}{P_1} \tag{2-S.12}$$

2. Droplets of two sizes

Considering the total number of droplets that ES process generates is N and there are only two droplet sizes with droplet volumes ,V_{d1} and V_{d2} respectively, and the fractions of total droplet number, f_1 and f_2 respectively, then the number of droplets that produce a monomer is $Nf_1\, P_1\big|_{V_d=V_{d1}} + Nf_2\, P_1\big|_{V_d=V_{d2}}$, and the number of droplets that produce a dimer is $Nf_1\, P_2\big|_{V_d=V_{d1}} + Nf_2\, P_2\big|_{V_d=V_{d2}}$. The observed dimer to monomer ratio is,

$$\frac{N_{o2}}{N_{o1}} = \frac{Nf_1\, P_2\big|_{V_d=V_{d1}} + Nf_2\, P_2\big|_{V_d=V_{d2}}}{Nf_1\, P_1\big|_{V_d=V_{d1}} + Nf_2\, P_1\big|_{V_d=V_{d2}}} = \frac{f_1\, P_2\big|_{V_d=V_{d1}} + f_2\, P_2\big|_{V_d=V_{d2}}}{f_1\, P_1\big|_{V_d=V_{d1}} + f_2\, P_1\big|_{V_d=V_{d2}}} \tag{2-S.13}$$

where V_d is the droplet volume.

3. Droplets following a size distribution, $f(D_d)$

Considering a droplet size distribution of ES, $f(D_d)$, a general relationship for the dimer to monomer ratio by generalizing (2-S.13) is given by,

$$\frac{N_{o2}}{N_{o1}} = \frac{\sum_i f(D_{d,i}) P_2}{\sum_i f(D_{d,i}) P_1} \tag{2-S.14}$$

or $$\frac{N_{o2}}{N_{o1}} = \frac{\int f(D_d) P_2 dD_d}{\int f(D_d) P_1 dD_d} \qquad \text{(2-S.15)}$$

where $\sum_i f(D_{d,i}) = 1$ and $\int f(D_d) dD_d = 1$

Chapter 3: Method for Determining the Absolute Number Concentration of Nanoparticles from Electrospray Sources

3.1. Introduction

Nanoparticles (NPs) are finding increased use in optical sensing, diagnostics, clinical chemistry, and therapeutics. For diagnostic and therapeutic applications of NPs in humans there will likely be strict requirements for regulatory approval such as extensive characterization of the properties of these products. In nearly all applications, one such attribute undoubtedly will be accurate determination of particle concentration. Because of the great diversity of NPs and their associated physical and chemical properties, there currently is no one broadly applicable method for measurement of nanoparticle concentration. For metallic nanoparticles, e.g., Au-NPs, and protein particles, e.g., Rmabs, UV/Vis spectroscopy is routinely used to determine the absolute concentration in solution[54, 55]. Accurate measurement, however, requires a precise knowledge of extinction coefficient which depends on particle composition, size, shape, dielectric environment, and surface coatings[56-59].

One of the tools I are investigating to measure concentration of NPs involves using electrospray (ES) to generate vapor phase dispersed material. These aerosol materials can then be analyzed by ion mobility methods such as differential mobility analyzer (DMA) also known as gas-phase electrophoretic molecular analysis (GEMMA)[18, 22-25, 43] or mass spectrometry (MS) methods[1, 27-30]. These techniques have the potential to characterize the full size distribution and concentration of NPs in solution. However, because this is a physical sampling approach measurements must be corrected for aerosol losses, which may depend in an unknown way on the nature of the ES-generation, ES efficiency[45, 60, 61], particle extraction to the DMA or MS, and the efficiency of particle counting instruments.

In this chapter I present a new approach that exploits what is typically considered an unwanted artifact of electrospray sources, namely droplet induced aggregation, to extract quantitative number concentration. By using a recently developed predictive algorithm for the measurement of oligomer distribution in an analyte solution[7], I are able to quantitatively measure the number concentration of an arbitrary colloidal solution. In this work I apply the theory in previous chapter [7] to obtain the absolute number concentration of intrinsic monomer and dimer in solution. The total number concentration of monodispersed Au nanoparticles and Rituxan monoclodal antibody (Rmab) obtained using this method in our ES-DMA work are verified by quantitative UV-Vis measurement. For users only interested in implementation of the theory I provide in section 3-5 a summary of relevant formulas.

3.2. Materials and Experimental Methods

I demonstrate my approach by examining gold nanoparticles (Au-NPs) with an ES-DMA system described previously[49]. I also show the method is applicable to biological molecules by examining Rituxan, a monoclonal antibody (Rmab), to quantify the absolute number concentration of protein oligomers in solution.

3.2.1. Gold nanoparticle preparation

Commercially available citrate-stabilized monodisperse Au-NPs (10nm, $5.7\text{x}10^{12}$ particles/mL, Ted Pella Inc.) were used. A 1.5 mL solution of the as-received Au-

NPs was centrifuged at 13,200 rpm for 45 minutes, and ≈1.47 mL of the supernatant was removed and replaced with an equivalent volume of aqueous 2 mmol/L ammonium acetate solution prepared by diluting 20 mmol/L ammonium acetate at pH 10. This step was performed to remove most of the citrate stabilizer, which would otherwise coat the Au-NPs upon ES. The pH of the 20 mmol/L ammonium acetate solution was adjusted by addition of ammonium hydroxide. The solution was then centrifuged again for 15 minutes, and 1.4 mL of supernatant was removed to obtain a highly concentrated Au-NPs sample. The number concentration of Au-NPs in 1.4 mL of supernatant, C_s, was measured by UV-VIS spectroscopy by comparison of the peak absorbance value of the supernatant solution with that of the as-received Au-NPs of known concentration at the wavelength of ~520 nm. Four replicate Au-NP samples were prepared following the protocol described above and are noted as sample #1 - #4. The as prepared Au-NP samples were then electrosprayed into the DMA-CPC system after dilution by 2×, 4×, or 8× with 2 mmol/L ammonium acetate solution.

3.2.2. Rmab solution preparation

Formulated Rmab (145 kDa) was purified using a Protein A affinity column. Purified Rmab was stored at -18° C in 25 mmol/L Tris buffer, pH 7.4, with 0.01% sodium azide (NaN_3) added as a preservative. Immediately prior to use in ES studies, the storage buffer was exchanged for 20 mmol/L ammonium acetate, pH 7 by washing all salts from Rmab using a centrifugal filter device with a weight cutoff of 30 kDa. The concentration of Rmab in 20 mmol/L ammonium acetate was adjusted to 1 mg/mL as verified by measuring the maximum absorbance at 280 nm and using a molar absorptivity of 236020 $(mol/L)^{-1}$ cm^{-1}. Working solutions of concentrations

100 µg/mL, 50 µg/mL, 25 µg/mL, 10 µg/mL, and 5 µg/mL were made by dilution with 20 mmol/L ammonium acetate and used for ES studies.

3.2.3. Electrospray Particle Generation and Differential Mobility Measurements

Aerosolized droplets were generated using a 40 µm inner diameter capillary for Au-NP samples and a 25 µm inner diameter capillary for Rmab mounted in an Electrospray Aerosol Generator (Model 3480, TSI Inc.) where the liquid flow rates through the capillaries were ~433 nL/min and ~66 nL/min, respectively[50]. The ES was operated with a carrier gas of 1 L/min purified air, and 0.2 L/min carbon dioxide to stabilize the Taylor cone. A stable Taylor cone is necessary to quantitatively determine droplet induced aggregation, and the absolute particle number concentration. The aerosolized droplets are then passed over a radioactive Po-210(α) source that reduces the charge on the droplets to a well-defined Fuchs equilibrium charge distribution[6]. With this known charge distribution, the total number of particles can be obtained by counting the number of single positively charged particles. The neutralized dry particles entered a Differential Mobility Analyzer (DMA) (Model 3485 Nano DMA column, TSI Inc.) for particle size measurement, and subsequently counted with an Ultrafine Condensation Particle Counter (CPC) (Model 3025A TSI Inc.). The DMA consists of a grounded cylinder and an inner negative high voltage rod with a slit for the particles of given mobility size to exit, and be counted by the CPC. By scanning the center rod voltage, different size particles can be extracted to build up a size distribution for a given particle population. Unlike a mass-spectrometer which selects particles based on mass/charge ratio, the DMA selects particles based on its equivalent mobility diameter. In the simplest case, i.e. particles in the free molecule regime, the mobility scales with the inverse of the projected area to charge ratio. The size-selection resolution of DMA is determined by the ratio of sheath-to-aerosol flow rates within the DMA. To achieve sufficient resolution in our experiment, the nano-DMA was operated with a sheath flow of 30 l/min and an aerosol flow 1.2 l/min, which enables an operating range of between 2 - 45 nm. For our operating conditions we have found a lower number concentration limit of $\sim 10^9$ particles/cc for particles < 100 nm. A different choice of flow rates and the use of a different length DMA would enable a different size range to be classified. Because this is an ion-mobility measurement the composition of the analyte particle is not relevant to the operational principles of the instrument. More details on the measurement method can be found in Tsai *et al.*[49].

3.2.4. Droplet Size Measurements

In order to employ our method for quantification, knowledge of the droplet size generated by the ES source is required. The statistical analysis of droplet induced aggregation requires a droplet size distribution. Further explanations are shown in the supporting information. The droplet size distribution was determined by electrospraying a known concentration (V/V) of sucrose solution, and measuring the resultant dry particle size distribution. Using this procedure, the original droplet size distribution can be determined directly. For droplet size evaluation, sucrose solution concentrations of 0.0315% V/V and of 0.063% V/V, were used for Au-NP, and Rmab measurements, respectively. At such low concentrations of sucrose, and analytes, the viscosity of solutions is governed by the buffer conditions, and the droplet size of these solutions can be evaluated by [41, 50]

$$D_d = \frac{1}{C_s^{1/3}} D_s \tag{3-1}$$

where D_d is the droplet diameter, D_s is the sucrose particle diameter after drying (measured by DMA), and C_s is the sucrose concentration (V/V) in the ES solution.

3.3. Theory of Determining the Absolute Number Concentration

In the oligomer distribution study of Li *et al.* [7], unintentional (non-specific) analyte aggregation in electrospray sampling, called droplet induced aggregation, was addressed and quantified. In any electrospray process, induced aggregation within a droplet can be a confounding artifact to prediction of the true oligomer distribution in solution. However, I have found that this effect can be a very useful probe to directly deduce the monomer concentration in solution without the need to calibrate the losses of the ES process and the losses post-electrospray. In order to explain this clearly, I first describe the electrospray process, and introduce the effect of droplet induced aggregation. The mechanism of ES has been treated in great detail by Kebarle *et al.*[31] and Gaskell[32] as well as others. In ES, the application of a high voltage to a capillary will induce, due to coulombic repulsion, small droplet formation. It is well accepted that large and compact multiply charged ions, which are the analytes of interest in this work, are produced as charged residues after complete drop evaporation after serial fission processes[36]. Evaporation of the solvent leaves behind the analyte (e.g. protein, particle, virus, etc) which is then passed to an analyzer such as a DMA or mass spectometer. When two or more analyte molecules or particles exist in a final droplet, and the droplet eventually dries, oligomers are observed in the spectrum of MS or DMA (Figure 3-1). I recently investigated this effect through a statistical model by Li *et al* [7] that allowed us to separate the true oligomer concentration from the induced concentration. In this work I extend the analysis to use the induced oligomer formation to extract the absolute number concentrations of monomers and oligomers in solution.

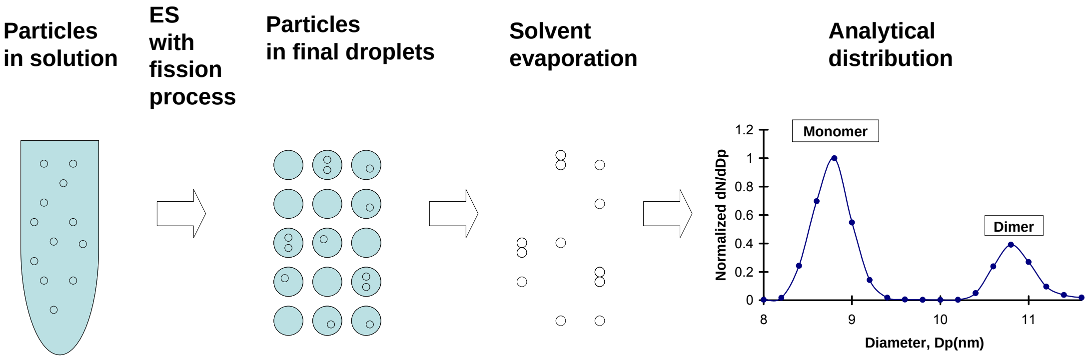

Figure 3-1. *Schematic of electrospray process showing the resulting measured particle size distribution observed due to droplet induced aggregation. There are no intrinsic dimers in the original solution. However, after the ES, induced dimers are observed in the analytical spectrum and statistical analysis can be used to deduce the original monomer concentration in solution . The y-axis label "dN/dD_p" is defined by the total number of particles in the range $[D_p, D_p + dD_p]$ divided by the size interval, dD_p.*

Physical Aggregation (droplet induced aggregation) of particles

In an electrospray of a colloid there is a finite probability, depending on particle concentration and droplet size, that more than one particle will be within a droplet. Upon evaporation of the solvent, aggregration of the particles is induced. If a final droplet generated in an ES after a series of fission process is a random sample of the solution, the size of a droplet is much greater than the size of particles, and the oligomer particles in the solution are random and independent, then the distribution of observed oligomers in droplets can be quantitatively described[7]. Here I first introduce a theory in general form describing the full droplet size distribution, then I derive two approximations under two different limiting cases and apply them to obtain the absolute number concentrations of monomers and dimers in solution. The essential feature of this approach is that the observed dimer/monomer ratio is a unique function of the droplet size and the initial monomer concentration. This same strategy can also be expanded to quantify the absolute concentrations of any higher-order aggregates. Below I derive working relationships for some useful cases:

3.3.1. Droplet induced aggregation of identical particles (monomers) from droplets of identical size generated by ES

If a final droplet generated in ES after the fission process is a random sample of the solution, and the particles in the solution are identical and exist only as monomers, the probability that there are k particles in a given droplet obeys a Poisson distribution[7, 22, 44,] and is given by

$$P(k,\lambda)=\frac{e^{-\lambda}\lambda^{k}}{k!} \tag{3-2}$$

where λ is the mean number of particles per droplet and is given by

$$\lambda=V_{d}C_{p}=\frac{1}{6}\pi D_{d}^{3}C_{p} \tag{3-3}$$

where V_d is the final droplet volume, D_d is the final droplet diameter and C_p is the number concentration of the particles in solution.

3.3.2. Droplet induced aggregation of monomers and dimers in solution from droplets : General case

If we consider an arbitrary droplet size distribution, f(D$_d$), from an ES-source and assume intrinsic monomers and dimers in solution, a general relationship for the observed dimer to monomer ratio is given by [21]

$$\frac{N_{o2}}{N_{o1}} = \frac{\int f(D_d) P_2 dD_d}{\int f(D_d) P_1 dD_d} \tag{3-4}$$

where

$\int f(D_d) dD_d = 1$.

$P_1 = e^{-(\lambda_1+\lambda_2)}\lambda_1$:the probability of monomers observed in the final droplet with diameter D$_d$ (3-5)

$P_2 = e^{-(\lambda_1+\lambda_2)}(\frac{\lambda_1^{\ 2}}{2}+\lambda_2)$:the probability of dimers observed in the final droplet with diameter D$_d$ (3-6)

$\lambda_1 = V_d C_{p1} = \frac{1}{6}\pi D_d^{\ 3} C_{p1}$: the mean number of monomers per droplet

$\lambda_2 = V_d C_{p2} = \frac{1}{6}\pi D_d^{\ 3} C_{p2}$: the mean number of dimers per droplet

V$_d$: the final droplet volume

D$_d$: the final droplet diameter

Here the number concentration of intrinsic monomers in solution is C$_{p1}$, and the number concentration of intrinsic dimers in solution is C$_{p2.}$ Then following electrospray we observe N$_{o1}$ monomers and N$_{o2}$ dimers.

Eqns.(3-5) and (3-6) were obtained assuming that the size of a droplet is much greater than the size of the analytes particles, and that the partial spatial distribution is independent of each other, i.e. oligomers in the ES process follow an independent joint Poisson distribution. A more accurate form of (P1, P2) can be obtained using the methodology I have previously described in the statistical online supplemental information in Li *et al.*[7]. In this work I use Eqns. (3-5) and (3-6)..

Although it is difficult to solve Eqn.(3-4) for C_{p1} and C_{p2} directly, accurate approximations can be obtained under some limiting conditions .

i. Monomodal and narrow droplet size distribution

For the first limiting condition, the droplet size distribution $f(D_d)$ is considered to be monomodal and relatively narrow. As an example I consider in Figure 3-2a a droplet size distribution from ES measured for sucrose in 20mmol/L Ammonium acetate. In this case Eqn. (3-4) can be evaluated with one average droplet volume [7],

$$\frac{N_{o2}}{N_{o1}} \approx \frac{P_2\big|_{V_d=\overline{V_d}}}{P_1\big|_{V_d=\overline{V_d}}} = \frac{\overline{V_d}C_{p1}}{2} + \frac{C_{p2}}{C_{p1}} \tag{3-7}$$

where

$$\overline{V_d} = \sum_i f(D_{d,i})V_{d,i} = \sum_i f(D_{d,i})\frac{1}{6}\pi D_{d,i}^{\ 3} \quad \text{and} \tag{3-8}$$

$$\sum_i f(D_{d,i}) = 1$$

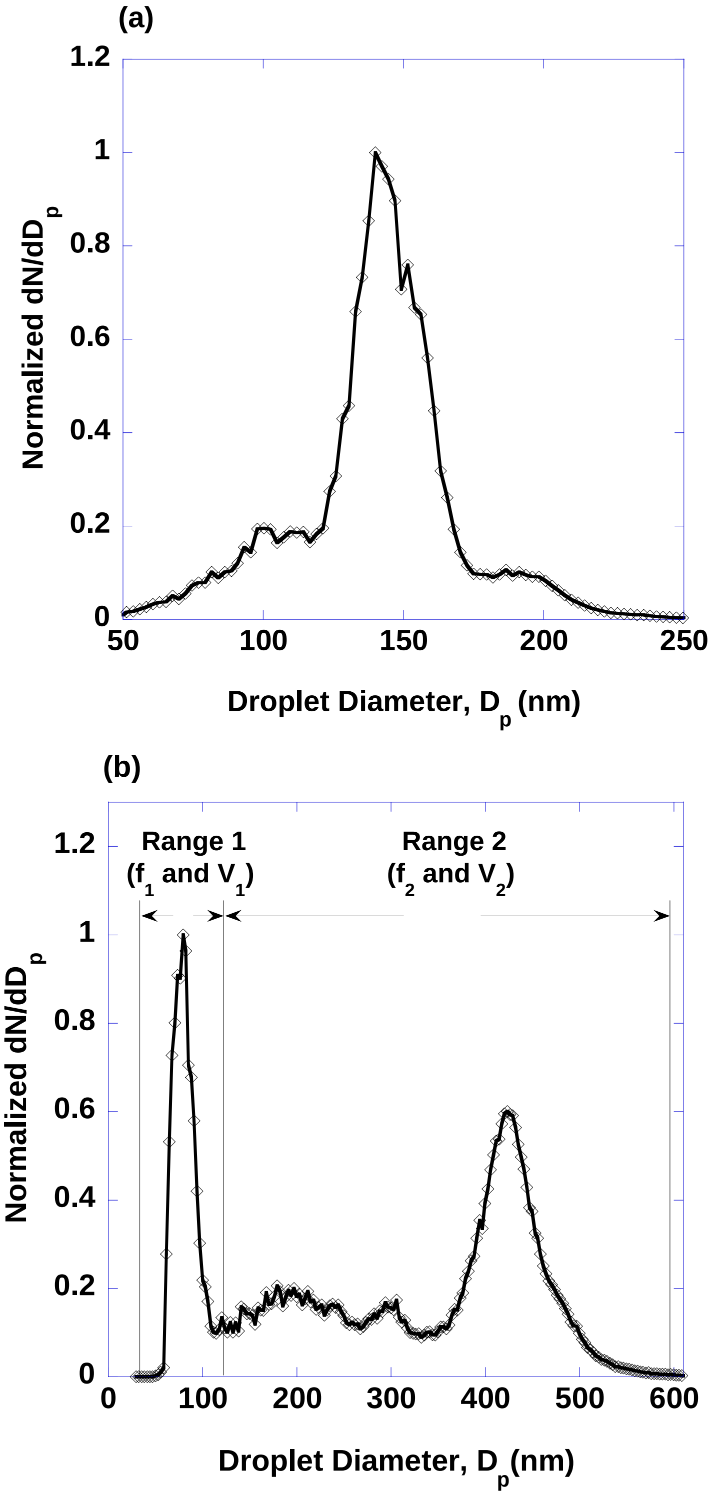

Figure 3-2. (a). *ES monomodal and narrow droplet size distribution measured from sucrose at 20 mmol Ammonium Acetate buffer (section3.2.4), and used for Rmab samples at the same*

buffer condition in section 3.4.1.ii. **(b).** *ES droplet with a bimodal size distribution measured from sucrose at 2 mmol Ammonium Acetate buffer (section3.2.4), and used for Au-NPs sample #3 and sample #4 in section 3.4.1.i. The y-axis label "dN/dD_p" is defined by the total number of particles in the range [D_p, D_p+ dD_p] divided by the size interval, dD_p.*

ii. Bimodal droplet size distribution f(D_d)

If the size distribution f(D_d) is bimodal as for example shown in Figure 3-2b, then Eqn. (3-4) can be approximated by using two average droplet volumes, $\overline{V_{d1}}$ in range 1, *and* $\overline{V_{d2}}$ in range 2. If the concentrations are not very high, that is $\overline{V_{d2}}(C_{p1}+C_{p2})$ is not much greater than unity, Eqn.(3-4) can be further approximated by using only one average droplet volume, $\overline{V_{d2}}$.

$$\frac{N_{o2}}{N_{o1}} \approx \frac{\overline{V_{d2}}C_{p1}}{2} + \frac{C_{p2}}{C_{p1}} \tag{3-9}$$

The derivations and more approximated formulas in those two limiting cases are shown in the supporting information.

Thus from a measurement of the "observed" monomers and dimers ($N_{o1,}$ N_{o2}), the absolute number concentration of intrinsic monomers, C_{p1}, can be obtained through evaluation of Eqns. (3-4) directly, or through its accurate approximations (3-7) (3-9), *under the appropriate conditions described above*. The only requirement for this method is that the final droplet size distribution be determined, which can be done in the absence of analyte as described above in Section 3.2.4. Thus, this method eliminates the need for sample specific calibration standards or detailed analysis of transport losses.

3.4. Results and Discussion

I will describe two approaches for making absolute concentration measurements and apply them to nanoparticles and protein.

(a) Determination of absolute number concentration by serial dilution.

(b) Determination of absolute number concentration by changing droplet size.

3.4.1. Determination of absolute number concentrations by serial dilution

i. **Absolute number concentrations of Au-NPs**

In this section I discuss how following an experimental strategy based on the relationship derived in the theory section, I can determine the absolute number concentrations of NP's in solution.

Figure 3-2b shows the droplet size distribution measured from sucrose solution in 2mmol/L ammonium acetate buffer, and the identical buffer solution used for Au-NPs samples. Based on the distribution in Figure 3-2b and the bimodal droplet size approximation, the absolute number concentrations of monomer and dimer of Au-NPs can be obtained by a series of measurements at various dilutions for irreversible aggregation

$$C_{p1} = \frac{4}{V_{d2}}\left(\frac{N_{o2}}{N_{o1}} - \frac{N_{o2,2x}}{N_{o1,2x}}\right) \tag{3-10}$$

$$C_{p2} = \frac{4}{V_{d2}}\left(\frac{N_{o2}}{N_{o1}} - \frac{N_{o2,2x}}{N_{o1,2x}}\right)\left(2\frac{N_{o2,2x}}{N_{o1,2x}} - \frac{N_{o2}}{N_{o1}}\right) \tag{3-11}$$

where $N_{o1,2x}$ is the observed number of monomers after 2× dilution and $N_{o2,2x}$ is the observed number of dimers after 2× dilution. The detailed derivation is shown in the supporting information.

Figure 3-3 shows the observed size distribution for 2×, 4× and 8× dilutions of 10 nm Au-NPs (sample #4). Using the data we can evaluate Eqn. (3-10) and (3-11) to determine the absolute concentrations in solution.

It would be best to use an orthogonal method to ascertain validity of our measurement and data analysis approach; but an independent measure of both the monomer and dimer concentration is unavailable. We can, however, compare the sum of our monomer and dimer measurement with the total number concentration of Au-NPs provided by the vendor and independent UV/VIS measurements.

Table 3-1 shows the intrinsic number concentrations for the 1× Au-NPs samples based on the observed numbers of monomer and dimer measured with ES-DMA at 2×, 4× and 8× dilutions for Au-NPs samples #1 - sample #4 using Eqn.(3-10) and (3-11). For each sample, the total number concentration of monomer, whether free or aggregated, $C_{p1}+2C_{p2}$, is calculated and compared with the total number concentration obtained from UV/VIS and the vendor's specification.

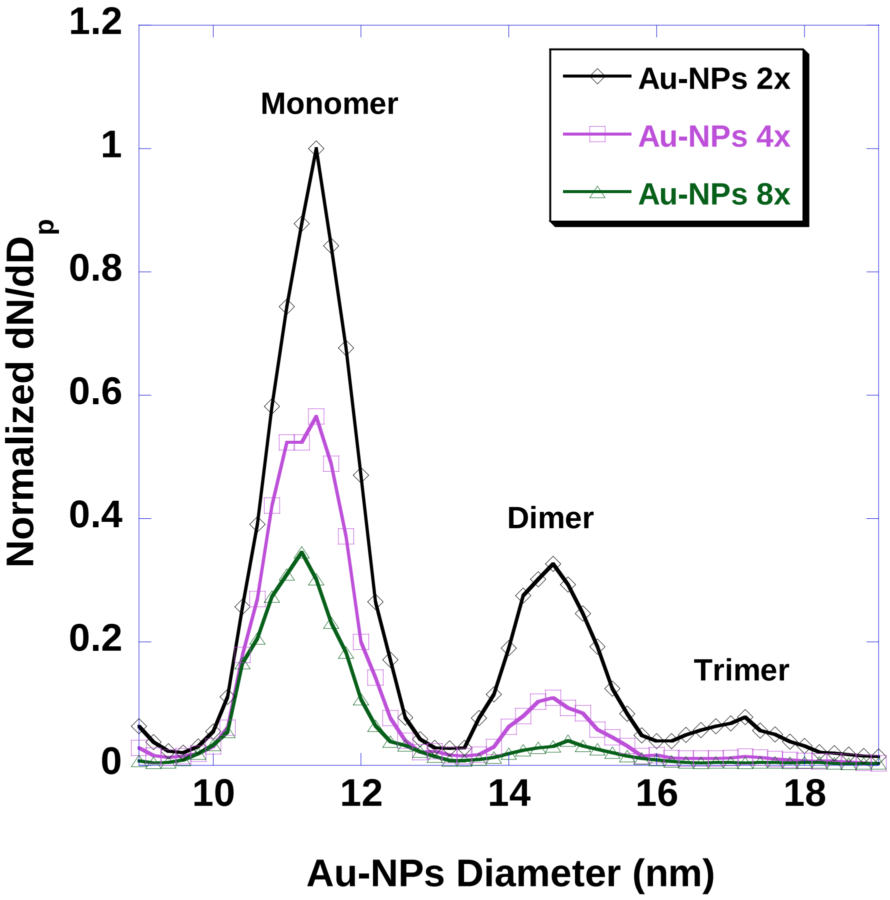

Figure 3-3. *ES-DMA size distributions of 10 nm Au-NPs, sample #4. The rhombus, square and triangle data markers are those of 2-times, 4-times and 8-times dilutions of the original sample, respectively. Each of the discernable oligomer peaks are labeled. The y-axis label "dN/dD_p" is defined by the total number of particles in the range [D_p, D_p+ dD_p] divided by the size interval, dD_p.*

Table 3-1. ***Comparison of ES-DMA measured concentrations for the 1× Au-NPs samples and that of UV/VIS of Au-NPs (sample #1 to sample #4).*** *For each sample, the total number concentration of monomer whether free or aggregated, Cp1+ 2Cp2, is calculated and compared with the total number concentration obtained from UV/VIS and supplier specification.*

Exp. number	Based on Au-NPs at	ES-DMA-CPC observed results + Droplet induced model (#/mL)	UV/VIS measurement (#/mL)
		$C_{p1}+2C_{p2}$	$C_{uv\text{-}vis}$
#1	2× and 4× of sample #1	5.20E+13	4.81E+13
#2	4× and 8× of sample #1	4.02E+13	4.81E+13
#3	2× and 4× of sample #2	5.07E+13	5.15E+13
#4	4× and 8× of sample #2	4.18E+13	5.15E+13
#5	2× and 4× of sample #3	4.59E+13	4.92E+13
#6	4× and 8× of sample #3	4.51E+13	4.92E+13
#7	2× and 4× of sample #4	5.15E+13	5.01E+13
#8	4× and 8× of sample #4	4.50E+13	5.01E+13

Another way to view these results is presented in Figure 3-4 which plots the ES-DMA to UV/VIS measurement as a function of the experiment number. In order to compare clearly the results from the two measurement methods above, the $C_{p1}+2C_{p2}$ (from droplet induced model) are normalized by $C_{uv\text{-}vis}$ (obtained from the UV/VIS measurements and the vendor specification) and displayed in Figure 3-4 as a function of experiment number.

These results show good agreement for the low dilution pairs, and poorer agreement with the high dilution pairs. The normalized value of $C_{p1}+2C_{p2}$ is 1.01±0.05 for low dilution pairs, and 0.87±0.04 for high dilution pairs. The calculations are based on bimodal droplet size approximation using Eqn. (3-10) and (3-11). The discrepancy between them can likely be attributed to the fact that the distribution in Fig. 3-2b is not truly bimodal (i.e. note satellite peaks). *However overall the method as outlined above allows a simple and reasonably accurate* *determination of particle concentration without the need for calibration of the ES-source or detector (CPC/DMA).*

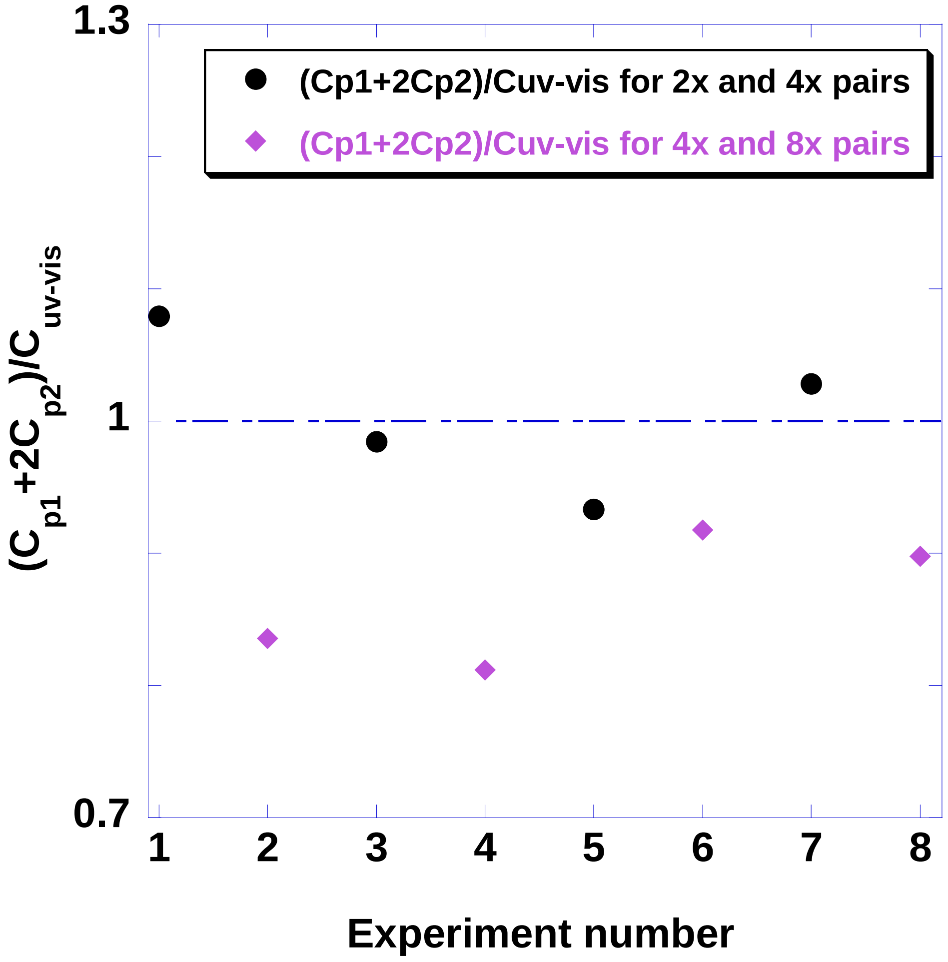

Figure 3-4. *The total number concentration of monomer whether free or aggregated,* C_{p1}+ $2C_{p2}$, *calculated based on Eqn.(3-10) and (3-11) is divided by the total number concentration* $C_{uv\text{-}vis}$ *obtained from UV/VIS and vendor specification. The x-axis is the experiment index number. The circle and rhombus symbols are those for 2x and 4x dilution pairs and for 4x and 8x dilution pairs, respectively. Lower dilution pairs (solid circles) provide more accurate results.*

ii. Determination of absolute number concentrations of Rmab protein by serial dilution

A serial dilution of the Rmab sample was prepared with concentrations of 100µg/mL (1×), 50µg/mL (2×), 25µg/mL (4×), 10µg/mL (10×), and 5µg/mL (20×) at pH7 in 20 mmol/L ammonium acetate buffer. The dilution method described in section 3.4.1.i was then used to estimate the total number concentration of monomer whether free or aggregated, $C_{p1}+2C_{p2}$, of the 1× sample, and this value was compared to the known concentration, 100µg/mL.

Figure 3-2a shows the droplet size distribution under the same experimental conditions. The distribution is monomodal. Using the dilution method described in section 3.4.1.i, the total number concentration of monomer whether free or aggregated of 1× sample, $C_{p1}+2C_{p2}$, are calculated and shown in Table 3-2.

Table 3-2. *The total number concentrations of monomer whether free or aggregated of 1× Rituxan sample,* $C_{p1}+2C_{p2}$, *are calculated based on the observed numbers of monomer and dimer measured with ES-DMA-CPC at various dilutions at pH7 in 20 mmol/L ammonium acetate buffer and the dilution-method, Eqn.(3-13,3-14). The values then are compared with the known total number concentration, 100 µg/mL.*

Exp. number	ES-DMA results + Droplet induced model		Known Concentration
	Rmab at	Measured (µg/mL)	C_p (µg/mL)
#1	100 and 50 µg/mL	110	100
#2	50 and 25 µg/mL	111	100
#3	25 and 10 µg/mL	104	100
#4	10 and 5 µg/mL	104	100

Examination of Table 3-2 shows that the total number concentration calculated from droplet induced model is 107.3 ± 3.3 μg/mL, which compares reasonably with the known value of 100 μg/mL.

The determination of absolute number concentration by serial dilution is expected only for irreversible aggregations. However, because the intrinsic dimer concentrations in Au-NPs and Rmab protein samples under the conditions in this work are at most 5% based on Li *et. al.*[7], i.e. essentially only monomers exist in solution, the serial dilution method can be used for both Au-NPs and Rmab protein.

3.4.2. Determination of absolute number concentrations by changing droplet size: Application to measurement of Rmab protein.

In this section I show another experimental strategy using a series of measurements under different droplet size distributions to measure the concentration of biological molecules, in this case the Rmab protein. This strategy can be used for both reversible and irreversible aggregation.

The ES droplet size distribution was changed by varying the chamber pressure across the capillary in the electrospray source. Figure 3-5a shows the droplet size distributions from sucrose solution at pH 7 in 20 mmol/L ammonium acetate buffer with chamber pressures 3.0 psi ($2.07*10^4$ Pa) and 3.7 psi ($2.55*10^4$ Pa). Figure 3-5b shows the observed size distributions of Rmab at a concentration of 100 μg/mL in the same buffer. Based on the droplet size distributions in Figure 3-5a, the average droplet volumes are calculated and shown in Table 3-3. Because the droplet size distributions in Fig. 3-5a are monomodal, the monomodal droplet size approximation is used, and the intrinsic number concentration of monomer and dimer of Rmab, C_{p1} and C_{p2}, can be obtained from (3-7) and (3-12),

$$\frac{N_{o2}}{N_{o1}} = \frac{\overline{V_d} C_{p1}}{2} + \frac{C_{p2}}{C_{p1}} \tag{3-7}$$

$$\frac{N_{o2,\overline{V_d}'}}{N_{o1,\overline{V_d}'}} = \frac{\overline{V_d}' C_{p1}}{2} + \frac{C_{p2}}{C_{p1}} \tag{3-12}$$

where N_{o1} and N_{o2} are the observed number of monomers and dimers, respectively, at average droplet volume $\overline{V_d}$, while $N_{o1,\overline{V_d}'}$ and $N_{o2,\overline{V_d}'}$ are the observed number of monomers and dimers, respectively, at average droplet volume $\overline{V_d}'$. The detail derivation of (3-7) and (3-12) is shown in the supporting information.

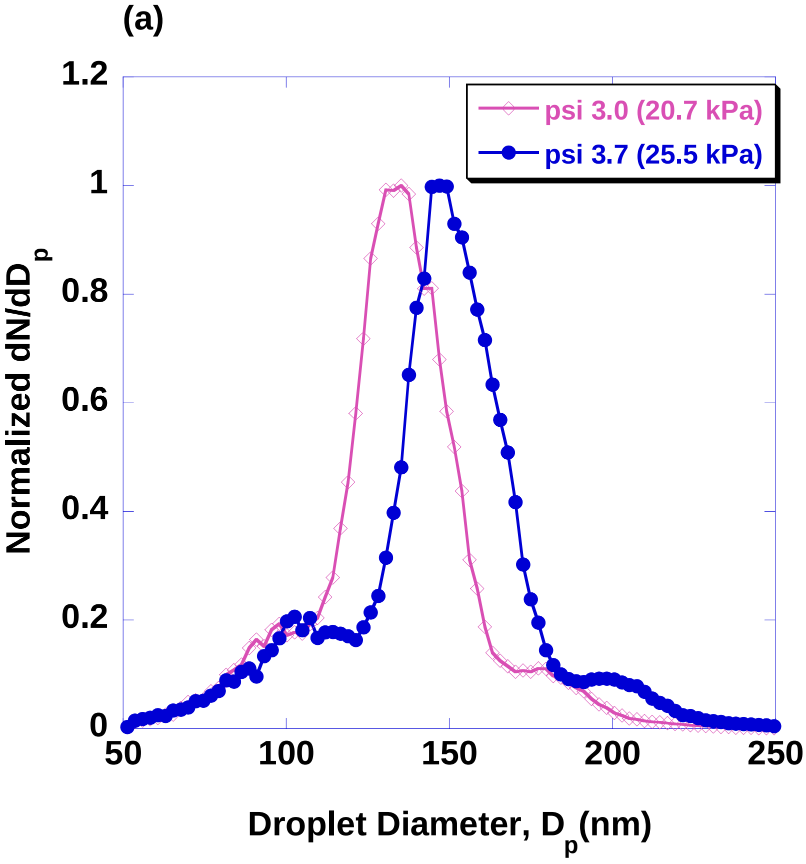

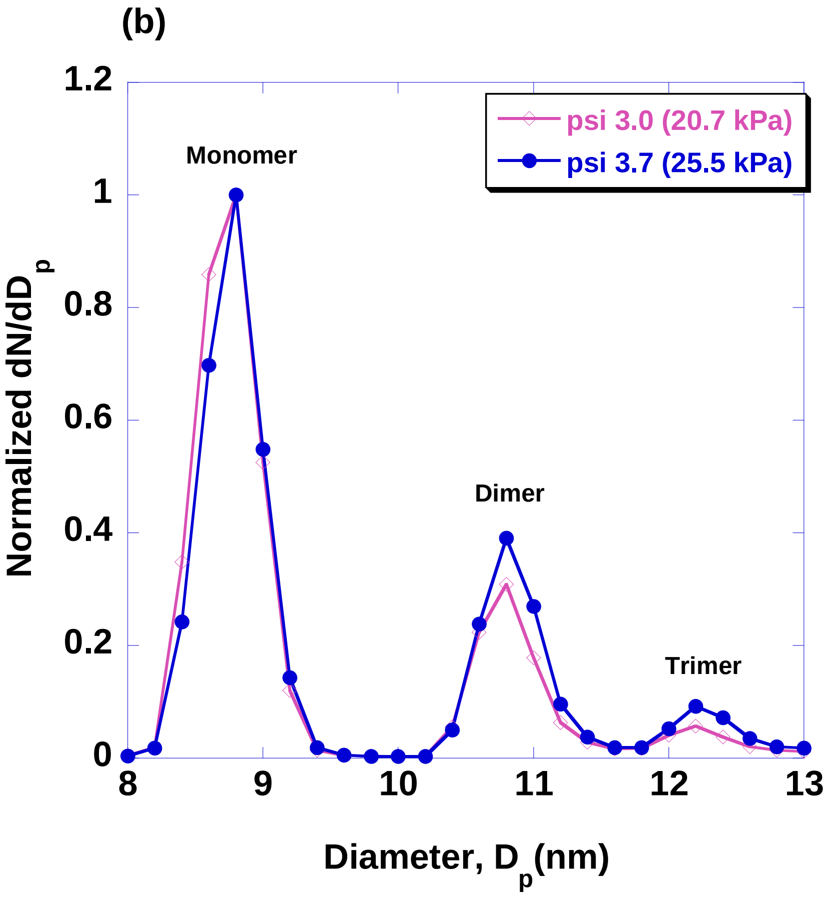

Figure 3-5. (a). *ES droplet size distributions measured from sucrose at pH 7 in 20 mmol/L ammonium acetate buffer(section3.2.4) at pressures of 3.0 psi (2.07*10^4 Pa) (open symbols) and 3.7 psi (2.55*10^4 Pa)(closed symbols).* **(b).** *Observed ES-DMA size distributions of Rmab at pH7 in 20 mmol/L ammonium acetate buffer at chamber pressures of 3.0 psi (2.07*10^4 Pa) (open symbols) and 3.7 psi (2.55*10^4 Pa) (closed symbols). Each of the discernable oligomer peaks are labeled. The y-axis label "dN/dD$_p$" is defined by the total number of particles in the range [D$_p$, D$_p$+ dD$_p$] divided by the size interval, dD$_p$.*

Table 3-3 shows the ratios of observed dimers to monomers for Rmab measured in ES-DMA experiments at a concentration of 100 µg/mL at pH 7 and with ES chamber pressures of 3.0 psi (2.07*10^4 Pa) and 3.7 psi (2.55*10^4 Pa). For each experiment, the total number concentration of monomer whether free or aggregated, $C_{p1}+ 2C_{p2}$, is calculated based on Eqns. (3-7) and (3-12), and compared with the known concentration of 100 μg/mL. Experiments were repeated twice with two different capillaries (Cap #1 and Cap #2) of nominally identical size.

Table 3-3. *The ratios of observed dimers to monomers for Rmab measured in ES-DMA experiments at pH 7 and at a concentration 100 μg/mL with the chamber pressures in ES at 3.0 psi (2.07*10⁴ Pa) and 3.7 psi (2.55*10⁴ Pa). For each experiment, the total number concentration of monomer whether free or aggregated,* $C_{p1}+ 2C_{p2}$, *is calculated based on Eqns. (3-7) (3-12) and compared with the known total concentration, 100 μg/mL.*

	3.7 psi ($2.55*10^4$ Pa)		3.0 psi ($2.07*10^4$ Pa)		From droplet induced theory		Known concentration
	Observed dimer to monomer ratio	Average droplet volume (m^3)	Observed dimer to monomer ratio	Average droplet volume (m^3)	$C_{p1}+2*C_{p2}$		C_p
Exp. index					#/mL	(μg/mL)	(μg/mL)
Cap #1	37.4%	1.64E-21	29.5%	1.22E-21	4.24E+14	102.2	100
Cap #2	40.6%	1.84E-21	31.0%	1.38E-21	4.26E+14	105.7	100

The results presented in Table 3-3 show that the total absolute number concentrations, $C_{p1}+ 2C_{p2}$, calculated from our droplet induced model is in reasonable agreement with the known concentration.

I have shown that two approaches, serial dilution and varying droplet size, can be used to determine absolute number concentration without the need for standards or system calibration as long as the ES-droplet size can be determined. I believe, however, that the approach of varying droplet size is a more general method, because serial dilution is valid only for irreversible aggregating systems.

3.5. Summary of Limiting Cases and Corresponding Formulas

In this section, each limiting case and the relevant formula are listed.

Definitions:

$f(D_d)$ = droplet size distribution, which can be measured experimentally from sucrose solution under the same buffer condition (section 3.2.4)

D_d = droplet diameter

$\overline{V_d}$ = average droplet volume as determined from $f(D_d)$

N_{o1} = observed number of monomers after Electrospray

N_{o2} = observed number of dimers after Electrospray

$N_{o1,2x}$ = observed number of monomers after 2× dilution

$N_{o2,2x}$ = observed number of dimers after 2× dilution.

C_{p1} = number concentration of monomers in original solution

C_{p2} = number concentration of dimers in original solution

3.5.1. Monomodal and narrow droplet size distribution, $f(D_d)$

METHOD:

i. **Absolute number concentrations by serial dilution (Irreversible aggregation):**

- $\overline{V_d}(C_{p1}+C_{p2})\leq 1$

The intrinsic number concentrations of monomer and dimer are

$$C_{p1}\approx\frac{4}{\overline{V_d}}\left(\frac{N_{o2}}{N_{o1}}-\frac{N_{o2,2x}}{N_{o1,2x}}\right) \tag{3-13}$$

$$C_{p2}\approx\frac{4}{\overline{V_d}}\left(\frac{N_{o2}}{N_{o1}}-\frac{N_{o2,2x}}{N_{o1,2x}}\right)\left(2\frac{N_{o2,2x}}{N_{o1,2x}}-\frac{N_{o2}}{N_{o1}}\right) \tag{3-14}$$

ii. **Absolute number concentrations by changing droplet size (Irreversible/Reversible):**

- $\overline{V_d}(C_{p1}+C_{p2})\leq 1$

The intrinsic number concentrations of monomer and dimer, C_{p1} and C_{p2}, can be obtained from (3-7) and (3-12).

$$\frac{N_{o2}}{N_{o1}}\approx\frac{\overline{V_d}C_{p1}}{2}+\frac{C_{p2}}{C_{p1}} \tag{3-7}$$

$$\frac{N_{o2,\overline{V_d}'}}{N_{o1,\overline{V_d}'}}\approx\frac{\overline{V_d}'C_{p1}}{2}+\frac{C_{p2}}{C_{p1}} \tag{3-12}$$

where $N_{o1,\overline{V_d}'}$ and $N_{o2,\overline{V_d}'}$ are the observed number of monomers and dimers respectively at average droplet volume $\overline{V_d}'$.

3.5.2. Bimodal droplet size distribution, $f(D_d)$

METHOD

i. **Absolute number concentrations by serial dilution (Irreversible aggregation):**

- $\overline{V_{d2}}(C_{p1}+C_{p2})\leq 1$

The intrinsic number concentrations of monomer and dimer can be obtained from (3-13) and (3-14) by replacing $\overline{V_d}$ with $\overline{V_{d2}}$, the average droplet volume within range 2 (see Figure 3-2b), in both equations.

ii. **Absolute number concentrations by changing droplet size (Irreversible/Reversible):**

- $\overline{V_{d2}}(C_{p1}+C_{p2})\leq 1$

The intrinsic number concentrations of monomer and dimer, Cp1 and Cp2, can be obtained from (3-7) and (3-12) by replacing $\overline{V_d}$ with $\overline{V_{d2}}$, the average droplet volume within range 2 (see Figure 3-2b) in Eqn. (3-7), and by replacing $\overline{V_d}'$with $\overline{V_{d2}}'$, the other average droplet volume within range 2 (see Figure 3-2b), in Eqn.(3-12).

3.6. Conclusions

I have developed a simple, fast and accurate method to measure the absolute number concentration of nanoparticles in solution from electrospray by understanding the statistical basis of induced oligomer formation during electrospray. I first introduce the droplet induced aggregation theory in Li *et al.* [7]in a general form, and then apply it to obtain the absolute number concentration of intrinsic monomer and dimer in solution using ES-DMA. The total number concentration of monodispersed Au nanoparticles obtained using this method is verified by UV-Vis measurements. I also show the approach is also applicable to biological molecules by measuring the concentration of Rmab monoclonal antibody (Rmab). I believe the methodology can be used with any electrospray process coupled to an analytical tool that can distinguish monomers from higher order oligomers. The only requirement is that the droplet size distribution be determined. The real power of the method is that it requires no calibration standards.

3.7. Supporting Information

Supplemental 1 provides two approximations for quantifying droplet induced dimers under some limiting conditions, a) monomodal droplet size approximation and b). bimodal droplet size approximation. Supplemental 2 gives the derivations of formulas applied in two experimental approaches, a) serial dilution and b) changing droplet size, to obtain absolute concentration concentrations of nanoparticles and protein, using the two approximations described in Supplemental 1. Supplemental 3 provides explanations of the droplet size distribution measured in section 3.2.4.

S1: Two approximations for quantifying droplet induced dimers under some limiting conditions

If we consider an arbitrary final droplet size distribution, f(D_d), from an ES-source, a general relationship for the observed dimer to monomer ratio is given in Eqn (3-4). However it is difficult to solve Eqn.(3-4) for C_{p1} and C_{p2} directly, but accurate approximations can be obtained under some limiting conditions.

S1.1. Monomodal droplet size distribution f(D_d)

If the droplet size distribution f(D_d) is monomodal and relatively narrow as shown in Figure 3-2a. In this case Eqn. (3-4) can be evaluated with one average droplet volume,

$$\frac{N_{o2}}{N_{o1}} \approx \frac{P_2\big|_{V_d=\overline{V_d}}}{P_1\big|_{V_d=\overline{V_d}}} = \frac{\overline{V_d}C_{p1}}{2} + \frac{C_{p2}}{C_{p1}} \tag{3-S1}$$

where N_{o1} is the observed monomer number,

N_{o2} is the observed dimer number,

$\overline{V_d} = \sum_i f(D_{d,i})V_{d,i} = \sum_i f(D_{d,i})\frac{1}{6}\pi D_{d,i}{}^3$ is the average droplet volume (3-8)

D_d is the final droplet diameter

$f(D_d)$ is the droplet size distribution

and $\sum_i f(D_{d,i}) = 1$

However in our example, since the distribution in Fig. 3-2a is not perfectly narrow and monomodal, where small satellite peaks are present at ~ 100 nm and ~190 nm, and when C_{p1}, Cp2 are large; then $\overline{V_d}(C_{p1}+C_{p2})$ is much greater than unity, and the satellite features cannot be neglected. In this case the exact form, Eqn. (3-4), rather than Eqn. (3-S1) (or Eqn. (3-7)) should be used.

If the intrinsic dimer concentration is negligible, i.e., only monomers exist in solution, then Eqn. (S1) can be further approximated to

$$\frac{N_{o2}}{N_{o1}} \approx \frac{P_2|_{V_d=\overline{V_d}}}{P_1|_{V_d=\overline{V_d}}} = \frac{\overline{V_d}C_{p1}}{2} \quad , \qquad \text{(3-S2)}$$

S1.2. Bimodal droplet size distribution $f(D_d)$

If the size distribution $f(D_d)$ is bimodal as for example shown in Figure 3-2b, then Eqn. (3-4) can be approximated by using two average droplet volumes, $\overline{V_{d1}}$ *and* $\overline{V_{d2}}$ *to give*

$$\frac{N_{o2}}{N_{o1}} \approx \frac{f_1 P_2|_{V_d=\overline{V_{d1}}} + f_2 P_2|_{V_d=\overline{V_{d2}}}}{f_1 P_1|_{V_d=\overline{V_{d1}}} + f_2 P_1|_{V_d=\overline{V_{d2}}}}$$

$$= \frac{f_1\left(\frac{\overline{V}_{d1}^{2} C_{p1}^{2}}{2} + \overline{V}_{d1} C_{p2}\right) e^{(\overline{V_{d2}}-\overline{V_{d1}})(C_{p1}+C_{p2})} + f_2\left(\frac{\overline{V}_{d2}^{2} C_{p1}^{2}}{2} + \overline{V}_{d2} C_{p2}\right)}{f_1 \overline{V}_{d1} C_{p1} e^{(\overline{V_{d2}}-\overline{V_{d1}})(C_{p1}+C_{p2})} + f_2 \overline{V}_{d2} C_{p1}} \qquad \text{(3-S3)}$$

where

$$\sum_i f(D_{d,i}) = 1$$

$f_1 = \sum_i^{range1} f(D_{d,i})$ is the fraction of droplets in size range 1 (3-S4)

$f_2 = \sum_i^{range2} f(D_{d,i})$ is the fraction of droplets in size range 2 (3-S5)

$\overline{V_{d1}}$ is the average droplet volume within range 1

$\overline{V_{d2}}$ is the average droplet volume within range 2

If $f_2 \overline{V_{d2}} / f_1 \overline{V_{d1}} >> e^{(\overline{V_{d2}}-\overline{V_{d1}})(C_{p1}+C_{p2})}$, the first terms in the denominator and numerator of the right side of Eqn.(3-S3) are negligible and Eqn.(3-S3) can be further approximated to

$$\frac{N_{o2}}{N_{o1}} \approx \frac{\overline{V_{d2}} C_{p1}}{2} + \frac{C_{p2}}{C_{p1}} \qquad \text{(3-9)}$$

Another limiting situation occurs if the first terms dominate the value of the denominator and numerator, e.g., when C_{p1},C_{p2} are large such that $e^{(\overline{V_{d2}}-\overline{V_{d1}})(C_{p1}+C_{p2})} >> f_2 \overline{V_{d2}} / f_1 \overline{V_{d1}}$, then Eqn. (3-S3) becomes,

$$\frac{N_{o2}}{N_{o1}} \approx \frac{\overline{V_{d1}} C_{p1}}{2} + \frac{C_{p2}}{C_{p1}} \qquad \text{(3-S6)}$$

Since $\overline{V_{d1}} < \overline{V_{d2}}$, the right side of Eqn. (3-S6) is smaller than the right side of Eqn. (3-9). The direct evaluation of Eqn. (3-S3) will give dimer-monomer ratios between the two limits imposed by equations (3-9) and (3-S6).

If the intrinsic dimer concentration is negligible, i.e., essentially only monomers in solution, then Eqn. (3-9) can be further approximated to

$$\frac{N_{o2}}{N_{o1}} \approx \frac{\overline{V_{d2}} C_{p1}}{2} \tag{3-S7}$$

Thus from a measurement of the "observed" monomers and dimers (N_{o1}, N_{o2}) under the appropriate conditions described above, the absolute number concentration of intrinsic monomers in solution, C_{p1}, can be obtained through evaluation of Eqns. (3-S1), (3-S2), (3-S3), (3-9), or (3-S7).

S2: Combining the approximations above with two experimental strategies, serial dilution and changing droplet size, to obtain absolute number concentration of nanoparticles and protein in solution.

S2.1. EXAMPLE: Determination of absolute number concentrations of Au-NPs by serial dilution

Based on the bimodal droplet size distribution in Figure 3-2b used for Au-NPs samples and Eqn.(3-S4), and (3-S5), the fractions of the droplets with the sizes within range 1 and range 2 are f_1=0.27 and f_2=0.73 and the average droplet volumes within those two ranges are $\overline{V_{d1}}$=2.33×10^{-22}m^3 and $\overline{V_{d2}}$=2.46×10^{-20}m^3. Since $f_2\overline{V_{d2}} / f_1\overline{V_{d1}}$(≈ 289) is much greater than $e^{(\overline{V_{d2}}-\overline{V_{d1}})(C_{p1}+C_{p2})}$ (≈ e$^{0.7}$~2), Eqn.(3-9) can be used here for the calculation.

The absolute number concentrations of monomer and dimer of Au-NPs can be obtained by a series of measurements at various dilutions for irreversible aggregation. Based on Eqn. (3-9), after a 2x dilution, an additional relationship can be obtained,

$$\frac{N_{o2,2x}}{N_{o1,2x}} = \frac{\overline{V_{d2}}C_{p1}/2}{2} + \frac{C_{p2}/2}{C_{p1}/2} = \frac{\overline{V_{d2}}C_{p1}}{4} + \frac{C_{p2}}{C_{p1}} \tag{3-S8}$$

where $N_{o1,2x}$ is the observed number of monomers after 2× dilution and $N_{o2,2x}$ is the observed number of dimers after 2× dilution.

Combining (3-9) and (3-S8), the number concentrations of monomer and dimer of Au-NPs are

$$C_{p1} = \frac{4}{\overline{V_{d2}}}\left(\frac{N_{o2}}{N_{o1}} - \frac{N_{o2,2x}}{N_{o1,2x}}\right) \tag{3-10}$$

$$C_{p2} = \frac{4}{\overline{V_{d2}}}\left(\frac{N_{o2}}{N_{o1}} - \frac{N_{o2,2x}}{N_{o1,2x}}\right)\left(2\frac{N_{o2,2x}}{N_{o1,2x}} - \frac{N_{o2}}{N_{o1}}\right) \tag{3-11}$$

S2.2. EXAMPLE: Determination of absolute number concentrations of Rmab protein by serial dilution

Figure 3-2a shows the droplet size distribution under the same experimental conditions for Rmab samples. The distribution is monomodal and the average droplet volume was calculated to be $\overline{V_d}$=1.64*10^{-21}m^3 using Eqn.(3-8). A 100µg/mL Rmab sample corresponds to C_p=4.15*10^{14} particles/mL. The value of $\overline{V_d}(C_{p1}+C_{p2})$ approximates to $\overline{V_d} * C_p$, which is less than unity, so we can use Eqn.(S1) and the dilution method described in S2.1 to obtain the number concentrations of Rmab,

$$C_{p1} \approx \frac{4}{\overline{V_d}}\left(\frac{N_{o2}}{N_{o1}} - \frac{N_{o2,2x}}{N_{o1,2x}}\right) \tag{3-13}$$

$$C_{p2}=\frac{4}{\overline{V_d}}\left(\frac{N_{o2}}{N_{o1}}-\frac{N_{o2,2x}}{N_{o1,2x}}\right)\left(2\frac{N_{o2,2x}}{N_{o1,2x}}-\frac{N_{o2}}{N_{o1}}\right) \tag{3-14}$$

S2.3. EXAMPLE: Determination of absolute number concentrations of Rmab protein by changing droplet size

I show another experimental approach using a series of measurements under different droplet size distributions to obtain the absolute number concentration of Rmab protein. This approach can be used for both reversible and irreversible aggregation.

Figure 3-5a shows two droplet size distributions used for Rmabs. The average droplet volumes can be calculated based on the figure. Because the droplet size distributions in Fig. 3-5a are monomodal, and the values, $\overline{V_d}(C_{p1}+C_{p2})$, are less than unity, Eqn.(3-SI1) (or Eqn.(3-7)) can be used for the calculations. If the average droplet volume is changed to $\overline{V_d}'$ another relationship can be obtained,

$$\frac{N_{o2,\overline{V_d}'}}{N_{o1,\overline{V_d}'}}=\frac{\overline{V_d}'C_{p1}}{2}+\frac{C_{p2}}{C_{p1}} \tag{3-12}$$

where $N_{o1,\overline{V_d}'}$ and $N_{o2,\overline{V_d}'}$ are the observed number of monomers and dimers, respectively, at average droplet volume $\overline{V_d}'$.

The intrinsic number concentrations of monomer and dimer, Cp1 and Cp2, can be obtained from (3-7) and (3-12).

$$\frac{N_{o2}}{N_{o1}}\approx\frac{\overline{V_d}C_{p1}}{2}+\frac{C_{p2}}{C_{p1}} \tag{3-7}$$

$$\frac{N_{o2,\overline{V_d}'}}{N_{o1,\overline{V_d}'}} \approx \frac{\overline{V_d}' C_{p1}}{2} + \frac{C_{p2}}{C_{p1}} \qquad (3\text{-}12)$$

where $N_{o1,\overline{V_d}'}$ and $N_{o2,\overline{V_d}'}$ are the observed number of monomers and dimers respectively at average droplet volume $\overline{V_d}'$.

S3:

In order to evaluate the aggregate distribution in a droplet anequivalent droplet size distributionmust be determined.. To illustrate the equivalent droplet size clearly, an ES process (simplified to final droplets of identical size for demonstration) is demonstrated in Figure 3-S1. Without losing the generality, I assume that there is only one evaporation step and one fission step for an original droplet generated at the end of the capillary tip to reach the final droplets, which then dry to form the observed particles. This evaporation-fission process is equivalent to a fission-evaporation process shown in Figure 3-S1. Since there is only fission but no evaporation for an original droplet to become an equivalent final droplet, the analyte concentration does not change between the original colloidal solution and the equivalent final droplets. Thus one can think that those equivalent droplets are random samples of the original colloidal solution where the statistical analysis applies. From the equivalent final droplets to to dried particles, is evaporation and thus nostatistics are needed. The equivalent final droplet size is calculated based on Eqn. (3-1). Since there are always evaporation and fission processes in the ES process, the real final droplet size is actually smaller than the equivalent final droplet size, which is required in the statistics. For convenience, I call this equivalent final droplet the final droplet in this work.

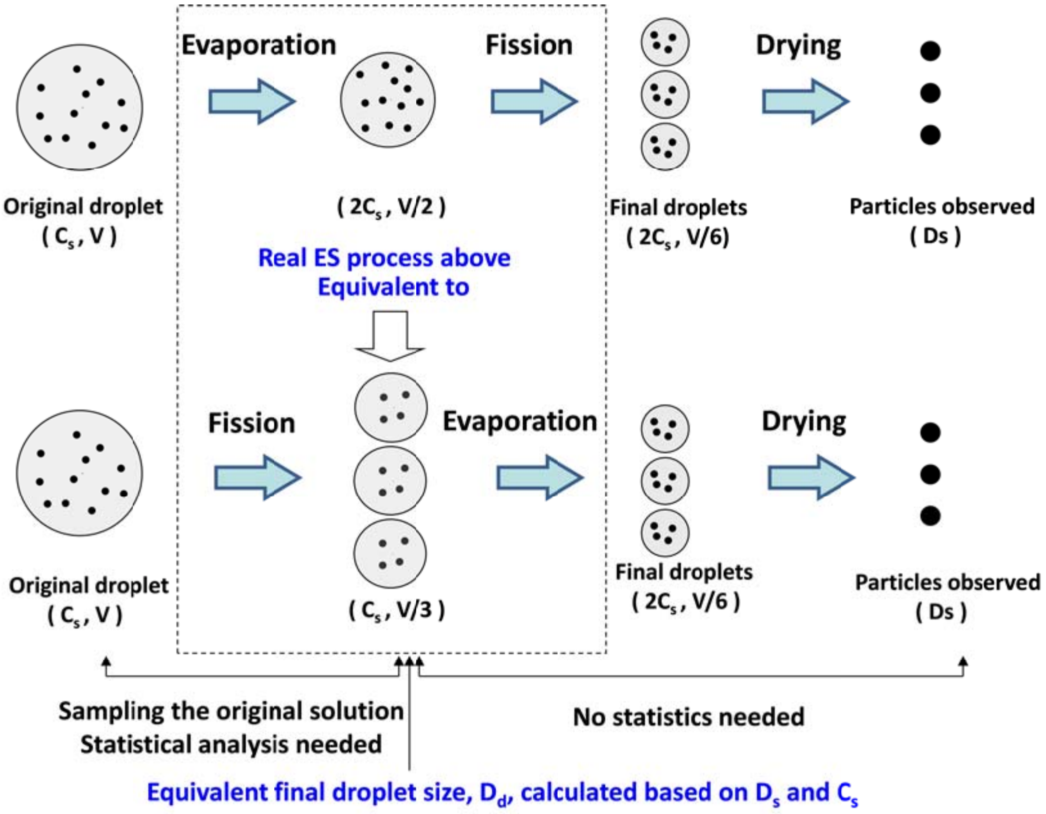

Figure 3-S1. *Equivalent final droplet size measurement using sucrose solution in section 3.2.4, where* C_s *is the sucrose concentration (volume to volume) and* D_s *is the dried sucrose diameter.*

Chapter 4: The Effect of Orientation on the Mobility and Dynamic Shape Factor of Charged Axially Symmetric Particles in an Electric Field

4.1. Introduction

The differential mobility analyzer (DMA) is widely used for measuring the size distribution of nanoparticles in the aerosol phase [7, 15, 18]. For a spherical particle, the electrical mobility diameter is equivalent to its geometric diameter. However, for nonspherical particles, the measured electrical mobility diameter is that for a sphere of equivalent mobility. This can be complex, because the mobility becomes a function of particle shape and orientation. The orientation and thus mobility, in turn depend on the magnitude of the electric field, which poses an additional complexity to predicting the mobility.

There have been several studies on the effect of the electric field on the orientation of nonspherical particles, whose mobility diameter is less than 0.5 μm. The most widely studied particles are doublets of polystyrene (PSL) spheres with primary sphere sizes in the range of 100 nm to 400m [62, 63]. Shin et al. [64] studied the alignment of silver agglomerates with up to about 1000 primary spheres of diameter ~20 nm. Several investigators have observed alignment in nanowires including Moisala et al. for single-walled carbon nanotubes (SWCNTs)[65], Song et al. for electrospray-generated gold nanorod particles[66], and Kim et al. for multiwalled CNTs [18].

The focus of this work is on the development of a general theory to compute the electrical mobility of axially symmetric particles, which includes doublets of spheres and nanowires. Kim et al.[18] developed a theory for calculating the orientation-averaged mobility of charged nanowires in an electric field based on a Boltzmann probability distribution for nanowire orientation. As an application of this theory, the lengths of monodisperse carbon nanowires were expressed as a function of the mobility diameter of the nanowires. However, there are some issues in Kim's approach. First, Kim et al. calculated the orientation-averaged mobility by using the friction coefficient expressed in the scalar form, which more rigorously should be expressed in a general tensor form. Secondly, the polarization energy for ellipsoid particle was a factor of '2π' higher than the correct value.

In this chapter, I develop a more robust theory of orientation-averaged mobility using the tensor form of drag force and the general expression for the polarization energy for an axially symmetric particle. I compare the results of my theory with the experimental mobility data for CNTs in Kim's study [18]. While our validation is based on experimental data for nanowires, our theory is generally applicable to any axially symmetric particle for which the friction tensor and the polarization energy are known, and is an extension of the Happel and Brenner theory [17] for the sedimentation of non-skew objects to include a Boltzmann probability distribution for the orientation. I also discuss the expression of dynamic shape factor common in the literature, and propose a clearer definition. Mathematica codes for the electrical mobility evaluations for six cases are provided in the Supplemental Information.

4.2. Theory

4.2.1. Orientation-Averaged-Mobility for axially symmetric particles

The mobility of a charged particle within a DMA is determined through a balance of the electrostatic (F_e) and drag force (F_{drag}) along the electric field direction (radial for a cylindrical DMA). In a cylindrical-DMA for example, both the magnitude and direction of electric field varies radially. However, so long as the characteristic time for a particle to reach its asymptotic drift velocity is small compared to the time over which there is a significant change in the electric field, we can assume that the particle follows the varying electric field instantaneously.

For axially symmetric particles, the drag force is [17]

$$\vec{F}_{drag} = -\hat{K} \cdot \vec{V}_d \tag{4-1}$$

where $\hat{K}$ is the friction coefficient tensor and $\vec{V}_d$ is the drift velocity of the particle. The particle will be undergoing Brownian rotation. I assume that the Brownian rotation is slow compared to the translational relaxation time, which is valid for particles in the continuum regime, most particles in transition regime, and high aspect ratio particles in free molecular regime. The detailed discussion will be described in a separate manuscript. For this quasi-equilibrium, the drag force is balanced by the electric force

$$\hat{K} \cdot \vec{V}_d = q\vec{E}, \tag{4-2}$$

where q is the free charge on the particle. Multiplying both sides of Eqn.(4-2) by $\hat{K}^{-1}$,

$$\vec{V}_d = q\hat{K}^{-1} \cdot \vec{E} \tag{4-3}$$

The quantity $\hat{K}$ is expressed in terms of the body fixed coordinate system ($\vec{i}', \vec{j}', \vec{k}'$) parallel to the three principal axes of the particle, and the direction of the electric field is expressed in terms of the unit vectors fixed in space ($\vec{i}, \vec{j}, \vec{k}$). The unit vector $\vec{k}$ is chosen along the electric field direction (radial) and $\vec{k}'$is chosen parallel to the axis of a axially symmetric particle. The angle between $\vec{k}$ and $\vec{k}'$ is θ. Then the tensor $\hat{K}$ can be expressed as the dyadic products of the unit vector.

$$\hat{K} = K_1\vec{i}'\vec{i}' + K_2\vec{j}'\vec{j}' + K_3\vec{k}'\vec{k}' \tag{4-4}$$

where K_1, K_2 and K_3 are three principal components. Since $\hat{K}$ is a diagonal matrix, the inverse of $\hat{K}$ is easily computed:

$$\hat{K}^{-1} = K_1^{-1}\vec{i}'\vec{i}' + K_2^{-1}\vec{j}'\vec{j}' + K_3^{-1}\vec{k}'\vec{k}' \tag{4-5}$$

$$\vec{E} = E\vec{k} \tag{4-6}$$

From Eqns.(5-3,5-5,5-6) one obtains:

$$\vec{V}_d = qE(K_1^{-1}\vec{i}'\vec{i}'\cdot\vec{k} + K_2^{-1}\vec{j}'\vec{j}'\cdot\vec{k} + K_3^{-1}\vec{k}'\vec{k}'\cdot\vec{k}) \tag{4-7}$$

For axially symmetric particles, $K_1 = K_2 = K_\perp$ where $K_\perp$ is the principal component of the friction coefficient tensor perpendicular to the axial direction and $K_3 = K_\parallel$ where $K_\parallel$ is the component parallel to the axial direction. In general, the drift velocity, $\vec{V}_d$, of nonspherical particles is orientation-dependent so that there will be components other than in the $\vec{k}$ direction (electric field direction).

For a particle population, the axial orientation of particles will show a distribution. If the particles are small enough, over the time scale of interest, the rotational Brownian motion will result in a steady state distribution of the orientation, i.e., Boltzmann angular distribution..

The orientation averaged velocity $\langle \vec{V}_d \rangle$ is expressed in terms of the Euler angles *θ, φ, ψ*, which relate body fixed coordinate system $(\vec{i}',\vec{j}',\vec{k}')$ to the space fixed coordinates $(\vec{i},\vec{j},\vec{k})$[67] ,and the orientational probability function *f*(*θ*) :

$$\langle \vec{V}_d \rangle = \frac{1}{4\pi^2}\iiint \vec{V}_d(\psi,\varphi,\theta) f(\theta)\sin\theta \, d\psi \, d\phi \, \mathrm{d}\theta \ , \tag{4-8}$$

where the integration for *ψ* and *φ* are from 0 to 2π and for *θ* is from 0 to π. This method applies to nonspherical particles with orientation probability dependent on only *θ*. Expressing the unit vector dyadic products in Eqn.(4-7) in terms of the Euler angles, for an axially symmetric particle, one obtains the following expression for the average drift velocity:

$$\langle \vec{V}_d \rangle = qE[K_\perp^{-1} + (K_\parallel^{-1} - K_\perp^{-1}) < \cos^2\theta >]\vec{k} \tag{4-9}$$

where

$$< \cos^2\theta > = \int_0^\pi \cos^2\theta f(\theta)\sin\theta d\theta, \text{ is the orientationally-averaged } \cos^2(\theta), \tag{4-10}$$

and $\frac{1}{4\pi^2}\iiint f(\theta) sin\,\theta \, d\psi \, d\varphi \, d\theta = 1$

I note that the average velocity has only a single component in the $\vec{k}$ direction (the electric field direction).

If we define the average electrical mobility as $\overline{Z}_p = \langle V_d \rangle / E$, then *a general expression for the average electrical mobility is*

$$\overline{Z_p} = q[K_\perp^{-1} + (K_\parallel^{-1} - K_\perp^{-1}) < \cos^2\theta >] \ , \tag{4-11}$$

Equation (4-11) provides a general expression for the average mobility of axisymmetric particles, whose evaluation requires a knowledge of $K_{\perp}$ and $K_{\parallel}$, which depend on drag model specific to the geometry of interest (e.g. ellipsoid, rod, doublets of spheres), and the orientation average value $<\cos^2\theta>$. The calculation of ($K_{\perp}$, $K_{\parallel}$) and $<\cos^2\theta>$ is discussed in the following sections (4.2.2 and 4.2.3). In what follows I evaluate and validate Eqn. (4-11) for a nanowire based on prior experimental measurements on carbon nanotubes[18], and then extend the analysis to other axisymmetric shapes.

The expression of electrical mobility above is also related to the definition of dynamic shape factor for nonspherical particles which is discussed in section 4.3.3.

4.2.2. Drag force, F_{drag}, and the expression of $K_{\parallel}$ and $K_{\perp}$

The values of $K_{\perp}$ and $K_{\parallel}$ depend on the expression of drag force in (4-1), which is dependent on particle shape and the flow regime appropriate for the particle.

In this work, I focus on the example of nanowires, for which I have experimental results for comparison. I will also compare my new result with the work of Kim et al [18].

4.2.2.1. Nanorod in free molecular regime.

In the free molecular regime, the drag force for a cylindrical particle (length L_f, diameter d_f) with hemispherical ends was developed by Dahneke [68],

$$F_{free-molecular} = -\frac{\pi\eta d_f^2 V_r}{2\lambda}[(\beta_1 f + \frac{\pi f}{6} + \frac{4}{3}) + \beta_1(2 - \frac{6-\pi}{4} f)\sin^2\theta] \qquad (4\text{-}12)$$

where η is the gas viscosity, λ the mean free path of gas, f the momentum accommodation coefficient and β1 the aspect ratio for rod defined by Lf /df,. For parallel and perpendicular orientations, Eqn. (4-1) is simplified to $F_{\parallel} = K_{\parallel} V_{\parallel}$ and $F_{\perp} = K_{\perp} V_{\perp}$, while $F_{\parallel}$ and $F_{\perp}$ can be obtained from Eqn. (4-12) with θ= 0 and θ= π/2, respectively. Then,

$$K_{\parallel} = \frac{\pi\eta d_f^2}{2\lambda}(\beta_1 f + \frac{\pi f}{6} + \frac{4}{3}) \tag{4-13}$$

and

$$K_{\perp} = \frac{\pi\eta d_f^2}{2\lambda}[\beta_1(2 + \frac{\pi - 2}{4} f) + \frac{\pi f}{6} + \frac{4}{3}] \tag{4-14}$$

4.2.2.2. Other expressions for $K_{\perp}$ and $K_{\parallel}$

Expressions for $K_{\perp}$ and $K_{\parallel}$ for nanorods and prolate spheroids in the free molecular, continuum, and transition regimes are shown in the Appendix A1, and can be applied to obtain the mobility through Eqn. (4-11).

4.2.3. Orientation distribution f(θ), and the expression of <cos^{2}θ>

The probability that the angle between the axis of an axially symmetric particle and the electric field direction lies in the interval (θ, θ+dθ) due to Brownian motion, follows Boltzmann's law [69],

$$f(\theta) = \frac{e^{-U/kT}}{\int_0^{\pi} e^{-U/kT} \sin\theta d\theta} \tag{4-15}$$

where $\int_0^{\pi} f(\theta)\sin\theta d\theta = 1$,and U is the interaction energy between the particle and the external electric field. The interaction energy may be from a permanent dipole[70], a free charge on the particle or an induced dipole due to polarization. In this work, I only consider the energy from the free charge and the energy due to polarization. Energies are expressed in SI units.

4.2.3.1. Evaluation of the Interaction energy, U for various situations

4.2.3.1.1. Interaction energy from the free charge

The interaction energy from the free charge depends on where the charge locates on the particle. For example, the free charge may stay at the ends of the particle, or uniformly distributed along the entire surface. In this work, I only provide the expressions of interaction energy from the free charge for conducting nanorod and conducting prolate spheroid.

- Conducting Nanorod

For conducting nanorod, using the same assumption as in Kim *et al.*[18], that the free charge can immediately respond, and freely move along the CNT surface to the end of the nanowire closest to the lowest voltage electrode, we obtain the electric energy from free charge q, ($\theta = \pi/2$ as the reference position), can be represented as,

$$U_e = \begin{bmatrix} -\frac{1}{2}qL_f E\cos\theta & 0 \le \theta < \pi/2 \\ -\frac{1}{2}qL_f E\cos(\pi-\theta) & \pi/2 \le \theta \le \pi \end{bmatrix} \tag{4-16}$$

- Conducting Prolate Spheroid

The electric energy can be obtained from (4-16) by replacing L_f with the major axis $2a$.

4.2.3.1.2. Interaction energy from an induced dipole for an axially symmetric particle

The polarization energy for a particle with polarizability $\hat{\alpha}$ is given by [71],

$$U_p = -\frac{1}{2}\vec{E}\cdot\hat{\alpha}\cdot\vec{E} \tag{4-17}$$

For an axially symmetric particle, Eqn. (4-17) becomes,

$$U_p = -\frac{1}{2}E^2(\alpha_\perp \sin^2\theta + \alpha_\parallel \cos^2\theta) = -\frac{1}{2}E^2\cos^2\theta(\alpha_\parallel - \alpha_\perp) - \frac{1}{2}E^2\alpha_\perp \tag{4-18}$$

where $\alpha_\perp$ is the principal component of polarizability perpendicular to the axial direction and $\alpha_\parallel$ the component parallel to the axial direction. For the orientational probability governed by Boltzmann's law, only the relative energy based on angle is relevant, so any term in the energy expression not related to angle can be neglected. Thus Eqn. (4-18), can be expressed as

$$U_p = -\frac{1}{2}E^2\cos^2\theta(\alpha_\parallel - \alpha_\perp) \tag{4-19}$$

4.2.3.1.3. Interaction energy from the free charge and an induced dipole for a nanorod or prolate spheroid assuming a conducting surface

From Eqn. (4-16) and (4-19), the total energy is given by,

$$U = U_e + U_p == \begin{bmatrix} -\frac{1}{2}qlE\cos\theta - \frac{1}{2}E^2\cos^2\theta(\alpha_\parallel - \alpha_\perp) & 0 \le \theta < \pi/2 \\ -\frac{1}{2}qlE\cos(\pi-\theta) - \frac{1}{2}E^2\cos^2\theta(\alpha_\parallel - \alpha_\perp) & \pi/2 \le \theta \le \pi \end{bmatrix} \tag{4-20}$$

where $l = L_f$ for nanorod and $l = 2a$ for prolate spheroid.

I approximate the polarization energy of a nanorod with that of a prolate spheroid with the same volume and the same aspect ratio as the rod. For a prolate spheroid with relative permittivity ε_k, aspect ratio β2 (major semi-axis a; minor semi-axis b; β2= a/b) and volume v, the two principal components of polarizability $\alpha_{\|}$ and $\alpha_{\perp}$ are expressed in Appendix A2. There is an error in the expression of the polarization energy for an ellipsoid in Kim et al.[18]. Their value is a factor of 2π times larger than the correct value given here. A similar factor error also occurs in Fuchs [69], where a 1/4π factor is missing for the polarization energy for an ellipsoid in Gaussian units.

4.2.3.2. Evaluation of $< \cos^2\theta >$.

Using Eqn. (4-10) ,(4-15) and (4-20), I calculate $< \cos^2\theta >$ for four cases.

4.2.3.2.1. Fully Random

When the electric field goes to zero, the orientation of particles are random and $< \cos^2\theta >$ =1/3.

4.2.3.2.2. Fully Aligned

When the electric field goes to infinity, the particles are fully aligned and $< \cos^2\theta >$ =1.

4.2.3.2.3. Free Charge and Induced Dipole Orientation for a nanorod or prolate spheroid assuming a conducting surface

Assuming that the free charge can immediately respond, and freely move along the surface of a particle to the end of the axially symmetric particle closest to the lowest voltage electrode, and the total interaction energy follows Eqn. (4-20), then

$$< \cos^2\theta > = \frac{\int_0^{\pi} \cos^2\theta e^{-U/kT} \sin\theta d\theta}{\int_0^{\pi} e^{-U/kT} \sin\theta d\theta} = \frac{\int_0^{1} x^2 e^{\mu x+\delta x^2} dx}{\int_0^{1} e^{\mu x+\delta x^2} dx}$$

$$=\frac{1}{2\delta}\left[\frac{2e^{\frac{\mu^2}{4\delta}}\left[\left(-\frac{\mu}{2\sqrt{\delta}}+\sqrt{\delta}\right)e^{\mu+\delta}+\frac{\mu}{2\sqrt{\delta}}\right]}{\sqrt{\pi}\left[Erfi\left(\frac{\mu}{2\sqrt{\delta}}+\sqrt{\delta}\right)-Erfi\left(\frac{\mu}{2\sqrt{\delta}}\right)\right]}+\frac{\mu^2}{2\delta}-1\right] \tag{4-21}$$

where x=cosθ

$\mu=\frac{qL_fE}{2kT}$ for nanorod and $\mu=\frac{aqE}{kT}$ for prolate spheroid,

$$\delta=\frac{(\alpha_{\parallel}-\alpha_{\perp})E^2}{2kT}$$

and $\mathrm{Erfi}(z)=\frac{2}{\sqrt{\pi}}\int_0^z e^{t^2}dt$, the imaginary error function.

4.2.3.2.4. Pure Induced Dipole Orientation for an axially symmetric particle

If we only consider the induced dipole energy,

$$<\cos^2\theta>=\frac{\int_0^\pi \cos^2\theta e^{-U_p/kT}\sin\theta d\theta}{\int_0^\pi e^{-U_p/kT}\sin\theta d\theta}=\frac{\int_{-1}^1 x^2 e^{\delta x^2}dx}{\int_{-1}^1 e^{\delta x^2}dx}$$

$$=\frac{1}{2\delta}\left[\frac{2\sqrt{\delta}e^{\delta}}{\sqrt{\pi}Erfi(\sqrt{\delta})}-1\right] \tag{4-22}$$

4.2.4. Voltage – Shape Information Relationship in a DMA Measurement (Step Mode)

A knowledge of the orientation-averaged mobility e.g. Eqn. (4-11), can be used to determine the voltage at which an axially symmetric particle can be detected in a DMA measurement. Following Kim *et al.*[18], the detection voltage (V_e) – shape information (hidden in orientation-averaged mobility $\overline{Z_p}$) relationship can be obtained as,

$$\frac{\pi(r_{out}^2 - r_{in}^2)L_d}{Q_{sh} + Q_a} = \frac{V_e}{\ln(r_{out}/r_{in})} \int_{E_a}^{E_{in}} \frac{dE}{\overline{Z_p} \cdot E^3} , \tag{4-23}$$

where

r_{in} the radius of inner electrode of DMA,

r_{out} the radius of outer electrode of DMA,

Q_{sh}, the sheath flow rate,

Q_a, the aerosol flow rate,

L_d, the length of DMA electrode,

$$E_{in} = \frac{V_e}{r_{in} \ln(r_{out}/r_{in})}$$

$$E_a = \frac{V_e}{r_a \ln(r_{out}/r_{in})}.$$

$$r_a^2 = \frac{Q_{sh} r_{out}^2 + Q_a r_{in}^2}{Q_{sh} + Q_a}$$

The averaged mobility, $\overline{Z_p}$,which is a function of electric field and contains the shape information, is given by Eqn.(4-11) for axially symmetric particles such as a nanowire. The derivation of Eqn.(4-23) is shown in Appendix A3.

4.2.5 Evaluation of Mobility for Special Cases.

Equation 4-11, shown again below is the general form for the orientation averaged mobility.

$$\overline{Z_p} = q[K_\perp^{-1} + (K_\parallel^{-1} - K_\perp^{-1}) < \cos^2\theta >] , \tag{4-11}$$

There are several advantages of this formulation over our previous analysis[18]

- I employ a more rigorous evaluation of the friction coefficient by using a tensor form.
- I are now able to find a closed form expression that is much easier to evaluate.
- Eqn. (4-11) is a general expression which can be applied to any axially symmetric shape, such as an ellipsoid or a doublet of spheres, assuming one has expressions for $K_\perp$ and $K_{\parallel}$, and the interaction energy.

In the following I provide six examples of mobility evaluation for nanorod and prolate spheroids using Eqn.(4-11). The $<\cos^2\theta>$ in Eqn. (4-11) can be evaluated based on Eqn.(4-10) generally, and for four specific conditions, it is given in section 4.2.3.2. Note that the polarization energy for ellipsoid contained in the expression for $<\cos^2\theta>$ corrects for the 2π error in Kim *et al.* [18] .

4.2.5.1. *Nanowire with semispherical ends in free molecular regime*

For the specifics of a nanowire with semispherical ends , the averaged electric mobility in free molecular regime is evaluated based on Eqn. (4-11) where $K_\perp$ and $K_{\parallel}$ are given by (4-13) and (4-14).

4.2.5.2. *Nanowire with flat ends in free molecular regime*

The expressions of $K_\perp$ and $K_{\parallel}$ required in Eqn. (4-11) are given in the Appendix by Eqns. (A1) and (A2).

4.2.5.3. *Prolate spheroids in free molecular regime*

$K_\perp$ and $K_{\parallel}$ are given in the Appendix by Eqns. (4-A3) and (4-A4).

4.2.5.4. *Slender rod in continuum regime.*

$K_\perp$ and $K_\parallel$ are given in the Appendix Eqns. (4-A5) and (4-A6).

4.2.5.5. *Prolate spheroids in continuum regime.*

$K_\perp$ and $K_\parallel$ are given the Appendix in Eqns. (4-A7) and (4-A8).

4.2.5.6. *Slender rod and prolate spheroids in transition regime.*

The mobility expressions for nanorods and prolate spheroids in the transition regime can be developed based on Eqn. (4-11) and the expressions of $K_\perp$ and $K_\parallel$ in Appendix A1.3.

The Mathematica codes for the electrical mobility evaluations for the above five cases (section 4.2.5.1. – section 4.2.5.5.) and the case for slender rod in transition regime are provided in the Supporting Information (section 4.6).

4.3. Results and Discussions

In this section, I compare the results for the electrical mobility of nanowires as a function of electric field to our previous theoretical treatment as well as compare with experiments on the mobility of carbon nanotubes [18]. I use the same values as in Kim et. al. for the relative permittivity of CNT $\varepsilon_k = \infty$ and the momentum accommodation f=0.9. At the end of this section, I also discuss the expression of dynamic shape factor common in the literature, and propose a clearer definition and an effective dynamic shape factor for a particle population.

4.3.1. Electrical mobility as a function of applied electric field

In Fig. 4-1, I plot normalized (relative to random orientation) electrical mobility vs. applied electric field for a wide range of aspect ratios, β, *with diameter* $d_f = 15nm$ *in free molecular regime* based on our theory (Section 4.2.5.1) and using our previous formulation[18]. At low field strengths, the thermal energy dominates the aligning energy, and Brownian dynamics results in a random orientation. As the electric field increases, the wire will tend to align resulting in a larger electric mobility. Both theories show a clear increase in mobility observed with increasing field strength for all β's and the onset of alignment occurring at lower field strength with increasing β. However, in all cases the normalized electrical mobility based on Kim *et al.* [18] , is substantially higher. This discrepancy of asymptotic behavior at high field is due to the scalar form of the friction coefficient used in Kim's theory instead of a general tensor form used here.

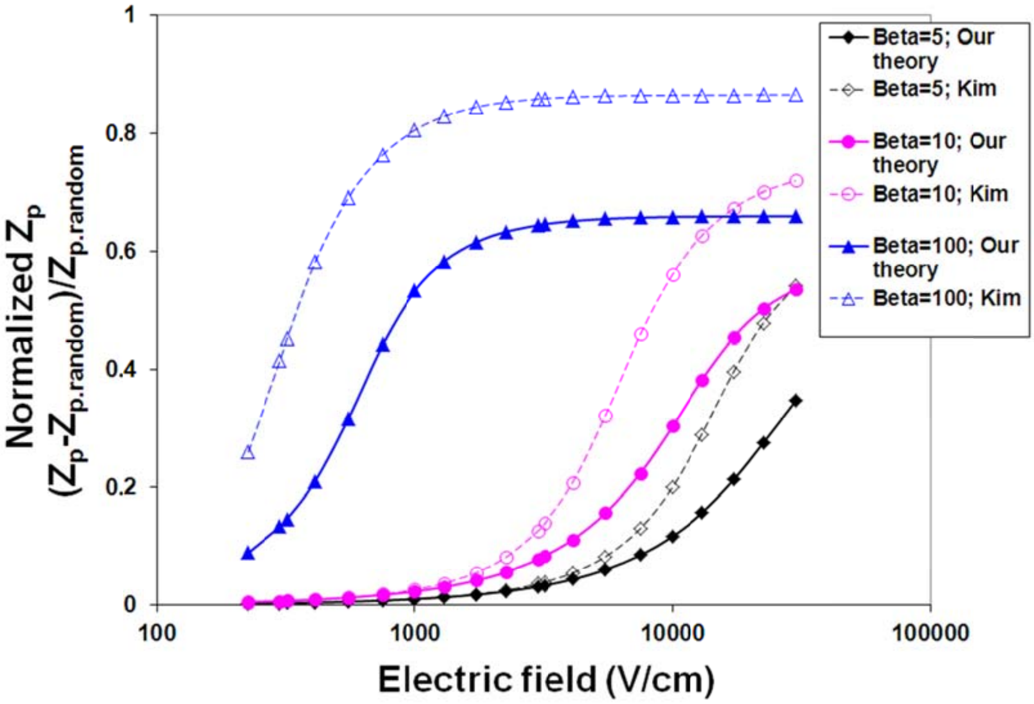

Figure 4-1. *Theoretical calculations of our theory and Kim's theory on the effect of the electric field on the scaled mobility,* $(Z_p-Z_{p,random})/Z_{p,random}$, *for nanowires with diameter* d_f*=15nm and various aspect ratios in free molecular regime. (30,000 v/cm is the air breakdown limit.)*

4.3.2 Experimental Validation

In Kim *et. al.* [18], CNTs were generated with a fixed diameter d_f=15nm and a wide range of lengths from 50 nm to 2000 nm. The CNTs were size-selected by a DMA and counted by a condensation particle counter (CPC). The size-selecting voltages of DMA (detection voltage; V_e) were chosen in a range from 465 to 4962 volts, with the corresponding equivalent spherical diameters (D_m) from 50nm to 150nm. The selected CNTs were also electrostatically deposited after the DMA and their lengths measured by TEM analysis.

The predicted length of those selected CNTs can be calculated based on Eqn. (4-23) and the averaged mobility given in Section 4.2.5.1. for free molecular regime or in Section 4.2.5.6. for transition regime. Eqn. (4-23) provides the relationship between the detection voltage (V_e) and the length of nanowire for given diameter (d_f), which is hidden in the expression of average electrical mobility provided in Section 4.2.5.1. or in Section 4.2.5.6.. In Fig. 4-2, I plot the theoretically predicted nanowire length using our theory in both free molecular and transition regimes assuming a nanowire is random rotating, fully aligned and aligned by combined energy (free charge + polarization) , as a function of experimentally measured electrical mobility diameter (D_m), which is basically derived from detection voltage V_e by assuming spherical particles.

The predicted lengths of CNT calculated above are compared with the lengths measured by TEM analysis in Kim *et al.*[18] in the same figure. It is seen that the TEM experimental results fall between the two limiting cases of random rotation and fully aligned using Dahneke's free molecular expression of drag force[68], and fall slightly lower than for random rotation at small nanowire lengths using Dahneke's transition expression of drag force[72]. The experimental data matches the predicted behavior of a randomly aligned nanowire for low mobility diameters, and then tends toward the curve corresponding to the totally aligned nanowires for the largest diameters. The data qualitatively follow the predicted trends; however, there is a slight discrepancy at small lengths using transition drag force expression and a discrepancy at large nanowire lengths in both regimes. These discrepancies likely results from kinks and bends in the nanotubes, while the theory assumes a perfect rod-like structure.

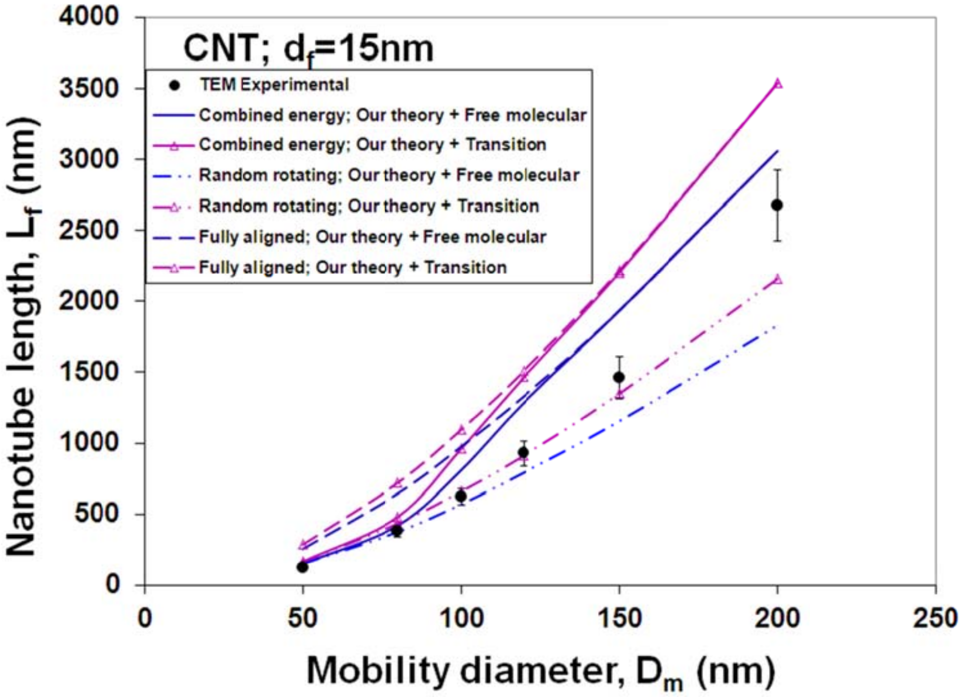

Figure 4-2. *Comparison of theoretically predicted nanowire length: curves are for nanowires random rotating, fully aligned and aligned by combined energy (i.e. free charge+polarization), respectively, with the lengths measured by TEM analysis in Kim et. al. (2007), as a function of electrical mobility diameter measured with DMA. The drag force expressions of rod in both free molecular and transition regimes are used.*

Fig.4-3 presents the relative combined electrical energy (i.e. free charge+polarization) in Eqn. (4-20) at θ=0 to thermal energy_as a function of experimentally measured electrical mobility diameter (D_m). In the same figure I draw the dipole polarization energy (U_p) normalized by the energy from free charge (U_e) at θ=0. It is seen that, for mobility diameter 100nm and larger, the aligning energy dominates thermal energy. Also for mobility diameter 100nm and larger, polarization energy starts to dominate the energy from free charge, which means that orientation due to polarization is the dominant effect.

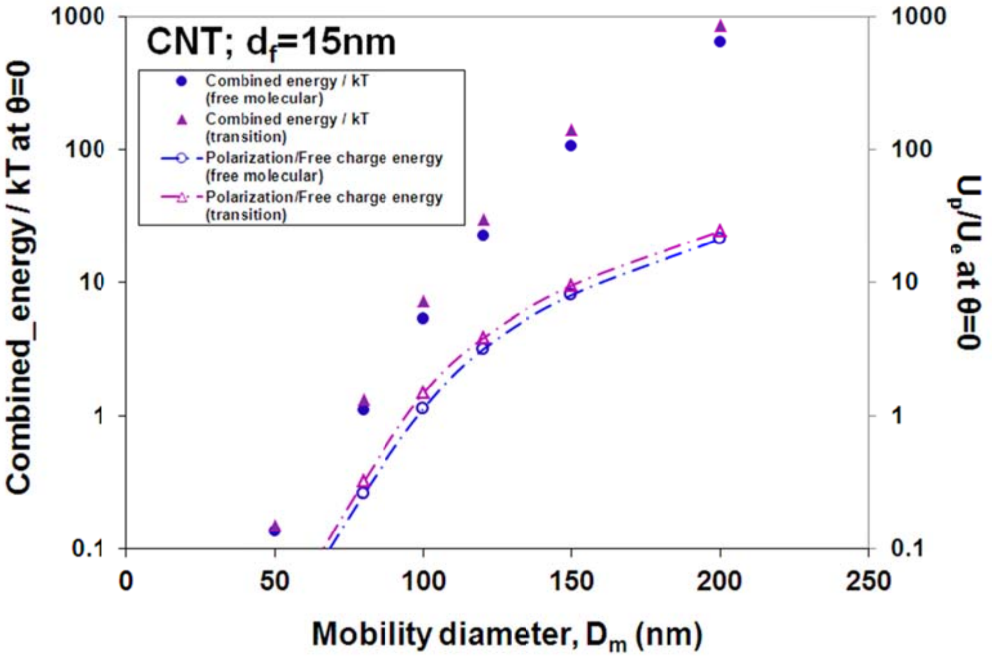

Figure 4-3. *The relative combined electrical energy (i.e. free charge+polarization) in Eqn. (4-20) at $\theta=0$ to thermal energy is shown as a function of experimentally measured electrical mobility diameter (D_m). At each points, the dipole polarization energy (U_p) normalized by the energy from free charge (U_e) at $\theta=0$ is plotted. The drag force expressions of rod in both free molecular and transition regimes are used in computing the aspect ratios.*

4.3.3. Defining the Dynamic Shape Factor

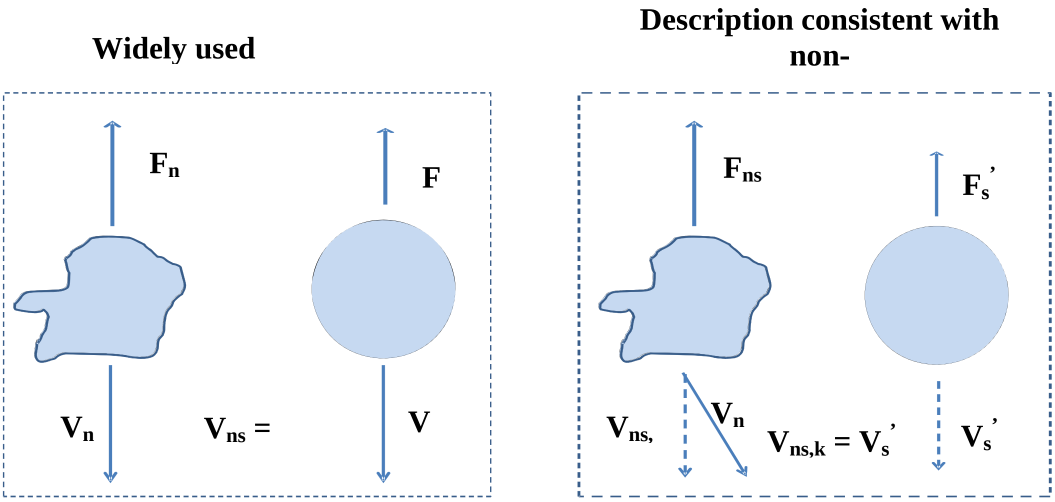

Figure 4-4. *Direction of drag force and velocity for a nonspherical particle and reference sphere used in the definition of dynamic shape factor are shown. The drift velocity of the nonspherical particle has components other than just the direction of the external force. The left side of this figure shows the basis of the widely-used shape factor , while the right side shows the basis of our proposed definition of dynamic shape factor.*

In this section, I review the expression for the dynamic shape factor found in the literature and suggest an alternative definition. I also propose an effective dynamic shape factor for a particle population.

For an axisymmetric particle, rewriting the drift velocity, $\vec{V}_d$, in Eqn. (4-7) in terms of the Euler angles θ, φ, ψ,

$$\vec{V}_d = V_{d,i}\vec{i} + V_{d,j}\vec{j} + V_{d,k}\vec{k} \qquad (4\text{-}24)$$

where $V_{d,i} = \frac{1}{2} qE \sin 2\theta \sin\phi (K_{\parallel}^{-1} - K_{\perp}^{-1})$ (4-25)

$$V_{d,j} = -\frac{1}{2} qE \sin 2\theta \cos\phi (K_{\parallel}^{-1} - K_{\perp}^{-1}) \tag{4-26}$$

$$V_{d,k} = qE[K_{\perp}^{-1} + (K_{\parallel}^{-1} - K_{\perp}^{-1})\cos^2\theta] \tag{4-27}$$

In general, the drift velocity, $\vec{V}_d$, of nonspherical particles is orientation-dependent so that there will be components other than in the $\vec{k}$ direction (external force direction). For example, $V_{d,i}$ and $V_{d,j}$ are not generally equal to 0 in Eqn. (4-25) and (4-26) for an axisymmetric particle.

The widely-used definition of dynamic shape factor, χ, is the ratio of the actual drag force of the nonspherical particle to the drag force of a sphere having the same volume and velocity as the nonspherical particle, as shown in Figure 4-4, [3, 6, 73] ,

$$\chi = \frac{F_{drag}}{3\pi\eta d_e V_d / C_c(d_e)} \tag{4-28}$$

where d_e is the equivalent volume diameter, and C_c is the slip correction factor.

Unfortunately this definition assumes that the drift velocity of the non-sphere is equivalent to a sphere, and can be treated as a scalar. However, as I showed above, for non-spherical particles the drift velocity is a vector, and has components other than just the direction of the external force.

To correct this inconsistency, I propose replacing V_d in eqn. (4-28) with $V_{d,k}$, which is the drift velocity component along the external force direction, as shown in Figure 4-4. Then the corresponding dynamic shape factor, χ'(θ), is defined as,

$$\chi' = \frac{F_{drag}}{3\pi\eta d_e V_{dk} / C_c(d_e)} \tag{4-29}$$

i.e., $\chi'(\theta)$, is defined as the ratio of the actual drag force of the nonspherical particle to the drag force of a sphere having the same volume as the non-sphere and the particle velocity which equals to the drift velocity component along the external force direction of the non-sphere.

For the polar axis of an axisymmetric particle making a fixed angle, θ, with the direction of electric field, using Eqn. (4-27), (4-29) and considering (4-1) and $F_{drag} = qE$, we obtain

$$\chi'(\theta)^{-1} = \frac{3\pi\eta d_e}{C_c(d_e)}\left[K_\perp^{-1} + \left(K_\parallel^{-1} - K_\perp^{-1}\right)\cos^2\theta\right] = \chi'^{-1}_\perp + (\chi'^{-1}_\parallel - \chi'^{-1}_\perp)\cos^2\theta \tag{4-30}$$

where $\chi'_\parallel$ is the dynamic shape factor when particle travels parallel to the axial direction, and $\chi'_\perp$ the dynamic shape factor when particle travels perpendicular to the axial direction. I note here that $\chi'_\parallel = \chi_\parallel$ and $\chi'_\perp = \chi_\perp$ because when θ=0 and π/2, based on (4-25) and (4-26), $V_{d,i}$ and $V_{d,j}$ vanish, and only a single component $V_{d,k}$ exists. In this case, Eqn. (4-28) is equivalent to Eqn. (4-29). This approach removes the ambiguity in the value of the drift velocity found in previous studies[3, 66, 73]

For axisymmetric particles with a distribution of orientations, *f*(*θ*), the average velocity has only a single component in the external force direction. In this case we can define an effective dynamic shape factor, χ_{eff}, based on orientation averaged velocity as,

$$\chi_{eff} = \frac{\vec{F}_{drag}}{3\pi\eta d_e \left\langle \vec{V}_d \right\rangle / C_c\left(d_e\right)} \tag{4-31}$$

A general relationship between the average electrical mobility, $\overline{Z}_p = \left\langle V_d \right\rangle / E$, and effective dynamic shape factor can also be obtained using Eqn.(4-31) and $\vec{F}_{drag} = q\vec{E}$:

$$\overline{Z_p} = q\frac{C_c(d_e)}{3\pi\eta d_e}\chi_{eff}^{-1} \qquad (4\text{-}34).$$

For the case of a Boltzmann distribution, f(θ) will be a function of the field strength and this will affect the values of both χ_{eff} and $\overline{\mathbf{Z}}_\mathbf{p}$.

Using (4-31), (4-9) and considering (5-1) and $\vec{F}_{drag} = q\vec{E}$, we obtain

$$\chi_{eff}^{-1} = \chi_{\perp}^{-1} + (\chi_{\parallel}^{-1} - \chi_{\perp}^{-1}) < \cos^2\theta > \tag{4-32}$$

For applications where the particles are small, the Brownian rotation will result in rapid approach the Boltzmann distribution. This is the case discussed in detail above for the nanowires.

In some applications one is interested in the behavior of a system of randomly oriented particles. For random orientation, Eqn. (4-32) becomes

$$\chi_{eff}^{-1} = \frac{1}{3}(2\chi_{\perp}^{-1} + \chi_{\parallel}^{-1}) \tag{4-33}$$

which is widely reported [3, 17, 66, 73, 74]. The dynamic shape factor for random orientation given by Fuchs [69], which differs from Eqn.(4-33), is slightly in error as was previously pointed out by Dahneke [74].

4.4. Conclusions

The approach of Happel and Brenner [17] for computing the average drift velocity for randomly oriented axially symmetric particles has been extended to include a Boltzmann probability distribution based on the orientation energy of the particle. This theory uses a tensor formulation for computing the orientation average mobility rather than a scalar analysis previously employed by Kim *et al.* [18]. The resulting equation for the average electrical mobility is a much simpler than the expression based on the scalar approach, and can be applied to other axially symmetric structures such as ellipsoids and touching spheres provided that the friction tensor and orientation energy are known.

The theory was applied to the specific case of nanowires, and the results are compared with with the experimental results on carbon nanotubes (CNT) in Kim *et al.* [18]. Based on the tensor approach I have reevaluated the derivation of the dynamic shape factor, to clarify its meaning. Finally I provide in the Supporting Information a set of programing codes for electrical mobility evaluation for some specific cases.

4.5. Appendix.

A1. Expressions for $K_{\parallel}$ and $K_{\perp}$.

The calculation of the average electrical mobility in Eqn. (4-11) requires a knowledge of $K_{\parallel}$ and $K_{\perp}$, which depend on the expression of drag force. In this appendix, I show some specific examples.

A1.1. In free molecular regime.

A1.1.1. Nanorod.

In free molecular regime, $K_{\parallel}$ and $K_{\perp}$ for a cylindrical particle (length L_f, diameter d_f, aspect ratio $\beta_1 = L_f / d_f$) with hemispherical ends is shown in Eqn.(4-13) and (4-14).

For a cylindrical particle with flat ends [68], we obtain

$$K_{\parallel} = \frac{\pi\eta d_f^2}{2\lambda}[(\beta_1 + \frac{\pi}{4} - 1)f + 2] \tag{4-A1}$$

$$K_{\perp} = \frac{\pi\eta d_f^2}{2\lambda}[(\frac{\pi - 2}{4}\beta_1 + \frac{1}{2})f + 2\beta_1] \tag{4-A2}$$

A1.1.2. Prolate spheroids.

For a prolate spheroid with semi-polar axis, *a*, and semi-equatorial axis, *b*, based on the drag force for a prolate spheroid in free molecular regime [68], we obtain,

$$K_{\parallel} = \frac{\pi\eta\beta_2 b^2}{\lambda}\{2A_p f + \frac{C_p}{B_p^2}[B_p^2(4 - 2f) - 4 + (3 - \frac{\pi}{2\beta_2^2})f]\} \tag{4-A3}$$

$$K_{\perp} = \frac{\pi\eta\beta_2 b^2}{\lambda}\{A_p[4 + (\frac{\pi}{2} - 1)f] + \frac{C_p}{B_p^2}[2 + \frac{4B_p^2 + \pi - 6}{4}f]\} \tag{4-A4}$$

where

$$\beta_2 = \frac{a}{b}, \quad B_p = (1 - \frac{1}{\beta_2^2})^{1/2}, \quad A_p = \frac{\arcsin B_p}{B_p} \text{ and } C_p = \frac{1}{\beta_2} - A_p \cdot$$

A1.2. In continuum regime

A1.2.1. Nanorod.

In continuum regime, for slender cylinders (length L_f, diameter d_f, $\beta_1 = L_f / d_f >> 1$) [75] the components of friction coefficient parallel and perpendicular to the radial moving direction are,

$$K_{\parallel} = 2\pi\eta L_f \left(\frac{\varepsilon + 0.307\varepsilon^2}{1-\varepsilon/2} + 0.426\varepsilon^3\right) \tag{4-A5}$$

and

$$K_{\perp} = 4\pi\eta L_f \left(\frac{\varepsilon + 0.307\varepsilon^2}{1+\varepsilon/2} + 0.119\varepsilon^3\right) \tag{4-A6}$$

where $\varepsilon = 1/\ln(2\beta_1)$.

A1.2.2. Prolate spheroids.

With semi-polar axis, *a*, semi-equatorial axis, *b,* and aspect ratio, $\beta_2 = a/b$ [74]

$$K_{\parallel} = \frac{8\pi\eta b\gamma^2}{\frac{2\gamma^2+1}{\gamma}\ln(\gamma+\beta_2) - \beta_2} \tag{4-A7}$$

and

$$K_{\perp} = \frac{16\pi\eta b\gamma^2}{\frac{2\gamma^2-1}{\gamma}\ln(\gamma+\beta_2) + \beta_2} \tag{4-A8}$$

where $\gamma = (\beta_2^{\,2} - 1)^{1/2}$

A1.3. Transition regime

For spherical particles in transition regime, the drag force in the continuum regime is reduced due to fluid molecular slipping along the particle surface, and the Stokes equation is modified by the Cunningham Slip Correction Factor C_c,

$$F_{transition} = F_{continuum} / \mathrm{C_c}(d_p), \tag{4-A9}$$

$$\mathrm{C_c}(d_p) = 1 + \frac{2\lambda}{d_p}[A_1 + A_2 \exp(-\frac{A_3}{2\lambda / d_p})]' \tag{4-A10}$$

where d_p is the diameter of spherical particle, and A_1=1.142, A_2=0.558, and A_3=0.999 were given by Allen and Raabe [9] at room temperature and atmosphere pressure.

Similarly, for a nonspherical particle, Dahneke [72] proposed an adjusted spherical diameter to calculate the drag force in the transition regime,

$$F_{transition} = F_{continuum} / \mathrm{C_c}(d_a) \tag{4-A11}$$

where d_a is the adjusted spherical diameter defined as Eqn. (4-A11) matches asymptotically the drag forces given in both free molecular and continuum equations when $2\lambda / d_a$ goes to either infinity or zero, that is (Cheng 1991),

$$d_a = 2\lambda(A_1 + A_2)F_{free-molecular} / F_{continuum} \tag{4-A12}$$

Once the drag force in transition regime is known by (4-A11), $K_{\perp}$ and $K_{\|}$ can be obtained with $\theta = \pi/2$ and 0, respectively.

A2. The expression of two principal components of polarizability, $\alpha_{\|}$ and $\alpha_{\perp}$ of prolate spherical particles.

I approximate the polarization energy of a nanorod with that of a prolate spheroid with the same volume and the same aspect ratio as the rod. For a prolate spheroid with relative permittivity ε_k, aspect ratio β_2 (major semi-axis a; minor semi-axis b; β_2= a/b) and volume v, the two principal components of polarizability are defined as [71, 76, 77],

$$\alpha_{\parallel} = \frac{\varepsilon_0 v}{\frac{1}{\varepsilon_k - 1} + \zeta_1} \tag{4-A13}$$

and

$$\alpha_{\perp} = \frac{\varepsilon_0 v}{\frac{1}{\varepsilon_k - 1} + \zeta_2} \tag{4-A14}.$$

where ε_0 is permittivity of free space,

$$\zeta_1 = \frac{1}{\beta_2^2 - 1}\left[\frac{\beta_2}{\sqrt{\beta_2^2 - 1}}\ln(\beta_2 + \sqrt{\beta_2^2 - 1}) - 1\right] \tag{4-A15}$$

$$\zeta_2 = \frac{\beta_2}{2(\beta_2^2 - 1)}\left[\beta_2 - \frac{1}{\sqrt{\beta_2^2 - 1}}\ln(\beta_2 + \sqrt{\beta_2^2 - 1})\right] \tag{4-A16}$$

For a slender cylinder, ζ_1 is approximated to $\ln(2\beta_2)/\beta_2^2$ and ζ_2 approximated to 0.5.

A3. Voltage – Shape Information Relationship for axisymmetric particles in a DMA Measurement

A knowledge of the orientation-averaged mobility e.g. Eqn. (4-11), can be used to determine the DMA precipitation time (t_p), the time for the axisymmetric particles to travel from the location of inlet slit to the location of outlet slit.. Following Kim et al. (2007), *the* precipitation time is,

$$t_p = \int_{r_{in}}^{r_a} \frac{dr}{\langle V_r \rangle} \tag{4-A17}$$

where $r_a^2 = \dfrac{Q_{sh} r_{out}^2 + Q_a r_{in}^2}{Q_{sh} + Q_a}$

r_{in} the radius of inner electrode of DMA,

r_{out} the radius of outer electrode of DMA,

Q_{sh}, the sheath flow rate,

Q_a, the aerosol flow rate,

$\langle V_r \rangle$ is the drift velocity of the particle in the radial direction.

Since $\langle V_r \rangle = \overline{Z_p} E$ for axisymmetric particles and the radial dependence of the electric field in a cylindrical DMA, $E = \dfrac{V_e}{r \ln(r_{out}/r_{in})}$, where V_e is the detection voltage in the DMA measurement, Eqn.(A17) becomes,

$$t_p = \frac{V_e}{\ln(r_{out}/r_{in})} \int_{E_a}^{E_{in}} \frac{dE}{\overline{Z_p} E^3} \,. \tag{4-A18}$$

where $E_{in} = \dfrac{V_e}{r_{in} \ln(r_{out}/r_{in})}$ and $E_a = \dfrac{V_e}{r_a \ln(r_{out}/r_{in})}$.

And the flow transit time in DMA is,

$$t_f = \frac{\pi(r_{out}^2 - r_{in}^2) L_d}{Q_{sh} + Q_a} \,. \tag{4-A19}$$

A particle is detected when its precipitation time, t_p, is equal to the flow transit time, t_f, in the DMA. By equating Eqn.(4-A18) and (4-A19), the detection voltage (V_e) – shape information (hidden in $\overline{Z_p}$) relationship can be obtained as,

$$\frac{\pi(r_{out}^{2}-r_{in}^{2})L_{d}}{Q_{sh}+Q_{a}}=\frac{V_{e}}{\ln(r_{out}/r_{in})}\int_{E_{a}}^{E_{in}}\frac{dE}{\overline{Z_{p}}\cdot E^{3}}\ , \tag{4-23}$$

where the averaged mobility, which is a function of electric field and contains the shape information, is given by Eqn. (4-11) for axially symmetric particles such as a nanowire.

4.6. Supporting Information

This Supporting Information provides Mathematica codes for evaluating the electric mobilities for rods and prolate spheriods in Section 4.2.5.1. - 4.2.5.5.

Part 1.2.1., Part 2.2.1.1. and Part 2.3.2.1. are for rod, and Part 1.2.2., Part 2.2.1.2. and Part 2.3.2.2. for prolate spheroid, respectively.

Part 2.1.1 - Part 2.1.5. corresponds to the cases for mobility evaluation in Section 4.2.5.1 - Section 4.2.5.5. Part 2.1.6. is the case of the mobility evaluation for slender rod in transition regime.

Part 2.2.4. - Part 2.2.7. corresponds to the cases for $<\cos^{2}\theta>$ evaluation in Section 4.2.3.2.1 - Section 4.2.3.2.4.

```
(* Part 1.---------Initialization values---------------
(* Part 1.1.--Setup parameters*)
dr=0.01;  (*[m];Distance between two parellel electrods*)


(* Part 1.2.--Particle Parameter; *)
(* Part 1.2.1.--rod: Diameter df; *)
df = 15*10^-9 ;  (*[m] *)
```

```
(* Part 1.2.2.--Prolate spheroid: half minor-axis b; *)
(*
b = 15*10^-9 /2;  (*[m] *)
*)

(* Part 1.3.---Constant values  related to Zp*)
e=1.602176*10^-19   ;(* [C] *)
k = 1.38065*10^-23 ;(*[J/K]*)
ϵ0 =8.8542*10^-12    ;(* [C^2/N*m^2] *)

(* Part 1.4.---Variable values related to Zp *)
n=1;               (* the number of elemental charges*)
q=n*e;             (* Charge *)
λ = 0.0673*10^-6;   (* [m] *) (*free path*)
η =1.8325*10^-5  ;  (* [Ns/m^2]*)(*Viscocity Coefficient*)
f = 0.9 ;
T = 296.15 ;       (* [K] *) (*Temperature*)

(*Part 2.-Evaluate Mobility by varying Voltages and
Aspect ratios----------*)

Clear[Ve,El,β,K3,K1]
Clear[L,Vo,μ, μ0,β0,κ1 ,κ2,δ,δ0,ϵk];
Clear[cos2average];
Clear[Zprandom,Zpfullyaligned,Zpx,Zp];
Clear[ResultMatrix]
```

```
ResultMatrix={{"El(V/cm)","β","df or
2b(nm)","Zp*10⁹","FullyAligned Zp*10⁹","Random
Zp*10⁹)","Zp/Zprandom-1"}};

Do[
 Do[
  Print["Ve =",Ve];
  El=Ve/dr    ;

  (*Part 2.1.--Calculations for K (parallel) and K
(perpendicular)  -----------*)
  (*Part 2.1.1.---Nanowire with semispherical ends in
free molecular regime*)
   K3=(β*f+π*f/6+4/3)*(π*η*df²)/(2*λ );(*K (parallel) *)
   K1=K3+β*(2-(6-π)/4*f)*(π*η*df²)/(2*λ ); (*K
(perpendicular) *)

  (*Part 2.1.2.---Nanowire with flat ends in free
molecular regime*)
  (*
   K3=((β+π/4-1)*f+2)*(π*η*df^2)/(2*λ );(*K (parallel) *)
   K1=(((π-2)/4*β+1/2)*f+2β)*(π*η*df^2)/(2*λ );  (*K
(perpendicular) *)
  *)

  (*Part 2.1.3.---Prolate spheroid in free molecular
regime*)
```

```
  (*
  Bp= (β^2-1)^(1/2)/β;
  Ap=ArcSin[Bp]/Bp;
  Cp=1/β-Ap;
  K3=(π*η*β*b^2)/λ *(2*Ap*f+Cp/Bp^2*(Bp^2*(4-2*f)-4+(3-
π/(2*β^2))*f));(*K (parallel) *)
  K1=(π*η*β*b^2)/λ *(Ap*(4+(π-
2)/2*f)+Cp/Bp^2*(2+(4*Bp^2+π-6)/4*f));  (*K
(perpendicular) *)
  *)

  (*Part 2.1.4.---Slender rod in continuum regime*)
  (*
  Clear[Dve,Δ χc0, χc90, K3, K1];
  Dve = (3β/2)^(1/3)*df;
  Δ = 1/Log[2*β];
  χc0 = (2/3)^(4/3)* β^(2/3) *(( Δ + 0.307* Δ^2)/(1 -
Δ/2) + 0.426* Δ^3)      ;
  χc90 = 2*(2/3)^(4/3)* β^(2/3)*(( Δ + 0.307* Δ^2)/(1 + Δ
/2) + 0.119* Δ^3);
  K3 = 3*π*η*Dve*χc0;   (*K (parallel) *)
  K1 = 3*π*η*Dve*χc90;  (*K (perpendicular) *)
  *)

  (*Part 2.1.5.---Prolate spheroid in continuum regime*)
```

```
  (*
   γ= (β^2-1)^(1/2);
   K3=(8*π*η*b*γ^2)/((2*γ^2+1)/γ*Log[γ+β]-
β );(*K(parallel)*)
   K1=(16*π*η*b*γ^2)/((2*γ^2-1)/γ*Log[γ+β]+β);
(*K(perpendicular)*)
   *)

  (*Part 2.1.6.--- Slender rod in transition regime*)
  (*
  Clear[Dve,Δ χc0, χc90, con, Kc0, Kc90, Kf0, Kf90, K3,
K1];
  (*Long rod in continuum regime*)
  Dve = (3β/2)^(1/3)*df;
  Δ = 1/Log[2*β];
  χc0 = (2/3)^(4/3)* β^(2/3) *(( Δ + 0.307* Δ^2)/(1 -
Δ/2) + 0.426* Δ^3)      ;
  χc90 = 2*(2/3)^(4/3)* β^(2/3)*(( Δ + 0.307* Δ^2)/(1 + Δ
/2) + 0.119* Δ^3);
  Kc0 = 3*π*η*Dve*χc0;    (*K (parallel) *)
  Kc90 = 3*π*η*Dve*χc90;  (*K (perpendicular) *)
  *)
  (* flat ends rod in free molecular regime*)
  con = (π*df^2* η)/(2*λ );
  Kf0 = ((β + π/4 - 1)*f + 2)*con;
```

```
Kf90 = (((π - 2)/4*β + 1/2)*f + 2*β)*con;
(*rod in transition regime*)
Clear[ A1, A2, A3, Cc];
A1 = 1.142;
A2 = 0.558;
A3 = 0.999;
Cc[Da_] = 1 + (2*λ)/Da*(A1 + A2*Exp[-A3/((2*λ)/Da)]);
Clear[ Da0, Da90, Kt0, Kt90, Ktrandom];
Da0 = (Kf0*(2*λ*(A1 + A2)))/Kc0;
Da90 = (Kf90*(2*λ*(A1 + A2)))/Kc90;
K3 = Kc0/Cc[Da0]; (*K (parallel) *)
K1 = Kc90/Cc[Da90]; (*K (perpendicular) *)
*)


(*Part 2.2.---- -Calculations for <cos^2 θ>-----*)
(*Part 2.2.1.-Give the particle length and particle
volume*)
(* Part 2.2.1.1.--Rod; *)
L=df*β;              (* Particle length *)
Vo=π/4*β*df³ ;       (* Particle volume *)

(* Part 2.2.1.2.--Prolate spheroid; *)
(*
L=2*b*β;                (* Particle length *)
Vo=(4*π)/3*β*b^3 ;      (* Particle volume *)
```

```
  *)

  (* Part 2.2.2.-----Calculation for μ*)
  μ=(L*q)/(2*k*T)*El ;
  μ0=(L*q)/(2*k*T);

  (* Part 2.2.3.-----Calculation for δ *)
  (* Part 2.2.3.1.----- assuming ϵk infinity *)
  β0 =(β^2-1)^(1/2);
  κ1 = 1/β0^2*(β/β0*Log[β+β0]-1);
  κ2 = β/(2*β0^2)*(β-1/β0*Log[β+β0]);

  δ=(ϵ0*Vo*(1/(κ1) -1/(κ2)))/(2*k*T)*El^2 ;
  δ0=(ϵ0*Vo*(1/(κ1) -1/(κ2)))/(2*k*T) ;

  (* Part 2.2.3.2.----- for finite ϵk *)
  (*
  ϵk=10^4;
  δ=(ϵ0*Vo*(1/(1/(ϵk-1)+κ1) -1/(1/(ϵk-1)+κ2)))/(2*k*T)*
El^2;
  δ0=(ϵ0*Vo*(1/(1/(ϵk-1)+κ1) -1/(1/(ϵk-1)+κ2)))/(2*k*T) ;
  *)

  (*  Part 2.2.4.-----Evaluate <cos^2 θ> for fully
random;*)
  (*
```

```
   cos2average[El_]=1/3;
  *)


  (*  Part 2.2.5.-----Evaluate <cos^2 θ> for fully
aligned;*)
  (*
   cos2average[El_]=1;
  *)


  (* Part 2.2.6.-----Evaluate <cos^2 θ> for total energy,
assuming free charge moving to the end along the field;
*)
  cos2average[El_]=1/(2*δ)*((Exp[μ2/(4*δ)]*((-
(μ/(2*δ^0.5))+ δ^0.5)*Exp[δ+μ]+μ/(2*
δ^0.5)))/( δ^0.5/2*(Erfi[μ/(2* δ^0.5)+ δ^0.5]-Erfi[μ0/(2*
δ0^0.5)]))+μ2/(2*δ)-1);


  (*Part 2.2.7.-----Evaluate <cos^2 θ> for only
polarization energy, no free charge energy; *)
  (*
  cos2average[El_]=1/(2*δ)*((Sqrt[δ]*Exp[δ])/(Sqrt[π]/2*E
  rfi[Sqrt[δ]])-1);
   *)
```

```
  (* Part 2.2.8.-----Evaluate <cos^2 θ> for only free
charge energy, assuming charge moving to the end along
the field and no polarization energy;*)
  (*
  cos2average[El_]=(1-2/μ)*Exp[μ]/(Exp[μ]-1)+ 2/μ^2;
  *)

  (* Part 2.3.- Evaluate electical mobility Zp --*)
  (* Part 2.3.1.-----*)
  Zprandom= Simplify[q*(1/K1+(1/K3-1/K1)*1/3)];
  Zpfullyaligned= Simplify[q*(1/K1+(1/K3-1/K1)*1)];
  Zpx[x_]=Simplify[q*(1/K1+(1/K3-1/K1)*cos2average[x])];
  Zp=Zpx[El];
  (* Part 2.3.2. Export to a matrix.-----*)
  (* Part 2.3.2.1. Export to a matrix for a rod-----*)

  ResultMatrix=Append[ResultMatrix,{El/100,β,N[df*10^9],N[Z
  p]*10^9,N[Zpfullyaligned]*10^9,N[Zprandom]*10^9,N[Zp]/N[Zpra
  ndom]-1}];
  (* Part 2.3.2.2. Export to a matrix for a prolate
spheroid-----*)
  (*
   ResultMatrix=Append[ResultMatrix,{El/100,β,N[2*b*10^9],
   N[Zp]*10^9,N[Zpfullyaligned]*10^9,N[Zprandom]*10^9,N[Zp
   ]/N[Zprandom]-1}];
  *)
```

```
  Print["ResultMatrix =",MatrixForm[ResultMatrix]],
{Ve,{225,300,320,410,550,750,1000,1300,1730,2250,3000,320
0,4100,5500,7500,10000,13000,17300,22500,30000}}
  ],
 {β ,{5,10,30,100}}
 ]
```

Chapter 5: Mobility and Dynamic Shape Factor of Particle Doublets in Electric Fields

5.1. Introduction

For a spherical particle, the electrical mobility diameter is equivalent to its geometric diameter or equivalent volume diameter. However, for a nonspherical particle, the measured electrical mobility diameter is defined as that for a sphere of equivalent mobility. However this is in principle a function of particle shape and orientation. A further complication is that for non-sperical particles the tendency to orient in the field results in a field intensity dependent mobility.

Most particles are non-spherical, and many are agglomerates of primary spheres. In this sense the doublet is the simplest aggregate we can evaluate. There have been several studies on the effect of the electric field on the orientation of non-spherical particles. Kousaka et al. [62] measured the dynamic shape factor (DSF, a characteristic value of particle asphericity) of doublets and triangular triplets of polystyrene latex (PSL) spheres, and concluded that the DSF of PSL doublets and triplets is a function of the intensity of electric field and the particle size. Kousaka et al. [62] asserted that both PSL doublets and triplets oriented with an angle of 45 ° between the axis of the doublet and the direction of the electric field at low electric field, assuming only a point charge randomly on the doublet surface, and ignoring the polarization energy and the Brownian rotation of particles. Zelenyuk and Imre [63] measured DSFs of PSL doublets and triplets with various primary particle sizes as a function of electric field, and concluded that polarized moments dominate the forces that determine particle orientation, and that point charge interactions are less important. Shin et al. [64] studied the alignment of silver agglomerates with up to about 1000 primary spheres of diameter ~20 nm. Several investigators have observed alignment in nanowires including Moisala et al. for single-walled carbon nanotubes (SWCNTs)[65] , and Kim et al. for multiwalled CNTs [18].

There are some theoretical models to descirbe and interpret the alignment of nonspherical particles in an electric field. Kim et al. [18] provided a theory for calculating the orientation-averaged mobility of charged nanowires in an electric field based on a Boltzmann probability distribution for nanowire orientation. In that work the orientation-averaged mobility was determined by using the friction coefficient expressed in the scalar form. More recently [16], I developed a more robust theory to determine the orientation-averaged mobility using the general tensor form of the drag force, and the general expression for the polarization energy for an axially symmetric particle. The results when compared to experimental data on CNTs qualitatively followed our predicted trends; however, there were discrepancies at large nanowire lengths, attributed to kinks and bends in the nanotubes. In this work, I apply our theory to doublets of spheres, and compared the theoretical values for the dynamic shape factor (DSF) with the measured values for doublets of NIST traceable size standard PSL particles. In general, the experimental results show good agreement with the expected values based on our theory.

5.2. Materials and Experimental Methods

To evaluate particle alignment and its effect on mobility I measure the electric mobility of Polystyrene latex (PSL) doubles using a Differential Mobility Analyzer (DMA).

NIST traceable size standards PSL particles with 103.6nm, 127.1nm, 149.4nm, 202.4nm, and 239.9nm primary PSL spheres (Thermo Scientific 3100A, 3125A, 3150A ,3200A and 3240A) were aerosolized using a constant output pressure atomizer(TSI Inc. Model 3076), and dried with two diffusion dryers before entering a neutralizer, which results in a Boltzmann charge distribution for the particles. The neutralized particles then pass through a long Differential Mobility Analyzer (DMA) column (TSI Inc. Model 3081) for particle mobility measurement and counted with an ultrafine Condensed Particle Counter (CPC) (TSI Inc. Model 3025A). More details on the measurement method can be found in Li el al. [15]

The distribution of mobility is measured with different sheath flow rates ranging from 1.5 l/min to 30 l/min to allow the measurement under from low to high electric field. The field strength in this work spans from 600V/cm to 9000V/cm. To avoid the effects of varying electric field encountered in a typical scanning mode (SMPS) experiment, I operated the DMA in the step mode and kept the step sufficiently long to ensure a complete transit through the DMA system (40 seconds to 20 seconds corresponds to Q_{sh} from 1.5L/min to 30L/min). The ratio of the sheath to aerosol flow rates was more than 20 to guarantee a high size resolution. The monomer sizes of all PSL spheres were calibrated using 100.7nm NIST standard reference material (PSL sphere) under the same experimental conditions.

Since the doublets of PSL spherical particles generated in the experiment are basically droplet induced [7, 15], sufficient number concentrations of PSL particles are needed to observe a clear doublet peak. For example, 80 drops added of 149.4 nm PSL spheres at a volume fraction of 1% were added to 80ml DI water .

5.3. Results and Discussions

In this section, I measure the effect of electric field on mobility and thus particle alignment for singly charged doublets of PSL spheres with five different primary sizes and compare the results to the theoretical values based on our theoretical model[16].

5.3.1. Measurement of dynamic shape factor.

As a first approximation by assuming the averaged mobility of a nonspherical particle in the DMA column is a constant (i.e. the radial change in E-field as negligible effect on average orientation), then the DMA is measuring the average mobility, [16]

$$\overline{Z_p} = \frac{Q_{sh} \ln(r_{out} / r_{in})}{2\pi V_e L_d} \tag{5-1}$$

where r_{in} is the radius of inner electrode of DMA, r_{out} is the radius of outer electrode of DMA, L_d is the length of DMA electrode, Q_{sh} is the sheath flow rate, and V_e is the DMA detection voltage. (There is a typo in Li et al. [16] for r_a, which is used to calculate Eqn.(23). The correct expression is $r_a^2 = (Q_{sh}\, r_{out}^2 + Q_a\, r_{in}^2)/(Q_{sh} + Q_a)$.)

The relationship between the averaged mobility and the effective dynamic shape factor of a nonspherical particle, χ_{eff} , is (Li et al. (2012) Eqn. (34))[16],

$$\overline{Z_p} = q\frac{C_c(d_{ve})}{3\pi\eta d_{ve}}\chi_{eff}^{-1} \tag{5-2}$$

where d_{ve} is the volume equivalent diameter of a nonspherical particle, C_c is the slip correction factor, q is the free charge on the particle, and η is the gas viscosity.

The DSF can also be expressed using mobility diameter, d_m, by combining the definition of mobility diameter d_m, $\overline{Z_p} = q\frac{C_c(d_m)}{3\pi\eta d_m}$ and Eqn. (5-2) to give (Zelenyuk and Imre 2007) ,

$$\chi_{eff} = \frac{d_m C_c(d_{ve})}{d_{ve} C_c(d_m)} \tag{5-3}$$

For a doublet of spheres, the equivalent volume diameter, d_{ve}, is expressed by the primary sphere diameter d_0 as, $d_{ve} = 2^{1/3}d_0$, and the expression for the slip correction factor is $C_c(d_p) = 1 + \frac{2\lambda}{d_p}[A_1 + A_2\exp(-\frac{A_3}{2\lambda/d_p})]$, where A_1=1.142, A_2=0.558, and A_3=0.999 given by Allen and Raabe [9] at room temperature and atmosphere pressure.

In Figure 5-1 I present an example of three mobility size distributions of PSL singlet and doublet particles with 149.4nm primary spherical particle diameter at three different sheath flow rate (Q_{sh} =2 l/min, 8 l/min, and 15 l/min) corresponding to three different magnitudes of electric field for each mobility size. The monomer ~ 149.4 nm is invariant, since they are spheres with no-preferred orientation in a field. On the other hand the variation of mobility diameter of the doublets in Figure 1 shows the effect of electric field induced alignment which results in smaller mobility diameters (i.e. higher mobility).

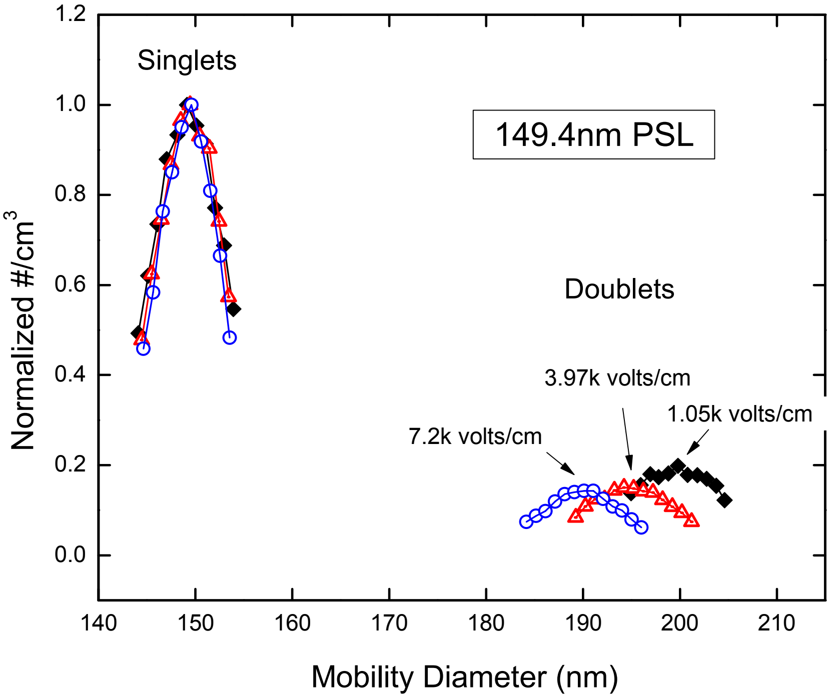

Figure.5-1. *Three mobility size distributions of PSL particles with 149.4nm primary particle diameter measured at 2 l/min, 8 l/min and 15 l/min sheath flow rates in a step mode DMA. The mobility diameter of doublets decreases with increasing sheath flow rate, which corresponds to increase the magnitude of electric field, while the mobility diameter of singlets does not change. This figure shows clearly the alignment effect of the electric field for doublets of PSL particles.*

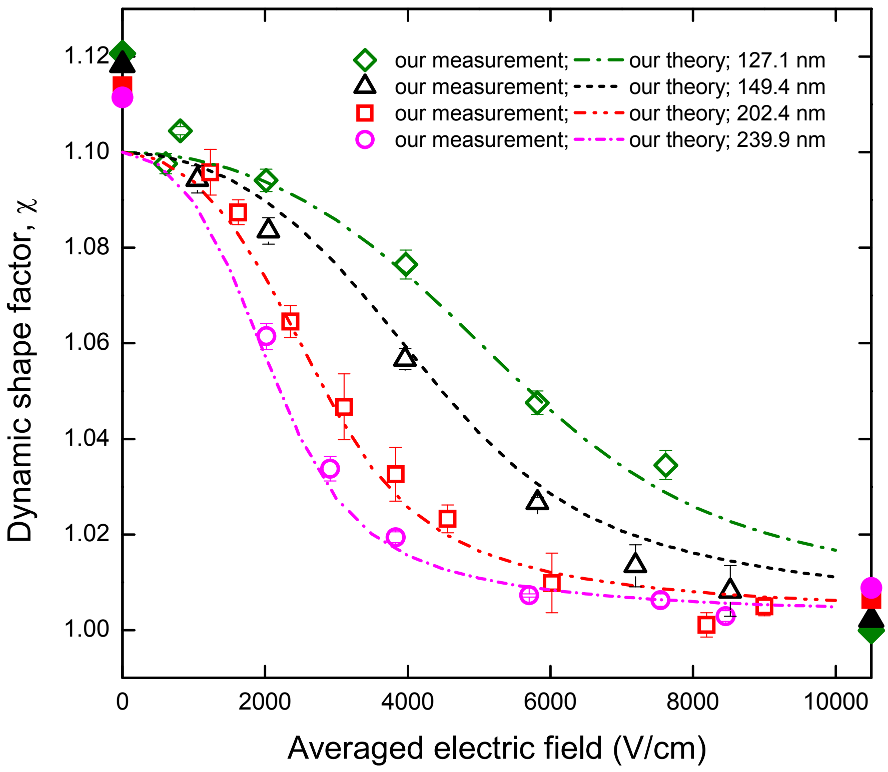

Figure 5-2. *The opened symbols are measured dynamic shape factors (DSF) of the doublets of 127.1nm, 149.4nm, 202.4nm, and 239.9nm primary PSL spheres based on Eqn.(5-3) for various magnitudes of electric field, which are corresponding to various sheath flow rates (Q_{sh} from 1.5 l/min to 20 l/min) in a step mode DMA. The dashed curves are theoretical DSF values from our model calculated based on Eqn. (5-4) with the permittivity of particles chosen as infinity. The filled symbols are theoretical DSF values at two limits, fully random (low electric field) and fully aligned (high electric field), based on Dahneke (1982)[2] and Cheng et al. (1988)[3].*

In Figure 5-2, I show the measured dynamic shape factors (DSF) for the doublets of 127.1nm, 149.4nm, 202.4nm, and 239.9nm primary PSL spheres based on Eqns.(5-1,5-2) for various applied electric fields.

The two asymptotic limits to the DSF can be obtained theoretically under a condition where the particle orientation is random (i.e. driven by Brownian dynamics), and full aligned corresponding to a very high electric field. These two theoretical limits are shown in Figure 5-2 as the filled symbols (at E=0 and E=infinity),) based on Dahneke [2] and Cheng et al. [3]. The asymptotic DSF value of the experimental data in Figure 5-2 at low electric field approaches 1.1, which is equivalent to the value for doublets in the continuum regime [3, 78], but is below the theoretical limit(filled symbols) expected in the transition regime using the interpolation method of Dahneke [2] and Cheng et al. [3]. At this time I have no explanation for this discrepancy. The high field asymptotic alignment is only achieved for the larger doublets (202.4nm and 239.9 nm) as expected, and agrees well with the theoretical value.

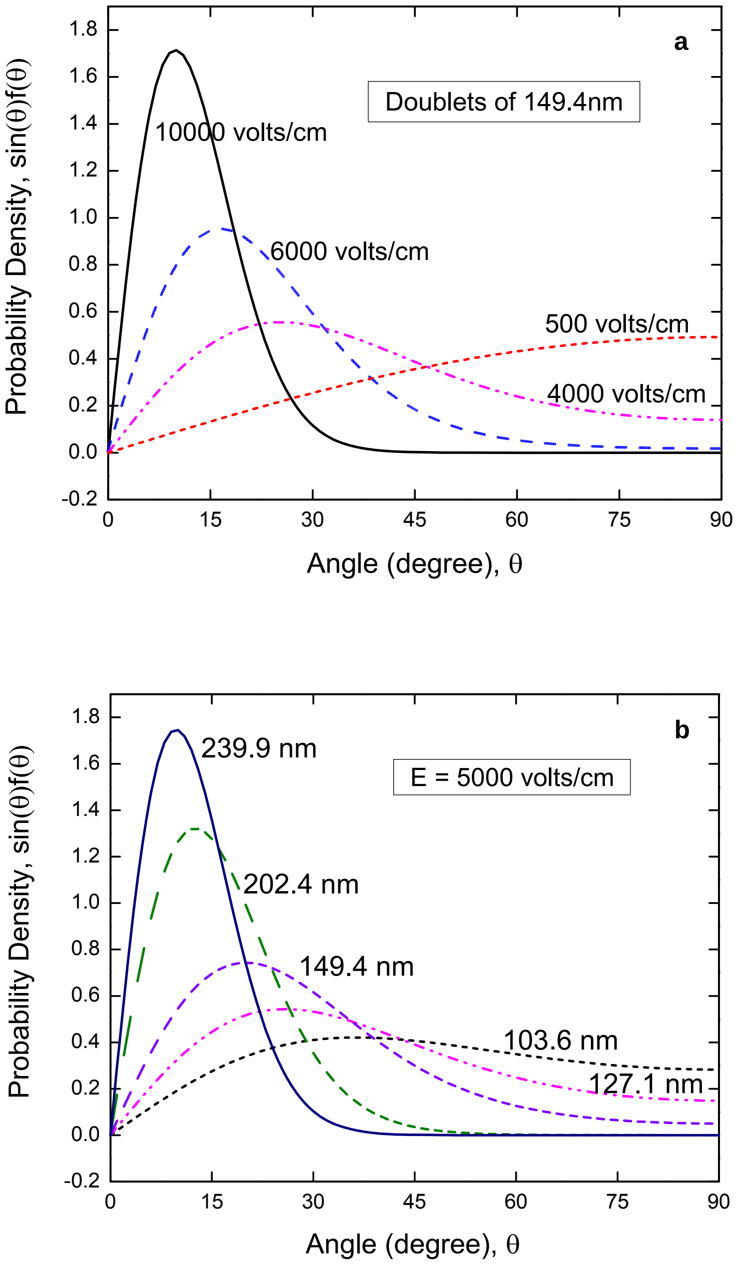

Figure 5-3. **(a)** *The orientation probability density sin(θ)f(θ) versus θ (where* $\int_0^\pi f(\theta)\sin\theta d\theta = 1$*) for the doublet of 149.4nm primary spheres at various electric fields.* **(b)** *The orientation probability density sin(θ)f(θ) versus θ at a fixed electric field (5k volts/cm) for doublets of various size primary spheres.*

5.3.2. Theoretical Development of the Dynamic Shape Factor of an Axisymmetric Particle in an Electric Field

The mobility of a non-spherical particle is a function of particle shape and orientation, the latter depends on the magnitude of electric field. If the particles are sufficiently small, over the time scale of interest, the rotational Brownian motion will result in a steady-state distribution of the orientation, i.e., Boltzmann angular distribution, *f(θ),* for an axisymmetric particle[16]. This angular distribution is related to the interaction energy between the particle and the external electric field. For particles of the size range being considered here, the primary interaction energy comes from polarization rather than the free charge [63]. If we only consider the induced dipole polarization energy, in Figure 5-3a and 5-3b, I draw the probability density $\sin(\theta)f(\theta)$versus θ (where $\int_0^{\pi} f(\theta)\sin\theta d\theta=1$) for the doublet of 149.4nm primary spheres at various electric fields, and at a fixed electric field (5k volts/cm) for the doublets of various size primary spheres. Figure 5-3a and 5-3b clearly show the effect of electric field and particle size on the orientation probability distribution of doubles. More specifically, higher fields result in a narrowed angular distribution (more aligned), and doublets composed of larger primaries are easier to align.

The dynamic shape factor of an axisymmetric particle in an electric field can be calculated based on our previous work (Li et al. [16] Eqn. (32) and (33)),

$$\chi_{eff}^{-1} = \frac{1}{2}(3\chi_{random}^{-1} - \chi_{\parallel}^{-1}) + \frac{3}{2}(\chi_{\parallel}^{-1} - \chi_{random}^{-1})\langle\cos^2\theta\rangle \qquad (5\text{-}4)$$

where χ_{random} is the measured dynamic shape factor of randomly oriented particles (low field), and $\chi_{\|}$ is the measured dynamic shape factor of fully aligned particles (high field). The $\langle \cos^2 \theta \rangle$ term arises due to the orientation distribution of particles. If we only consider the induced dipole polarization energy, (Li et al., 2012[16], Eqn. 22), then

$$\langle \cos^2 \theta \rangle = \frac{1}{2\delta}[\frac{2\sqrt{\delta}e^{\delta}}{\sqrt{\pi}Erfi(\sqrt{\delta})} - 1] \tag{5-5}$$

where $\delta = \frac{(\alpha_{n,\|} - \alpha_{n,\perp})\varepsilon_0 VE^2}{2kT}$, $\alpha_{n,\|}$ is the normalized principal component of polarizability parallel to the axial direction, $\alpha_{n,\perp}$ is the normalized component perpendicular to the axial direction , V is the volume of nonspherical particle, E is the electric field magnitude , ε$_0$ is free-space permittivity, *k* is the Boltzmann constant, T is the temperature, and $\mathrm{Erfi}(\mathrm{z}) = \frac{2}{\sqrt{\pi}}\int_0^z e^{t^2}dt$, is the imaginary error function.

If only considering the distortion polarization, for a doublet of spheres, the normalized components of polarizability, $\alpha_{n,\|}$ and $\alpha_{n,\perp}$, are only functions of the relative permittivity of the particle and the separation distance between the center points of the two spheres [79, 80]. For conducting touching spheres, where the relative permittivity $\varepsilon_r = \infty$, and the distance between the centers of two primary spheres $d=d_0$, we have $\alpha_{n,\|} \approx 7.212$ and $\alpha_{n,\perp} \approx 2.705$ [77]. It is generally understood that aerosol particles are considered conducting, probably due to surface ion contamination of even nominally insulating materials[69](Fuchs, 1964, pages 55 and 247).

Using the two asymptotic DSF experimental values in low and high electric fields in Figure 5-2, $\chi_{random} = 1.1$, $\chi_{\parallel} = 1.003$, and treating the doublets as conducting touching spheres, I obtain the theoretical curves in Figure 5-2 based on Eqn.(5-4). These theoretical results are in very good agreement with the experimentally measured DSF values.

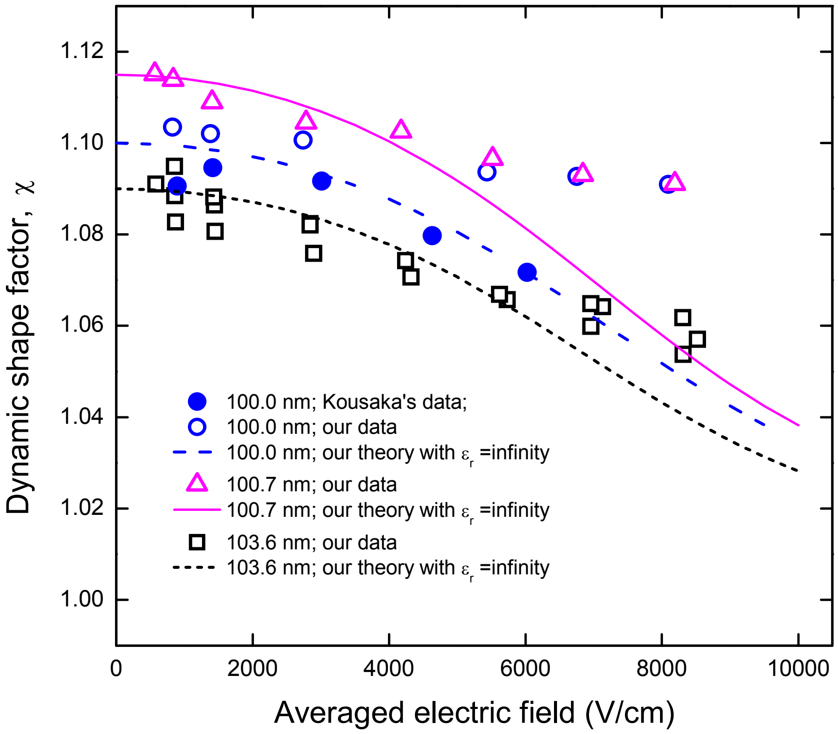

Figure 5-4. *The square symbols and triangle symbols are measured dynamic shape factors (DSF) of the doublets of 103.6nm, of 100.7nm and of 100nm primary PSL spheres based on Eqn.(5-1,5-2) for various magnitudes of electric field, which are corresponding to various sheath flow rates (Q_{sh} from 1.5 l/min to 30 l/min) in a step mode DMA. I also include the DSF data from Kousaka et al.* [62]*for the doubles of 100nm primary PSL spheres. The curves are theoretical DSF values from our model calculated based on Eqn. (5-4) with* $\chi_{\parallel} = 1.003$ *from Figure 5-2 and with the relative permittivity of particles equal to infinity. Our*

theoretical curves with the relative permittivity of particles equal to infinity is in good agreement with the data from Kousaka, but are off our experimental results with unknown reason.

One exception to this good agreement is for doublets of 100nm primary PSL spheres (103.6nm and 100.7nm), which I have separately plotted in Figure 5-4. The calculated theoretical values is in good agreement with the data from *Kousaka et al.* [62]*, but* are off our measured results in Figure 6-4. It is as if there is some unaccounted for effect causing a more random orientation of the doublet. One possible reason is the 100nm PSL cannot be considered as fully conducting material but with a limited relative permittivity, ε_r. Another possible reason would be some unknown effects existing which cause the orientation of doublets tending to random in DMA column. Those effects start becoming apparent compared to the polarization energy for the doublets of 100nm PSL particles in high electric fields (or in high flow rates). The third possible reason is that for sufficiently small particles, the Happel and Brenner's approach and our extended approach are not appropriate anymore. Imagining a very small particle which rotates considerably fast comparing with its translational relaxation time, there would be no preferred orientation, and the particle shows as oriented randomly with mobility

$$Z_p = \frac{3q}{K_1 + K_2 + K_3} \qquad (5\text{-}6)$$

The doublet of 100nm probably falls between the limit of Happel and Brenner's approach and the randomly oriented approach which is characterized by (5-6) . Further analyses and detail discussions are shown in next chapter.

5.4. Conclusions

Our general theory for the orientation-averaged mobility and the dynamic shape factor applicable to any axially symmetric particles in an electric field is applied to the specific case of doublets of spheres and the theoretical values are compared with the experimental results of well-defined doublets of NIST traceable size standards PSL particles with various primary sizes measured in a step mode DMA. In general, the experimental results show good agreement with the expected values based on our theory, except that the doublets of 100 nm spheres not consistent with our theory. I also found the deviation at low field between the measured DSFs of doublets and the predicted values based on the model of Dahneke and Cheng.

Chapter 6: Understanding the Mobility of a Non-spherical Particle

6.1. Introduction

Mobility as an important particle transport property is critical to the measurement of the dynamics of gas-phase ions and nanoparticles in fluid, which is of interest to a wide range of research area, such as the structure study of atomic clusters and macromolecules [81-84] and the scientific research in aerosol area [7, 16, 18, 20]. The relationships between mobility and diameter of a specular spherical ion in gas media and a spherical particle in fluid are well-established and governed by Chapman-Enskog theory [20](Ferziger and Kaper, 1972 ,Sec. 7.3)[85] and Stokes-Cunningham empirical formula (Hinds, 1999; Li and Wang, 2003)[6, 20], respectively. However, most ions and particles are non-spherical and the relationship between their geometric shape and their mobility of non-spherical ions or particles is much more complicated.

Mason and McDaniel [86] extended Chapman-Enskog theory for the mobility calculation of a non-spherical small ion by calculating its orientationally averaged cross section which has been widely applied to the structure determination of molecular clusters[87] and macromolecules, such as proteins and their complexes [84, 88] using ion mobility spectrometry (IMS) combined with mass spectrometry (MS). There are two estimates of the orientationally averaged cross section, exact hard-spheres scattering (EHSS) cross section [82] and projected area (PA)[81]. The structure of a molecular cluster or a macromolecule can be determined by comparing the measured mobility with the calculated mobility based on either of the two cross sections for an assumed geometry. However, when an ion becomes large and approaches the size of an aerosol particle, the surface of the particle relative to very small gas molecules cannot be treated as a simple specular surface, but rather a surface with inelastic interactions (or energy inter-conversion between the kinetic energy of a gas molecule and the internal energy of the target particle)[89, 90], thus the above relationships between mobility and the two cross sections used for a small ions need to be reexamined. For a hard-body spherical particle in the free molecular regime, Epstein [89] proposed an accommodation factor and incorporated inelastic collisions (or diffuse reflections), resulting in an enhancement factor $\xi=1+\pi f/8$ compared with the drag force for small molecules with fully specular reflections from Chapman-Enskog theory. Tammet[90] suggested this enhancement factor as 1.32 for macroscopic spherical particles, and Hogan and de la Mora[91] took 1.36 for all sizes of protein particles, both based on Epstein's spherical theory. Hogan et al. [92] applied this 1.36 factor to a protein complex GroEL and found GroEL become more compact after Electrospraying. In this work, I give a more robust derivation by first extending Epstein's approach to a convex non-sphere with cross section integrals using Li and Wang's theory [20], which extended Epstein's theory to include long-range potential forces for a spherical particle, and propose an orientationally averaged cross section approach to obtain the drag force and mobility of a convex non-spherical particle in free molecular regime. After approximating a hard collision and ignoring the long-range potential interactions between the gas molecular and a non-spherical particle, for a convex particle, I will show that the cross integral simplifies to an averaged projection area multiplied by a factor $1+\pi f/8$. So the enforcement factor in this work is defined as the ratio of the true cross section and the averaged projection area for a convex particle. The concept of averaged projection area has been used often in aerosol research, however, in some cases [18], the averaging was taken in 2-dimension and others use the average of the projected area calculated in three orthogonal directions [93]. In this work, I will show clearly that the average of projected area should be taken along all 3-dimentions.

Another approach to obtain the mobility of non-spherical particles is the averaged-drift-velocity approach proposed by Happel and Brenner[17] for particles in low Reynolds number flows. Beginning with the friction coefficient expressed in a tensor form, the averged mobility or averaged drag force of randomly oriented particles is obtained by averaging the drift velocity of those particles by equating the drag force to the external force for each particle orientation . This quasi-equilibrium approach has been widely used in the study of aerosol particles in all three regimes, free molecular, transition and continuum regimes[2, 3, 73, 74, 94]. Dahneke[2] used it to obtain the orientation-averaged resistance coefficient of straight-chain aggregates of uniform spheres in all three regimes. Mackowski[94] employed this approach for simulating the averaged drag force acting on a randomly oriented cluster in the free molecular regime. Li et al.[16] extended this approach for axisymmetric particles followed a Boltzmann orientation distribution arising from Brownian motion. In this work, I extend this approach further and show the expression of the mobility of non-spherical particles in a general form and discuss more symmetric cases. Furthermore, I point out that this approach is only valid when the particle Brownian rotation is slow compared with the particle translational relaxation time; typically for particles in transition and continuum regimes. If the particle Brownian rotation is fast compared with the particle translational relaxation time, typically for small ions and for particles in the free molecular regime, I propose a new approach using the friction coefficient in a tensor form, called averaged-drag-force, which shares some common assumptions with the averaged-cross-section approach. A simple criterion was developed for the validation of using each approach above. The three approaches were then compared with each other for randomly oriented rods. The averaged-cross-section and averaged-drag-force approaches provide very close values as expected in free molecular regime where they are valid. The averaged-drag-force approach uses the friction coefficient of a rod in free molecular regime from Dahneke's expression[68] which there has been little experimental data to test[95]. Since the averaged-cross-section approach has been used often, the calculated results based on the two approaches showing very close to each other in free molecular regime is a valid test for Dahneke's expression of a rod in free molecular regime[68].

Finally, I compared the calculation results of the three approaches to the experimental value of Tobacco mosaic virus (TMV), which is a rigid rod in the transition regime, and show that the mobility diameter obtained from the Averaged-Drift-Velocity is the closest to the experimental value, and I also showed the calculation results for GroEL are in good agreement with our calculations using the three approaches in this work.

6.2. Theory

6.2.1. Mobility of a nonspherical particle from the Averaged-Cross-Section

The momentum transfer (or drag force) between a small spherical ion and gas molecules is determined by the cross section $\Omega^{(1,1)}$ (or simply Ω) and governed by Chapman-Enskog relationship in a first approximation[20, 85]. Mason and McDaniel [86] extended it for a non-spherical small ion by replacing Ω with an orientationally averaged cross section $<\Omega>$,

$$\vec{F}_{drag} = -\frac{8}{3}\sqrt{\frac{2m_r k_B T}{\pi}} N <\Omega> \vec{V}_d \tag{6-1}$$

$$<\Omega> = \frac{1}{8\pi^2}\int_0^{2\pi} d\varphi \int_0^{\pi} d\theta \sin\theta \int_0^{2\pi} d\psi \Omega(\varphi,\psi,\theta) \tag{6-2}$$

where N is the gas number density, m_r is the reduced mass, k_B is the Boltzmann constant, T is the gas temperature, V_d is the ion drift velocity, and φ, ψ, θ, are the Euler angles to determine orientations of ions (See Appendix A.1). The collision cross section Ω in Eqns. (6-1 and 6-2) assumes specular collision, i.e. $\Omega = \Omega_s$

By equating the averaged drag force, $<F_{drag}>$, to the external force $F_{ext}=qE$ in an electric field E, where *q* is the free charge on the small ion, the electric mobility of small non-spherical ion (or particle) is obtained by

$$Z_p = \frac{V_d}{E} = \frac{3q}{16N}\sqrt{\frac{2\pi}{m_r k_B T}}\frac{1}{<\Omega>} \tag{6-3}$$

There are three implicit assumptions in the derivations above. First, the collision between an ion and gas molecules are specular. Second, the drift velocity is assumed independent of ion orientation, which is valid for small ions and for small particles and will be discussed in Section 6.3.1. The third assumption is that the expression of the cross section of a non-spherical ion or particle at a given orientation, that is, with fixed (φ, ψ, θ,), has the similar form as for a sphere with the corresponding scattering angle. Considering this scattering-cross-section is finally averaged over all orientations, the third assumption is reasonable.

This method has been increasingly employed to macromolecular ions such as proteins and other biological particles. Typically, the expressions of cross section Ω (projection and trajectory) are only based on elastic collisions [82, 83, 96]. However, when an ion becomes large and approaches the size of an aerosol particle, the surface of the particle relative to small gas molecules cannot be treated as a simple specular surface , rather a surface with inelastic interactions with energy inter-conversion between the kinetic energy of a gas molecule and the internal energy of the relatively big particle. [89, 90]

For a spherical particle with hard collisions, Epstein[89] incorporated inelastic collisions by using an accommodation factor, and this approach was extended by Li and Wang[20] to include long-range potential forces for a spherical particle,

$$\Omega = \Omega_{\text{Epstein}} = f\Omega_d + (1-f)\Omega_s \tag{6-4}$$

where Ω_S is specular-scattering cross section with the same expression as in Eqn. (6-2), Ω_d is diffuse-scattering cross section[20], and f is a switch function (or momentum accommodation factor). Epstein's approach assumes that a fraction of gas molecules, f, that collides with the particle surface are instantaneously absorbed on the surface and then re-emitted with a Maxwell velocity distribution corresponding to the temperature of the surface. Thus, *f* represents the fraction of diffuse reflections, while the 1-*f*, represents the fraction of specular reflections. In both scattering situation, the particle surface is treated as smooth surface.

I then propose an orientationally averaged cross section approach to obtain the drag force and mobility of a convex non-spherical particle in free molecular regime by extending Li and Wang's theory[20]. Using a similar way as Mason and McDaniel[86], Eqn.(6-4) can be extended for non-spherical particles as,

$$\langle\Omega\rangle = \langle\Omega_{\text{Epstein}}\rangle = f\langle\Omega_d\rangle + (1-f)\langle\Omega_s\rangle \tag{6-5}$$

and the averaging for Ω_S and Ω_d is the same as in eqn.(6-2) for Ω.

With the orientationally averaged cross section $<\Omega>$ for a non-spherical convex particle in (6-5), the drag force and the mobility are given by (6-1) and (6-3) respectively.

- Hard-body collision approximation(i.e. ignoring the long-range potential interactions)

Considering that the long range potential force is extremely computationally intensive, and for a large particle the hard-body model is usually adequate as evidenced by the good agreement between Millikan's data and Epstein's theory. Considering only hard-body collisions and ignoring the long range potential force, the orientationally averaged cross section for a convex particle calculated in (6-5) is simplified to the averaged projection area with a factor. The derivation is shown in Appendix A.2., and the final result is

$$\langle\Omega\rangle = \langle\Omega_{\text{Epstein}}\rangle = (1+\frac{\pi f}{8})\langle\Omega_{pa}\rangle = \xi\langle\Omega_{pa}\rangle \tag{6-6}$$

where $\xi = \langle \Omega \rangle / \langle \Omega_{pa} \rangle = 1 + \frac{\pi f}{8}$ is 'the enhancement factor' used in literature,

$$\langle \Omega_{pa} \rangle = \frac{1}{8\pi^2} \int_0^{2\pi} d\varphi \int_0^{\pi} d\theta \sin\theta \int_0^{2\pi} d\psi \Omega_{pa}(\varphi, \psi, \theta) \qquad (6\text{-}7)$$

is the averaged projection area over all orientations of particle (or ion), and $\Omega_{pa}(\varphi, \psi, \theta) = \int_{-\infty}^{+\infty} \int_{-\infty}^{+\infty} M(\varphi, \psi, \theta, x, y) dxdy$ is the projected area (or shade area) at a particular orientation (φ, ψ, θ,) (Appendix A.1) in a Cartesian coordinates inside a rectangle with sides along x and y axis, and M is unity when a hard collision occurs and zero otherwise[81, 83]. The enhanced factor in Eqn.(6-6) for a hard convex particle is basically the same as the factor in Epstein[89] for a hard spherical particle. The averaged projection area of particles with any shape can be calculated using the open source software program MOBCAL[82, 84]. I will provide an analytical expression for a rod in Section 6.4.2.

For a small specular convex ion, the cross-section area Ω is equal to the averaged projection area Ω_{pa}, while for a convex particle, there is an enhanced factor $\xi=1+\pi f/8$ in Eqn.(6-6). Tammet[90] gave this enhancement factor as 1.32 for macroscopic spherical particles, and Hogan et al.[91, 92] took 1.36 for small and big protein particles, both based on Epstein's spherical theory. In this work, I derive it for a convex non-spherical ion or particle, and show it as the ratio between the true cross section area and the projected area. For a small specular ion, this factor is unity with $f \sim 0$, while for a relatively big ion or particle, this enhanced factor is greater than one.

Combining Eqns. (6-1) and (6-6), we obtain the drag for a convex hard-body particle

$$\vec{F}_{drag} = -\frac{8}{3}\xi\sqrt{\frac{2m_r k_B T}{\pi}}N\langle\Omega_{pa}\rangle\vec{V}_d \tag{6-8}$$

Or, the mobility is

$$Z_p = \frac{1}{\xi}\frac{3q}{16\mathrm{N}}\sqrt{\frac{2\pi}{m_r k_B T}}\frac{1}{\langle\Omega_{pa}\rangle} \tag{6-9}$$

If we define an averaged projection area diameter as $d_{pa} = \sqrt{4\langle\Omega_{pa}\rangle/\pi}$, then Eqn.(6-8) becomes

$$\vec{F}_{drag} = -\frac{2}{3}\xi\sqrt{2\pi m_r k_B T}Nd_{pa}^{2}\vec{V}_d \tag{6-10}$$

which is similar to Epstein's equation for a spherical particle except the diameter of a sphere is replaced by the averaged projection area diameter of a non-spherical convex particle.

- Connecting Epstein to Stokes-Cunningham for a non-spherical convex particle

Furthermore, if we consider the expression of coefficient of viscosity in Allen and Raabe (1982)[97] and assume the continuum accommodation factor *f* for a non-sphere has the same relationship with Cunningham parameters as for a sphere in free molecular regime as in Allen and Raabe[9, 97],then Eqn (6-10) becomes

$$F_{drag} = -\frac{3\pi\eta d_{pa}^{2}V_d}{2\lambda(A_1 + A_2)} \tag{6-11}$$

where A1=1.165 and A2=0.483 for solid particles with averaged free path λ=67.3nm for ambient air at sea level and 23°C given by Kim[98], which gives *f*=0.868 and the enhanced factor ξ = 1+π*f*/8 = 1.34.

Eqn.(6-11) is similar to Stokes-Cunningham formula for a sphere particle in free molecular regime except that the diameter of a sphere is replaced by an averaged projection area diameter for a non-spherical convex particle. Since Eqn.(6-11) is exactly the definition of mobility diameter for a non-spherical particle, d_m, in free molecular regime, $F_{drag} = -\frac{3\pi\eta d_m^2 V_d}{2\lambda(A_1 + A_2)}$ it results in $d_m=d_{pa}$,that is, the mobility diameter is equal to the averaged projection area diameter for a convex particle in the free molecular regime.

I note here that this diameter of a non-spherical particle is averaged over all directions in 3-D, not just in 2-D or along 3 orthogonal directions as is assumed in some example in the literature.

6.2.2. Mobility of a non-spherical particle from Averaged-Drif-Velocity

The averaged drift velocity approach is well accepted for non-spherical particles at low Reynolds number [17]. However, I will discuss in section 6.4.1 that this approach is only valid for particles in the continuum and transition regime where Brownian rotation is slow compared to the translational relaxation time.

Assuming that the friction coefficient is in tensor form, the drag force is expressed as[17]

$$\vec{F}_{drag} = -\hat{K} \cdot \vec{V}_d \tag{6-12}$$

where $\hat{K}$ is the friction coefficient tensor and $\vec{V}_d$ is the drift velocity of the particle. The explicit expressions of the three principle components (K_1,K_2,K_3) of the friction coefficient tensor for hard-body rods and prolate spheroids in the free molecular, transition and continuum regimes were provided in Li et al.[16]. A general expression of the friction coefficient tensor $\hat{K}$ of a convex hard-body particle in free molecular regime was proposed by de la Mora based on Garcia-Ybarra & Rosner's approach[99, 100].

Assuming at each orientation of the particle, the drag force is balanced by the electric force, we obtain

$$\hat{K} \cdot \vec{V}_d = q\vec{E}\,, \tag{6-13}$$

and $\vec{V}_d = q\hat{K}^{-1} \cdot \vec{E}$ (6-14)

The orientation averaged velocity $\langle \vec{V}_d \rangle$ can be expressed in terms of the Euler angles *φ, ψ, θ,* which relate body fixed coordinate system ($\vec{i}\,',\vec{j}\,',\vec{k}\,'$) to the space fixed coordinates ($\vec{i},\vec{j},\vec{k}$) (Appendix A.1), and the orientational probability function *f*(*φ, ψ, θ*). $\vec{k}$ is defined as the external force direction, here the electric force. In Appendix A3, I discuss the orientational probability function *f*(*φ, ψ, θ*) due to Brownian rotation.

In general, the drift velocity, $\vec{V}_d$, of a non-spherical particle in Eqn.(6-14) is orientation-dependent, and the orientation averaged velocity $\langle \vec{V}_d \rangle$ may have components other than in the $\vec{k}$ direction (external force direction) . In such a situation, we can consider the component of the average velocity along the external force direction to define its mobility as,

$$\langle Z_p \rangle_{\vec{k}} = \langle V_{d,z} \rangle / E = q(K_1^{-1} < \sin^2\theta \sin^2\psi > + K_2^{-1} < \sin^2\theta \cos^2\psi > + K_3^{-1} < \cos^2\theta >) \tag{6-15}$$

All the averaging above in Eqn.(6-15) is defined in the form of

$$< X >= \int_0^{2\pi} d\varphi \int_0^{\pi} d\theta \sin\theta \int_0^{2\pi} d\psi f(\varphi,\psi,\theta) X(\varphi,\psi,\theta) \tag{6-16}$$

where $\iiint f(\varphi,\psi,\theta)\sin\theta \, d\psi \, d\phi \, \mathrm{d}\theta = 1$ (6-17)

and the integration for ψ and φ are from 0 to 2π and for θ is from 0 to π. The derivation of (6-17) is shown in Appendix A.1.

In some specific situations, the averaged drift velocity $\langle \vec{V}_d \rangle$ only has one component along the external force direction ($\vec{k}$ direction), that is $\langle \vec{V}_d \rangle = \langle V_d \rangle \vec{k}$, and the averaged mobility can be conveniently obtained by $\langle Z_p \rangle = \langle V_d \rangle / E$. I discuss three such cases below.

- Fully random[17].

The averaged mobility is

$$\langle Z_p \rangle = \frac{1}{3} q \left(\frac{1}{K_1} + \frac{1}{K_2} + \frac{1}{K_3} \right) \tag{6-18}$$

- Axisymmetric particles with orientation distribution *f(θ)*[16].

For axially symmetric particles, $K_1 = K_2 = K_\perp$ where $K_\perp$ is the principal component of the friction coefficient tensor perpendicular to the axial direction and $K_3 = K_\parallel$ where $K_\parallel$ is the component parallel to the axial direction. If the orientation distribution can be expressed as *f(θ)*, for example, the axisymmetric particles orientated based on Boltzmann angular distribution due to Brownian rotation (Appendix A.3) , we obtain

$$\langle Z_p \rangle = q[K_\perp^{-1} + (K_\parallel^{-1} - K_\perp^{-1}) < \cos^2\theta >] \tag{6-19}$$

where

$< \cos^2\theta >= \frac{1}{4\pi^2}\int_0^\pi \cos^2\theta f(\theta)\sin\theta d\theta$, is the orientationally-averaged $\cos^2(\theta)$.

The calculation of (6-19) was described in details in Li et al. [16]and shown that the averaged mobility is a function of particle orientation which in turn depends on the magnitude of the electric field.

- More general symmetric case with orientation distribution f(ψ, θ).

I extend the axisymmetric case above to a more symmetric case where the orientation distribution $f(\psi,\theta)$ is only a function of ψ and θ, for example a uniform right angled parallelepiped orientated based on Boltzmann angular distribution due to Brownian rotation (Appendix A.3). In this case the mobility becomes,

$$\langle Z_p \rangle = q(K_1^{-1} < \sin^2\theta \sin^2\psi > + K_2^{-1} < \sin^2\theta \cos^2\psi > + K_3^{-1} < \cos^2\theta >) \qquad (6\text{-}20)$$

Furthermore, if $K_1 = K_2$, such as a uniform right angled parallelepiped with square bases, Eqn. (6-27) becomes

$$\langle Z_p \rangle = q[K_1^{-1} + (K_3^{-1} - K_1^{-1}) < \cos^2\theta >] \qquad (6\text{-}21)$$

I note that all the averaging above is related to orientation distribution $f(\psi, \theta)$ and defined as in the form of Eqn.(6-A2).

Eqn. (6-19) for axisymmetric particles is a special case of eqn.(6-21) with orientation distribution function expressed $f(\theta)$.

If $K_1 = K_2 = K_3$ such as a uniform cubic, $\langle Z_p \rangle = qK_1^{-1}$

6.2.3. Mobility of a nonspherical particle from Averaged-Drag-Force Approach

If Brownian rotation is fast compared to the translational relaxation time of a non-spherical particle, then Eqn.(6-15) does not hold at each orientation and the averaged-drift-velocity approach is not valid anymore. Considering an extreme situation for a particle with a single rotation axis, if the particle rotates so fast for a 2π rotation that its drift velocity does not even have time to respond to the particle orientation change, then the drift velocity can be treated as independent of particle orientation and always along the external force direction $\vec{k}$. In this situation, we can think that the external force is balanced by an orientation averaged drag force with the form expressed in Eqn.(6-12) along the external force direction,

$$F_{external} = -\langle \vec{F}_{drag} \rangle \cdot \vec{k} = \langle \hat{K} \cdot \vec{V}_d \rangle \cdot \vec{k} \tag{6-22}$$

and $\vec{V}_d = V_d \vec{k}$, (6-23)

Further discussion of the prerequisite of this approach is shown in Section 6.4.1 which suggests that it is valid for very small ions and for small particles in free molecular regime, and similar to the Averaged-Cross-Section approach by averaging the drag force orientationally and assuming the drift velocity independent of particle orientation. The difference between the two is the drag force in this approach is expressed in tensor multiplication form while in Averaged-Cross-Section approach the drag force is expressed in cross-section integral or cross-section area. The explicit expressions of the three principle components of friction coefficient tensor $\hat{K}$ used in (6-22) for hard-body rods and prolate spheroids in free molecular regimes were provided in Li et al. [16]. A general expression of friction coefficient tensor for any hard-body convex particles in free molecular can be obtained in de la Mora[99] and Garcia-Ybarra and Rosner[100].

Combining (6-22), (6-23) and considering the external force is an electric force, we have

$qE = V_d \langle \vec{k} \cdot \hat{K} \cdot \vec{k} \rangle$ and,

$$Z_p = V_d / E = q / \langle \vec{k} \cdot \hat{K} \cdot \vec{k} \rangle \tag{6-24}$$

Expressing (6-24) in terms of the Euler angles φ, ψ, θ, and considering the random orientational probability function, we obtain the averaged mobility as,

$$Z_p = \frac{3q}{K_1 + K_2 + K_3}. \tag{6-25}$$

The expressions of the mobility for a general orientational probability and the averaged drag forces in those cases are shown in Appendix A.1.2.

Three approaches in this Section 6-2 for the expressions of drag force and electric mobility are summarized in Table 6-1.

Table 6-1. *Summarizing three approaches in Section 6-2 for the expressions of drag force and electric mobility of non-spherical particles.*

Avg $\langle\Omega\rangle$	$\vec{F}_{drag} = -\frac{8}{3}\xi\sqrt{\frac{2m_r k_B T}{\pi}} N \langle\Omega_{pa}\rangle \vec{V}_d$ (6-8)	Free molecular regime/ Random orientation
	$Z_p = \frac{1}{\xi}\frac{3q}{16\mathrm{N}}\sqrt{\frac{2\pi}{m_r k_B T}}\frac{1}{\langle\Omega_{pa}\rangle}$ (6-9)	
Avg $\langle\vec{V}_d\rangle$	$\vec{F}_{drag} = -\hat{K} \cdot \vec{V}_d$ (6-12)	Continuum and transition regime
	$\langle Z_p \rangle_{\vec{k}} = q(K_1^{-1} < \sin^2\theta \sin^2\psi > + K_2^{-1} < \sin^2\theta \cos^2\psi > + K_3^{-1} < \cos^2\theta >)$ (6-15)	
Avg $\langle\vec{F}_{drag}\rangle$	$\langle\vec{F}_{drag}\rangle = -\frac{K_1 + K_2 + K_3}{3} V_d \vec{k}$ (6-A1)	Free molecular regime / Random orientation
	$Z_p = \frac{3q}{K_1 + K_2 + K_3}$ (6-25)	

6.3. Materials and Experimental Methods

Tabaco mosaic virus (TMV) sample was provided by the group of James N. Culver (University of Maryland), and was purified as described in Gooding *et al.*[101], concentrated and resuspended in water with a high concentration about 26mg/ml. The highly concentrated TMV sample was then diluted with aqueous 2mmol/L ammonium acetate at pH7 to about 50μg/ml for elecrospraying study.

The as-prepared TMV samples were sprayed in an electrospray aerosol generator (model 3480, TSI Inc.) mounted with a 40μm inner diameter capillary and operated with a carrier gas of 1.2L/min of purified air. The aerosolized sample droplets were then passed over a radioactive Po-210(α) source to reduces the charge on the droplets to a well-defined charge distribution with most neutral and singly charged particles. The neutralized dry particles entered a differential mobility analyzer (model 3081 Long DMA column, TSI Inc.) for particle mobility measurement and were subsequently counted with an ultrafine CPC (model 3025A, TSI Inc.). The long DMA was set with a sheath flow of 2L/min and an aerosol flow of 0.063L/min to guarantee the TMV detected at a very low voltage (~146volts). At this low voltage, the TMV basically was randomly oriented. The long DMA was operated in a step-voltage-mode for precise measurement and calibrated with a standard reference material (polystyrene latex spherical particle) with known sizes of 100.7 nm. By scanning the center rod voltage of DMA, different mobility particles can be exacted to build a mobility distribution for a given particle population. Unlike a mass spectrometer, which selects particles on the basis of the mass/charge ratio, the differential mobility analyzer (DMA) selects particles on the basis of their mobility. The mobility can be converted to an equivalent spherical diameter, called mobility diameter which will be discussed in Section 6.4.2. More details on the measurement method can be found in the paper by Li *el al.*[15].

6.4. Results and Discussions

I start the discussion with the prerequisite conditions for the three approaches, Averaged-Cross-Section, Averaged-Drift-Velocity and Averaged-Drag-Force, and propose a simple criterion used for the validation of each approach. Mobility based on Averaged-Cross-Section can be calculated using the open source software program MOBCAL. Similarly, for a convex particle, using the general expression of friction coefficient tensor [99, 100], the mobility for any convex shape could also be obtained using Averaged-Drag-Force approach for small ions and for small particles in free molecular regime. Without losing generality, in this section, I discuss the three approaches by applying them to a rod with fully random orientation where I have the analytical expressions. Then the three approaches will be compared with the experimental measurement of Tabaco mosaic virus (TMV), which is a good example of a straight rigid rod, and with the calculation results for GroEL (a protein) in literature.

6.4.1. The prerequisite of three approaches

The Averaged-Cross-Section approach considers the molecular collision mechanism and obtains the averaged mobility of nonspherical particles based on a cross section calculation, while the Averaged-Drag-Force approach calculates particle mobility by averaging the drag force in a tensor form, but both approaches are proposed for small ions and for small particles in the free molecular regime, and both have a common assumption, that is, the drift velocity is independent of particle orientation and always along the direction of external force if the Brownian rotation is fast compared with the particle translational relaxation process. On the other hand, the Averaged-Drift-Velocity approach assumes that the particle Brownian rotation is slow compared with the particle translational relaxation time, so that at each orientation the drag force is immediately balanced by the external force and the drift velocity of a non-spherical particle depends on particle orientation. So the Averaged-Drift-Velocity approach is expected for particles in the continuum regime and transition regime. In this section, I provide a simple quantitative criterion for cylindrical particles to define if the particle Brownian motion is 'slow' or 'fast' by comparing to the particle translational relaxation process.

6.4.1.1. The translational relaxation time

The translational relaxation time characterizes the time required for a particle to adjust its velocity to a new condition of forces in straight-line movement[6]

$\tau_t = m/K$

where m is the mass and K is a scalar friction coefficient. For a rod, I use the friction coefficient along the perpendicular direction which gives the minimum of τ_t.

$$\tau_{t,\mathrm{rod}} = \mathrm{m}/K_{\perp} \tag{6-26}$$

where

$K_{\perp,f} = \frac{\pi\eta d_r L_r}{2\lambda}[(\frac{\pi-2}{4}+\frac{1}{2\beta})f+2]$ for a rod with flat ends in free molecular regime

and

$K_{\perp,c} = 4\pi\eta L_r(\frac{\varepsilon+0.307\varepsilon^2}{1+\varepsilon/2}+0.119\varepsilon^3)$ in the continuum regime where $\varepsilon = 1/\ln(2\beta)$

(length L_r, diameter d_r , aspect ratio β=L_r / d_r) [16] .

6.4.1.2. The Brownian rotation and the rotational diffusion coefficients of a rod

For Brownian rotation, in order to simplify the calculation but without losing the important physical features, I consider the simplest case, 1-dimentional rotation, that is, the particle rotates about a given axis. For one dimension rotation, assuming particles are aligned in one direction at the beginning, then after time t, the angular distribution of those particles follows a Gaussian distribution with standard deviation [69],

$$\sigma_r = \sqrt{2D_r t} \tag{6-27}$$

where D_r is the rotational diffusion coefficient.

In continuum regime, the rotational diffusion coefficient of a rod rotating around a perpendicular axis is [4],

$$D_{r,c} = \frac{3k_B T(\ln\beta + C_r)}{\pi\eta L_r^3} \tag{6-28}$$

where $C_r = -0.662+0.917/\beta-0.050/\beta^2$ for $2\leq\beta\leq20$.

In free molecular regime, Kim et al.[18] used a simple method to obtain the rotational diffusion coefficient of a rod. After correcting the missing factor '2' and considering the effect of the two ends of the rod, we obtain,

$$D_{r,f} = \frac{2\lambda k_B T}{\pi\eta d_r L_r^3[(\frac{1}{6}+\frac{\pi-2}{48}f)+\frac{f}{8\beta}]} \tag{6-29}$$

Eisner and Gallily[102] proposed a more accurate approach to calculate the rotational diffusion coefficient in free molecular regime. However, they did not express the velocity of specular reflection correctly (Eisner and Gallily, 1981 Eqn.(3.6)) and made their final results slightly in error. The corrected final result of the rotational diffusion coefficient is,

$$D_{r,f} = \frac{2\lambda k_B T}{\pi\eta d_r L_r^3[(\frac{1}{6}+\frac{\pi-2}{48}f)+\frac{f}{8\beta}+\frac{f}{8\beta^2}+(1+\frac{\pi-4}{8}f)\frac{1}{8\beta^3}]} \tag{6-30}$$

Comparing (6-29) with (6-30), for β>>1, (6-29) is a good approximation of (6-30) by ignoring the higher order than one terms of 1/ β in the denominator. In this work, I use (6-30) for calculations below.

6.4.1.3. A simple criterion to determine if particle translational motion relaxation is fast or slow compared with Brownian rotation relaxation

Assuming there are *n* particles along orientation at $\theta=\theta_0$ at time 0, after time τ, there are *p* fraction particles falling in the angular range $(\theta_0 - \Delta\theta , \theta_0 + \Delta\theta)$ because of Brownian rotation, using Eqn.(6-27), we obtain,

$$\tau = [\frac{\Delta\theta}{2erf^{-1}(p)}]^2 \frac{1}{D_r}$$

where $\mathrm{erf}^{-1}(x)$ is inverse error function.

In this work, I choose a criterion as: After translational relaxation time τ_t , if there are less than 50% particles within angular range $(\theta_0 - \pi/2 , \theta_0 + \pi/2)$, the Brownian rotation is treated as 'fast' compared with the particle translational relaxation process, and the Averaged-Cross-Section and Averaged-Drag-Force approaches are assumed valid, that is,

$$\tau_0 / \tau_t \le 1$$

where $\tau_0 = [\frac{\pi/2}{2erf^{-1}(50\%)}]^2 \frac{1}{D_r} = 2.7 / D_r$

and D_r is from (6-28) in continuum regime and from (6-30) in free molecular regime.

On the other hand, after τ_t if more than 90% particles within angular range $(\theta_0 - \pi/18 , \theta_0 + \pi/18)$, the Brownian rotation is treated as 'slow' compared with the particle translational relaxation process and the Averaged-Drift-Velocity approach is valid, that is,

$\tau_0 / \tau_t \geq 482$.

In the range of $1 < \tau_0 / \tau_t < 482$, we can think that it is a mixed picture.

I calculate the values of τ_0 / τ_t for various diameters and aspect ratios of rods in Table 6-2, where the particle density for τ_t calculation in Eqn.(6-26) is chosen as 1g/cm^3. τ_0 / τ_t is calculated separately in free molecular regime and in continuum regime.

Table 6-2. *The* τ_0 / τ_t *for various diameters and aspect ratios of rods. For each rod with random orientation, the corresponding averaged projected diameter and the mobility diameters from Averaged-Drift-Velocity and Averaged-Drag-Force approaches, respectively, are also shown.*

Diameter, d_r (nm)	Aspect ratio,β	τ_0/τ_t Continuum	τ_0/τ_t Free Molecular	$\langle A_{pa}\rangle$ (nm^2)	d_{pa} (nm)	d_{dv} (nm)	d_{df} (nm)
1	2	--	0.0	2.0	1.6	1.6	1.6
1	3	--	0.0	2.7	1.9	1.8	1.9
1	5	--	0.0	4.3	2.3	2.2	2.3
1	10	--	0.1	8.2	3.2	3.0	3.2
1	20	--	0.6	16.1	4.5	4.2	4.5
1	30	--	1.8	24.0	5.5	5.1	5.5
5	2	--	0.1	49.1	7.9	7.8	7.9
5	3	--	0.3	68.7	9.4	9.1	9.4
5	5	--	1.2	108.0	11.7	11.2	11.7

5	10	--	9.0	206.2	16.2	15.2	16.2
5	20	--	68.9	402.5	22.6	21.0	22.8
5	30	--	229.4	598.9	27.6	25.6	27.9
10	2	--	0.9	196.4	15.8	15.7	15.9
10	3	--	2.4	274.9	18.7	18.3	18.7
10	5	--	9.8	432.0	23.5	22.5	23.5
10	10	6891.1	71.8	824.7	32.4	30.6	32.6
10	20	32741.3	551.2	1610.1	45.3	42.5	46.0
10	30	85746.0	1835.5	2395.5	55.2	52.0	56.6
15	2	--	3.0	441.8	23.7	23.6	23.8
15	3	--	8.2	618.5	28.1	27.5	28.1
15	5	2566.9	33.2	971.9	35.2	33.8	35.3
15	10	10336.7	242.5	1855.5	48.6	46.0	49.1
15	20	49111.9	1860.4	3622.7	67.9	64.4	69.6
15	30	128619.0	6194.9	5389.8	82.8	79.2	86.2
30	2	1299.3	23.7	1767.2	47.4	47.4	47.9
30	3	2181.9	65.8	2474.0	56.1	55.2	56.4
30	5	5133.8	265.5	3887.7	70.4	68.0	70.8
30	10	20673.4	1939.8	7422.0	97.2	93.4	99.2
30	20	98223.8	14882.9	14490.6	135.8	133.0	143.4
30	30	257238.0	49559.0	21559.2	165.7	166.4	180.8
100	2	4330.9	877.2	19635.0	158.1	163.4	164.3
100	3	7272.9	2435.6	27488.9	187.1	188.6	191.5
100	5	17112.8	9834.2	43196.9	234.5	233.8	240.9
100	10	68911.4	71843.9	82466.8	324.0	331.8	348.0
100	20	327413.0	551217.0	161007.0	452.8	501.6	533.2

As shown in Table 6-2, the criterion values τ_0 / τ_t for almost all rods are larger than 482 using the values of τ_0 and τ_t in continuum regime; with the values of τ_0 and τ_t in free molecular regime, the criterion values τ_0 / τ_t are less than 1 for small rods, more than 482 for large rods and greater than 1 but less than 482 for rods with size in between. I will continue my discussion below by combining their equivalent spherical diameters in ambient air obtained from the Averaged-Projection-Area, Averaged-Drift-Velocity and Averaged-Drag-Force approaches.

6.4.2. Comparing three approaches by applying to a rod in fully random orientation.

In this section, I compare the calculation results from the three approaches applied to a serial rod in fully random orientation.

The averaged projection area in (6-7) for any crystal structure of ion or particle can be obtained by the open source software program MOBCAL. For a particle with cylinderal geometric shape, I give the exact analytical expression as,

$$<\Omega_{pa}>=\frac{\pi}{4}(d_r L_r+\frac{1}{2}d_r^2) \tag{6-31}$$

The averaged projection area diameter is defined as $d_{pa}=\sqrt{4<\Omega_{pa}>/\pi}$, which has been proved equivalent to the mobility diameter of a convex particle in free molecular regime in Eqn.(6-11).

The average mobility of a fully random rod can also be obtained by (6-18) and (6-25) for Averaged-Drift-Velocity and Averaged-Drag-Force approaches, respectively. Each of the three principle components of the friction coefficient tensor (K_1, K_2 and

K_3) used in the two approaches for a rod is calculated using the interpolation method proposed by Dahneke[72] in transition regime[16]. The averaged mobilities, Z, are then converted to an equivalent spherical diameter, d_m, as,

$$Z = \frac{qC_c(d_m)}{3\pi\eta d_m} \qquad (6\text{-}32)$$

where $C_c(d_{pa}) = 1 + \frac{2\lambda}{d_{pa}}[A_1 + A_2 \exp(-\frac{A_3}{2\lambda / d_{pa}})]$'

A1=1.165, A2=0.483 and A3=0.997, respectively for solid particles with averaged free path λ=67.3nm for ambient air at sea level and 23°C given by Kim[98]. d_m is denoted as d_{dv} from Averaged-Drift-Velocity approach and as d_{df} from Averaged-Drag-Force approach.

$<A_{pa}>$, d_{pa} ,d_{dv} and d_{df} are calculated for a serial rod with various diameters and aspect ratios in ambient air and shown in Table 6-2. Based on the criterion values of τ_0 / τ_t , I highlight the 'appropriate' mobility diameters in Table6-2.

Based on the discussions in Section 6.4.1 and the values in Table 6-2, I conclude that

a) Averaged-Cross-Section and Averaged-Drag-Force approaches are appropriate for small ions and for small particles in free molecular regime.
b) Averaged-Drift-Velocity approach is appropriate for relatively big particles in transition regime and continuum regime. Each component of the friction coefficient tensor (K_1, K_2 and K_3) is calculated using the interpolation method proposed by Dahneke (1973c) [72] in transition regime [16].

c) For particles in transition regime (close to Free molecular regime), the mechanism is mixed.

I note that in Table 6-2, the equivalent diameters from Averaged-Projected-Area approach and Averaged-Drag-Force approach are very close to each other for small particles (highlighted values for d_{pa} ,d_{df}), which is consistent with our expectation because the two approaches have a common assumption, i.e. drift velocity independent of particle orientation, as mentioned before, even one approach from cross-section calculation while the other from the tensor form of friction coefficient. Furthermore, the friction coefficient of a rod in free molecular regime is from the Dahneke's expression[68] where there has been little experimental data [95], while the projection area has been often used in literature. The calculated results showing very close match in free molecular regime in Table 6-2 can be a valid test for Dahneke's expression of a rod in free molecular regime[68].

6.4.3. Comparing three approaches with the experimental result for TMV

Tabaco mosaic virus(TMV) is a good example as a straight rigid rod which has a length $L_r \approx$ 300nm and diameter $d_r \approx$ 16-18nm under electron microscopy[4]. In this work I take L_r=300nm and d_r =17nm. Considering the finite diameter of the bath gas molecules, d_g=0.3nm, by approximately increasing L_r and d_r by 0.3nm[103], the calculate values are shown in Table 6-3.

Since the criterion value τ_0/τ_t is much greater than 20, the Averaged-Drift-Velocity is appropriate for the spherical diameter calculation which is highlighted in Table 6-3 as 69.5 nm. The experimental value of the mobility of TMV at very low electric field (random orientation) was measured using Differential Mobility Analyzer and then converted to mobility diameter 63.7nm based on (6-32). The calculated value from Averaged-Drift-Velocity is the closest value among the three approaches to the experimental result as I expected. The discrepancy between the experimental value and the calculated value is probably from the interpolation method for a non-spherical particle of Dahneke[72] used here for the calculation for the principle components of the friction coefficient tensor (K_1, K_2 and K_3).

I note here that for comparing the experimental value with model calculation value, the calibration for the finite diameter of the bath gas molecules, 0.3nm, should only do once. For example, we already considered this 0.3nm effect for the calculations of TMV in there models above, and then we do not need to consider this effect again for converting the experimental mobility to mobility diameter using (6-32). In some literature[92], this effect was considered twice.

Table 6-3. *The experimental mobility diameter from DMA is compared with the three diameters calculated from three approaches. The diameter from averaged-drift-velocity approaches shows the closed value to experimental value as expected.*

Diameter, d_r (nm)	Aspect ratio,β	Experimental Mobility diameter by DMA (nm)	τ_0/τ_t Free Molecular	<A_{pa}> (nm^2)	d_{pa} (nm)	d_{dv} (nm)	d_{df} (nm)
17.3	300.3/17.3	63.7	1877.6	4197.8	73.1	**69.5**	74.9

6.4.4. Comparing three approaches with the calculation results for GroEL in literature

The Geometric approximation of GroEL 14-mer is a cylinder with a length L~14nm, and as base diameter ~13 nm [88, 92]. Using atomic coordinates derived from X-ray diffraction data of GroEL 14-mer and using a modified version of software program MOBCAL[82, 84] , the averaged projection area was calculated as 220 nm^2 [88], and 217.6 nm^2 [92]. To compare with the result from the software program, Hogan el al. [92] developed a simple algorithm model and obtained the projected area as 197 nm^2.

Using the three approaches in this work and approximating GroEL as a rod with length =14.3nm and diameter =13.3nm accounting for the finite diameter of air 0.3nm, I calculated the results of GroEL in Table 6-4. The projected area $<\Omega_{pa}>$ is based on Eqn.(6-35). A_{dv} and A_{df} are equivalent areas converted from d_{dv} and d_{df} by $A=\pi d^2/4$ respectively. All three values, 218.8, 223.2 and 223.2 from the three approaches in this work are very close to the projected areas, 217.6 and 220 nm^2 , from software program using the crystal structure of GroEL [88, 92], and even better than the value calculated from Hogan's model.

Table 6-4. *Using the three approaches in this work and approximating GroEL as a rod with length =14.3nm and diameter =13.3nm accounting for the finite diameter of air 0.3nm, I calculated the results of GroEL in the table, and compared to the values from software program using the crystal structure of GroEL, and also compared with the value calculated from Hogan's model.*

Diameter, d_r	Aspect ratio, β	$<\Omega_{pa}>$ Obtained	$<\Omega_{pa}>$ Obtained	$<\Omega_{pa}>$ From	$<\Omega_{pa}>$	A_{dv}	A_{df}

(nm)		from software (nm^2)	from software (nm^2)	Hogan's model (nm^2)	In this work (nm^2)	In this work (nm^2)	In this work (nm^2)
13.3	14.3/13.3	[a] 217.6	[b] 220	[a] 197	218.8	223.2	223.2

[a] Hogan et al. [92]. [b] van Duijn et al. [88].

6.5. Conclusion

I propose a new approach to obtain the mobility of non-spherical particles by averaging the drag force orientationally, and summarize and extend two other approaches common in the literature, averaged-cross-section and averaged-drift-velocity. In the averaged-cross-section approach, I extended the cross-section integral theory for a spherical particle in Li and Wang [20] to a convex non-spherical particle and derived this cross-section integral simplifying to an averaged projection area multiplied by an enhancement factor for hard collisions. I also showed that the averaged projection area of a convex particle is equal to its mobility diameter based on the Stokes-Cunningham formula. The approach of Li et al.[16] for computing the average mobility for an axially symmetric particle by averaging its drift velocity has been further extended to a general form and for more symmetric cases. I also pointed out that this Averaged-Drift-Velocity approach is only valid for relatively large particles in the transition regime and continuum regime where the Brownian rotation is slow compared with the particle translational relaxation time. For small ions and for particles in free molecular regime, where the Brownian rotation is fast compared with the particle translational rotation I propose an averaged-drag-force approach which calculates particle mobility by averaging the drag force in a tensor form. A simple criterion was developed for the validation of using each approach of the three above. The three approaches were then compared with each other by applied to a randomly oriented rod. The averaged-cross-section and averaged-drag-force approaches provide very close values as expected in free molecular regime where they are valid. The averaged-drag-force approach uses the friction coefficient of a rod in free molecular regime from Dahneke's expression where there has been little experimental data to validate. Since averaged-cross-section has been often used in literature, the calculated results based on the two approaches show similar results in the free molecular regime validates Dahneke's expression for a rod in free molecular regime. Finally, I compared the calculation results of the three approaches to the experimental value of Tabaco mosaic virus (TMV), which is a rigid rod, and showed that the mobility diameter obtained from Averaged-Drift-Velocity is the closest to the experimental value as expected, and I also showed the calculation results for GroEL from software program in literature are in good agreement with our calculations using the three approaches in this work.

6.6. Appendix.

A.1. Particle body fixed coordinate, space fixed coordinate and Euler angles φ, ψ, θ

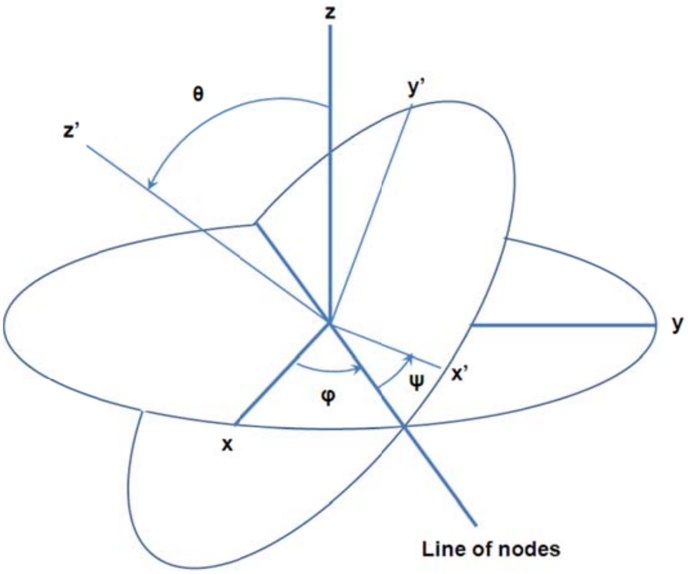

Figure 6-A.1. *Three Euler angles φ, ψ, θ, relate the particle body fixed coordinate system (x', y', z') to the space fixed coordinate system (x, y, z).*

A space fixed coordinate system (x, y, z) with unit vector ($\vec{i},\vec{j},\vec{k}$) respectively, and a particle body fixed coordinate system (x', y', z') with unit vector ($\vec{i}',\vec{j}',\vec{k}'$) are shown in Figure 6-A.1, where z direction (unit vector $\vec{k}$) is chosen along the external force direction. Three Euler angles φ, ψ, θ, relate body fixed coordinate system to the space fixed[67].

Assuming that the friction coefficient is in a tensor form, the drag force is expressed as [17]

$$\vec{F}_{drag} = -\hat{K}\cdot\vec{V}_d \tag{6-12}$$

where $\hat{K}$ is the friction coefficient tensor and $\vec{V}_d$ is the drift velocity of the particle.

A.1.1.The velocity expression in Averaged-Drift-Velocity Approach

Assuming at each orientation of the particle the drag force is balanced by the electric force, we obtain

$$\hat{K} \cdot \vec{V}_d = q\vec{E}, \tag{6-13}$$

and $$\vec{V}_d = q\hat{K}^{-1} \cdot \vec{E} \tag{6-14}$$

If we define the particle body fixed coordinate system ($\vec{i}\,', \vec{j}\,', \vec{k}\,'$) parallel to the three principal axes of the tensor $\hat{K}$ of the particle, then,

$$\vec{V}_d = V_{d,x}\vec{i} + V_{d,y}\vec{j} + V_{d,z}\vec{k}$$

$$V_{d,x} = qE(K_1^{-1}a_1 + K_2^{-1}a_2 + K_3^{-1}a_3)$$

$$V_{d,y} = qE(K_1^{-1}b_1 + K_2^{-1}b_2 + K_3^{-1}b_3)$$

$$V_{d,z} = qE(K_1^{-1}c_1 + K_2^{-1}c_2 + K_3^{-1}c_3)$$

$$a_1 = \cos\psi\cos\varphi\sin\theta\sin\psi - \cos\theta\sin\varphi\sin^2\psi\sin\theta$$

$$a_2 = -\sin\psi\cos\varphi\sin\theta\cos\psi - \cos\theta\sin\varphi\cos^2\psi\sin\theta$$

$$a_3 = \sin\theta\sin\varphi\cos\theta$$

$$b_1 = \cos\psi\sin\varphi\sin\theta\sin\psi + \cos\theta\sin\varphi\sin^2\psi\sin\theta$$

$$b_2 = -\sin\psi\sin\varphi\sin\theta\cos\psi + \cos\theta\cos\varphi\cos^2\psi\sin\theta$$

$$b_3 = -\sin\theta\cos\varphi\cos\theta$$

$$c_1 = \sin^2\theta\sin^2\psi$$

$$c_2 = \sin^2\theta\cos^2\psi$$

$$c_3 = \cos^2\theta$$

where K_1, K_2 and K_3 are three principal components.

If particle orientation follows a distribution function $f(\varphi, \psi, \theta)$, then

$$\langle \vec{V}_d \rangle_{\vec{k}} = \langle V_{d,z} \rangle = qE(K_1^{-1} < \sin^2\theta \sin^2\psi > + K_2^{-1} < \sin^2\theta \cos^2\psi > + K_3^{-1} < \cos^2\theta >)$$

(6-15)

In symmetric situations, such as $f(\varphi, \psi, \theta) = f(\psi, \theta)$, $f(\varphi, \psi, \theta) = f(\theta)$ or $f(\varphi, \psi, \theta) = 1/8\pi^2$, $\langle V_{d,x} \rangle$ and $\langle V_{d,y} \rangle$ vanish, and we have $\langle \vec{V}_d \rangle = \langle V_{d,z} \rangle \vec{k}$ or $\langle \vec{V}_d \rangle = \langle V_d \rangle \vec{k}$.

A.1.2. The Drag force expressions in Averaged-Drag-Force approach

In Averaged-Drag-Force approach, we can think that the external force is balanced by an orientation averaged drag force with the form expressed in Eqn.(6-13) along the external force direction,

$$F_{external} = -\langle \vec{F}_{drag} \rangle \cdot \vec{k} = \langle \hat{K} \cdot \vec{V}_d \rangle \cdot \vec{k} \tag{6-22}$$

and $\vec{V}_d = V_d \vec{k}$, (6-23)

Combine (6-22), (6-23) and consider the external force is an electric force, we have

$qE = V_d \langle \vec{k} \cdot \hat{K} \cdot \vec{k} \rangle$ and,

$$Z_p = V_d / E = q / \langle \vec{k} \cdot \hat{K} \cdot \vec{k} \rangle \quad . \tag{6-24}$$

If we define the particle body fixed coordinate system ($\vec{i}', \vec{j}', \vec{k}'$) parallel to the three principal axes of the tensor $\hat{K}$ of the particle, then,

$$\langle \hat{K} \cdot \vec{k} \rangle_i = K_1 \langle a_1 \rangle + K_2 \langle a_2 \rangle + K_3 \langle a_3 \rangle$$

$$\langle \hat{K} \cdot \vec{k} \rangle_j = K_1 \langle b_1 \rangle + K_2 \langle b_2 \rangle + K_3 \langle b_3 \rangle$$

$$\langle \hat{K} \cdot \vec{k} \rangle_k = \langle \vec{k} \cdot \hat{K} \cdot \vec{k} \rangle = K_1 \langle c_1 \rangle + K_2 \langle c_2 \rangle + K_3 \langle c_3 \rangle$$

where K_1, K_2 and K_3 are three principal components. The expressions of a_1 to c_3 were shown in section 6.A.1.1.

If particle orientation follows a distribution function $f(\varphi,\ \psi,\ \theta)$, then (6-24) becomes,

$$Z_p = q / (K_1 < \sin^2\theta \sin^2\psi > + K_2 < \sin^2\theta \cos^2\psi > + K_3 < \cos^2\theta >)$$

All the averages in above fomular are related to orientation distribution $f(\varphi,\ \psi,\ \theta)$ in the form of Eqn.(6-16).

Based on (6-23), the averaged drag force can be expressed as,

$$\langle \vec{F}_{drag} \rangle = -\langle \hat{K} \cdot \vec{V}_d \rangle = -\langle \hat{K} \cdot \vec{k} \rangle V_d$$

In symmetric situations, such as $f(\varphi,\ \psi,\ \theta)= f(\psi,\ \theta)$, $f(\varphi,\ \psi,\ \theta)= f(\theta)$ or $f(\varphi,\ \psi,\ \theta)= 1/8\pi^2$, $\langle \hat{K} \cdot \vec{k} \rangle_i$ and $\langle \hat{K} \cdot \vec{k} \rangle_j$ vanish, and we have

$$\langle \vec{F}_{drag} \rangle = -\langle \vec{k} \cdot \hat{K} \cdot \vec{k} \rangle V_d \vec{k}$$

Applying Eqn. above to three symmetric situations, we have

- Fully random

$$\langle \vec{F}_{drag} \rangle = -\frac{K_1 + K_2 + K_3}{3} V_d \vec{k} \tag{6-A1}$$

- Axisymmetric particles; Orientation distribution $f(\theta)$

$$\langle \vec{F}_{drag} \rangle = -[K_\perp + (K_\parallel - K_\perp) < \cos^2\theta >] V_d \vec{k}$$

$< \cos^2\theta > = \dfrac{1}{4\pi^2} \int_0^\pi \cos^2\theta f(\theta) \sin\theta d\theta$, is the orientationally-averaged $\cos^2(\theta)$.

- More general symmetric case with orientation distribution $f(\psi,\ \theta)$.

If orientation distribution function $f(\psi,\ \theta)$ is only a function of ψ, θ, for example, a uniform right angled parallelepiped, then

$$\langle \vec{F}_{drag} \rangle = -(K_1 < \sin^2\theta \sin^2\psi > + K_2 < \sin^2\theta \cos^2\psi > + K_3 < \cos^2\theta >) V_d \vec{k}$$

if $K_1 = K_2$, such as a uniform right angled parallelepiped with square top and bottom

$\langle \vec{F}_{drag} \rangle = -[K_1 + (K_3 - K_1) < \cos^2\theta >]V_d\vec{k}$ All the averages above are related to orientation distribution $f(\psi, \theta)$ as

$$< X >= \int_0^{2\pi} d\varphi \int_0^{\pi} d\theta \sin\theta \int_0^{2\pi} d\psi f(\psi,\theta) X(\psi,\theta) = \frac{1}{2\pi} \int_0^{\pi} d\theta \sin\theta \int_0^{2\pi} d\psi f(\psi,\theta) X(\psi,\theta)$$

If $K_1 = K_2 = K_3$ such as a uniform cubic, $\langle \vec{F}_{drag} \rangle = -K_1 V_d \vec{k}$

A.2. Simplifying the averaged cross-section integral in Eqn.(6-5) for a convex particle with hard collisions

If we extend Epstein's approach for a convex particle and simplify the collision calculation by still treating the particle surface as a smooth surface, then we need to compensate our calculation by incorporating a term of inelastic collisions (or diffuse reflections). And the orientationally averaged cross section for a convex particle with rough surface is,

$$< \Omega >= f < \Omega_d > +(1-f) < \Omega_s > \tag{6-5}$$

If we only consider hard collisions and ignore long-range potential, the specular collision integral (Li and Wang, 2003)[20] becomes,

$$\Omega_S = 2\pi \int_0^{b_{\max}} b[1-\cos\chi]db \tag{6-A2}$$

and the diffuse collision integral (Li and Wang, 2003)[20] becomes

$$\Omega_d = 2\pi \int_0^{b_{\max}} b[1+\frac{3\pi}{16}\sin\frac{\chi}{2}]db \tag{6-A3}$$

I note here that in extended Epstein's approach, that is, Eqn.(6-5), both $< \Omega_s >$ and $< \Omega_d >$ should be calculated assuming particle surface is smooth. Using the idea in Shvartsburg and Jarrold [82], I will show below that under this condition the two averaged cross section integrals $<\Omega_s>$ and $<\Omega_d>$ can be further simplified to the averaged projected area multiplied by a factor.

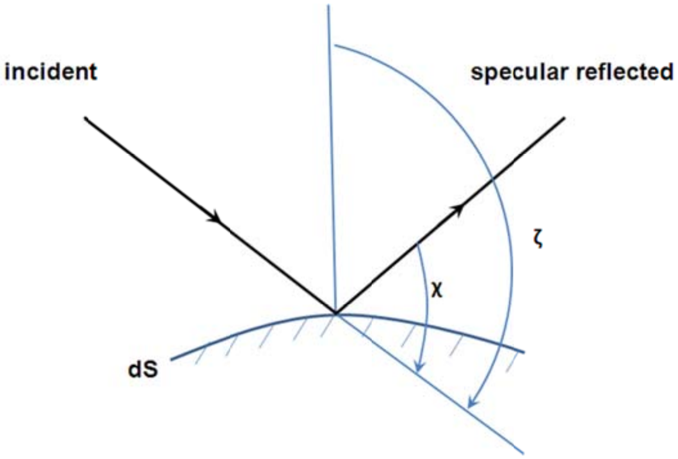

Figure 6-A.2. *Demonstrating an incident molecule hitting small area dS on a convex particle and showing the relationship between the angle* χ *and angle* ζ.

Considering an infinitesimally small surface of a convex particle with area dS and the angle between the normal direction of this surface and the molecule incident direction is ζ as shown in Figure 6-A.2, the relationship between ζ and χ is

$$\zeta = \frac{\chi + \pi}{2}$$

And the projected area is

$$a_{pa} = -dS\cos\zeta$$

Based on Eqn.(6-A.2), the specular collision integral element for this small surface is

$$\omega_S = (1-\cos\chi)a_{pa} = (1-\cos\chi)(-\cos\zeta)dS = -2\cos^3\zeta dS \cdot$$

Averaging a_{pa} and ω_s over all possible values of ζ from π/2 to π, we obtain,

$$\langle a_{pa} \rangle = \frac{2\pi \int_{\pi/2}^{\pi} a_{pa} \sin\zeta \, d\zeta}{2\pi \int_{\pi/2}^{\pi} \sin\zeta \, d\zeta} = \frac{dS}{2} \qquad (6\text{-A4})$$

and

$$\langle \omega_s \rangle = \frac{2\pi \int_{\pi/2}^{\pi} \omega_s \sin\zeta \, d\zeta}{2\pi \int_{\pi/2}^{\pi} \sin\zeta \, d\zeta} = \frac{dS}{2} \qquad (6\text{-A5}).$$

Based on (6-A4) and (6-A5), we have $\langle a_{pa} \rangle = \langle \omega_s \rangle$. Since any finite geometric surface can be considered as a set of infinitesimally small surfaces above, then the total averaged specular cross section $\langle \Omega_s \rangle$ is the sum of $\langle \omega_s \rangle$, as long as there is no mutual shadowing of small surfaces and no multiple collisions where molecules are reflected from one small surface to another, which are satisfied by a convex and smooth surface. The total averaged projection area $\langle \Omega_{pa} \rangle$ is the sum of $\langle a_{pa} \rangle$. So one concludes for any convex particle with a smooth surface

$$\langle \Omega_s \rangle = \langle \Omega_{pa} \rangle \qquad (6\text{-A6})$$

Similarly, the diffuse collision integral element of Eqn. (6-A4) for the infinitesimally small surface above is

$$\omega_d = (1 + \frac{3\pi}{16} \sin\frac{\chi}{2}) a_{pa} = (1 + \frac{3\pi}{16} \sin\frac{\chi}{2})(-\cos\zeta) dS = (1 - \frac{3\pi}{16} \cos\zeta) \cos\zeta \, dS$$

Averaging ω_d over all possible values of ζ from $\pi/2$ to π, we obtain,

$$\langle \omega_d \rangle = \frac{2\pi \int_{\pi/2}^{\pi} \omega_d \sin\zeta \, d\zeta}{2\pi \int_{\pi/2}^{\pi} \sin\zeta \, d\zeta} = (\frac{\pi}{8} + 1) \frac{dS}{2} = (\frac{\pi}{8} + 1) \langle a_{pa} \rangle$$

which results in   for any convex particle with a smooth surface

$$\langle \Omega_d \rangle = (\frac{\pi}{8} + 1)\langle A_{pa} \rangle \tag{6-A7}$$

Combining Eqns. (6-5), (6-A6) and (6-A7), we obtain the cross-section for a convex particle with rough surface as

$$< \Omega >= (1 + \frac{\pi f}{8}) < A_{pa} > \tag{6-6}$$

A.3. Orientation distribution due to Brownian rotation

If the particles are small enough, over the time scale of interest, the rotational Brownian motion will result in a steady state distribution of the orientation, i.e., Boltzmann angular distribution

$$f(\varphi, \psi, \theta) = \frac{e^{-U/kT}}{\int_0^{2\pi} d\varphi \int_0^{\pi} d\theta \sin\theta \int_0^{2\pi} d\psi e^{-U/kT}}$$

where $\int_0^{2\pi} d\varphi \int_0^{\pi} d\theta \sin\theta \int_0^{2\pi} d\psi f(\varphi, \psi, \theta) = 1$,and U is the interaction energy between the particle and the external electric field and is addressed in details in Li et al.[16].

- Symmetric case with orientation distribution *f(ψ, θ).*

If the interaction energy U is only a function of *ψ, θ, then f*(*φ, ψ, θ*) becomes *f*(*ψ, θ*). Following I give an example by only considering the polarization energy U_p, that is, $U = U_p$.

The interaction energy, U, is usually dominated by polarization energy U_p [16] and U_p is given by [71]

$$U_p = -\frac{1}{2}\vec{E}\cdot\hat{\alpha}\cdot\vec{E}$$

where $\hat{\alpha}$ is polarizability tensor. If we assume that U = U$_p$, then as long as the three principal axes of the friction coefficient tensor $\hat{K}$ are the same as for polarizability tensor $\hat{\alpha}$, for example, a uniform right angled parallelepiped, $f(\varphi, \psi, \theta)$ becomes $f(\psi, \theta)$

$$f(\psi,\theta) = \frac{e^{-U_p/kT}}{\frac{1}{2\pi}\int_0^{\pi} d\theta \sin\theta \int_0^{2\pi} d\psi e^{-U_p/kT}} \quad , \tag{6-A8}$$

where $U_p = -\frac{E^2}{2}(\alpha_1 \sin^2\theta \sin^2\psi + \alpha_2 \sin^2\theta \cos^2\psi + \alpha_3 \cos^2\theta)$ and (α_1, α_2, α_3) are the principal components of the polarizability tensor.

- <u>Axisymmetric particles with orientation distribution $f(\theta)$[16]</u>

The expression of Boltzmann angular distribution of $f(\theta)$ for axisymmetric particles was described in details in Li *et al.*[16].

Chapter 7: Development of a Pulsed-Voltage Differential Mobility Analyzer: A Method for Measuring Shape Parameters for Non-Spherical Particles.

7.1. Introduction

Nanomaterials are widely applied and studied in medicine, electronics, biomaterials and environmental science. Effective measurement and accurate characterization of nanomaterials play a critical role in the development of nanotechnology. It is well-known that many of the properties of particles are size dependent. Moreover, for aspherical structures such as nanorods, nanowires, the properties are also greatly influenced by their shapes. Nanoparticles with nonspherical shapes exhibit some unique physical and chemical properties and have potential for biological label fabrication, disease monitoring, and medical clinical diagnosis. For example gold nanorods are useful for the formation of many functional composite materials due to their special light scattering and absorption properties [104]. Nonspherical particles also have important effects on environment and human health. Soot aggregates produced by combustion are highly non-spherical ramified structures with non-integer fractal dimensions. Another important form of carbon materials are carbon nanotubes which actually are just one chemical form for what has become an almost infinite variety of nanowires.

The common feature of all these materials is that they are non –spherical and thus cannot be dimensionally characterized by just one length scale. To obtain the size and shape information of nanoparticles, microscopy techniques, such as transmission or scanning electron microscopy (TEM/SEM), are traditionally applied. However, in these off-line methods, good sampling methodsand time-consuming operations are needed for a precise distribution measurement. It is also reported that the sampling and imaging process itself may cause coalescence of small clusters.The differential mobility analyzer (DMA) is the gold-standard measurement method for obtaining a complete size distribution of nanoparticles in the aerosol phase [7]. For a spherical particle, the electrical mobility diameter is equivalent to its geometric diameter. However, if the particle is nonspherical, the resulting electrical mobility diameter is that diameter for a sphere with the same mobility as the analyte particle. For example Song et al. [66] investigated the relationship between the electrical mobility size and particles shape, by changing the particle shape from nanorod to sphere by heating the particles from 25 C to 800 C, and showed that the mobility diameters decreased from 55nm to 25nm.

Since the mobility size measured in the DMA depends on the drag force on the particles, thus for a non-spherical particle, mobility necessarily depends on orientation with respect to the applied electric field[8, 16, 68, 72, 74]. In principle then, an orientation dependent mobility measurement should yield some information on particle shape. Kousaka et al.[62] measured the dynamic shape factor for doublets of uniform spheres (Polystyrene latex particles; PSL) in the transition regime and pointed out that the orientation of doublets is a function of electric field in the DMA and the size of doublets. Zelenyuk and Imre [63] applied this idea to more aspherical particles and showed that the dependence of electrical mobility size on electric field can be applied to separate particles based on their shape.

However, none of these studies provide a rigorous expression, which can present the relationship between the measured electrical mobility size (or detection voltage) and the geometric shape of particles. In the studies of Li et al. [8, 16], I developed an orientation-averaged electrical mobility theory for rigid axisymmetric particles undergoing Brownian motion by considering the electrical polarization of the particles in an electric field.

In this work, I use this theory for a prolate ellipsoid. The ellipsoid has the possibility to be a model system for any arbitrary shaped particle or aggregate that might be described with a major and minor axis.

To obtain the shape information by measuring the electrical mobility under different electric fields, I also propose a new instrument, a pulsed differential mobility analyzer (PDMA). This new method enables one to change the peak E-field experienced by the particle, while still maintaining the same time averaged field. In so doing one could in principle systematically change the average orientation of a non-spherical particle and thus its mobility. The instrument is tested on PSL singlets and doublets with precisely known size and shape, and the result shows that the PDMA would be a potential method for particle sizing and particle shape information measurements. I also report an unexplained phenomenon which is an unknown relaxation process for non-spherical particles in a PDMA.

7.2. Theoretical models for shape measurement

The particle electrical mobility, Z_p, is defined by: $Z_p = v_r / E$, where v_r is the particle drift velocity and E is the magnitude of the electric field.

By equating the electrostatic attraction force to the drag force on a spherical particle, electrical mobility, Z_p can be obtained as:

$$Z_p = \frac{neC_c(d_p)}{3\pi\eta d_p} , \tag{7-1}$$

where n is the number of elementary charges on the particle, d_p the electrical mobility diameter, and $C_c(d_p)$ the Cunningham Slip Correction Factor, which was parameterized by Allen and Raabe [9]. The electrical mobility diameter d_p of a sphere is equal to its geometric diameter, and the electrical mobility Zp is only a function of this spherical diameter based on Eqn. (7-1) and independent of electric field in the DMA.

However, for a nonsherical particle, d_p is the equivalent diameter of a sphere having the same drag force, and the size and shape information of this nonspherical particle is contained in the electrical mobility, Z_p. Unlike a spherical particle for which the electrical mobility is independent of field strength, the non-sperical particle because of its field dependent orientation will have a field dependent mobility.

I begin my discussion, by using the specifics of a cylindrical DMA [105]. For a sphere, if the sheath in-flow rate, Q_{sh}, is the same as the sheath out-flow rate, the electrical mobility in the DMA can also be described as

$$Z_p = \frac{Q_{sh} \ln(r_{out} / r_{in})}{2\pi V_e L_d} , \tag{7-2}$$

where V_e is the detecton voltage of the DMA, r_{out} the radius of outer electode of DMA, r_{in} the radius of inner electrode of DMA and L_d the DMA length. By combining Eqn.(7-1) and Eqn.(7-2), the diameter of a sphere can be derived from the following detection voltage – mobility diameter relationship,

$$V_e = \frac{3\eta \ln(r_{out} / r_{in}) Q_{sh} d_p}{2neL_d C_c(d_p)} \quad (7\text{-}3)$$

For non-spherical particles, Eqn. (7-3) can be used to get an equivalent diameter, but is not sufficient to obtain the geometric shape information. Li *et al.* [16] presented a general form for the orientation-averaged mobility and the effective dynamic shape factor for an axisymmetric particle in an electric field and this theory shows excellent agreement with experimental results of doublets with primary particle size larger than 125nm [8]. In section 7.2.2, I use the theory in Li *et al.* [16] for prolate ellipsoid, which can be considered general for any non-symmetric and non-spherical aggregate considered having a major axis and a minor axis. In section 7.2.3, using the expression of orientation-averaged mobility, the relationship between applied voltage and the shape information can be obtained[16].

7.2.1 Orientation-Averaged-Mobility for Axisymmetric Particles

The mobility increases (due to an increase in drift velocity) as the nanowire or prolate ellipsoid orientation is changed from perpendicular to parallel relative to the field direction. A torque arising from the electric field, and the free charge tend to align axisymmetric particles, for example a nanowire, in the direction of the electric field as shown in Figure 7-1. A second torque arises from the polarizability of the particle, and is typically the dominant factor in the alignment.

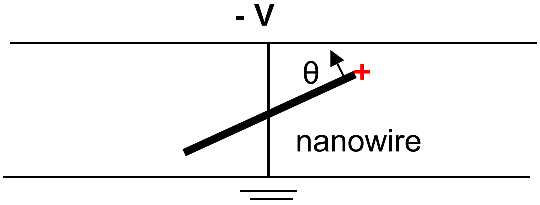

Figure 7-1. *Axisymmetric particles, for example a nanowire, alignment in a uniform electric field with charge at the end of the wire.*

The Brownian thermal energy will oppose this alignment. The orientation electrical energy in Figure 7-1 arises from the torques acting on the axisymmetric particle (showing example as a nanowire) from the free charge, $\Phi_q(\theta)$, at the end of the axisymmetric particle and from the polarizability, $\Phi_P(\theta)$, of the axisymmetric particle. By considering the Brownian motion to disorient the particle , the probability, $f(\theta)\sin(\theta)d\theta$, for the axisymmetric particle to be oriented at an azimutal angle θ relative to the direction of the electric field based on the Boltzmann probability distribution is [16, 69],

$$f(\theta)\sin\theta d\theta = \frac{e^{-\frac{\Phi_q(\theta)+\Phi_P(\theta)}{kT}}\sin\theta d\theta}{\int_0^{\pi} e^{-\frac{\Phi_q(\theta)+\Phi_P(\theta)}{kT}}\sin\theta d\theta} \tag{7-4}$$

Experimentally we can only measure the orientation averaged mobility. A general expression for the average electrical mobility for an axisymmetric particle is [16]

$$\overline{Z_p} = q[K_{\perp}^{-1} + (K_{\parallel}^{-1} - K_{\perp}^{-1}) < \cos^2\theta >] \quad , \tag{7-5}$$

where $K_{\perp}$ is the principal component of the friction coefficient tensor perpendicular to the axial direction, $K_{\parallel}$ is the component parallel to the axial direction, and

$< \cos^2\theta >= \int_0^{\pi} \cos^2\theta f(\theta)\sin\theta d\theta$, is the orientationally-averaged $\cos^2(\theta)$,

The two torque energies are a function of the electric field strength which leads to the *E* dependence of the average mobility.

The evaluation of Eqn.(7-5) requires a knowledge of $K_{\perp}$ and $K_{\parallel}$, which depend on drag model ($\vec{F}_{drag} = -\hat{K} \cdot \vec{V}_d$)specific to the geometry of interest (e.g. ellipsoid, rod, doublets of spheres), and the orientation average value $< \cos^2\theta >$. The detail calculations of $K_{\perp}$ and $K_{\parallel}$ for nanorod and ellipsoid in three regimes and the calculations for $< \cos^2\theta >$ were shown in Li *et al.* [16].

7.2.2 Orientation-Averaged-Mobility for Prolate Ellipsoid: Applied to General Agglomerate Structure

While fractal agglomerates are not as well defined in terms of shape as a dimer or nanorod, they are often elongated in one direction. Our current thinking is to consider the agglomerate as a diffuse ellipsoid.

At low field strengths, the thermal energy dominates the aligning energy, and Brownian dynamics results in a random orientation. As the electric field increases, the prolate ellipsoid will tend to align and results in a larger electric mobility. In Fig. 7-2, I plot as a normalized (relative to random orientation) electrical mobility vs. applied electric field for a wide range of aspect ratios, β, *with the minor axis 2b = 15nm*. The aspect ratio β defined by a/b of the ellipsoid, where a is the major semi-axis. A clear increase in mobility is observed with increasing field strength for all β's. The onset of alignment occurs at lower field strength with increasing β. The sigmoidal shape of the curves is key to being able to size nanowires and separate them from spheres and aggregates.

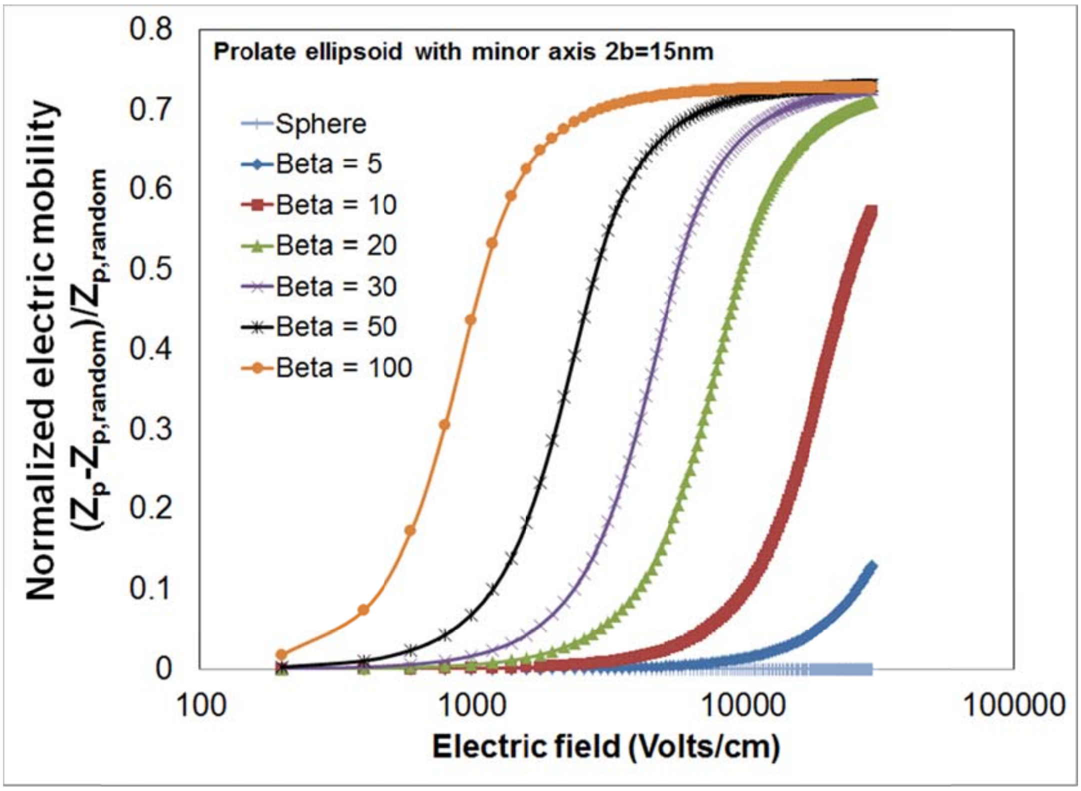

Figure 7-2. *Theoretical calculation of the effect of t electric field on the scaled mobility for various aspect ratios for a prolate ellipsoid with minor axis 2b =15nm . 30,000 v/cm is the air breakdown limit.*

7.2.3 Voltage – Shape Information Relationship in a DMA Measurement (Step Mode)

A knowledge of the orientation-averaged mobility, Eqn. (7-5), can be used to determine the precipitation time of a particle across two electrodes. By equating the precipitation time of a particle in a DMA to the flow transit time traveling along with the sheath flow, the voltage – shape information relationship can be obtained as[16],

$$\frac{\pi(r_{out}^{2}-r_{in}^{2})L_{d}}{Q_{sh}+Q_{a}}=\frac{V_{e}}{\ln(r_{out}/r_{in})}\int_{E_a}^{E_{in}}\frac{dE}{\overline{Z_{p}}(E,shape)\cdot E^{3}}, \qquad (7\text{-}6)$$

where

r_{in} the radius of inner electrode of DMA,

r_{out} the radius of outer electrode of DMA,

Q_{sh}, the sheath flow rate,

Q_{a}, the aerosol flow rate,

L_{d}, the length of DMA electrode,

$$E_{in}=\frac{V_{e}}{r_{in}\ln(r_{out}/r_{in})}$$

$$E_{a}=\frac{V_{e}}{r_{a}\ln(r_{out}/r_{in})}.$$

$$r_{a}^{2}=\frac{Q_{sh}r_{out}^{2}+Q_{a}r_{in}^{2}}{Q_{sh}+Q_{a}}$$

The averaged mobility, $\overline{Z_{p}}$,which is a function of electric field and contains the shape information, is given by Eqn.(7-5) for axially symmetric particles such as a prolate ellipsoid.

7.3. Pulsed Differential Mobility Analyzer (PDMA)

The shape information for nonspherical particles is contained in the electrical mobility as shown above, which is usually a nonlinear function of electric field. One way of measuring the effect of particle alignment under different electric fields is to vary the sheath flow in the DMA [8, 16, 62, 63]. By varying the flow, particles can be detected under different electric fields. However, changing flow is not very convenient, and in so doing the instrument resolution is also changed. In this section, I introduce a new instrumental technique, employing a Pulsed DMA, which allow one to change the electric field acting on the non-spherical particle by only changing the duty cycle of a pulsed electric field in a DMA instead of changing the flow.

Consider a square wave pulse going from zero to –V with a duty cycle equal to a fraction of the period. As illustrated in Fig. 7-3, while the particle is exposed to the high field, it will be partially aligned and then return to a random orientation when the field is removed. When the field is removed, there is no radial movement of the particle in the DMA, so the effective movement in the radial direction only takes place when the particle is exposed to the high field. The change in the electrical mobility is measured as the alignment field intensity is changed.

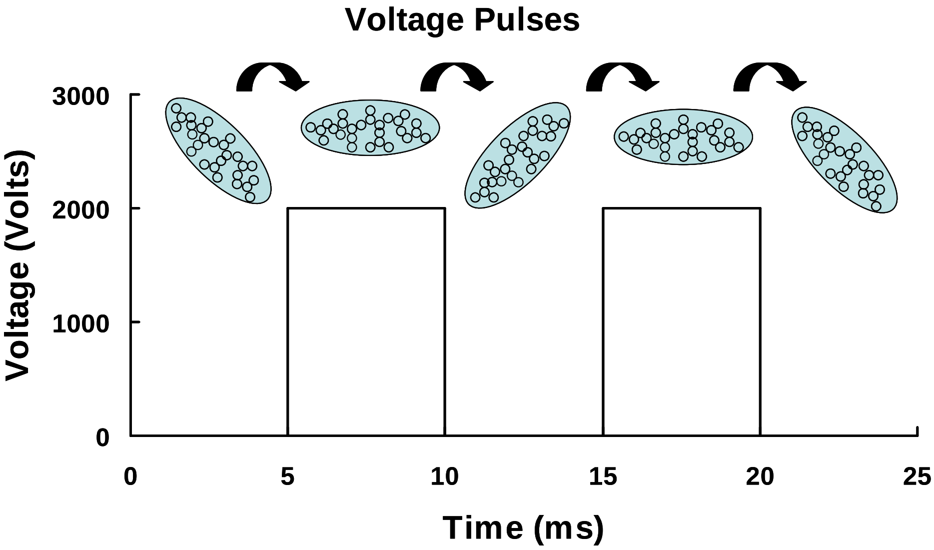

Figure 7-3. *Oscillating electric field to align particles (wires or aggregates). In this example, the pulse frequency is 100Hz, the duty cycle is 50%, with a 2000 volts pulse on.*

A key concept is that for a spherical particle the precipitation time from the inlet to the central rod is only a function of the time averaged potential. So for example, 1000 volts with a DMA sheath flow rate, Q_{sh} , corresponds to particles exiting the DMA at the peak in the mobility distribution for spherical particles, then a pulsed field with a 25 % duty cycle and a 4000 V at the DMA sheath flow rate, Q_{sh} ,will also result in the peak mobility exiting the DMA. Fig. 7-4 shows how one can vary the pulse field by about a factor of 4 while still keeping the average field constant. On the other hand, if a non-spherical particle passes through the DMA, it will be partially aligned by the field so that the peak mobility will be shifted as the pulse width is decreased. During the period of alignment under high field, which is the effective time for particles traveling along the radial direction its drag will be lower and thus its mobility higher than the equivalent sphere. If the effect of the rise time of the pulse on the electrical mobility is negligible, the pulsed field with a 25% duty cycle at sheath flow, Q_{sh}, is equivalent to a DC field at sheath flow, $4*Q_{sh}$.

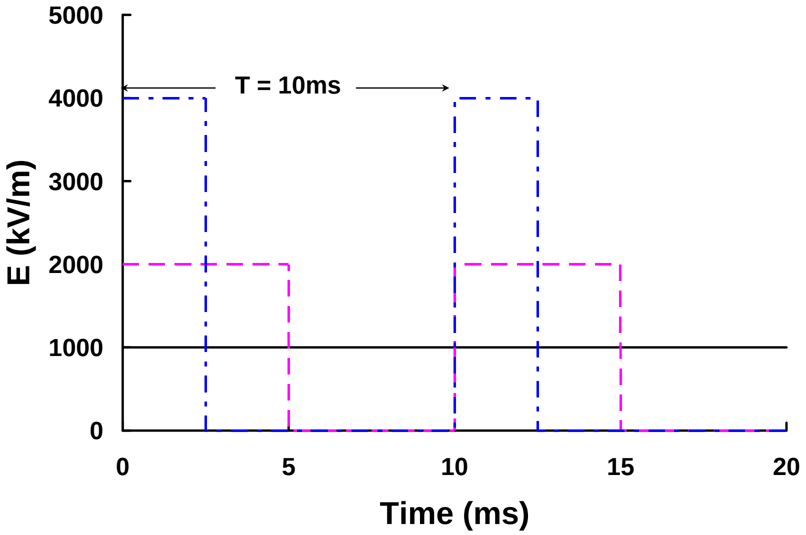

Figure 7-4. *Illustration of the relationship between the electric field and the pulse width to maintain a constant average field. Duty cycles vary from 100% , 50% to 25% with pulse frequency 100Hz, and the corresponding fields are 1000, 2000 and 4000 kV/m respectively.*

To perform a measurement of the effect of particle alignment under different pulsed fields in the DMA requires a TDMA. Fig. 7-5 provides a schematic of the operation of tandem DMAs in series with the second DMA employing a pulsed field. Conceptually if we have a polydisperse distribution of spheres and nanrods entering the first DMA, which is operating at a low enough field that the particle's orientation is nearly random. Exiting the first DMA is a mixture of nanowires with fixed length and diameter, (nanowires at inlet assumed to have the same diameter), and a fixed diameter of spheres. The alignment effect caused by the second DMA operating in a pulsed mode results in the separation of the nanowires at a lower voltage than the spheres. The mobility distribution of the particles exiting the first and second DMA are schematically shown in Figure 7-6.

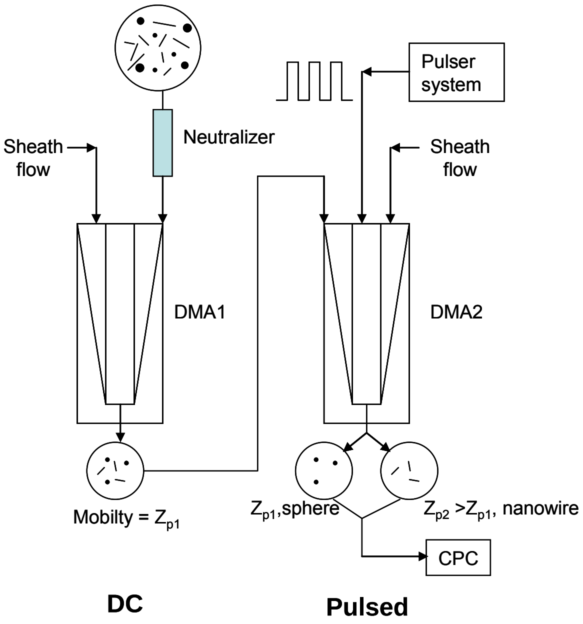

Figure 7-5. *Measurement system with the first DMA used to separate mono-mobility particles and the pulsed DMA to both separate spheres from nanowires and to measure the aspect ratio of the nanowires.*

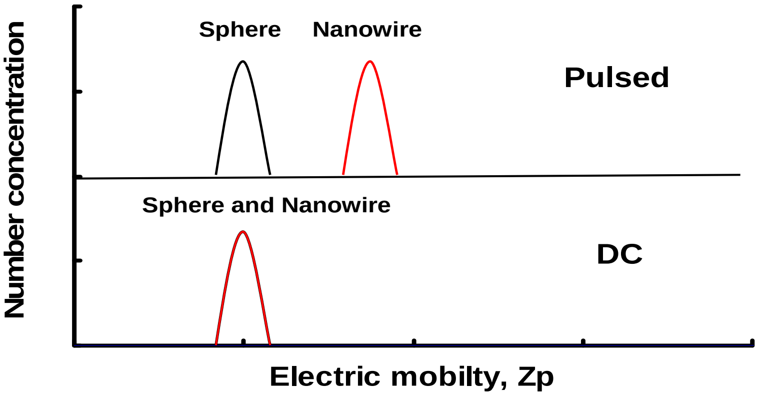

Figure 7-6. *Schematic illustration of the mobility distribution of particles exiting the DMA-PDMA system.*

Our pulsed DMA is experimentally tested on Polystyrene latex (PSL) singlets (sphere) and doublets (nonsphere) with precisely known sizes and shapes, and the result show that a PDMA would be an effective tool for particle sizing and particle shape information measurements.

7.4. Experimental

In this section below, I first show the experimental evidences of the alignment effects of non-spherical particles in an electric field using doublets of NIST traceable size standards PSL spherical particles and a nanorod with well-defined size and shape, tobacco mosaic virus (TMV) in traditional DMAs. Second, I present the PDMA and the experimental evaluation using spheres (the singlets) and non-sphere, the doublet of PSL spheres.

7.4.1. Alignment effects of non-spherical particles in an electric field.

To evaluate particle alignment and its effect on mobility I measure the electric mobility of Polystyrene latex (PSL) doubles using a commercial Differential Mobility Analyzer (DMA) and a well-defined-rod, TMV, using a homemade high electric field DMA (the electric field can reach up to 3.3 times of a commercial DMA).

- Polystyrene latex (PSL) double of spheres

NIST traceable size standards PSL particles 149.4nm primary PSL spheres (Thermo Scientific 3150A) were aerosolized using a constant output pressure atomizer(TSI Inc. Model 3076), and dried with two diffusion dryers before entering a neutralizer, which provides results in a Fuchs charge distribution for the particles. The neutralized particles then pass through a long Differential Mobility Analyzer (DMA) column (TSI Inc. Model 3081) for particle mobility measurement and counted with an ultrafine Condensed Particle Counter (CPC) (TSI Inc. Model 3025A).

The distribution of mobility is measured with different sheath flow rates ranging from 2 lpm to 18 lpm to allow make the measurement under from low to high electric field. The field strength in this work spans from 1kV/cm to 8.5kV/cm. To avoid the effects of varying electric field encountered in a typical scanning mode (SMPS) experiment, I operated the DMA in the step mode and kept the step sufficiently long to ensure a complete transit through the DMA system (40 seconds to 25 seconds corresponds to Qsh from 2 lpm to 18 lpm). The ratio of the sheath to aerosol flow rates was kept more than 20 to guarantee a high size resolution. The monomer size of PSL sphere were calibrated as 149.4nm using 100.7nm NIST standard reference material (PSL sphere) under the same experimental conditions.

- Tabaco mosaic virus (TMV), a well-defined nanorod

Tabaco mosaic virus (TMV) sample was provided by the group of James N. Culver (University of Maryland), and was purified as described in Gooding et al. (1967)[101], concentrated and resuspended in water with a high concentration about 26mg/ml. The highly concentrated TMV sample was then diluted with aqueous 2mmol/L ammonium acetate at pH7 to about 50μg/ml for elecrospraying study.

The as-prepared TMV samples were sprayed in an electrospray aerosol generator (model 3480, TSI Inc.) mounted with a 40μm inner diameter capillary and operated with a carrier gas of 1.2 lpm of purified air. The aerosolized sample droplets were then passed over a radioactive Po-210(α) source to reduces the charge on the droplets to a well-defined charge distribution with most neutral and singly charged particles. The neutralized dry particles entered a differential mobility analyzer (model 3081 Long DMA column, TSI Inc.) and a homemade differential mobility analyzer (which can reach up to 33000/cm electric field) for particle mobility measurement and were subsequently counted with an ultrafine CPC (model 3025A, TSI Inc.). The long DMA was set with sheath flow rates of 2, 3 and 20 lpm to guarantee the TMV detected at a very low electric field, ~146 volts/cm, to ~1.4k volts/cm. In this low electric field, ~146volts/cm, the TMV basically was randomly oriented. The homemade DMA was operated with sheath flow rates at 3, 10 and 20 lpm and the detection electric fields from 2.85k volts/cm to 17.3k volts/cm. The long DMA and homemade DMA were operated in a step-voltage-mode for precise measurement and calibrated with a standard reference material (polystyrene latex spherical particle) with known sizes of 100.7 nm. By scanning the center rod voltage of DMAs, different mobility particles can be exacted to build a mobility distribution for a given particle population. Unlike a mass spectrometer, which selects particles on the basis of the mass/charge ratio, the differential mobility analyzer (DMA) selects particles on the basis of their mobility. The mobility can be converted to an equivalent spherical diameter, called mobility diameter which was discussed in Section 7.2. More details on the measurement method can be found in the paper by Li el al.[8].

7.4.2. Pulser system and PDMA Evaluation

To produce a square wave pulsed field requires a function generator (gate signal source), a pulse generator, and a 10 kV DC power supply. The pulse generator converts the DC voltage input to a square wave based on the wave shape, frequency, and pulse width from the signal generator as shown in Figure 7-7. The critical component is the pulse generator, which is a more specialized device because of the high voltage needed, the need for a rapid rise time, adjustable pulse width, and a clean square wave. A key constraint for high voltage high frequency output, is that the output capacitance be less than about 200 pF. The performance of the pulse generator with the DMA attached was verified by monitoring the output of the pulse generator using an oscilloscope. The generated pulse had at most a 60 ns rise and fall time, and an adjustable pulse width from 200 ns to DC.

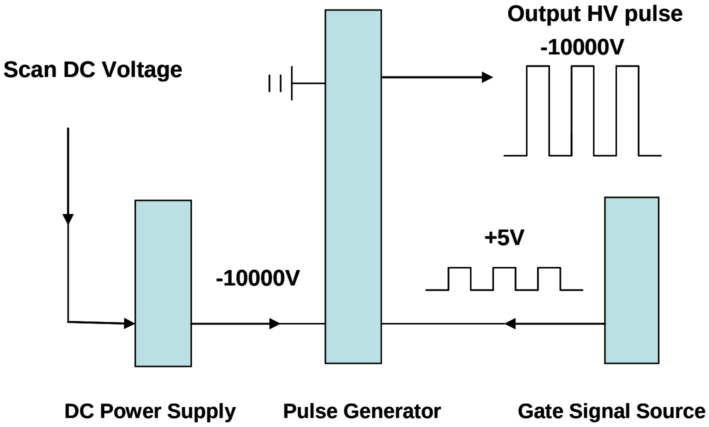

Figure 7-7. *Schematic of pulser system for generating square wave high voltage pulses.*

The PDMA was evaluated first with a solution by mixing two spherical singlet NIST traceable size PSL particles, 127.1nm (Thermo Scientific 3125A) and 202.4nm (Thermo Scientific 3200A) to test the mobility distribution of two spherical particles at various frequencies. Then I evaluated the PDMA with the singlet and doublet of 149.4nm PSL spheres (Thermo Scientific 3150A) to test the mobility of non-spherical particles, doublets, at various frequencies. The PSL particles were aerosolized using a constant output pressure atomizer(TSI Inc. Model 3076), and dried with two diffusion dryers before entering a neutralizer, which provides a Fuchs charge distribution to the particles. The neutralized particles then pass through the PDMA for particle mobility size measurement and counted with a CPC (TSI Inc. Model 3025A). The PDMA is a traditional long differential mobility analyzer column (TSI Inc. Model 3081) connected to high-voltage-pulses generated with a pulser system described in Fig.7-7.

Table 7-1. *The experimental conditions on which the system yields data for low electric field and high electric field.*

Low electric field	DC voltage ;Qsh =3 lpm (Qa =0.07 lpm)
High electric field	DC voltage ;Qsh =12 lpm (Qa =0.3 lpm)
	Pulsed voltage with duty cycle=1/4;Qsh =3 lpm (Qa =0.07 lpm);1Hz
	Pulsed voltage with duty cycle=1/4;Qsh =3 lpm (Qa =0.07 lpm);2Hz
	Pulsed voltage with duty cycle=1/4;Qsh =3 lpm (Qa =0.07 lpm);5Hz
	Pulsed voltage with duty cycle=1/4;Qsh =3 lpm (Qa =0.07 lpm);10Hz
	Pulsed voltage with duty cycle=1/4;Qsh =3 lpm (Qa =0.07 lpm);50Hz
	Pulsed voltage with duty cycle=1/4;Qsh =3 lpm (Qa =0.07 lpm);200Hz
	Pulsed voltage with duty cycle=1/4;Qsh =3 lpm (Qa =0.07 lpm);500Hz

The experimental conditions on which the system yields data for low electric field and high electric field are shown in Table 7-1. Particle mobility diameters were measured by step-scanning the magnitude of voltage of the power supply. Since the doublets (dimer) generated in the experiment are basically droplet induced [7, 15], sufficient number concentrations of PSL particles are needed to observe a clear doublet peak. For example, 40 drops added of 149.4 nm PSL spheres at a volume fraction of 1% were added in 80ml DI water for preparing 149.4nm PSL sample.

7.5. Results and Discussion

7.5.1. Evidence for the alignment effect of non-spherical particles in a constant electric field

In this section, I show the effect of electric field induced alignment for two kinds of non- spherical particles, doublets of spheres and nanorods.

- The effect of electric field induced alignment for PSL doublet

In Fig. 7-8, I present an example of three mobility size distributions of PSL singlet and doublet particles with 149.4nm primary spherical particle diameter at three different sheath flow rate (Qsh=4 lpm, 8 lpm, and 18 lpm) corresponding to three different magnitudes of electric field for each mobility size. The mobility size of singlet ~149.4nm is invariant, since they are spheres with no preferred orientation. On the other hand, the mobility size of doublet varying as the electric field changes shows clearly the effect of electric field induces alignment which results in smaller mobility (or high mobility). The experimental alignment effect of PSL doublets of 127.1nm, 149.4nm, 202.4nm, and 239.9nm shows excellent agreement with our theory[8].

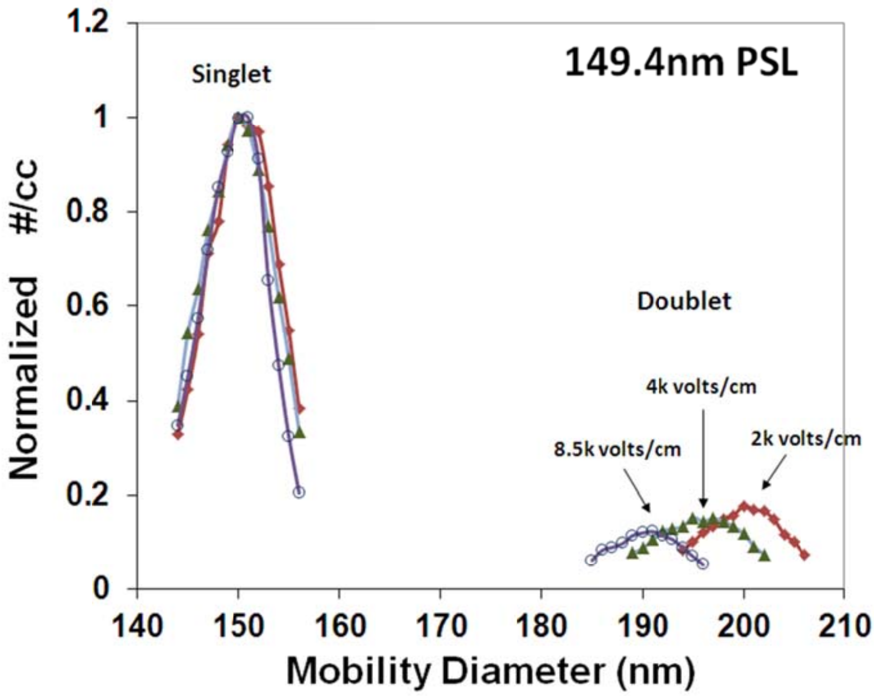

Figure 7-8. *Three mobility size distributions of PSL particles with 149.4 primary particle diameter measured at 4 lpm, 8 lpm and 18 lpm sheath flow rates in a step mode DMA. The mobility diameter of doublets decreases with increasing sheath flow rate, which corresponds to increase the magnitude of electric field, while the diameter of singlets does not change. This figure demonstrates clearly the alignment effect of the electric field for doubles of PSL particles.*

- The effect of electric field induced alignment for TMV nanorods

In Fig. 7-9, the mobility size of TMV nanorods (a straight rigid rod which has a length $L_r \approx 300$nm and diameter $d_r \approx 16$-18nm) [4] was measured at 2 lpm, 3 lpm and 20 lpm sheath flow rates in a step mode long-DMA, and at 3lpm, 10lpm and 20 lpm sheath flow rates in a step mode homemade high electric field DMA. The mobility diameter of TMV decreases from ~64nm to ~60nm with increasing magnitude of electric field from 2.5kV/cm to 17 kV/cm. This figure shows clearly the alignment effect of the electric field for TMV nanorod. However, our theory [16] expects more alignment in this case than experimental results assuming that TMV can be considered as a conducting particle. At this time, I have no explanation for this discrepancy.

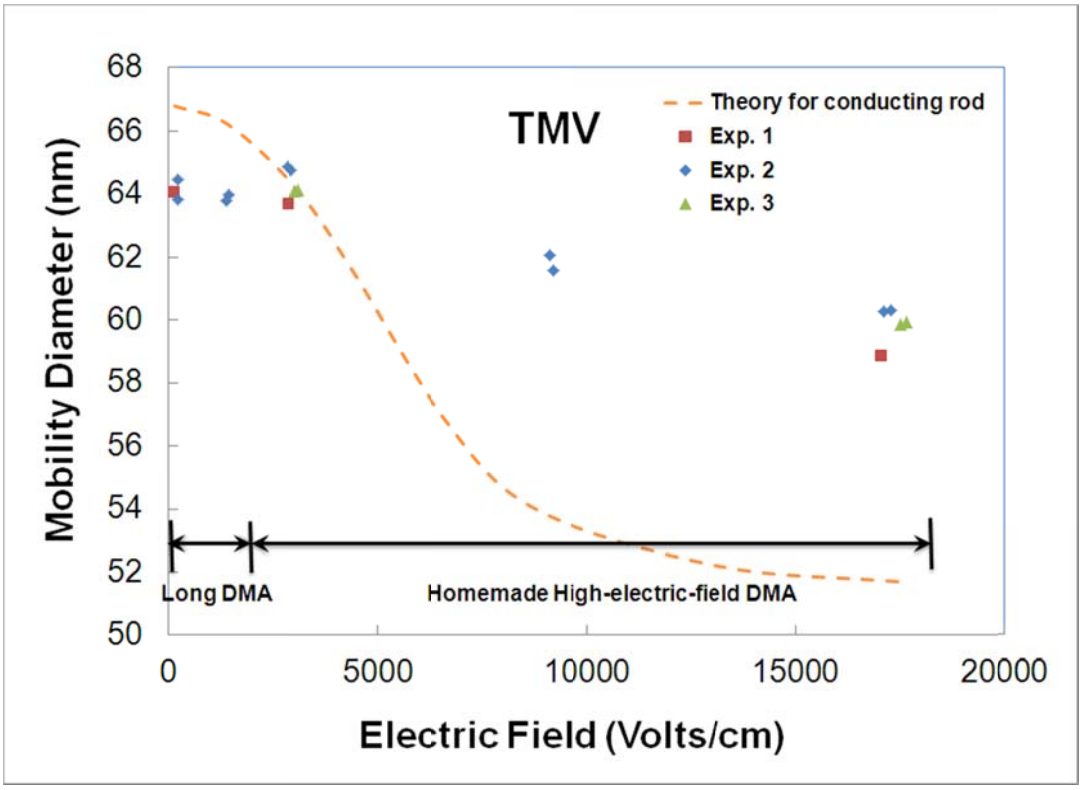

Figure 7-9. *The mobility size of TMV nanorod (*a straight rigid rod which has a length $L_r \approx 300$nm and diameter $d_r \approx 16$-18nm) [4]. *measured at 2 lpm, 3 lpm and 20 lpm sheath flow rates in a step mode long-DMA, and at 3lpm, 10lpm and 20 lpm sheath flow rates in a homemade high electric field DMA. The mobility diameter of TMV decreases with increasing*

the magnitude of electric field. This figure shows clearly the alignment effect of the electric field for TMV nanorod.

7.5.2. The alignment effect of non-spherical particles in a pulsed electric field

In this section, I present the effect of electric field induced alignment for doublets of PSL spheres in a pulsed DMA (PDMA).

7.5.2.1 Validation of PDMA using spherical particles

Before measuring the doublets of spheres, I validated the PDMA system by measuring spherical particles, and comparing the results from a traditional DMA. The PSL 127.1nm and 200nm spheres were mixed in one sample, and then measured at DC voltages using traditional long-DMA at sheath flow rates Q_{sh} =3 lpm and Q_{sh} =12 lpm. The same sample was also measured in a PDMA with flow rates Q_{sh} =3 lpm and duty-cycle=1/4 at 1Hz, 2Hz, 5Hz, 10Hz, 50Hz, 200Hz and 500Hz. I calibrated the sheath flows and duty cycles in all experiments by using the singlet peaks of 127.1 nm, i.e., obtaining the sheath flow rates and duty cycles by making the first singlet peaks showing exactly as 127.1nm. After the calibrations, the mobility sizes of the second singlet peaks (200nm PSL) were shown in Fig. 7-10. The mobility sizes of the 200nm PSL areconsistent among all experiments, particularly the results between a traditional DMA and the PDMA with the same flow rate. And there is no apparent frequency dependency among all measured frequencies.

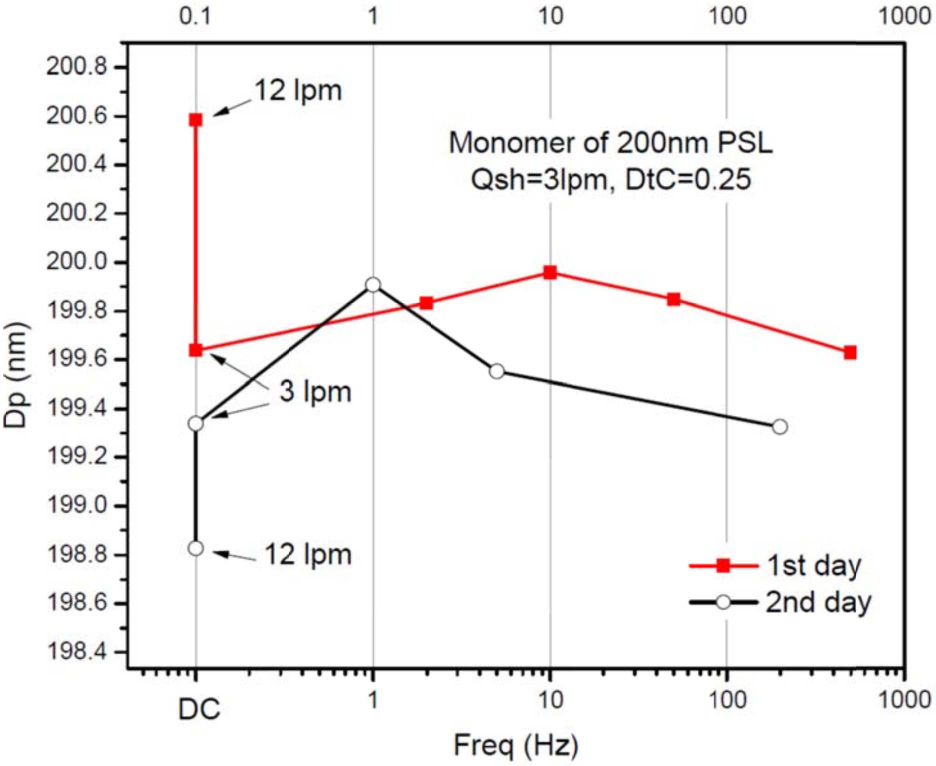

Figure 7-10. *The PSL 127.1nm and 200nm spheres were mixed in one sample, and then measured at DC voltages using a traditional long-DMA at sheath flow rates* Q_{sh} *=3 lpm and* Q_{sh} *=12 lpm. The same sample was also measured in a PDMA with flow rates* Q_{sh} *=3 lpm and duty-cycle=1/4 at 1Hz, 2Hz, 5Hz, 10Hz, 50Hz, 200Hz and 500Hz. The sheath flow rates and duty cycles were calibrated by making the first singlet peaks showing exactly as 127.1nm. The mobility sizes of the second singlet peaks (200nm PSL) are presented after calibrations.*

7.5.2.2. Measuring the mobility of doublets of spheres using PDMA

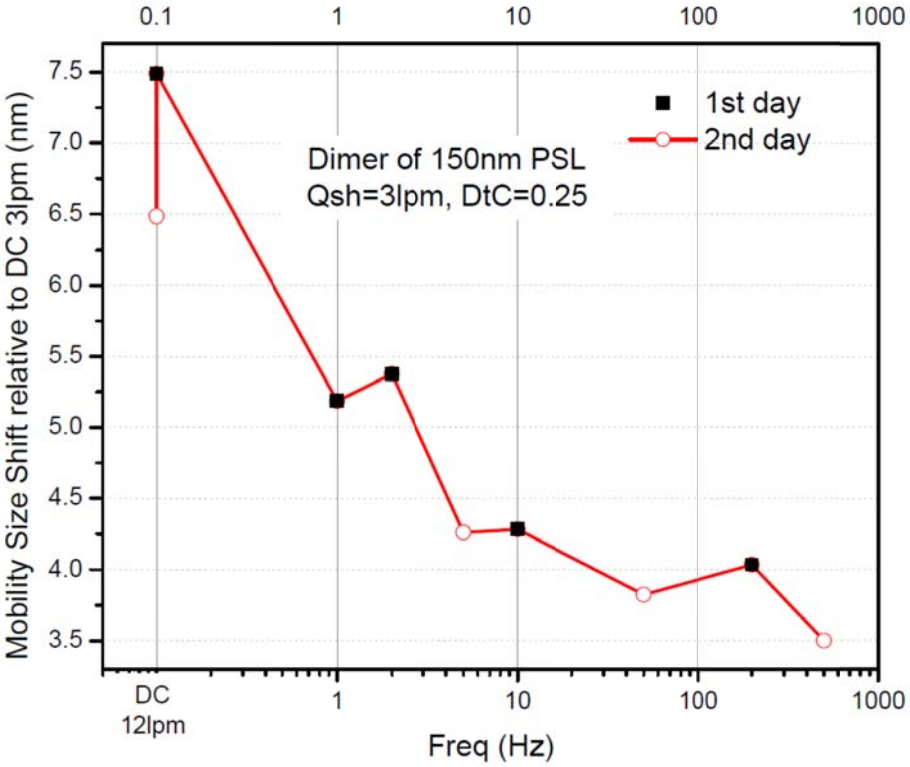

Figure 7-11. *Doublet mobility size shift of 149.4nm PSL particles with respect to the low DC voltage 3 lpm case as a function of pulse frequency, The zero frequency condition is the high DC voltage 12 lpm case. .*

Singlets and doublets of monodisperse polystyrene latex (PSL) spheres are used for validating the performance of the PDMA method for a non-sphere because they are well-defined and require only a single DMA. The mobility size of doublets of PSL 149.4 nm primary spheres are measured under DC voltages at 3 lpm and 12 lpm DMA sheath flow respectively, and under pulsed voltages at 3 lpm DMA sheath flow with a pulse duty cycle of 25%, and frequencies of 1Hz, 2Hz, 5Hz, 10 Hz , 50Hz, 200Hz and 500Hz, respectively.

Run conditions at low electric field under DC at 3 lpm, and high electric fields under DC at 12 lpm, and under pulsed voltages at 3 lpm. For singlets (sphere), all mobility sizes (DC or pulsed) are essentially identical with a peak mobility size of ~150 nm. However, for the doublet (non-sphere), there are obvious differences between the mobility size at high and low DC-electric fields. Furthermore, the mobility shifts in the doublets seem to depend on the pulse frequency, when in fact the effective nominal field is the same of all conditions. Drawing the doublet mobility diameter at high electric field shift with respect to the low electric field (DC, 3 lpm), we can more clearly see the effect of frequency on the mobility size in Fig 7-11.

In Fig. 7-11, the zero frequency point is the DC voltage case at 12 lpm sheath flow, which shows the largest shift, of ~7nm, while the smallest shift is ~3.5nm, is seen at 500Hz. Working from low frequencies to high I see that increasing frequencies initially leads to a very rapid decrease in the peak shift to smaller values, but becomes progressively less sensitive to frequencies above about 50Hz. Basically there are two relaxation processes for the doublet shown in Fig 7-11. One is a quick relaxation, from the mobility diameter at low electric field (DC, 3 lpm) to the mobility diameter at 50-500 Hz, with characteristic relaxation time about 0.1-1ms. The second relaxation process is slow, from 50 Hz to 0 Hz (DC, 12 lpm) , with characteristic relaxation time about 0.5-1 s.

These results show two important results. One, is that the PDMA experiments shows that one can modify in a systematic way the mobility if non-spherical particles while keeping spherical particle motilities constant. However there is a second result that is perhaps more subtle. In the cases presented in Fig 7-11, it is clear there is a significant effect of pulse frequency on mobility size. However, the theory I have described does not account for this effect.

There are at least two possibilities which may contribute to this frequency dependence, and which presumably involve a characteristic relaxation time of some physical process. They are Brownian rotation of nonspherical particles and the time for polarization of particles. The Brownian rotation time is described by [69],

$$t_{rotate} = \frac{\overline{\theta^2}}{2kTB_\omega}, \tag{7-7}$$

where $\overline{\theta^2}$ is the mean square angle of rotation of a particle, T is the temperature, and B_ω is angular mobility of the particle. For a prolate ellipsoid having a minor semi-axis b and an axial ratio β, the angular mobility about the minor axis is given by[69],

$$B_\omega = \frac{3[\frac{2\beta^2-1}{\sqrt{\beta^2-1}}\ln(\beta+\sqrt{\beta^2-1})-\beta]}{16\pi\eta b^3(\beta^4-1)} \tag{7-8}$$

For a doublet with 150 nm primary particle diameter, using b=(150/2) nm, β=2 and $\overline{\theta^2}=(2\pi)^2$, based on Eqn.(16) , the rotation time is about 3ms. Since the characteristic time given in Eqn.(7.7) is the value without electric field, the characteristic time in an electric field is expected to be even shorter and considerably faster than the pulse frequency employed in the experiment. . I also consider the time for a particle to polarize. This is not easy to do rigorously, but to obtain a rough estimate I evaluate the relaxation time constant of polarization, for the transient response of an ohmic dielectric sphere to a suddenly applied DC electric field using the Maxwell-Wagner charge relaxation mechanism[106],

$$\tau_{MW} = \frac{\varepsilon + 2\varepsilon_0}{\sigma + 2\sigma_0} \quad , \tag{7-9}$$

where ε and σ are the dielectric constant and conductivity of particles, ε_0 and σ_0 the dielectric constant and conductivity of air in DMA. For SWNT-semiconductors, the value is ~10^{-14} s, which is considerably faster than the pulse frequency employed in the experiment.

In general, even for nonconductive PSL particles with low aspect ratio ~2, by operating at low frequencies, for instance, 0.75Hz or 1Hz, our pulsed DMA is proved to be an effective method to classify spherical and nonspherical particles. I expect that the pulsed DMA can also work at high frequencies for conductive particles. The fast relaxation process is probably from the rotation movement of non-spherical particles, but the slower relaxation process is unexplained at this time.

7.6. Conclusion

In this work, I use the theory in Li et al. [8, 16] for an orientation-averaged electrical mobility for a prolate ellipsoid. To obtain shape information by measuring the electrical mobility under different electric fields, I also propose a pulsed differential mobility analyzer, which allows one to change the electric field acting on the non-spherical particle by only changing the pulse duty cycle.. Our new instrument operating at low frequencies proved to be an effective method for particle sizing and particle shape information measurement using PSL singlets and doublets with precisely known size and shape. I also show a slower than expected relaxation process of electrical mobility size of PSL doublets at different pulse frequencies in our experiment. In our future study, I will use a rigid rod and conductive particles to further test our pulsed DMA and try to understand more the fundamental physical meaning of this electrical mobility relaxation processes of PSL doublets shown in this work.

Chapter 8: Conclusion and Future Work

8.1. Conclusion

Nanotechnology is a key technology for the future which creates many new materials and devices with dimensions on the nanoscale with a vast range of applications, such as in medicine, electronics, biomaterials and energy production. Knowledge on the characteristic behaviors of nanostructure materials is essential for understanding their capabilities and identifying their potential utilizations. The objective of this work is to understand the fundamental physics of properties of nanomaterials and develop novel diagnostic tools and methods to characterize this class of materials quantitatively.

The theme of this dissertation can be considered as two parts.

First, a statistical model, called 'droplet-induced-aggregation' model is developed in chapter 2, to determine the extent to which the ES process induces the formation of nonspecific dimers and higher order aggregates. Electrospray (ES) sources are commonly used to introduce non-volatile materials (e.g. nanoparticles, proteins, etc.) to the gas phase for characterization by mass spectrometry or ion mobility. However, the electrospray itself can induce aggregation and thus corrupts the results of nanoparticle aggregation characterization. This 'droplet-induced-aggregation' model is a statistic approach to determine and correct this undesired artifact. The model is validated through ES- differential mobility experiments using gold nanoparticles and protein particles. Furthermore, in chapter 3, I used this 'droplet-induced-aggregation' model described above and developed a simple, fast, and accurate method to measure the absolute number concentration of nanoparticles in solution. A key feature of this method is that it allows determination of the absolute number concentration of particles by knowing only the droplet size generated from a particular ES-source, thereby eliminating the need for sample specific calibration standards or detailed analysis of transport losses. This approach was validated by comparing the total number concentration of monodispersed Au nanoparticles determined by ES-DMA with UV-Vis measurements and by comparing the absolute number concentration of Rituxan monoclonal antibody (Rmab) in solution determined by this method with pre-known concentration of Rmab. This methodology is applicable for quantification of any electrospray process coupled to an analytical tool that can distinguish monomers from higher order oligomers.

Second, I systematically studied the mobility property of non-spherical particles. In Chapter 4, a general theory to quantify the effect of orientation on the mobility and dynamic shape factor of charged axially symmetric particles in an electric field is developed. The mobility of a nonspherical particle is a function of both particle shape and orientation. Thus unlike spherical particles the mobility, through its orientation, depends on the magnitude of the electric field. In this chapter, I develop a general theory with tensor formulation for computing the orientation average mobility by using a Boltzmann probability distribution for the orientation. The resulting equation for the average electrical mobility is simple and can be applied to any axially symmetric structures such as rods, ellipsoids and touching spheres. In this chapter, I also examine the expression of dynamic shape factor common in the literature, and propose a clearer definition based on the tensor approach.[16] In chapter 5, the theory above in chapter 4 is applied to the doublets of spheres and compared with the experimental results of well-defined doublets of NIST traceable size standard PSL particles. The experimental results of doublets of 127nm, 150nm, 200nm and 240nm PSL spheres are shown to be in excellent agreement with the expected values based on our theory. Chapter 6 provides a systematic study of the mobility of a non-spherical particle. A new approach to obtain the mobility of non-spherical particles is proposed by averaging the drag force orientationally, and two other approaches in literature, averaged-cross-section and averaged-drift-velocity, are summarized and extended. Finally in chapter 7, I use the theory in chapter 4 for a prolate ellipsoid, which has the possibility to be a model system for any arbitrary shaped particle or aggregate that might be described with a major and minor axis. To obtain the shape information by measuring the electrical mobility under different electric fields, I also propose a new instrument, a pulsed differential mobility analyzer (PDMA). This new instrument enables one to change the peak E-field experienced by the particle, while still maintaining the same time averaged field. In so doing method enables one to systematically change the average orientation of a non-spherical particle and thus its mobility. The instrument is tested on PSL singlets and doublets with precisely known size and shape, and the result shows that the PDMA would be a potential method for particle sizing and particle shape information measurements. I also report an unexplained phenomenon which is an unknown relaxation process for non-spherical particles in PDMA measurements.

8.2. Future Work

The future extension of this work is listed below.

8.2.1. On the Potential of using Bio-Nanoparticles as Standard Reference Materials for Mobility Calibration

Nanotoxicology studies, nanobiotechnology research and aerosol technology studies require accurate physical and chemical characterizations of the nanoparticles. Standard reference materials with accurate and precise size characterization play a key role for attaining comparability of results among laboratories. Commonly used reference materials are PSL nanoparticles and gold nanospheres. However, I have found that some stable bio-nanoparticles such as some viruses, are more monodisperse, and highly concentrated than some current standard reference particles. Because bio-nanoparticles undergo highly precise replication they have the potential to be a source of highly monodisperse and concentrated standard reference materials.

The commonly used reference materials, Au10nm, Au 20nm, Au 30nm, Au 60, PSL 20nm, PSL 30nm,PSL 60nm, and PSL 100nm, which are non-bio particles, and examples of bio colloidal nano-particles, proteins (Tnf, BSA, IgG, IgM) and virus particles (PP7,PR772, TMV) were electrosprayed (ES; TSI 3480), sized by a nano-DMA (TSI 3485), and counted with an ultrafine CPC (TSI 3025A). The measured size distributions for commonly used references are presented in Fig. 8-1, and for bio particles presented in Fig.8-2. (Part of data shown in Fig. 8-1 and 8-2 are from Dr. Guha)

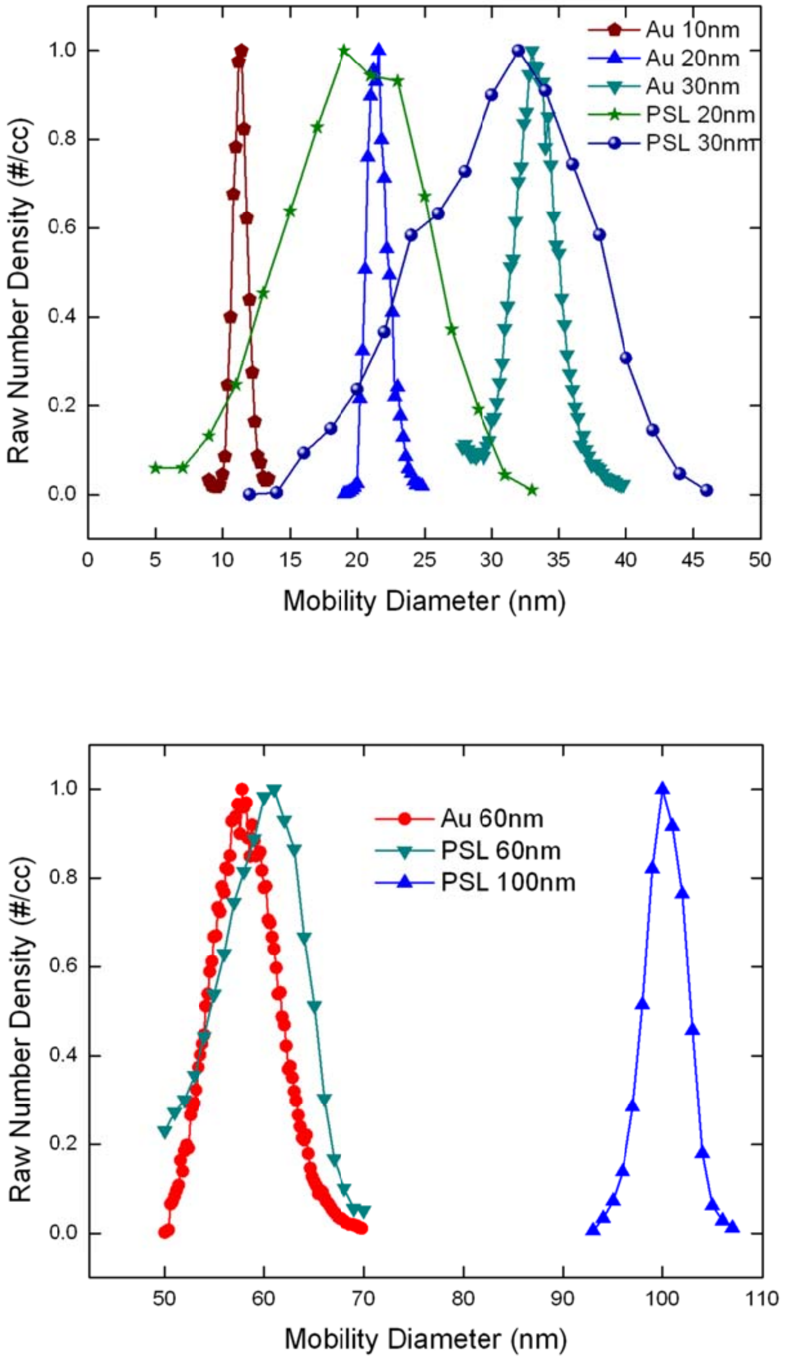

Figure 8-1. The *Size distributions of commonly used reference materials, Au10nm, Au 20nm, Au 30nm, Au 60, PSL 20nm, PSL 30nm,PSL 60nm, and PSL 100nm, which are non-bio particles.*

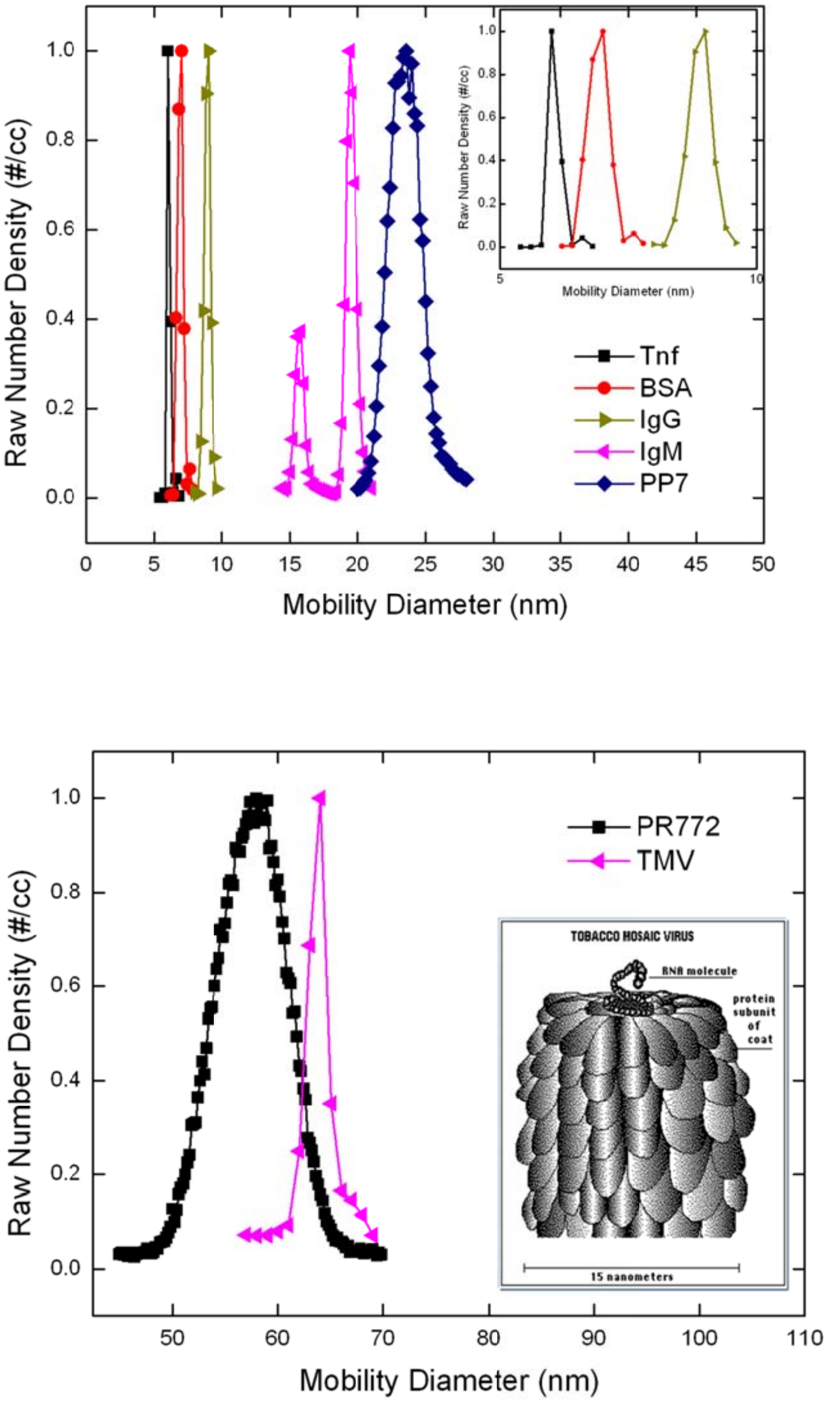

Figure 8-2. *The Size distributions of examples of bio particles which have potential as reference materials.*

Table 8-1. *Full Width at Half Maximum normalized by Mean of the size distributions of Au, PSL and Bio colloidal nano-particles in Fig. 8-1 and 8-2.*

	FWHM/Mean			**FWHM/Mean**
Tnf	0.021		Au 10nm	0.110
BSA	0.070		Au 20nm	0.082
IgG	0.057		Au 30nm	0.107
IgM	0.042		Au 60nm	0.134
IgM	0.048		PSL 20nm	0.620
PP7	0.117		PSL 30nm	0.494
PR772	0.142		PSL 60nm	0.167
TMV	0.030		PSL 100nm	0.048

Full Width at Half Maximum normalized by Mean of the size distributions of Au, PSL and Bio colloidal nano-particles in Fig. 8-1 and 8-2 are shown in Table 8-1. Based on Table 8-1, bio particles in many cases are more monodisperse than the standard PSL spheres and Au spheres typically used for calibration. As an example, TMV ~64nm (Fig. 8-2) shows a size distribution which is considerably narrower that the corresponding 60 nm PSL or Au reference particles (Fig.8-1). Those bio particles have the potential to be a source of highly monodisperse and concentrated standard reference materials.

8.2.2. Droplet Size Measurements

In the study of ‘droplet-induced-aggregation’ in electrospray process in chapter 2 and 3, in order to employ our method for quantification, a key measurement is to determine the droplet size distribution generated by the ES source The droplet size distribution was determined by electrospraying a known concentration (V/V) of sucrose solution, and measuring the resultant dry particle size distribution. Using this procedure, the original droplet size distribution can be evaluated by [41, 50]

$$D_d = \frac{1}{C_s^{1/3}} D_s \tag{2-29}$$

where D_d is the droplet diameter, D_s is the sucrose particle diameter after drying (measured by DMA), and C_s is the known sucrose concentration (V/V) in the ES solution.

In equation (2-29) above, the droplet size in ES process is determined by a 1/3 power of known sucrose solution $C_{s,}$ i.e., the droplet is $1/\ C_s^{\ 1/3}$ times larger than the residue sucrose particle. However, it is found that if one uses other solutes instead of sucrose in ES process, for example, sodium chloride, the power law is not 1/3, but close to 1/5. And for most other aerosol generators, such as a pressure atomizer, the power law is always close to 1/5 for whatever solute. This phenomenon is interesting and important, and would be part of my future work, since the knowledge of droplet-size-power-law for an aerosol generator is critical for one to apply ‘droplet-induced-aggregation’ model to determine and correct this undesired artifact during the aerosolizing process, furthermore, to calculate back to obtain the absolute number concentration of analyte colloidal nanoparticles in solution.

8.2.3. Pursuing a general theory to quantify the mobility of non-spherical particles

The mobility of a nonspherical particle is a function of both particle shape and orientation. Thus unlike spherical particles the mobility, through its orientation, depends on the magnitude of the electric field. In chapter 4, a theory to quantify the effect of orientation on the mobility and dynamic shape factor of charged axially symmetric particles in an electric field was developed based on an extension of the work of Happel and Brenner[17]. In chapter 6, this theory has been further extended for particles with arbitrary shape. Using well-defined doublets of NIST traceable size standards PSL spheres of 127nm, 150nm, 200nm, and 240nm, the experimental results show in excellent agreement with our theory. However, one exception to this good agreement is for doubles of 100nm primary PSL spheres (103.6nm and 100.7nm). The calculated theoretical values are off our measured results in Figure 6-4. It is as if there is some unaccounted for effect causing a more random orientation of the doublet. One possible reason is the 100nm PSL cannot be considered as fully conducting material but with a limited relative permittivity, ε_r. Another possible reason would be some unknown effects existing which cause the orientation of doublets tending to random in DMA column. Those effects start becoming apparent compared to the polarization energy for the doublets of 100nm PSL particles in high electric fields (or in high flow rates). The most possible reason is that for sufficient small particles in air, the Happel and Brenner's approach and our extended approach are not appropriate anymore. To understand this discrepancy and develop a more general model of mobility of non-spherical particles which can apply to all size range will be part of my future work.

Bibliography

1. Nettleton, E. J.; Paula Tito, M. S.; Bouchard, M.; Dobson, C. M.; Robinson, C. V., Characterization of the Oligomeric States of Insulin in Self-Assembly and Amyloid Fibril Formation by Mass Spectrometry. *Biophys. J.* **2000,** *79*, 1053 - 1065.

2. Dahneke, B., Viscous Resistance of Straight-Chain Aggregates of Uniform Spheres. *Aerosol Science and Technology* **1982,** *1*, (2), 179-185.

3. Cheng, Y. S.; Allen, M. D.; Gallegos, D. P.; Yeh, H. C.; Peterson, K., Drag Force and Slip Correction of Aggregate Aerosols. *Aerosol Science and Technology* **1988,** *8*, (3), 199-214.

4. Ortega, A.; de la Torre, J. G., Hydrodynamic properties of rodlike and disklike particles in dilute solution. *Journal of Chemical Physics* **2003,** *119*, (18), 9914-9919.

5. Baron, P. A.; Willeke, K., *Aerosol measurement : principles, techniques, and applications*. 2nd ed.; Wiley: New York, 2001; p xxiii, 1131 p.

6. Hinds, W. C., *Aerosol technology : properties, behavior, and measurement of airborne particles*. 2nd ed.; Wiley: New York ; Chichester, 1999; p xx, 483 p.

7. Li, M.; Guha, S.; Zangmeister, R.; Tarlov, M. J.; Zachariah, M. R., Quantification and Compensation of Nonspecific Analyte Aggregation in Electrospray Sampling. *Aerosol Science and Technology* **2011,** *45*, (7), 849-860.

8. Li, M.; Mulholland, G. W.; Zachariah, M. R., Mobility and Dynamic Shape Factor of Particle Doublets in Electric Fields. **2012**.

9. Allen, M. D.; Raabe, O. G., Slip Correction Measurements of Spherical Solid Aerosol-Particles in an Improved Millikan Apparatus. *Aerosol Science and Technology* **1985,** *4*, (3), 269-286.

10. Wiedensohler, A., An Approximation of the Bipolar Charge-Distribution for Particles in the Sub-Micron Size Range. *Journal of Aerosol Science* **1988,** *19*, (3), 387-389.

11. Guha, S.; Li, M.; Tarlov, M. J.; Zechariah, M. R., Electrospray-differential mobility analysis of bionanoparticles. *Trends in Biotechnology* **2012,** *30*, (5), 291-300.

12. Guha, S.; Wayment, J. R.; Li, M. D.; Tarlov, M. J.; Zachariah, M. R., Characterizing the Adsorption of Proteins on Glass Capillary Surfaces Using Electrospray-Differential Mobility Analysis. *Langmuir* **2011,** *27*, (21), 13008-13014.

13. Guha, S.; Wayment, J. R.; Li, M.; Tarlov, M. J.; Zachariah, M. R., Protein adsorption-desorption on electrospray capillary walls - No influence on aggregate distribution. *Journal of Colloid and Interface Science* **2012,** *377*, 476-484.

14. Flagan, R. C., History of electrical aerosol measurements. *Aerosol Science and Technology* **1998,** *28*, (4), 301-380.

15. Li, M.; Guha, S.; Zangmeister, R.; Tarlov, M. J.; Zachariah, M. R., Method for determining the absolute number concentration of nanoparticles from electrospray sources. *Langmuir* **2011,** *27*, (24), 14732–14739.

16. Li, M.; Mulholland, G. W.; Zachariah, M. R., The Effect of Orientation on the Mobility and Dynamic Shape Factor of Charged Axially Symmetric Particles in an Electric Field. *Aerosol Science and Technology* **2012,** *46*, (9), 1035 -1044.

17. Happel, J.; Brenner, H., *Low Reynolds number hydrodynamics, with special applications to particulate media*. Prentice-Hall: Englewood Cliffs, N.J.,, 1965; p xiii, 553 p.

18. Kim, S. H.; Mulholland, G. W.; Zachariah, M. R., Understanding ion-mobility and transport properties of aerosol nanowires. *Journal of Aerosol Science* **2007,** *38*, (8), 823-842.

19. Li, M.; Mulholland, G. W.; Zachariah, M. R., Understanding the Mobility of a Non-spherical Particle. **2012**.

20. Li, Z.; Wang, H., Drag force, diffusion coefficient, and electric mobility of small particles. I. Theory applicable to the free-molecule regime. *Physical Review E* **2003,** *68*, (6).

21. Li, M.; You, R.; Mulholland, G. W.; Zachariah, M. R., Development of a Pulsed-Voltage Differential Mobility Analyzer: A Method for Measuring Shape Parameters for Non-Sperical Particles. **2012**.

22. Kaufman, S. L.; Skogen, J. W.; Dorman, F. D.; Zarrin, F., Macromolecule Analysis Based on Electrophoretic Mobility in Air: Globular Proteins. *Anal. Chem.* **1996,** *68*, (11), 1895 - 1904.

23. Bacher, G.; Szymanski, W. W.; Kaufman, S. L.; Zo¨llner, P.; Blaas, D.; Allmaier, G. n., Charge-reduced nano electrospray ionization combined with differential mobility analysis of peptides, proteins, glycoproteins, noncovalent protein complexes and viruses. *J. Mass Spectrom.* **2001,** *36*, 1038 - 1052.

24. Kim, S. H.; Zachariah, M. R., In-flight size classification of carbon nanotubes by gas phase electrophoresis. *Nanotechnology* **2005,** *16*, 2149 - 2152.

25. Kim, S. H.; Zachariah, M. R., In-Flight Kinetic Measurements of the Aerosol Growth of Carbon Nanotubes by Electrical Mobility Classification. *J. Phys. Chem. B* **2006,** *110*, 4555 - 4562.

26. Pease III, L. F.; Elliott, J. T.; Tsai, D.-H.; Zachariah, M. R.; Tarlov, M. J., Determination of Protein Aggregation With Differential Mobility Analysis: Application to IgG Antibody. *Biotechnology and Bioengineering* **2008,** *101*, (6), 1214 - 1222.

27. Light-Wahl, K. J.; Winger, B. E.; Smith, R. D., Observation of the Multimeric Forms of Concanavalin A by Electrospray Ionization Mass Spectrometry. *J. Am. Chem. Soc.* **1993,** *115*, 5869 - 5870.

28. Light-Wahl, K. J.; Schwartz, B. L.; Smith, R. D., Observation of the Noncovalent Quaternary Associations of Proteins by Electrospray Ionization Mass Spectrometry. *J. Am. Chem. Soc.* **1994,** *116*, 5271 - 5278.

29. Ayed, A.; Krutchinsky, A. N.; Ens, W.; Standing, K. G.; Duckworth, H. W., Quantitative Evaluation of Protein–Protein and Ligand–Protein Equilibria of a Large Allosteric Enzyme by Electrospray Ionization Time-of-flight Mass Spectrometry. *Rapid Commun. Mass Spectrom.* **1998,** *12*, 339 - 344.

30. Lane, L. A.; Ruotolo, B. T.; Robinson, C. V.; Favrin, G.; Benesch, J. L. P., A Monte Carlo approach for assessing the specificity of protein oligomers observed in nano-electrospray mass spectra. *International Journal of Mass Spectrometry* **2009,** *283*, 169-177.

31. Kebarle, P.; Tang, L., From ions in solution to ions in the gas phase : The mechanism of Electrospray Mass Spectrometry. *Anal. Chem.* **1993,** *65*, (22), 972 - 986.

32. Gaskell, S. J., Electrospray : Principles and Practice. *J. Mass Spectrom.* **1997,** *32*, 677 - 688.

33. Dole, M.; Mack, L. L.; Hines, R. L., Molecular Beams of Macroions. *J. Chem. Phys.* **1968,** *49*, 2240–2249.

34. Iribarne, J. V.; Thomson, B. A., On the evaporation of small ions from charged droplets. *J. Chem. Phys.* **1976,** *64*, (6), 2287–2294.

35. Kebarle, P., A brief overview of the present status of the mechanisms involved in electrospray mass spectrometry. *J. Mass Spectrom.* **2000,** *35*, 804–817.

36. Fernandez de la Mora, J., Electrospray ionization of large multiply charged species proceeds via Dole's charged residue mechanism. *Analytica Chimica Acta* **2000,** *406*, (1), 93-104.

37. Gamero-Castano, M.; Fernandez de la Mora, J., Kinetics of small ion evaporation from the charge and mass distribution of multiply charged clusters in electrosprays. *Journal of Mass Spectrometry* **2000,** *35*, (7), 790-803.

38. Gamero-Castano, M.; Fernandez de la Mora, J., Mechanisms of electrospray ionization of singly and multiply charged salt clusters. *Analytica Chimica Acta* **2000,** *406*, (1), 67-91.

39. Ku, B. K.; Fernandez de la Mora, J., Cluster ion formation in electrosprays of acetonitrile seeded with ionic liquids. *Journal of Physical Chemistry B* **2004,** *108*, (39), 14915-14923.

40. Hogan, C. J.; Carroll, J. A.; Rohrs, H. W.; Biswas, P.; Gross, M. L., Combined Charged Residue-Field Emission Model of Macromolecular Electrospray Ionization. *Analytical Chemistry* **2009,** *81*, (1), 369-377.

41. Chen, D.-R.; Pui, D. Y. H.; Kaufman, S. L., Electrospraying of conducting liquids for monodisperse aerosol generation in the 4 nm to 1.8 micronm diamter range. *J. Aerosol Sci.* **1995,** *6*, 963 - 977.

42. Lenggoro, I. W.; Xia, B.; Okuyama, K., Sizing of Colloidal Nanoparticles by Electrospray and Differential Mobility Analyzer Methods. *Langmuir* **2002,** *18*, 4584 - 4591.

43. Pease, L. F.; Elliott, J. T.; Tsai, D.-H.; Zachariah, M. R.; Tarlov, M. J., Determination of Protein Aggregation With Differential Mobility Analysis: Application to IgG Antibody. *Biotechnol. Bioeng.* **2008,** *101*, (6), 1214 - 1222.

44. Lewis, K. C.; Dohmeier, D. M.; Jorgenson, J. W., Electrospray-Condensation Particle Counter: A Molecule-Counting LC Detector for Macromolecules. *Anal. Chem.* **1994,** *66*, 2285 - 2292.

45. Hogan, C. J.; Biswas, P., Monte Carlo simulation of macromolecular ionization by nanoelectrospray. *Journal of the American Society for Mass Spectrometry* **2008,** *19*, (8), 1098-1107.

46. Hogan, C. J.; Biswas, P., Porous Film Deposition by Electrohydrodynamic Atomization of Nanoparticle Sols. *Aerosol Science and Technology* **2008,** *42*, 75-85.

47. Edd, J. F.; Carlo, D. D.; Humphry, K. J.; K¨oster, S.; Irimia, D.; Weitzb, D. A.; Toner, M., Controlled encapsulation of single-cells into monodisperse picolitre drops. *Lab on a Chip* **2008,** *8*, 1262-1264.

48. Abate, A. R.; Chen, C. H.; Agresti, J. J.; Weitz, D. A., Beating Poisson encapsulaion statistics using close-packing ordering. *Lab on a Chip* **2009,** *9*, (18), 2628-2631.

49. Tsai, D.-H.; Zangmeister, R. A.; III, L. F. P.; Tarlov, M. J.; Zachariah, M. R., Gas-Phase Ion-Mobility Characterization of SAM-Functionalized Au Nanoparticles. *Langmuir* **2008,** *24*, 8483 - 8490.

50. TSI Model 3480 Electrospray Aerosol Generator Menu In TSI inc.

51. Ebel, C., Analytical ultracentrifugation for the study of biological macromolecules. *Prog. Colloid Polym. Sci.* **2004,** *127*, 73–82.

52. Howlett, G. J.; Minton, A. P.; Rivas, G., Analytical ultracentrifugation for the study of protein association and assembly. *Curr. Opin. Chem. Biol.* **2006,** *10*, 430-436

53. Kaufman, S. L., Electrospray diagnostics performed by using sucrose and proteins in the gas-phase electrophoretic mobility molecular analyzer (GEMMA). *Anal. Chim. Acta* **2000,** *406*, (1), 3–10.

54. Daniel, M. C.; Astruc, D., Gold Nanoparticles: Assembly, Supramolecular Chemistry, Quantum-Size-Related Properties, and Applications toward Biology, Catalysis,and Nanotechnology. *Chem. Rev.* **2004,** *104*, 293 - 346.

55. Haiss, W.; Thanh, N. T. K.; Aveard, J.; Fernig, D. G., Determination of Size and Concentration of Gold Nanoparticles from UV-Vis Spectra. *Anal. Chem.* **2007,** *79*, 4215-4221.

56. Mulvaney, P., Surface Plasmon Spectroscopy of Nanosized Metal Particles. *Langmuir* **1996,** *12*, 788 - 800.

57. Khlebtsov, N. G.; Bogatyrev, V. A.; Dykman, L. A.; Melnikov, A. G., special exinction of colloidal gold and its biospecific conjugates. *J. Colloid Interface Sci.* **1996,** *180*, 436 - 445.

58. Yang, Y.; Matsubara, S.; Nogami, M.; Shi, J., Controlling the aggregation behavior of gold nanoparticles. *Materials Science and Engineering: B* **2007,** *140*, 172-176

59. Khlebtsov, N. G., Determination of Size and Concentration of Gold Nanoparticles from Extinction Spectra. *Anal. Chem.* **2008,** *80*, 6620 - 6625.

60. LOO, R. R. O.; N. DALES; ANDREWS, P. C., Surfactant effects on protein structure examined by electrospray ionization mass spectrometry. *Protein Science* **1994,** *3*, 1975-1983.

61. Cech, N. B.; Enke, C. G., PRACTICAL IMPLICATIONS OF SOME RECENT STUDIES IN ELECTROSPRAY IONIZATION FUNDAMENTALS. *Mass Spectrometry Reviews* **2001,** *20*, 362– 387.

62. Kousaka, Y.; Endo, Y.; Ichitsubo, H.; Alonso, M., Orientation-specific dynamic shape factors for doublets and triplets of spheres in the transition regime. *Aerosol Science and Technology* **1996,** *24*, (1), 36-44.

63. Zelenyuk, A.; Imre, D., On the effect of particle alignment in the DMA. *Aerosol Science and Technology* **2007,** *41*, (2), 112-124.

64. Shin, W. G.; Mulholland, G. W.; Pui, D. Y. H., Determination of volume, scaling exponents, and particle alignment of nanoparticle agglomerates using tandem differential mobility analyzers. *Journal of Aerosol Science* **2010,** *41*, (7), 665-681.

65. Moisala, A.; Nasibulin, A. G.; Shandakov, S. D.; Jiang, H.; Kauppinen, E. I., On-line detection of single-walled carbon nanotube formation during aerosol synthesis methods. *Carbon* **2005,** *43*, (10), 2066-2074.

66. Song, D. K.; Lenggoro, I. W.; Hayashi, Y.; Okuyama, K.; Kim, S. S., Changes in the shape and mobility of colloidal gold nanorods with electrospray and differential mobility analyzer methods. *Langmuir* **2005,** *21*, (23), 10375-10382.

67. Goldstein, H.; Poole, C. P.; Safko, J. L., *Classical mechanics*. 3rd ed.; Addison Wesley: San Francisco, 2002; p xviii, 638 p.

68. Dahneke, B. E., Slip correction factors for nonspherical bodies—II free molecule flow. *Journal of Aerosol Science* **1973,** *4*, (2), 147-161

69. Fuchs, N. A., *The mechanics of aerosols*. Rev. and enl. ed.; Pergamon Press; distributed in the Western Hemisphere by Macmillan: Oxford, New York,, 1964; p xiv, 408 p.

70. Fredericq, E.; Houssier, C., *Electric dichroism and electric birefringence*. Clarendon Press: Oxford,, 1973; p xi, 219 p.

71. Böttcher, C. J. F.; Belle, O. C. v., *Dielectrics in static fields*. 2d ed.; Elsevier Scientific Pub. Co.: Amsterdam, New York,, 1973; p xx, 376 p.

72. Dahneke, B. E., Slip correction factors for nonspherical bodies—III the form of the general law. *Journal of Aerosol Science* **1973,** *4*, (2), 163-170

73. Cheng, Y. S., Drag Forces on Nonspherical Aerosol-Particles. *Chemical Engineering Communications* **1991,** *108*, 201-223.

74. Dahneke, B. E., Slip correction factors for nonspherical bodies—I Introduction and continuum flow. *Journal of Aerosol Science* **1973,** *4*, (2), 139-145

75. Batchelor, G. K., Slender-Body Theory for Particles of Arbitrary Cross-Section in Stokes Flow. *Journal of Fluid Mechanics* **1970,** *44*, (Nov26), 419-440.

76. Sihvola, A. H.; Institution of Electrical Engineers., *Electromagnetic mixing formulas and applications*. Institution of Electrical Engineers: London, 1999; p xii, 284 p.

77. Sihvola, A., Dielectric polarization and particle shape effects. *Journal of Nanomaterials* **2007**.

78. Goldman, A. J.; Cox, R. G.; Brenner, H., Slow Motion of 2 Identical Arbitrarily Oriented Spheres through a Viscous Fluid. *Chemical Engineering Science* **1966,** *21*, (12), 1151-&.

79. Pitkonen, M., Polarizability of the dielectric double-sphere. *Journal of Mathematical Physics* **2006,** *47*, (10).

80. Pitkonen, M., http://anim.radio.aalto.fi/. In Polarizability-Applet-page.

81. von Helden, G.; Hsu, M. T.; Gotts, N.; Bowers, M. T., Carbon Cluster Cations with up to 84 Atoms: Structures, Formation Mechanism, and Reactivity. *J. Phys. Chem.* **1993,** *97*, (31), 8182 - 8192.

82. Shvartsburg, A. A.; Jarrold, M. F., An exact hard-spheres scattering model for the mobilities of polyatomic ions. *Chemical Physics Letters* **1996,** *261*, (1-2), 86-91.

83. Shvartsburg, A. A.; Mashkevich, S. V.; Baker, E. S.; Smith, R. D., Optimization of algorithms for ion mobility calculations. *Journal of Physical Chemistry A* **2007,** *111*, (10), 2002-2010.

84. Ruotolo, B. T.; Benesch, J. L. P.; Sandercock, A. M.; Hyung, S. J.; Robinson, C. V., Ion mobility-mass spectrometry analysis of large protein complexes. *Nature Protocols* **2008,** *3*, (7), 1139-1152.

85. Ferziger, J. H.; Kaper, H. G., *Mathematical theory of transport processes in gases*. North-Holland Publishing Co.: Amsterdam ; London, 1972.

86.Mason, E. A.; McDaniel, E. W., *Transport properties of Ions in gases*. Wiley: 1988.

87. Brocker, E. R.; Anderson, S. E.; Northrop, B. H.; Stang, P. J.; Bowers, M. T., Structures of Metallosupramolecular Coordination Assemblies Can Be Obtained by Ion Mobility Spectrometry-Mass Spectrometry. *Journal of the American Chemical Society* **2010,** *132*, (38), 13486-13494.

88. van Duijn, E.; Barendregt, A.; Synowsky, S.; Versluis, C.; Heck, A. J. R., Chaperonin Complexes Monitored by Ion Mobility Mass Spectrometry. *Journal of the American Chemical Society* **2009,** *131*, (4), 1452-1459.

89. Epstein, P. S., On the resistance experienced by spheres in their motion through gases. *Physical Review* **1924,** *23*, (6), 710-733.

90. Tammet, H., Size and Mobility of Nanometer Particles, Clusters and Ions. *Journal of Aerosol Science* **1995,** *26*, (3), 459-475.

91. Hogan, C. J.; de la Mora, J. F., Ion Mobility Measurements of Nondenatured 12-150 kDa Proteins and Protein Multimers by Tandem Differential Mobility Analysis-Mass Spectrometry (DMA-MS). *Journal of the American Society for Mass Spectrometry* **2011,** *22*, (1), 158-172.

92. Hogan, C. J.; Ruotolo, B. T.; Robinson, C. V.; de la Mora, J. F., Tandem Differential Mobility Analysis-Mass Spectrometry Reveals Partial Gas-Phase Collapse of the GroEL Complex. *Journal of Physical Chemistry B* **2011,** *115*, (13), 3614-3621.

93. Pease, L. F.; Tsai, D. H.; Hertz, J. L.; Zangmeister, R. A.; Zachariah, M. R.; Tarlov, M. J., Packing and Size Determination of Colloidal Nanoclusters. *Langmuir* **2010,** *26*, (13), 11384-11390.

94. Mackowski, D. W., Monte Carlo simulation of hydrodynamic drag and thermophoresis of fractal aggregates of spheres in the free-molecule flow regime. *Journal of Aerosol Science* **2006,** *37*, (3), 242-259.

95. DeCarlo, P. F.; Slowik, J. G.; Worsnop, D. R.; Davidovits, P.; Jimenez, J. L., Particle morphology and density characterization by combined mobility and aerodynamic diameter measurements. Part 1: Theory. *Aerosol Science and Technology* **2004,** *38*, (12), 1185-1205.

96. Mesleh, M. F.; Hunter, J. M.; Shvartsburg, A. A.; Schatz, G. C.; Jarrold, M. F., Structural information from ion mobility measurements: Effects of the long-range potential. *Journal of Physical Chemistry* **1996,** *100*, (40), 16082-16086.

97. Allen, M. D.; Raabe, O. G., Re-Evaluation of Millikan Oil Drop Data for the Motion of Small Particles in Air. *Journal of Aerosol Science* **1982,** *13*, (6), 537-547.

98. Kim, J. H.; Mulholland, G. W.; Kukuck, S. R.; Pui, D. Y. H., Slip correction measurements of certified PSL nanoparticles using a nanometer differential mobility analyzer (nano-DMA) for Knudsen number from 0.5 to 83. *Journal of Research of the National Institute of Standards and Technology* **2005,** *110*, (1), 31-54.

99. de la Mora, J. F., Free-molecule mobility of polyhedra and other convex hard-bodies. *Journal of Aerosol Science* **2002,** *33*, (3), 477-489.

100. Garcia-Ybarra, P.; Rosner, D. E., Thermophoretic Properties of Nonspherical Particles and Large Molecules. *Aiche Journal* **1989,** *35*, (1), 139-147.

101. Gooding, G. V.; Hebert, T. T., A Simple Technique for Purification of Tobacco Mosaic Virus in Large Quantities. *Phytopathology* **1967,** *57*, (11), 1285-&.

102. Eisner, A. D.; Gallily, I., On the Stochastic Nature of the Motion of Nonspherical Aerosol-Particles .3. The Rotational Diffusion Diadic and Applications. *Journal of Colloid and Interface Science* **1981,** *81*, (1), 214-233.

103. Ku, B. K.; de la Mora, J. F., Relation between Electrical Mobility, Mass, and Size for Nanodrops 1-6.5 nm in Diameter in Air. *Aerosol Science and Technology* **2009,** *43*, (3), 241-249.

104. Ni, W.; Kou, X.; Yang, Z.; Wang, J. F., Tailoring longitudinal surface plasmon wavelengths, scattering and absorption cross sections of gold nanorods. *Acs Nano* **2008,** *2*, (4), 677-686.

105. TSI Model Series 3080 Electrostatic Classifiers Operation and Service Manual. In TSI Inc. Shoreview, MN.

106. Jones, T. B., *Electromechanics of particles*. Cambridge University Press: Cambridge ; New York, 1995; p xxii, 265 p.